
Emission nebulae at high redshift

Anna Raiter



München 2010

Emission nebulae at high redshift

Anna Raiter

Dissertation
an der Fakultät für Physik
der Ludwig–Maximilians–Universität
München

zur Erlangung des Grades
Doktor der Naturwissenschaften
Dr.rer.nat.

vorgelegt von
Anna Raiter
aus Szczecin, Polen

München, September 2010

Erstgutachter: Prof. Andreas Burkert

Zweitgutachter: Prof. Hans Böhringer

Tag der mündlichen Prüfung: 9 November 2010

Contents

Abstract	xv
Zusammenfassung	xvii
1 Introduction	1
1.1 Population III stars and transition to Population II	5
1.2 Emission lines	8
1.3 Lynx arc	13
1.4 GOODS survey	16
1.5 This thesis	18
2 Tools	21
2.1 CLOUDY photoionization code	21
2.2 Structure of H II region	22
2.3 Stellar population synthesis models	23
3 Predicted UV properties of very metal-poor starburst galaxies	27
3.1 Introduction	27
3.2 Modelling techniques	29
3.2.1 Synthesis models	29
3.2.2 Photoionization models	33
3.3 Predicted UV properties from synthesis models	34
3.3.1 Ionizing photon production	35
3.3.2 Properties of the ionizing spectra	36
3.3.3 SFR calibrations from the UV continuum	37
3.3.4 Predicted Ly α emission	39
3.3.5 He II line emission from very metal-poor starbursts	41
3.3.6 Importance of the nebular continuum	42
3.3.7 Predicted UV slope	43
3.4 Nebular predictions using photoionization models	43
3.4.1 Ly α line and two-photon continuum emission	44
3.4.2 Other H lines	46
3.4.3 He II lines	47

3.4.4	Nebular continuum emission	47
3.5	Photoionization models for realistic SEDs	48
3.5.1	How to connect realistic SEDs with black body calculations	48
3.5.2	Ly α equivalent width predictions	49
3.5.3	He II λ 1640 equivalent width	50
3.5.4	Summary	51
3.6	Discussion and implications	51
3.6.1	Dependence on model assumptions	51
3.6.2	Lyman continuum output	52
3.6.3	SFR(UV)	52
3.6.4	Ly α	52
3.6.5	He II emission	53
3.6.6	Nebular continuous emission	54
3.7	Conclusions	54
4	Lyα emitters in the GOODS-S field: The powerful pure nebular SED	65
4.1	Introduction	65
4.2	Data	67
4.2.1	Sample	67
4.2.2	Photometry	68
4.2.3	The N IV] emitter	68
4.3	SED modelling	69
4.3.1	GDS J033218.92-275302.7	69
4.3.2	Sample modelling	73
4.4	Discussion	73
4.5	Conclusions	75
5	Analysis of other examples of N IV] emitters	83
5.1	J033217.22-274754.4	83
5.1.1	IRAC bands fluxes	88
5.2	DLS 1053–0528	90
5.3	GOODS-N source	90
5.4	Conclusions	91
6	Observational attempts to study objects with strong nebular emission	95
6.1	GDS J033218.92-275302.7 – X-shooter follow-up	95
6.1.1	X-shooter	95
6.1.2	The proposal	95
6.1.3	Observations	96
6.1.4	Data reduction	96
6.1.5	Results	97
6.1.6	Conclusions	97
6.2	GDS J033218.92-275302.7 – APEX follow-up – FIR [C II] cooling line	105

Content	vii
6.3 The effect of [O III] lines for $z \sim 3.5$ galaxies	107
6.4 Low redshift analogs ? - “Green Pea” galaxies	112
7 Conclusion and future prospects	115
Appendix	119
Bibliography	131
Acknowledgements	137
CV	139

List of Figures

1.1	Comparison of popular IMFs	3
1.2	Black body ionizing spectra for different temperatures	5
1.3	Star formation rate and metallicity as a function of redshift	7
1.4	Evolution of zero metallicity stars	9
1.5	Electron number density from UV line ratios	10
1.6	An example of the BPT diagram	12
1.7	Lynx arc spectra - part 1.	13
1.8	Lynx arc spectrum (H-band) - part 2.	14
1.9	Lynx arc spectrum (K-band) - part 3.	15
1.10	Nebular nitrogen line spectrum for black body ionizing source	17
1.11	Nebular nitrogen line spectrum for power law ionizing source	18
2.1	CLOUDY geometries	22
2.2	CLOUDY continua	23
2.3	Example case: distribution of the electron temperature	24
2.4	Example case: ionization fractions	25
2.5	Characteristics of the stellar population synthesis models	26
3.1	Relative output of hydrogen ionizing photons to UV continuum light	33
3.2	Temporal evolution of Q_H/L_{1500} for selected IMFs	35
3.3	Mean ionizing photon energy in units of 13.6 eV as a function of metallicity	37
3.4	Dependence of the SFR(UV) calibration on metallicity and IMF	38
3.5	Predicted Ly α equivalent width as a function of metallicity	39
3.6	Fraction of the Ly α luminosity to the total bolometric luminosity	40
3.7	Predicted He II $\lambda 1640$ equivalent width as a function of metallicity	41
3.8	Nebular continuum emission/total emission at 1500 Å	42
3.9	Predicted UV slopes for all IMFs and metallicities	44
3.10	Ly α , 2γ , H α , H β , He II 1640 Å luminosities over their case B luminosities	56
3.11	f_{coll} factor accounting for the density effects	57
3.12	Balmer decrement as a function of T_{bb} and n_H for primordial metallicity	58
3.13	Continuum of $T_{\text{bb}}=100,000$ K models as a function of the nebular metallicity	59
3.14	Continuum of $T_{\text{bb}}=100,000$ K models as a function of the density	60
3.15	Comparison of black body and real SED input stellar spectra	61

3.16	Equivalent widths of Ly α at 1240 and 1500 Å and He II λ 1640	62
3.17	Equivalent widths of Ly α at 1240 Å: zoom	63
4.1	Image cutouts of GDS18.92–02.7	67
4.2	FORS2 spectra and photometric SED – part 1 (redshifts 3.6–4.8)	77
4.3	FORS2 spectra and photometric SED – part 2 (redshifts 4.8–5.9)	78
4.4	FORS2 spectrum of source GDS18.92–02.7	79
4.5	Observed and modelled SED of GDS18.92–02.7	80
4.6	The effect of varying nebular parameters on the observed SED	81
5.1	FORS2 spectrum of J033217.22-274754.4 source	84
5.2	SED of J033217.22-274754.4 source at $z=3.652$	85
5.3	SED of J033217.22-274754.4 source and the nearby source at $z=3.76$	86
5.4	The spectrum of DLS 1053–0528 at $z = 4.02$	89
5.5	Rest-frame SED of DLS 1053–0528	89
5.6	N IV] emission line in the spectrum of DLS 1053–0528	91
5.7	Ly α line and no detection of N V in the spectrum of the GOODS-N source	92
5.8	N IV] line in the spectrum of the GOODS-N source	93
5.9	C IV lines in the spectrum of the GOODS-N source	94
6.1	VIS X-shooter results: Ly α	98
6.2	VIS X-shooter results: N IV]	99
6.3	NIR X-shooter results: C IV	100
6.4	NIR X-shooter results: He II	101
6.5	NIR X-shooter results: O III]	102
6.6	NIR X-shooter results: N III]	103
6.7	NIR X-shooter results: C III]	104
6.8	$L_{[\text{C III}]}/L_{\text{FIR}}$ as a function of L_{FIR}	106
6.9	Normalized total flux in U, B, V, i, z, J, K and 3.6, 4.5, 5.8, 8 μm	108
6.10	Figure similar to figure 1 but showing the results for the models	109
6.11	CLOUDY model (νF_ν versus λ) calculated for 10^{-1} solar nebular metallicity	110
6.12	Evolution of J - Ks colour with redshift	111
6.13	SED of an example ‘Green Pea’ galaxy	112
6.14	[O III] λ 5007 equivalent widths distribution	113
7.1	EW(N V 1240 Å)	119
7.2	EW(Si IV 1397 Å)	120
7.3	EW(N IV] 1486 Å)	121
7.4	EW(C IV 1549 Å)	122
7.5	EW(O III] 1665 Å)	123
7.6	EW(N III] 1750 Å)	124
7.7	EW(C III] 1909 Å)	125
7.8	EW(C II] 2326 Å)	126
7.9	EW([O II] 3727 Å)	127

7.10 EW([O III] 4363 Å)	128
7.11 EW([O III] 5007 Å)	129

List of Tables

3.1	Summary of IMF model parameters	30
4.1	Physical quantities of GDS18.92–02.7 from the optical spectrum	69
4.2	Parameters of GDS18.92–02.7 fiducial photoionization model	71
4.3	GDS18.92–02.7 fiducial model emission line spectrum	72
4.4	Photometry of sample sources	82

Abstract

The study of the high redshift (high- z) Universe is one of the great challenges of modern observational astrophysics. Using survey data we begin to learn about the nature of galaxies in the early Universe, approaching redshift 6, when the Universe was $\sim 10\%$ of its current age. However, limited observations hamper the application of the methodology developed for local galaxies to the distant ones.

This thesis is an attempt to study high- z objects using their line emission, which is interpreted with photoionization models. The observational part, inspired by the discovery of the prototype object – the Lynx arc, contains the analysis of several galaxies which show clear N IV] $\lambda 1486$ emission, which is rarely detected in astronomical objects. The analysis of N IV]-emitting galaxies brings interesting conclusions on the nature of their ionizing source, as well as on the properties of their diffuse gas. The favored thermal ionizing source must be very hot ($\sim 80,000$ K), which implies a young age and a very low metallicity of the stellar population, while the gas needs to be slightly polluted with metals.

In the theoretical part I present the study of the UV part of the spectrum of very metal-poor starbursts. The environment that is studied is representative of the one we expect for the first luminous objects that appeared in the Universe. The analysis is focused on the Ly α line, the 2γ continuum and the He II $\lambda 1640$ line emission. This study will serve as a theoretical framework for the interpretation of high- z sources and has been performed without applying the common assumption of case B recombination. An enhancement of the Ly α line as well as the 2γ continuum emission is obtained. Additionally, the He II $\lambda 1640$ line, considered a sign of very metal-poor environment (or the presence of Wolf-Rayet stars), is analysed. Its equivalent width can decrease due to the ionization parameter dependence and/or due to the influence of the underlying enhanced 2γ emission.

It is beyond our current possibilities to provide a detailed scenario of the evolution of N IV]-emitting galaxies. Detailed future studies and the access to more UV emission lines will allow us to infer the nature of the ionizing source, and perhaps this line will help to identify sources that are candidates of primordial star formation sites. This will be possible with JWST and E-ELT IR spectroscopy and ALMA millimeter observations of cooling lines.

Our theoretical predictions are of relevance in the context of searches and interpretation of Ly α -emitting galaxies at high- z and of the future observations of the first objects that appeared in the Universe.

Zusammenfassung

Die Untersuchung des Universums bei hoher Rotverschiebung ist eine der größten Herausforderungen der modernen beobachtenden Astrophysik. Himmelsdurchmusterungen erlauben das Studium von Galaxien im jungen Universum bis zu einer Rotverschiebung von $z = 6$, als das Universum nur ein zehntel seines heutigen Alters hatte. Jedoch ist es mithilfe der (vergleichsweise) beschränkten Beobachtungsdaten nicht möglich, die Methoden, die anhand lokaler Galaxien entwickelt wurden, auf die entfernten Objekte anzuwenden.

Diese Arbeit beschreibt den Versuch, hochrotverschobene Objekte anhand ihrer Emissionslinien zu untersuchen, welche mit Hilfe von Photoionisationsmodellen interpretiert werden. Der Beobachtungsteil wurde durch die Entdeckung des prototypischen Lynx Arc angeregt, und beschreibt die Analyse mehrerer Galaxien, die eindeutig die in astronomischen Objekten selten auftretende N IV] $\lambda 1486$ Emission zeigen. Die Analyse von N IV]-emittierenden Galaxien erlaubt interessante Schlussfolgerungen, sowohl über ihre ionisierenden Quellen, als auch über Eigenschaften ihres diffusen Gases. Die wahrscheinlichste Quelle der ionisierenden thermischen Strahlung muss sehr heiss sein ($\sim 80,000$ K); dies bedeutet, dass die Sternpopulation sehr jung und metallarm sein muss. Das Gas muss leicht mit Metallen verunreinigt sein.

Im theoretischen Teil dieser Arbeit stelle ich eine Untersuchung des UV-Spektrums sehr metallarmer Starbursts vor. Diese Umgebung ist repräsentativ für eine Umgebung, die wir für die Zeit annehmen, zu der sich die ersten leuchtenden Objekte im Universum formten. Die Analyse konzentriert sich auf die Ly α Linie, das 2γ Kontinuum sowie die He II $\lambda 1640$ Linienemission. Diese Studie dient als theoretischer Rahmen für die Interpretation hochrotverschobener Objekte und nimmt nicht, wie sonst üblich, case B Rekombination an. Wir erhalten eine Verstärkung der Ly α Linie sowie die 2γ Kontinuumsstrahlung. Desweiteren wird die He II $\lambda 1640$ Linie, welche als Zeichen einer sehr metallarmen Umgebung (oder der Gegenwart von Wolf-Rayet Sternen) interpretiert wird, analysiert. Ihre Äquivalentbreite kann durch Abhängigkeit von den Ionisationsparametern oder den Einfluss der verstärkten 2γ Emission verringert werden.

Es liegt derzeit noch ausserhalb unserer Möglichkeiten, ein detailliertes Szenario N IV]-emittierender Galaxien zu beschreiben. Künftige, detailliertere Untersuchungen und der Zugang zu weiteren UV-Emissionslinien werden es möglich machen, auf die Natur der ionisierenden Quellen zu schliessen, und vielleicht hilft uns diese Linie, Kandidaten für primordiale Sternentstehung zu identifizieren. JWST und E-ELT IR-Spektroskopie sowie ALMA Beobachtungen von Kühlungslinien im Millimeterbereich werden dies ermöglichen.

Unsere theoretischen Vorhersagen haben Bedeutung im Zusammenhang mit der Suche nach und Interpretation von hoch-rotverschobenen Ly α -emittierenden Galaxien sowie künftigen Beobachtungen der ersten Objekte im Universum.

Chapter 1

Introduction

In the Λ CDM scenario, structures in the Universe form “bottom-up” i.e. hierarchically, which means first on small scales. The formation of the first stars is followed by galaxy and galaxy cluster formation. Numerical simulations predict that the first stars were formed in dark matter minihaloes with masses $\sim 10^6 M_{\odot}$ at redshifts $z \approx 50 - 10$. Already in the late sixties Partridge & Peebles (1967) predicted the nebular emission from young galaxies in the early Universe and proposed that they should emit a strong Ly α line in the first stages of their formation.

With the advent of 4 meter telescopes in the 1970’s and 1980’s began the search to discover the era of galaxy formation. Stellar synthesis models at that time predicted that the present-day passive systems could have formed at high- z via a luminous initial burst (Tinsley 1980). Therefore, they should be detectable at $z \simeq 2-3$ at magnitudes $B \simeq 22-23$ and produce a population of blue galaxies (Ellis 2008). However, the first searches for luminous Ly α emitters were unsuccessful (Pritchett 1994).

The development of theoretical models in the 1980’s changed our thinking about primeval galaxies. Dark-matter based predictions emphasized the gradual assembly of massive galaxies implying their much reduced number at $z \simeq 2-3$. Additionally, it was realized that the flux limits had been optimistically bright. Only with the advent of ground-based optical/infrared 8-10 meter telescopes, like Keck, and the Hubble Space Telescope in the 1990’s did the era of collecting high- z galaxy data start.

Since then surveys, like GOODS, have observed thousands of objects, including some with redshifts 6 and beyond, mainly due to the possibility of using multi-object spectrographs. Two main techniques are used to identify objects at high- z . The broadband technique (or drop-out) relies on the detection of the characteristic break in the spectrum at rest-frame wavelengths shorter than 1216 Å (Ly α line) produced by the absorption of the Lyman continuum by neutral hydrogen and the Ly α forest. It selects the so-called Lyman Break Galaxies (LBGs). The ones with Ly α emission can be also identified with the narrowband technique. In this case two filters are used (the spectral range observed should not be affected so much by the night sky) where one searches for the flux excess due to Ly α line at a certain redshift in one filter with respect to the other which measures the continuum around the line.

Although Ly α can be considered a sign of ongoing star formation, it is not trivial to draw any conclusion on the nature of the source from this line itself. Several effects affect the intrinsic Ly α flux (and therefore also its equivalent width, EW) and its profile, including scattering and destruction by dust grains. That can result in only part of the Ly α flux escaping from the galaxy which is defined by Ly α escape fraction.

Apart from the Ly α line itself, multi-wavelength data are also used to interpret the nature of the observed sources. Large number statistics allowed the studies of stellar mass assembly and the discovery of the “downsizing” effect (Cowie et al. 1996), morphology and star formation history and their dependence on the environment, AGN activity, dust properties, luminosity functions etc. from only 1 Gyr after the Big Bang ($z \sim 6$) until now.

The galaxy observations are usually interpreted by comparing them to the stellar population synthesis models, where one of the most popular are those of Bruzual & Charlot (2003). The models are constructed based on observed stellar spectra. The luminosity, colours and spectrum of the stellar population as a function of age is obtained by summing up the individual stellar templates after weighting them by the initial mass function (IMF). The most commonly used is the Salpeter IMF (Salpeter 1955, see the comparison of popular IMFs in Fig. 1.1) which is a pure power law with slope $x = 1.35$. Additionally, a certain star formation history is used. These kinds of models are treated as templates to be compared to the observed galaxy spectral energy distribution (SED). The observed SED is composed of a number of photometric magnitudes in different filters over a wide wavelength range and can be treated as a very low resolution spectrum. The SED fitting technique gives as output a number of best-fitting parameters characterising the galaxy. With the best-fitting template SED one obtains the age, metallicity, star formation history (SFH), star formation rate (SFR), extinction E(B-V) and also the photometric redshift.

The same models are used to interpret high- z observations. However, at high redshifts we approach the era of early star formation where the first generation of stars was formed. The nature of the objects is unclear. A number of simplifications/assumptions commonly used might not be appropriate for application in this case.

For example, due to the lack of knowledge on the early IMF, it is normally assumed to be the Salpeter one. However, if it is top-heavy (mainly massive stars), as suggested by simulations, the stars have very high effective temperatures and a large number of ionizing photons is produced per second. Ionizing the gas around such stars produce ionized “bubbles” (nebulae). If the ionizing spectrum is approximated by a black body (which is justified in this case), only the Rayleigh - Jeans tail part remains not absorbed in the surrounding gas. The entire emission observed in this case would be dominated by the nebular contribution. This effect is shown in Fig. 1.2, where the dotted lines are the black body ionizing spectra with different temperatures, the dashed lines represent the nebular continuum emission and the solid lines are the sum of the attenuated (so emitted beyond the nebula) black body continua and the nebular continua. In this case it becomes difficult to analyse the nature of the underlying stellar population since we do not observe any stellar light longward of the Lyman limit. Therefore, the standard SED fitting technique cannot be applied since one does not know the amount of the nebular emission contributing to the observed SED. Not including nebular flux in the SED fitting can cause serious

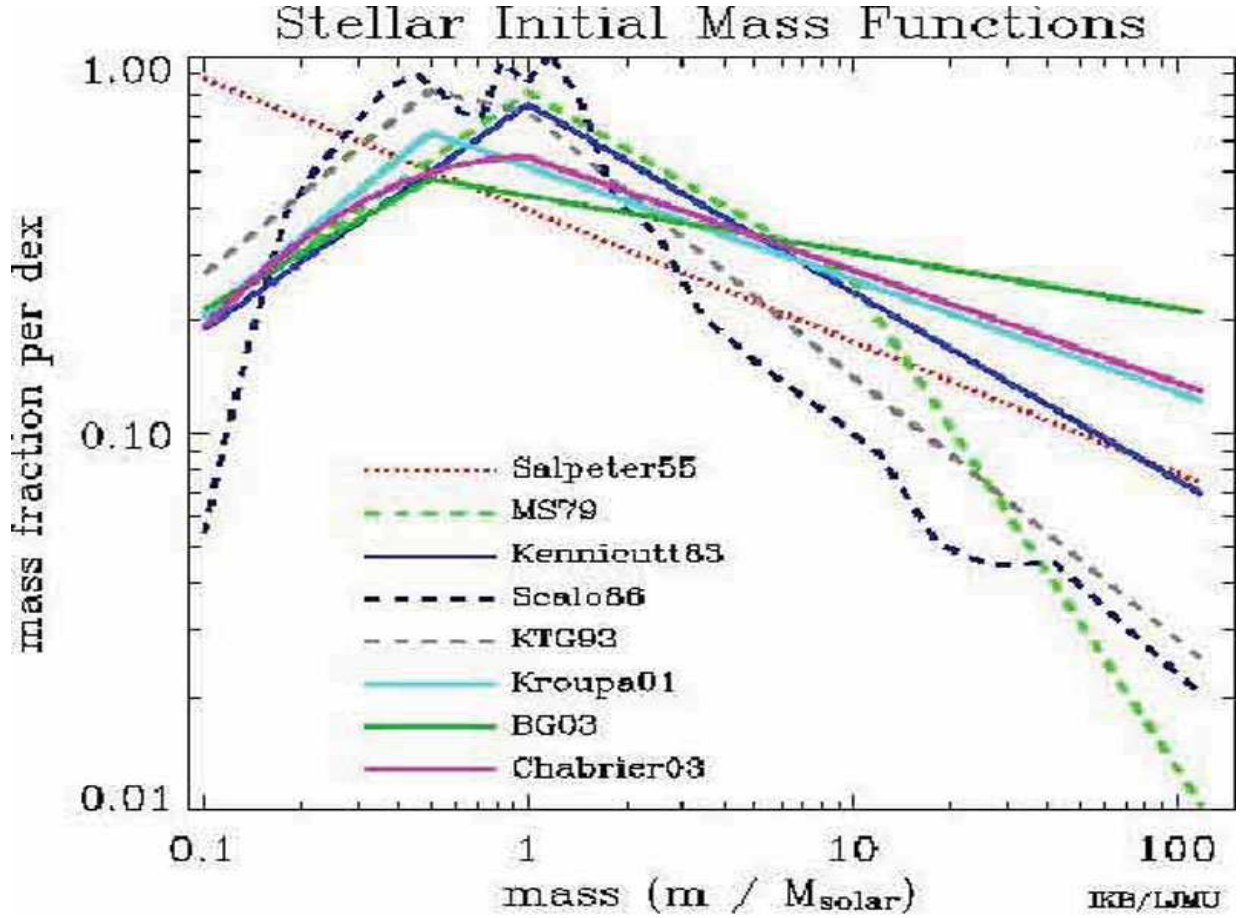


Figure 1.1: Comparison of popular IMFs (from Ellis 2008), the Salpeter one is shown with the red dotted line.

errors in the whole procedure and can be a reason of confusion. For example, in the low metallicity regime, the $[\text{O III}] \lambda\lambda 4959, 5007$ lines are the dominant coolants and if they become very strong they can influence the SED shape. Chapter 4 and Schaerer & de Barros (2009) discuss the influence of the nebular emission lines on the overall SED, especially on the calculation of the galaxy age. Recently, several authors have attempted to include the nebular emission in the SED fitting procedure (Schaerer & de Barros 2010; Ono et al. 2010). They assume the standard case B theory which is not necessarily suitable for a hot ionizing source and very low nebular metallicity. In particular, those conditions might result in enhanced 2γ continuum emission (to be discussed in detail in Chapter 3) in the rest-frame UV, changing the shape of the SED in that spectral region.

The same stellar population synthesis models were used to calibrate the SFR indicators. One of them is the UV ($\lambda\lambda = 1250 - 2500 \text{ \AA}$) luminosity. It measures the SFR because in the UV the integrated spectrum is dominated by young stars, therefore SFR scales linearly with luminosity. It is longward of the $\text{Ly}\alpha$ forest region as well as shortward of the possible region contaminated by older stellar population radiation (Kennicutt 1998).

The contamination from or the dominance of the nebular continuum, particularly strong 2γ continuum in the UV, would invalidate this SFR indicator, since it is based on the assumption of stellar radiation.

Another problem, perhaps the most important one, is the measurement of the galaxy metallicity. When the nebular emission is not included in the templates used for the SED fitting, the metallicity effect on the SED can be confused with the effect of age and/or dust. When the nebular contribution is included, it is assumed to be equal to the stellar one for modelling purposes and the abundances of elements are scaled solar abundances. Then in the fitting procedure the metallicity is like other parameters obtained based on the shape of the SED. To really measure the gas phase metallicity/ elemental abundances we need to observe emission lines. The Lynx arc (to be discussed in Section 1.3) is one of the few examples of high- z objects where we have the data available over a wide wavelength range and can observe (thanks to lensing) many emission lines and measure the abundances of elements. An example of determining the nebular (gas phase) metallicity for high- z galaxies is the work of Maiolino et al. (2008) where the authors study the mass-metallicity relation at redshift ~ 3.5 with VLT SINFONI ¹. For this redshift, H (centered at $1.65 \mu\text{m}$) and K (centered at $2.2 \mu\text{m}$) bands contain redshifted [O II] $\lambda 3727$, H β and [O III] $\lambda\lambda 4959, 5007$ emission lines which allows the use of R23 method (to be explained in Section 1.2) to determine the metallicity. At even higher redshifts (> 3.5) we can usually see only Ly α redshifted to the optical regime, making impossible the proper metallicity estimate.

The observation of metal emission lines at high- z is particularly interesting since we approach the era of early star formation where we believe that the metals observed are the ones produced by the underlying stellar population (the gas was not much metal-enriched before). Therefore, we could be observing some of the first stellar nucleosynthetic products in the Universe.

Emission lines carry information on the diffuse gas where they have been formed and, combined with the shape of the continuum / multi-wavelength SED, give some information on the ionizing source. Many lines that are commonly used as nebular parameter diagnostics are not accessible for observations in the case of high- z galaxies since they are shifted to the infrared, therefore it is difficult to detect them from the ground. However, the access to the rest-frame UV part of the spectrum for galaxies at $z > 2.5$ with current observing facilities opens the possibility of detecting emission lines in the UV. In most of the cases only the Ly α line is observed. Hot stars and low metallicity nebular gas produce a richer UV emission line spectrum. Therefore, it is important to understand this part of the spectrum especially before the era of large telescopes like E-ELT and JWST to anticipate the expected properties of the objects which are going to be detected like the nature of the ionizing sources, early chemical evolution and mixing processes in the first galaxies. That pushes the investigation of metal enrichment process and the searches for very first, very metal-poor stellar populations that appeared in the Universe to higher redshifts.

¹SINFONI is near-IR (1.1 - 2.45 μm) integral field spectrograph installed at the Cassegrain focus of VLT UT4.

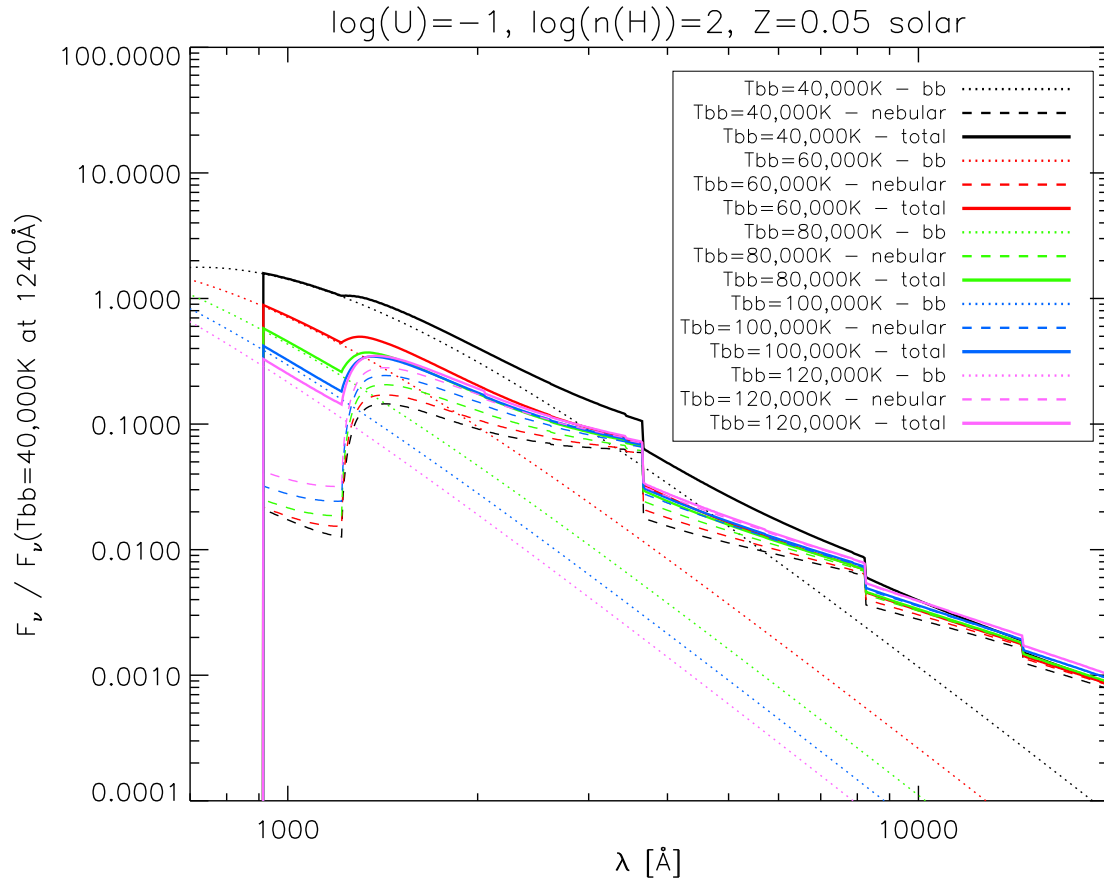


Figure 1.2: Black body ionizing spectra for different temperatures (dotted lines), corresponding nebular continuum emission (dashed lines) and the synthetic (total) continuum emission (solid lines) for each of the cases including attenuated part of the black body spectra and the nebular contribution. Notice that for the hottest black bodies the nebular emission is the dominant one. The nebular line emission is not shown.

1.1 Population III stars and transition to Population II

The first stellar population (Population III, hereafter Pop III stars) that appeared in the Universe, and preceded known Population II and I, is believed to be formed out of the primordial gas. Its mechanical, radiative and chemical feedback on the surrounding medium is being studied by simulations. The first stars are believed to form between redshifts ~ 50 and 10 and to light up (reionize) the Universe after the so called “dark ages” that started at $z \sim 1000$ (last scattering surface) and finished around $z \sim 6$ when the reionization is completed. Their feedback strongly depends on the IMF, which might have favored massive stars i.e. $\gtrsim 100 M_{\odot}$ (Bromm et al. 1999; Abel et al. 2000). The argument that supports

massive star formation at high- z is that the metals are observed in quasar spectra at redshifts corresponding to only 10% of the current age of the Universe. Therefore, they must have been synthesized, released and distributed in the intergalactic medium (IGM) within the first billion years. The supernovae of short lived massive stars are known to provide such an enrichment mechanism (Abel et al. 2002). High effective temperature, $T_{eff} \sim 10^5$ K for stellar masses $M \gtrsim 100 M_{\odot}$ (almost independent on mass; Bond et al. 1984; Bromm et al. 2001) makes the stars efficient in ionizing hydrogen and helium. Therefore, we expect to observe bubbles of ionized gas - emission nebulae, where most of the radiation emitted longward from Lyman limit (912 Å) is the stellar radiation absorbed by the gas and then reemitted at longer wavelengths in the form of nebular continuum and line emission.

The chemical feedback is dependent on the final fate of the star, which in case of being very massive, can end its life either directly becoming a black hole, without any metal ejection into the IGM, or as pair instability supernova (PISN, Heger et al. 2003a). There is a narrow range of initial stellar masses when the latter is supposed to happen: 130 – 260 M_{\odot} and only they contribute to the pollution of the IGM. The metal yields from those objects are given by Heger & Woosley (2002) as a function of the initial stellar mass. However, another source of metal pollution might be stellar winds. While metal-free non-rotating hot stars are unlikely to develop winds (Krtićka & Kubát 2006), Meynet et al. (2006) show that the very metal-poor ones due to strong internal mixing show large mass loss. Rotationally enhanced winds are largely enriched with CNO cycle products, particularly abundant primary nitrogen.

Until now we have not found a single clear example of Pop III object but the models have been developed predicting their intrinsic properties like spectral energy distributions and nebular emission (Schaerer 2002, 2003), the radiative transfer processes and the observable properties like the redshift evolution of the colours (Tumlinson et al. 2003) of those stars/stellar populations. Due to high effective temperatures in the case of a small escape fraction of the Lyman continuum photons the overall resulting spectrum of Pop III starburst contain only a small fraction of the stellar continuum, which has not been absorbed by the gas and is dominated by the nebular emission (continuum and lines). Therefore, the methods of finding them rely on searching for some nebular emission features. The most likely signature of Pop III starburst is a strong Ly α and He II $\lambda 1640$ Å emission line. Therefore, there have been searches conducted in order to identify such “dual emitters”, but none has been found at high- z (Nagao et al. 2008). However, there have been interesting discoveries related with this topic, i.e. Ouchi et al. (2009) have identified a giant, extended Ly α emitter at redshift $z=6.595$, Prescott et al. (2009) have found spatially extended Ly α + He II (with weak C IV $\lambda 1549$ and C III] $\lambda 1909$ lines) emitter at $z=1.67$. The nature of those objects still remains unclear.

Theoretical findings suggest that the early mode of star formation could continue until quite low redshift. Tornatore et al. (2007) based on the numerical simulations of Pop III – Pop II transition find Pop III star formation until $z \approx 2.5$ (Fig. 1.3) due to the fact that pockets of primordial gas continue to exist because of inefficient metal mixing. Jimenez & Haiman (2006) find a similar conclusion. Consequently the metal distribution in the enriched gas becomes inhomogeneous. Also Mori & Umemura (2006) performed

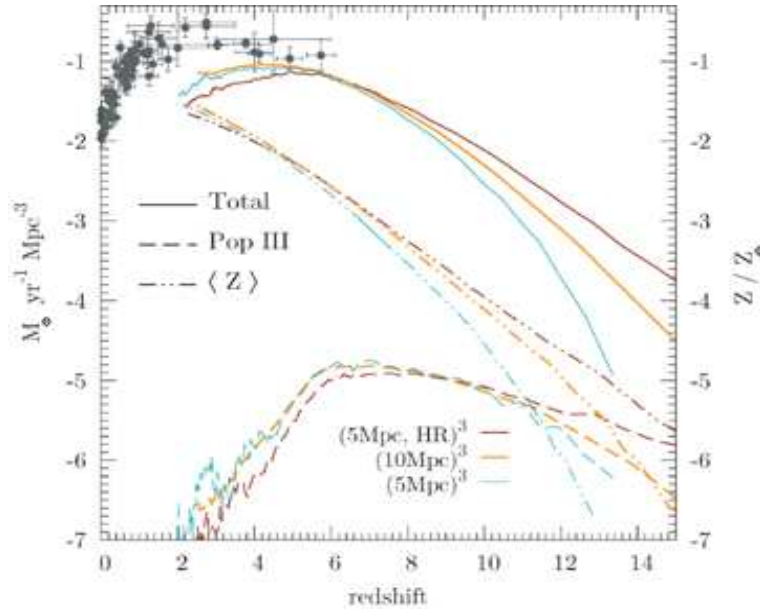


Figure 1.3: Star formation rate and metallicity as a function of redshift (from Tornatore et al. 2007). Solid and dashed lines show the redshift evolution of Pop II and Pop III stars respectively. Dot-dot-dashed line presents the evolution of metallicity. Different colours correspond to 3 different simulation runs and the observational points are the measurements as listed in Hopkins (2004).

ultra-high-resolution simulations of galaxy formation and studied the star formation, gas dynamics and chemical enrichment. Their simulation shows that the mixing of metals from exploding SNe with the ISM is inhomogeneous on the kpc scale in the first 10^8 years, therefore the quickly enriched regions in the SN vicinity coexist with the primordial gas.

Numerical simulations show that PISNe, possibly the first source of metals in the Universe, enriched the surrounding gas up to metallicity $Z \approx 10^{-4}Z_{\odot}$ (Schneider et al. 2002), the critical metallicity when the formation of $\lesssim 1 M_{\odot}$ stars occurs. Studying the abundance patterns in different kind of objects may reveal the imprint of the early mode of star formation. The detectability of the nucleosynthetic pattern of Pop III depends on the epoch when star formation occurred, stellar IMF, efficiency of enrichment processes and mixing. In our Galaxy in ESO/Hamburg survey data, very metal-poor stars have been found (in terms of iron abundance Fe/H), HE0107-5240 (Christlieb et al. 2002) and HE1327-2326 (Frebel et al. 2005) with iron abundances $[\text{Fe}/\text{H}] \approx -5.3$ ². However, we have not found yet objects showing a PISN nucleosynthetic pattern of abundances. Karlsson et al. (2008) construct a theoretical model of the chemical enrichment of the Galaxy, particularly by PISNe. They argue that the fact that we have not observed very metal-poor stars in the galactic halo that show abundance pattern characteristic for PISN is due to a selection effect, i.e. the PISN sign is to be found in star samples of higher metallicity than those

² $[A/X] = \log(N_A/N_X) - \log(N_A/N_X)_{\odot}$

where the most metal-poor stars have been found.

Alternatively, at high- z , the studies of abundance patterns of Ly α forest examine the metal content of the IGM (Ellison et al. 2000; Songaila 2001). This is difficult because only a limited number of elements is available and the ionization correction ³ is unknown. Scannapieco et al. (2003) discuss another possible detection method – studying the enrichment of the intracluster medium (ICM).

1.2 Emission lines

This section is based partially on the lectures “What can emission lines tell us” (Stasińska 2007) and on the book “Astrophysics of gaseous nebulae and active galactic nuclei” (Osterbrock & Ferland 2006).

Depending on the redshift, different emission lines can be detected in the spectra. Emission lines arise in the diffuse gas and carry the information on the regions where they have been formed. The main production mechanisms are recombination, collisional excitation and fluorescent excitation. The most commonly observed recombination lines are those of hydrogen and helium. Roughly two thirds of recombinations lead to deexcitation onto excited levels which is followed by cascade. The recombination line intensities increase with decreasing electron temperature. Collisionally excited lines (CELs) arise once the thermal electrons collide with atoms and lead to excitation of low energy levels. It is therefore dependent on the electron temperature of the gas whether a certain level of the atom can be collisionally excited. The highest electron temperatures are needed in order to produce UV collisionally excited lines, “typical” nebular electron temperatures ($\sim 10,000$ K) are enough to give rise to optical lines. CELs are divided into forbidden, semi-forbidden (intercombination) and permitted lines depending on the spontaneous transition probability. The *critical density* is reached when the collisional and radiative deexcitation rates are equal.

Emission lines can be used to determine:

- electron temperature (T_e)

In the low density limit (collisional deexcitation is negligible) the line ratios of collisionally excited lines of a certain element will depend only on the atomic transition probabilities and electron temperature. The most commonly used temperature sensitive line ratio is [O III] $\lambda\lambda 4959, 5007 / \lambda 4363$.

- electron number density (n_e)

Can be measured by observing the effects of collisional deexcitation, by comparing the line intensities of two lines arising from levels with the same excitation energy. The ratio of line intensities will depend on the density if those two levels have different radiative transition probabilities or collisional deexcitation rates. Commonly

³Ionization correction – factor accounting for the fact that not all the ionization stages of a certain element have been observed.

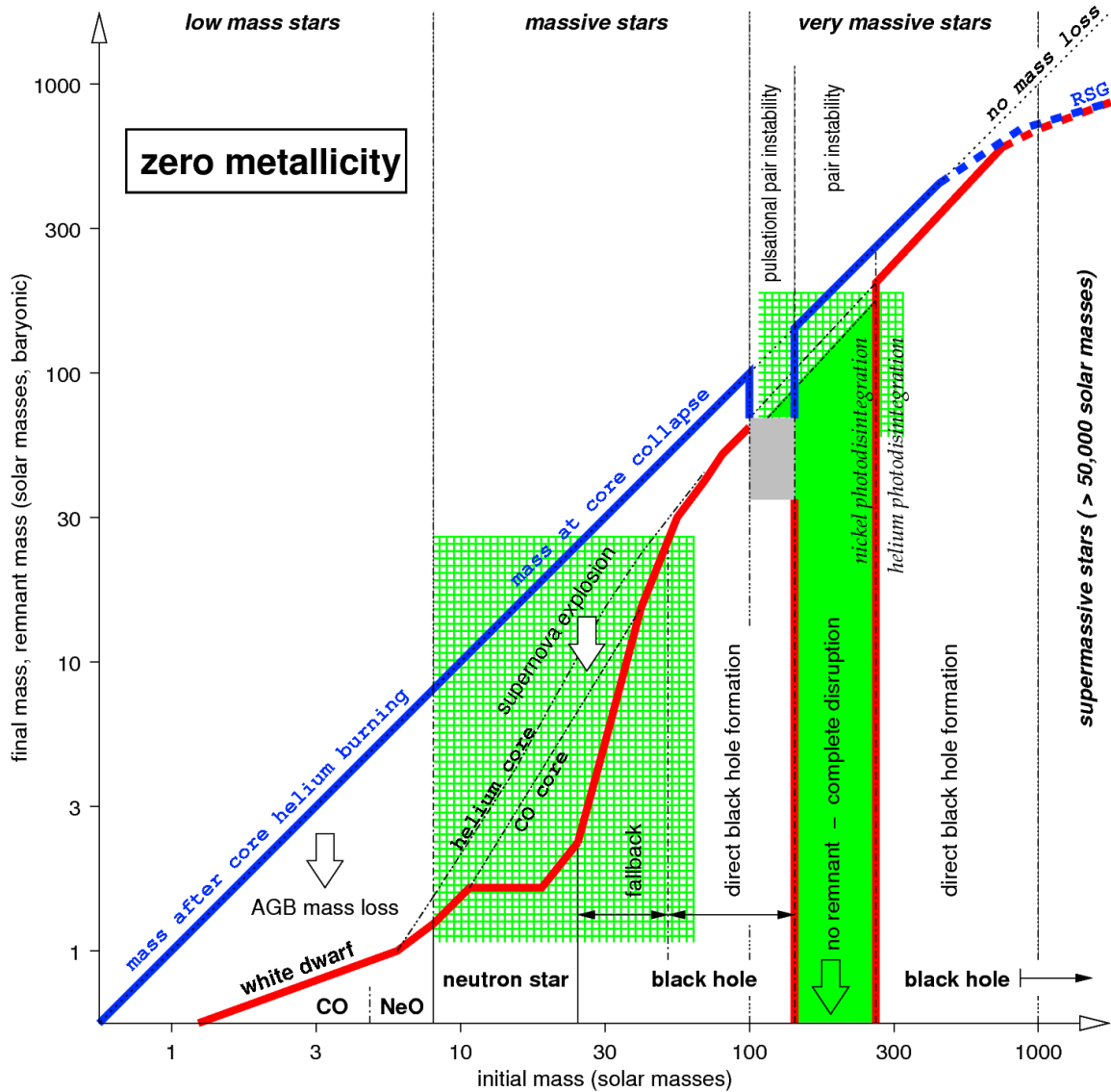


Figure 1.4: Evolution of zero metallicity stars. Massive/very massive stars can end their life either directly becoming a black hole with no remnant or exploding as pair instability supernova enriching the IGM with metals which happens for initial stellar masses between 130 and 260 M_{\odot} (from Heger et al. 2003b).

used line ratios are $[\text{O II}] \lambda 3729/\lambda 3726$ and $[\text{S II}] \lambda 6716/\lambda 6731$. Electron temperatures determined in that way might not always be representative for the entire nebula. In higher density environments also the ratio of forbidden and semi-forbidden lines can be used where the density dependence will reflect the different *critical densities* for those transitions. In the UV, the electron densities can be derived from $[\text{C III}] \lambda 1907/\text{C III}] \lambda 1909$, $[\text{N IV}] \lambda 1483/\text{N IV}] \lambda 1487$, $[\text{S III}] \lambda 1883/\text{S III}] \lambda 1892$ line

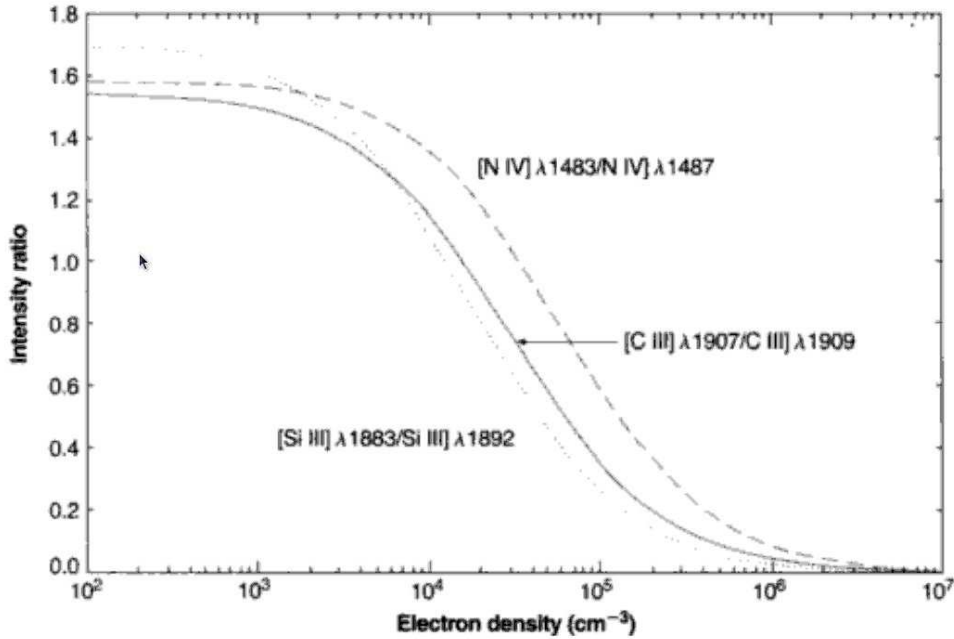


Figure 1.5: Electron number density dependence on the UV line ratios of forbidden and semi-forbidden emission lines (from Osterbrock & Ferland 2006).

ratios (Fig. 1.5).

- metallicity/ionic and elemental abundances

direct method: the abundance of a certain ion or the total abundance of an element is determined based on line intensity and electron temperature (T_e), electron number density (n_e) and ionization correction factor;

statistical methods: in other words “strong line methods”. They can be used when the determination of T_e or/and n_e is impossible and have been calibrated using photoionization models for other objects. The most popular is the method based on the oxygen lines, so called R23 or O23 introduced by Pagel et al. (1979), later refined to account for the ionization parameter. It determines the oxygen abundance (O/H) from the $([\text{O II}] \lambda 3727 + [\text{O III}] \lambda\lambda 4959, 5007)/\text{H}\beta$ line ratio. However, this method does not give unique solution, which is due to the fact that at low metallicities the ratio increases with increasing metallicity (oxygen abundance), but at high metallicities it decreases since the cooling by infrared lines becomes more efficient. Other line ratios must be checked in order to decide whether the object is in the low or high metallicity regime.

tailored photoionization modelling: the procedure is to run the photoionization models with an appropriate code after defining the input parameters which can be derived

from the available observations and iterate until the observations are reproduced.

comparison with a grid of models: building the grid of models and comparing the observations with them might be useful for statistical purposes when one deals with a large samples and tailored model fitting is impossible.

- dynamics

Doppler shifts and line profiles carry information on radial velocities, i.e. about the dynamics of the object, particularly interesting is the opportunity of using integral field (IFU) spectroscopy which provides also the spatial information, therefore allows the study of velocity gradients.

- the nature of the ionizing source

It was proposed already in 1981 by Baldwin, Phillips & Terlevich (Baldwin et al. 1981, thus called BPT diagram following the first letters of the authors' names) to use emission line ratios as a diagnostics to distinguish normal star forming galaxies from active galactic nuclei (AGN). In case of AGNs the optical collisionally excited lines are brighter with respect to the recombination lines than in the case of H II regions (ionization by massive stars) due to the fact that the ionizing photons carry higher energies. An example of the BPT diagram is shown in Fig. 1.6.

- star formation rate (SFR)

Can be determined from recombination lines as well as from forbidden lines (Kennicutt 1998).

In the case of the recombination lines, it is assumed that every ionizing photon is absorbed by the gas (therefore these lines can be used as indicators of the number of ionizing photons) and based on the evolutionary synthesis models the conversion factors between the ionizing flux and SFR can be determined. In the review article on star formation Kennicutt (1998) writes:

$$\text{SFR} [\text{M}_{\odot}\text{year}^{-1}] = 7.9 \times 10^{42} \text{L}(\text{H}\alpha) [\text{ergs s}^{-1}] = 1.08 \times 10^{-53} Q(\text{H}) [\text{s}^{-1}], \quad (1.1)$$

the calibration being obtained using case B recombination theory for $T_e = 10,000$ K, where $\text{L}(\text{H}\alpha)$ is the luminosity of $\text{H}\alpha$ emission line and $Q(\text{H})$ is the hydrogen number of ionizing photons. Similar equations can be written for other recombination lines.

SFR has also been calibrated using the forbidden $[\text{O II}] \lambda 3727$ line, because it can be observed at larger redshifts than $\text{H}\alpha$ and $\text{H}\beta$. However, it is risky to use it due to its dependence on the metallicity and the ionization parameter. In Kennicutt (1998) the following calibration is given:

$$\text{SFR} [\text{M}_{\odot}\text{year}^{-1}] = (1.4 \pm 0.4) \times 10^{-41} \text{L}([\text{O II}]) [\text{ergs s}^{-1}], \quad (1.2)$$

where $\text{L}([\text{O II}])$ is the luminosity of the $[\text{O II}] \lambda 3727$ line.

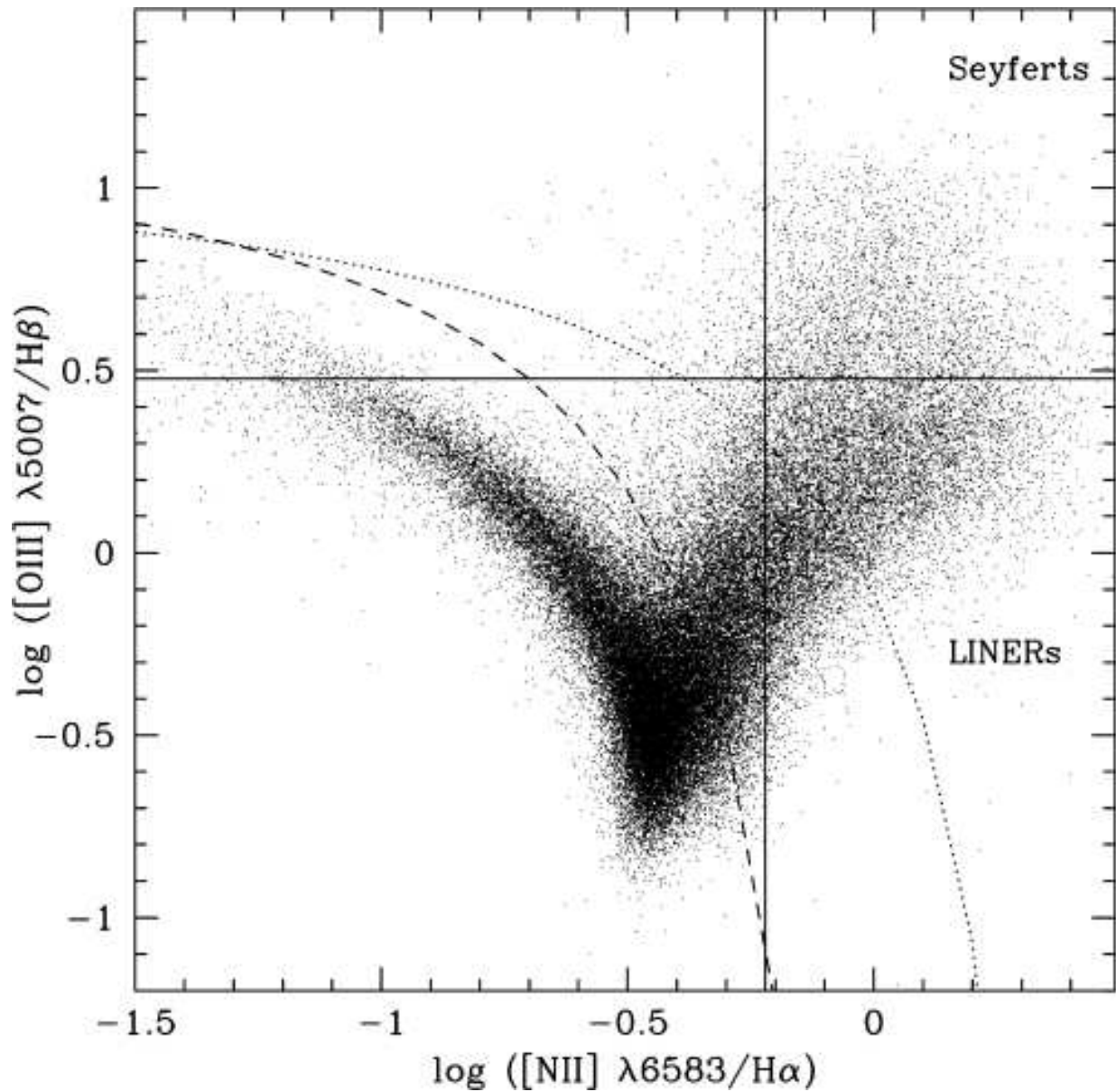


Figure 1.6: An example of the BPT diagram used to distinguish normal star forming galaxies from AGN hosts (from Kauffmann et al. 2003).

- redshifts

More reliable than the photometric ones, spectroscopic redshifts are usually inferred from strong emission lines (along with the characteristic breaks in the spectra).

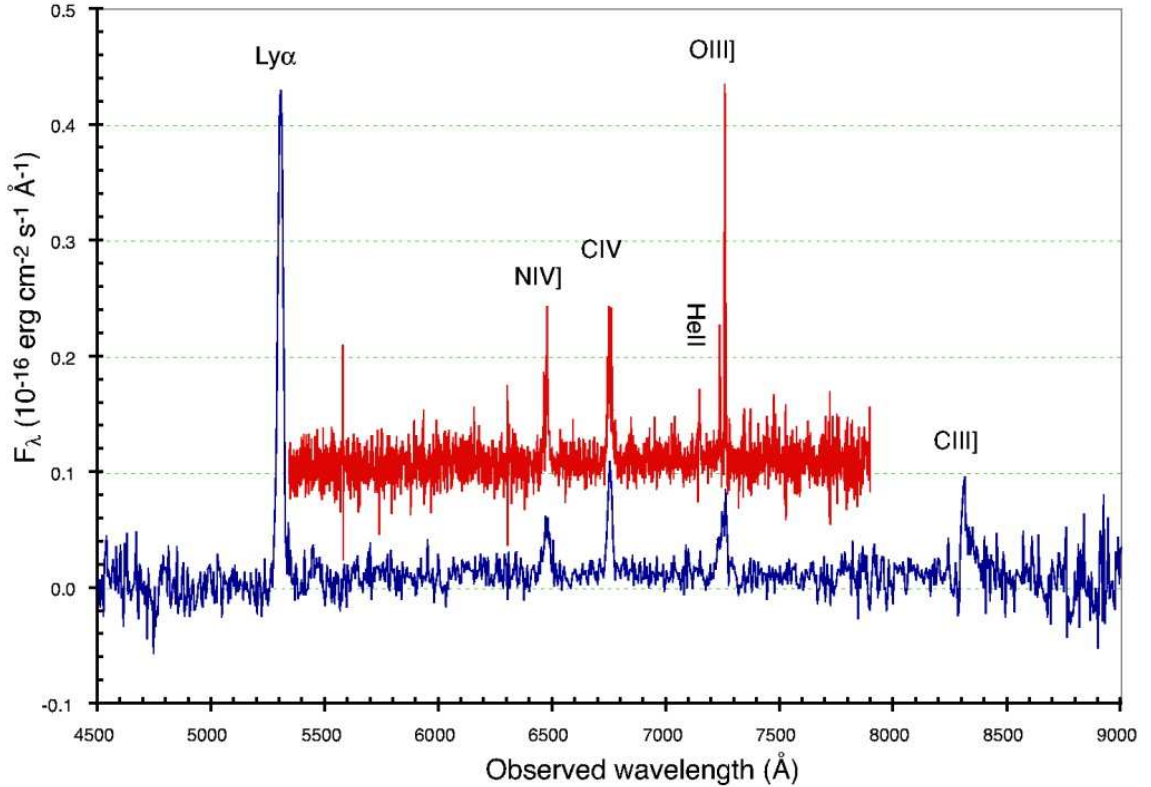


Figure 1.7: Lynx arc spectra - part I (from Fosbury et al. 2003). Spectra taken with the Keck I telescope using Low Resolution Imaging Spectrograph (LRIS), shown in the observed frame. The rest frame wavelengths of the lines marked are: Ly α λ 1216, N IV] $\lambda\lambda$ 1483, 1487, C IV $\lambda\lambda$ 1548,1551, He II λ 1640, O III] $\lambda\lambda$ 1661,1666 and C III] $\lambda\lambda$ 1907, 1909.

1.3 Lynx arc

Although no clear example of a Pop III object has been found, the real motivation for this project was the discovery of a very peculiar $z=3.357$ lensed galaxy with an unusual rich emission line spectrum (Figs. 1.7, 1.8, 1.9), the so called Lynx arc (Fosbury et al. 2003). The Lynx arc shows very flat continuum and large equivalent widths of emission lines. This is consistent with a continuum dominated by nebular continuum emission and Fosbury et al. (2003) conclude that there is no evidence for any underlying stellar continuum visible longward of Ly α . They infer high Lyman continuum luminosity, implying large number of massive stars in the cluster. They also analyse the chemical composition of the gas concluding that it has been already contaminated until metallicity $Z=0.05 Z_{\odot}$ ⁴.

⁴Here the metallicity is defined by scaling solar abundance pattern which means that the solar number densities of all the elements have been scaled by factor 0.05.

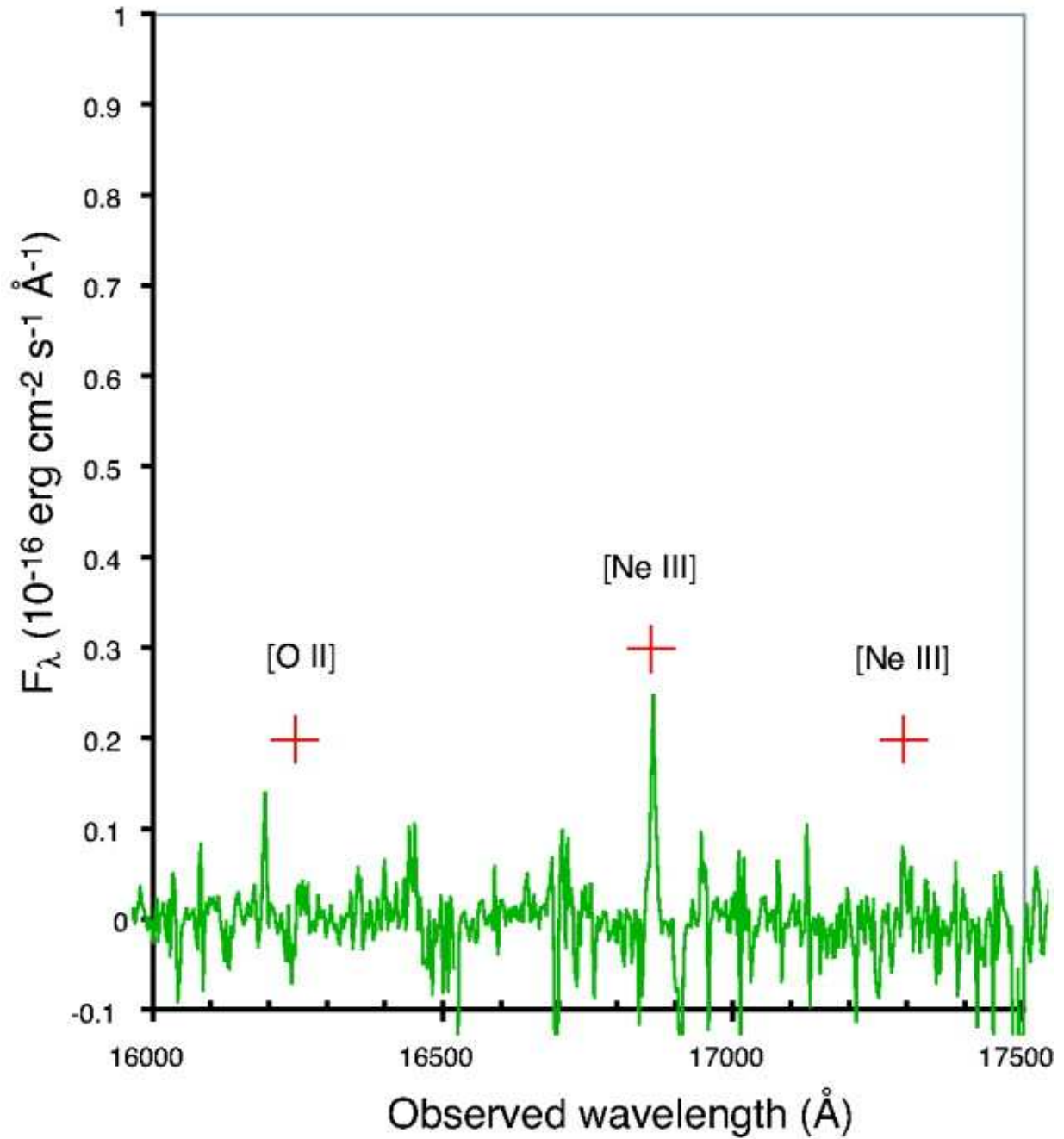


Figure 1.8: Lynx arc spectrum (H-band) - part II (from Fosbury et al. 2003). Spectrum taken with the Keck II telescope using NIRSPEC instrument, shown in the observed frame. The rest frame wavelengths of the lines marked are [O II] $\lambda 3727$ and [Ne III] $\lambda\lambda 3869, 3969$.

However, the stellar effective temperature must be high in order to produce high electron temperature, i.e. emission lines of highly ionized species in the UV. The Lynx arc is well

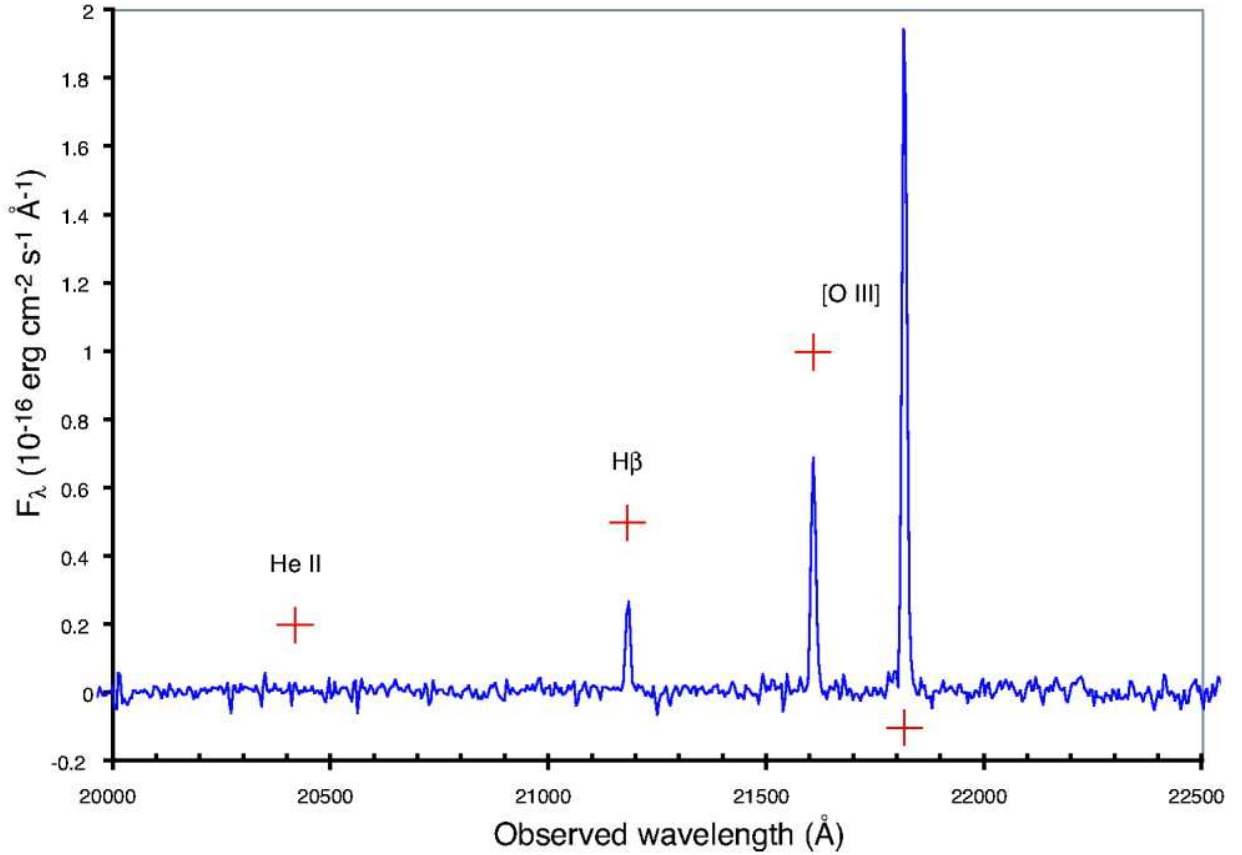


Figure 1.9: Lynx arc spectrum (K-band) - part III (from Fosbury et al. 2003). Spectrum taken with the Keck II telescope using NIRSPEC instrument, shown in the observed frame. The rest frame wavelengths of the lines marked are: He II $\lambda 4686$, H β $\lambda 4861$ and [O III] $\lambda\lambda 4959, 5007$.

modelled by the black body ionizing source with high effective temperature ($\sim 80,000$ K), high ionization parameter ($\log U = -1$), mentioned $Z=0.05 Z_{\odot}$ nebular metallicity and low nebular gas number density ($n_e = 50 \text{ cm}^{-3}$). Therefore, it is similar to the very metal-poor stellar population but with the gas already polluted with some metals, perhaps implying different stellar and nebular metallicity.

Particularly interesting is the nitrogen spectrum, i.e. N V $\lambda 1240$, N IV] $\lambda 1486$ and N III] $\lambda 1750$ emission lines, which can be used to investigate the nature of the ionizing source and determine its effective temperature. Luckily, all those lines are accessible in the Lynx arc spectrum. Figs. 1.10 and 1.11 show how the nitrogen lines behave for the case of the ionizing spectrum being a black body with different T_{bb} and a power law with different slopes. Strong N V emission would imply either an extremely hot black body or a power law. The dominance of N IV] $\lambda 1486$ and no detection of N V $\lambda 1240$ suggests the thermal ionizing source with $T_{\text{bb}} = 80,000 \pm 10,000$ K.

Additionally, an argument against the AGN (power law) ionization is the lack of any

X-ray or radio emission.

Fosbury et al. (2003) have calculated that to provide the required amount of ionizing photons and produce the observed emission line spectrum 10^6 massive stars must be embedded in the cluster.

The possibility of Wolf-Rayet (WR) stars being the source of ionizing radiation has been studied by Villar-Martín et al. (2004). They study individual ionic and elemental abundances using a direct method (after deriving the electron temperature from [O III] $\lambda\lambda 1661, 1666/\lambda 5007$ ratio) and using a grid of photoionization models. They find a nitrogen overabundance with respect to other elements ($[N/O] \sim 2-3 \times [N/O]_{\odot}$). That scenario can reproduce the observed line ratios. However, they overproduce the stellar continuum, which significantly reduces the observed equivalent widths of emission lines.

Binette et al. (2003) discuss the possibility of an obscured QSO being the ionizing source, they find that while this scenario is able to produce the observed line ratios (relative to $H\beta$) of N IV], C IV], O III] and He II], it overproduces the UV lines: N v $\lambda 1240$, O VI $\lambda 1035$, [Ne v] $\lambda 3426$, Mg II $\lambda 2800$ and C II] $\lambda 2326$, as well as the optical lines [O I] $\lambda 6300$ and [S II] $\lambda 6731$.

The black body scenario is the only one that reproduces the observations. The most puzzling issue is the gas enrichment. Is it possible that exploding SNe would rapidly enrich the surrounding gas until $Z=0.05 Z_{\odot}$ while the other stars would be still forming from unpolluted gas? Perhaps that would happen in case of PISNe produced by very massive stars. This kind of episode in the galaxy evolution must be very short lived since the massive stars live just a few million years. Therefore, the detection of such sources is statistically unlikely.

1.4 GOODS survey

GOODS (Great Observatories Origins Deep Survey)⁵ is a multiwavelength, public survey combining the deepest data over the widest wavelength range. It covers two fields centered around the Hubble Deep Field North (HDF-N) and the Chandra Deep Field South (CDF-S), each one 150 arcmin^2 large. Here I will describe the second one where ESO telescopes have been involved. The following ESO observations are available for CDF-S:

- imaging:
 - VIMOS U and R band (Nonino et al. 2009),
 - ISAAC in J,H and Ks imaging (Retzlaff et al. 2010);
- spectroscopy:
 - FORS2 (observed wavelength range: 5500-10000 Å) containing 1635 spectra of 1236 targets (Vanzella et al. 2008) for redshifts until $z=6.3$,

⁵www.stsci.edu/science/goods/
www.eso.org/sci/activities/projects/goods/

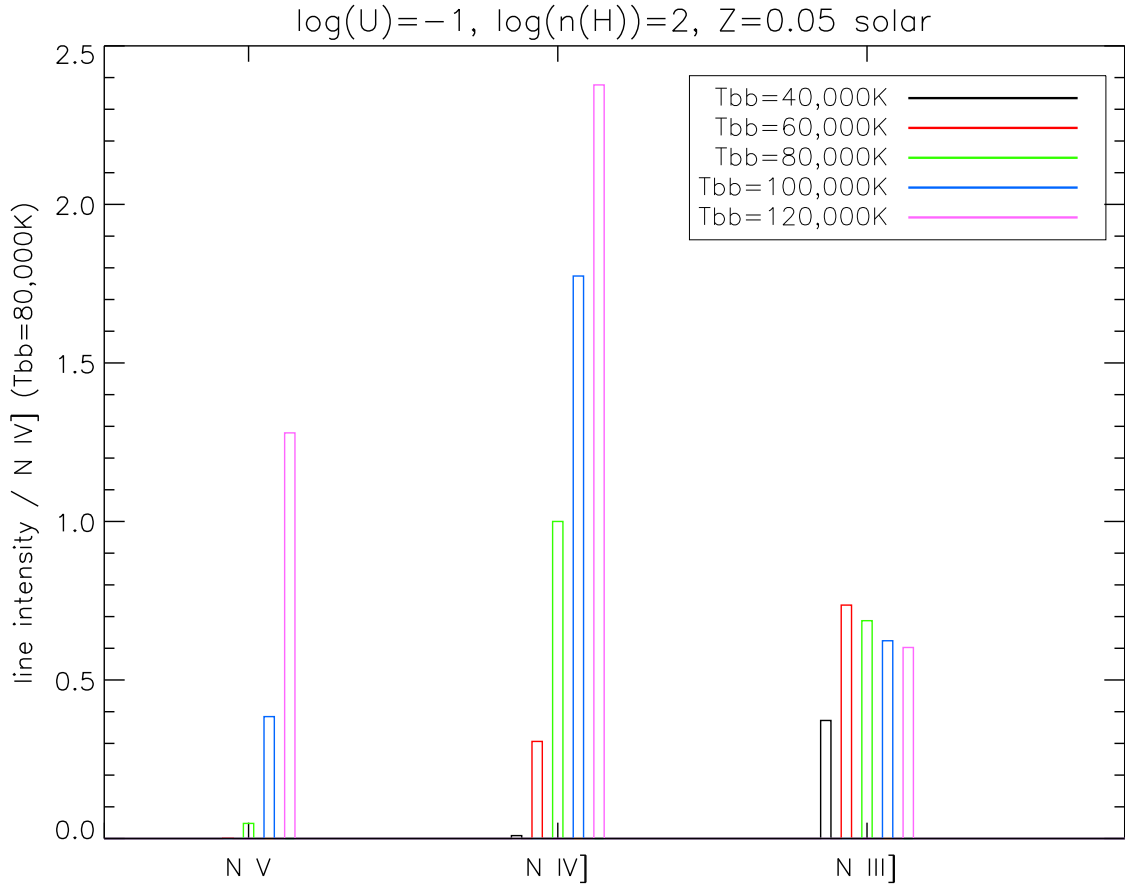


Figure 1.10: Nebular nitrogen line spectrum for black body ionizing source shown for different T_{bb} and normalized at the N IV] flux for the $T_{bb} = 80,000$ K case.

- VIMOS low resolution blue (observed wavelength range: 3500-6900 Å) containing 3634 spectra of 3271 targets (Popesso et al. 2009) for redshifts $1.8 < z < 3.5$,
- VIMOS medium resolution (observed wavelength range: 4000-10000 Å) containing 1418 spectra of 1294 targets (Balestra et al. 2010) for redshifts $z < 1$ and $z > 3.5$.

Additionally, Hubble Space Telescope imaging in B, V, i and z filters and Spitzer IRAC 3.6, 4.5, 5.8, 8 μm and MIPS 24 μm as well as the X-ray Chandra imaging are available. The combination of the UV/optical/IR data with the 24 μm and X-ray data helps to investigate the nature of the sources, i.e. identify the AGNs. The photometric catalog which consists of magnitudes in all the bands from U band until 24 μm is published by Santini et al. (2009).

In this thesis the GOODS imaging and spectroscopic data will be used in Chapter 4, Section 5.1 and Chapter 6.

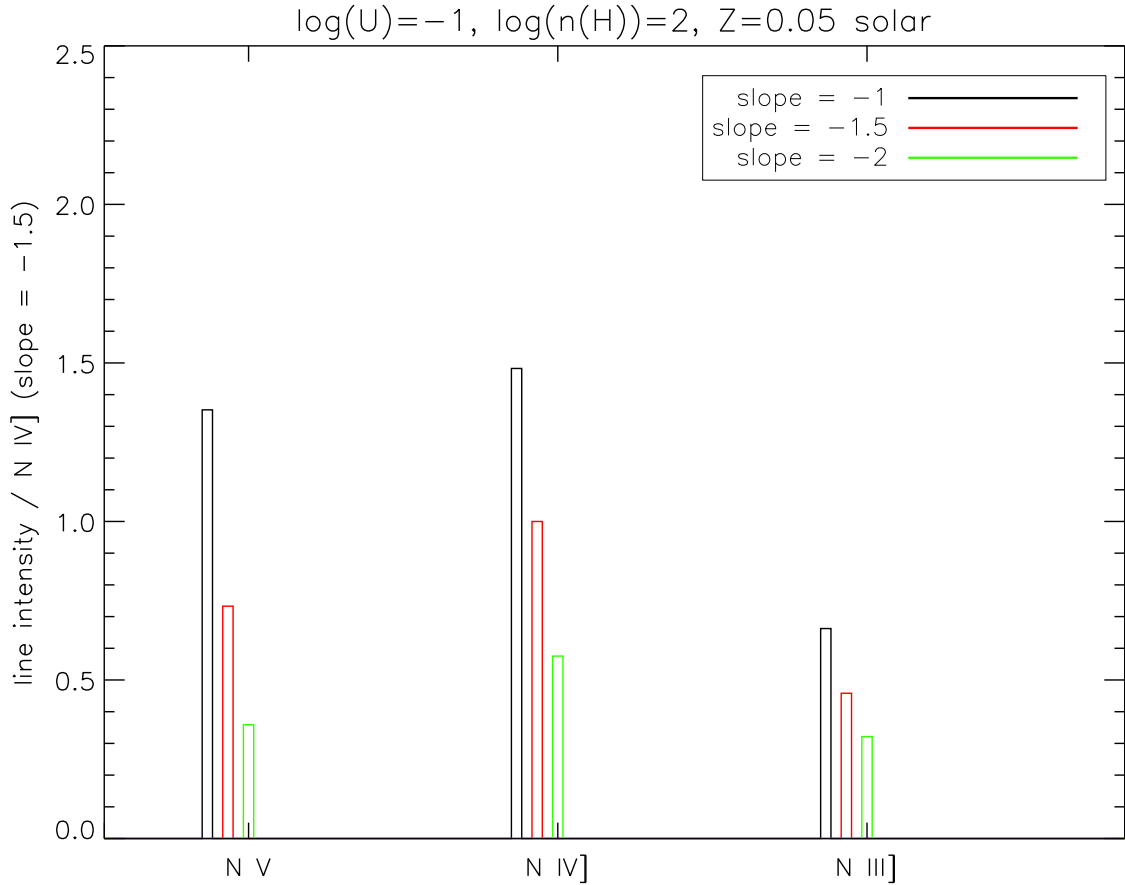


Figure 1.11: Nebular nitrogen line spectrum for power law ionizing source shown for different slopes and normalized at the N IV] flux for the slope = -1.5 case.

1.5 This thesis

Studying chemical evolution of the early Universe is one of the challenges of modern astrophysics. Metal emission lines arising from the gas surrounding the primordial/very metal-poor stellar clusters expected at high- z gives an insight into the first nucleosynthetic products. The discovery of the Lynx arc (Fosbury et al. 2003) which might be one of the first objects found containing very hot (very metal-poor) stars justifies the searches for those sources in already existing data. It is also motivated by simulations suggesting the existence of primordial material until quite low redshifts ($z \sim 3-2$). However, until now only a few of objects like this have been found.

In this thesis I will show that already nowadays, before the era of extremely large telescopes (ELTs) and JWST, we can use some of the existing observations in order to access the measurements of nebular/stellar metallicity in the high- z galaxies and therefore get some hints on the chemical enrichment.

The UV lines are our interest here since they are what we can possibly detect in the existing optical spectra of high- z galaxies from large surveys. The metal UV lines are important because they require a hot ionizing source i.e. with a bulk of ionizing photon energies emitted between 20 - 54.4 eV which produces a large fraction of ions in the triply ionized stage producing strong lines of for example C IV and N IV] (Binette et al. 2003). Most of this thesis will be concentrated on the rest frame UV part of the spectrum described from the observational as well as the theoretical point of view.

Since the most commonly observed line is Ly α and there have been scenarios employing top-heavy IMF and/or Pop III in order to explain some of the observations (namely large equivalent widths of Ly α line found for some high- z Ly α emitters) it is important to understand by means of models what observational characteristics of the first stars/galaxies we expect, i.e. the hydrogen and helium emission.

In this thesis I will concentrate on the analysis and discussion of the galaxies which are not AGNs. I will focus on nebular emission, so it will be biased towards very young objects.

This thesis is organized as follows: Chapter 2 presents the description of the tools I have used i.e. the stellar population synthesis models and the photoionization code; Chapter 3 presents the modelling of the hydrogen and helium emission (nebular emission lines and continuum) from starbursts galaxies; Chapter 4 presents the analysis of the peculiar N IV] emitting galaxy and the consequences of the strong nebular emission in the context of a sample of high- z Ly α emitters from the GOODS-S field; Chapter 5 presents other N IV] emitters found and their analysis; Chapter 6 describes several observing attempts (ESO proposals) aimed to study objects with strong nebular emission; Chapter 7 contains the conclusions and future prospects.

Chapter 2

Tools

2.1 CLOUDY photoionization code

CLOUDY¹ is a photoionization code commonly used by astronomers. It calculates the synthetic spectrum of the ionized nebula given the parameters of the star(s) and of the diffuse gas as well as its thermal, ionization and chemical structure. The luminosity (or other parameters that allow to infer it) and the shape of the ionizing continuum, as well as the particle density and the chemical composition of the gas must be defined. One can use the black body shape as the ionizing continuum or define a certain shape based on the stellar population synthesis predictions. Additionally, the geometry of the gas must be defined. A schematic illustration of open and closed spherical geometries is shown in Fig. 2.1. The geometry can be either density (matter)-bounded or ionization (radiation)-bounded. The first case corresponds to the optically thin nebula and non-zero escape fraction² and may be defined by setting the outer radius, the second case corresponds to the situation where the H II region is optically thick to the hydrogen ionizing continuum and all of it is absorbed in the gas (escape fraction = 0).

Once the conditions in the cloud are defined, its resulting emission-line spectrum is calculated in a self-consistent manner i.e. by simultaneously solving the equations of statistical and thermal equilibrium which balance ionization-neutralization and heating-cooling processes respectively. Once the incident continuum is defined, the synthetic spectrum predicted by the code (Figure 2.2) consists of the transmitted (attenuated) incident continuum (the part of the incident continuum that is not absorbed by the gas), diffuse continuum (coming from the gas), reflected continuum (only in case of the open geometry) and emission lines.

Definitions used by the code:

- density: n_{H} or $n(\text{H})$, is the total hydrogen number density per cm^3 ;
- metallicity / chemical composition: the metallicity of the gas might be defined by

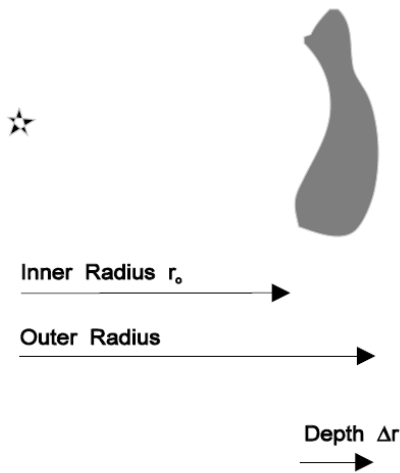
¹www.nublado.org

²Escape fraction – fraction of Lyman continuum photons that escape from the nebula to the IGM.

scaling the solar abundance pattern of the elements (CLOUDY contains the elements from hydrogen to zinc). By default abundances are defined by number relative to hydrogen. Also the abundance of each element can be defined separately. Similarly, the abundances of the dust grains along with the depletion factors can be defined;

- ionization parameter: U , is a dimensionless ratio of hydrogen ionizing photon to total hydrogen density.

Open Geometry



Closed Geometry

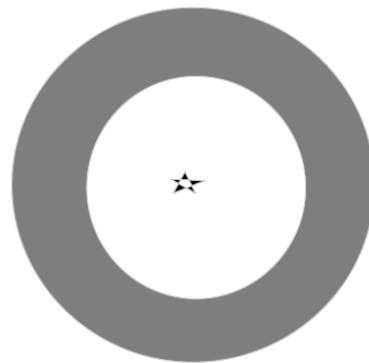


Figure 2.1: Open and closed spherical geometry used by CLOUDY (Ferland 2008).

2.2 Structure of H II region

CLOUDY calculates the thermal and ionization structure of the ionized cloud. The example case ($T_{\text{bb}} = 100,000$ K, $\log U = -1$, $n_H = 10^3$ cm $^{-3}$, primordial abundances of elements in the nebula) is presented in Figs. 2.3 and 2.4 which show the distribution of the electron temperature and the ionization fractions for hydrogen and helium species respectively.

In the work presented in this thesis I used constant hydrogen number density, however that is only a simplification, since in the real nebula denser and sparser regions might coexist. That is easier to conclude when one observes many emission lines which provide density diagnostics, i.e. in the Lynx arc two line doublets give a hint of different densities. The lines might have been formed in different regions in the nebula. This kind of detail could provide some information on the mixing processes and help for example to identify denser and more enriched gas in the inner parts of the nebula (where the mixing processes happened). Since for high- z objects this kind of detail is not available, one is forced to simplify the problem and use constant density.

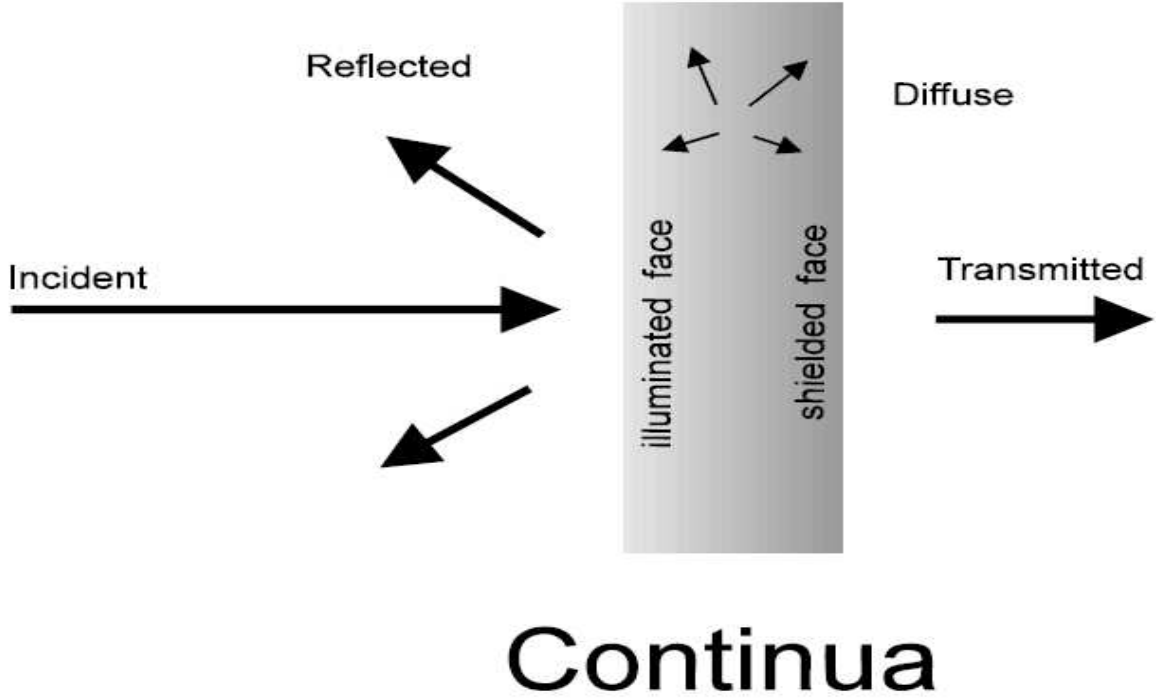


Figure 2.2: Continua being calculated by CLOUDY (Ferland 2008).

The electron temperature can be determined from certain emission lines as mentioned in the previous chapter. In this work the electron temperature in the models is not defined, but rather is a consequence of defining other parameters. It is not constant throughout the nebula (Fig. 2.3) but changes (decreases) in the outer parts. The thermal equilibrium is defined by heating and cooling processes (Osterbrock & Ferland 2006):

$$G = L_R + L_{FF} + L_C, \quad (2.1)$$

where G is the energy input by photoionization, L_R – energy loss by recombination, L_{FF} – energy loss by free-free radiation and L_C – by collisionally excited lines. When the collisional deexcitation becomes important, the cooling rate due to collisionally excited lines decreases.

The size of the modelled H II regions is not set, it changes depending on the radiation field, particle density and the recombination coefficient which is electron temperature dependent.

2.3 Stellar population synthesis models

In this thesis the evolutionary stellar population synthesis models used are the ones presented in Schaerer (2002, 2003). They include zero metallicity and very low metallicity population spectra for different ages, IMFs and SFHs.

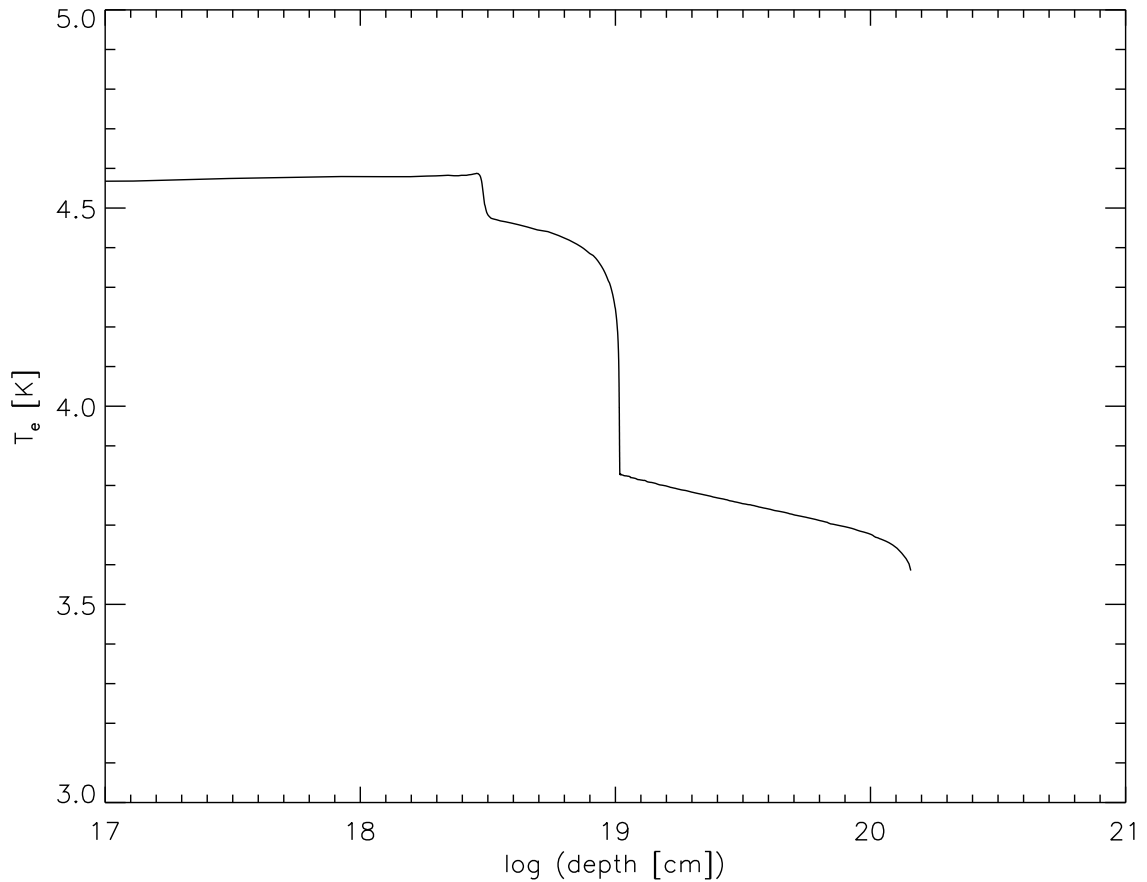


Figure 2.3: Example case: distribution of the electron temperature throughout the ionized cloud.

The model ingredients are the atmospheric models (accounting for the non-LTE and mass loss effects), stellar tracks, evolutionary synthesis models additionally adapted to the metal-free case. What defines the particular model is the IMF, metallicity, age and SHF. They also predict H and He nebular continuum and line emission from the ionized diffuse gas, assuming case B recombination (Chapter 3 presents the results for nebular emission for case B and the discussion as well as the comparison with the results obtained without this simplification). For higher metallicity models Wolf-Rayet (WR) stars are included. The characteristics of the models for all available metallicities are presented in Figure 2.5.

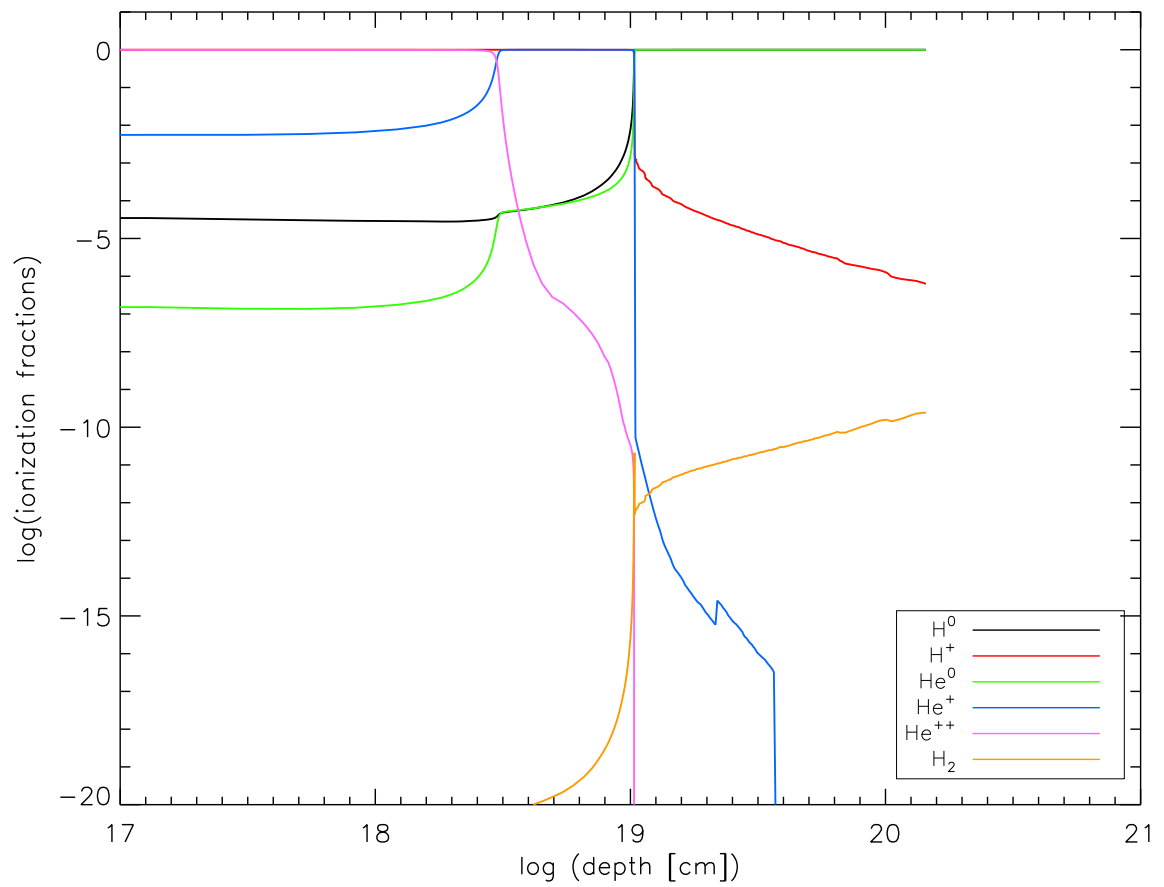


Figure 2.4: Example case: distribution of the ionization fractions of H and He throughout the ionized cloud.

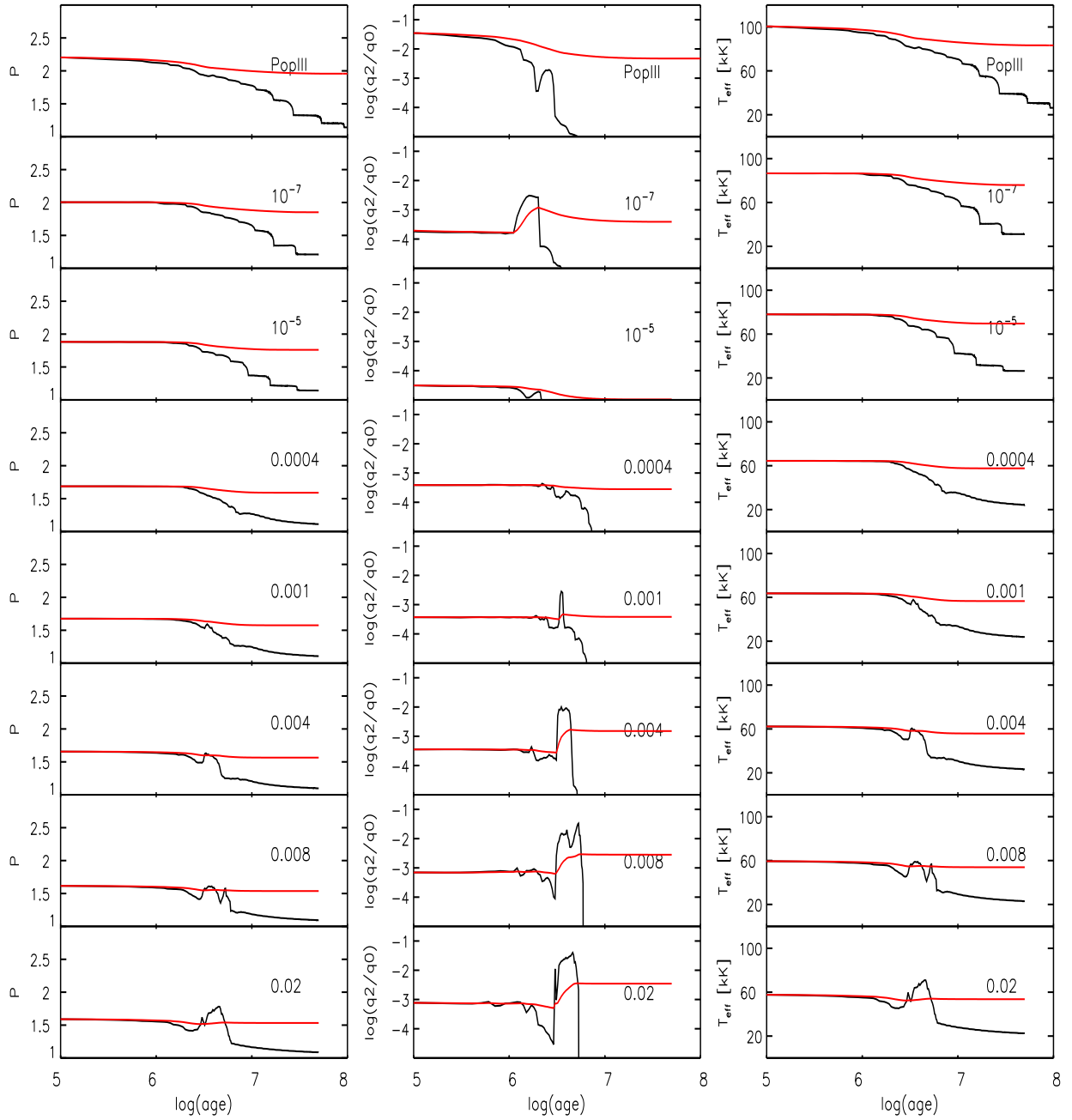


Figure 2.5: Mean ionizing photon energy (in Rydbergs) – P , the hardness of the Lyman continuum $Q(\text{He}^+)/Q(\text{H})$ and the effective stellar temperature (calculated from P , see later) for all metallicities available in Schaerer’s models as a function of age. The models presented here are with Salpeter 1-100 M_{\odot} IMF and SFH=“instantaneous burst” (black solid line) and “constant star formation” (red solid line). The peaks that appear for all of those parameters at around $\log(\text{age}) = 6.5$ are due to the presence of WR stars for higher metallicity models.

Chapter 3

Predicted UV properties of very metal-poor starburst galaxies

Raiter A., Schaerer D., Fosbury R.

accepted for publication in A & A, arXiv:1008.2114

3.1 Introduction

Over the last decade, the execution of deep multi-band imaging surveys like GOODS (Vanzella et al. 2005, 2006, 2008, 2009; Popesso et al. 2009; Balestra et al. 2010) has resulted in catalogues of significant numbers of galaxies with photometric redshifts greater than five when the Universe was only a little over a Gyr old. In some cases, these redshifts have been spectroscopically confirmed by the detection of Ly α in emission and/or the presence of an identifiable Lyman break. The availability of an increasing sensitivity in the NIR, notably with the newly-installed WFC3 camera in the HST and with the JWST in the near future, opens the possibility of selecting high quality candidates up to and beyond a redshift of 10. This is the epoch where it can be expected that stellar populations have a very low metallicity, which may result in an excess of hot, high mass stars radiating strongly in the Lyman continuum.

To provide appropriate spectral templates for such metal-poor star-forming galaxies and to predict the observable properties of starbursts with primordial and more evolved chemical compositions Schaerer (2002, 2003) has computed new evolutionary synthesis models and has demonstrated the importance of nebular emission (lines and continua) at low metallicity. These and other studies (see e.g. Tumlinson & Shull 2000; Tumlinson et al. 2001; Bromm et al. 2001) have in particular highlighted the use of strong Ly α emission and

nebular He II emission to search for objects containing Population III (hereafter Pop III) stars. Since then, various searches for the He II $\lambda 1640$ signature from Pop III have been undertaken at different redshifts, yielding so far non-detections and interesting upper limits on the Pop III star-formation rate density (see Schaerer 2008; Nagao et al. 2008, and references therein). Furthermore, among the numerous surveys for Ly α emitters at different redshifts, some studies have found objects with apparently usually strong Ly α emission (high equivalent widths), which could be indicative of very metal-poor (even Pop III) stellar populations or unusual IMFs (see e.g. Malhotra & Rhoads 2002; Yamada et al. 2005). Other groups have invoked “unusual” IMFs, extremely metal-poor stellar populations, and/or leakage of Lyman continuum radiation to explain the apparently very blue UV slopes found for some very high redshift ($z \sim 7$) galaxies (Bouwens et al. 2010). However, the significance of these results is questionable, and the present data does not require such “non-standard” assumptions (Schaerer & de Barros 2010; Finkelstein et al. 2010). In any case, it is of interest to examine how reliable some of the major observables predicted by standard evolutionary synthesis are.

Indeed, a shortcoming of evolutionary synthesis models such as the ones mentioned above is that they calculate nebular emission in an approximate manner assuming simplified physics, such as case B recombination theory (cf. Osterbrock & Ferland 2006), and constant emissivities for adopted constant values of the electron temperature and density in the H II region surrounding the starburst. In fact, as demonstrated in this paper, significant departures from case B are expected at low metallicities leading to stronger Ly α emission, and the strength of nebular He II emission predicted by full photoionization models can be reduced with respect to simple recombination theory. Indeed these physical effects, related to an increased importance of collisional effects at low metallicity due to lower radiative cooling and harder ionizing spectra – for Ly α – and due to competition between H and He for ionizing photons – for the intensity of He II/H – have been known for a while in studies of metal-poor H II regions (cf. Davidson & Kinman 1985; Stasińska & Schaerer 1999; Luridiana et al. 2003) and planetary nebulae (Stasińska & Tylenda 1986). Panagia (2002, 2005) has recently explored photoionization models for primordial nebulae. However, the importance of the above effects for the UV emission lines has so far not been thoroughly examined, in particular in the context of metal-poor and distant starburst galaxies and using up-to-date evolutionary synthesis models. The photoionization models presented here, combined with our evolutionary synthesis models, are intended to provide a framework within which to improve our knowledge of primeval galaxies and related objects.

Another limitation of the synthesis models of Schaerer (2002, 2003) concerns the initial mass function (IMF). For simplicity, three different choices of the IMF were adopted for the bulk of the calculations in these papers. However, different IMFs have been suggested in other studies related to Pop III and early stellar generations, and considerable uncertainties remain on the true shape of the IMF in the early Universe and its dependence (or not) on physical parameters. To enable the examination of the effects of a broader choice of IMFs on the expected observable properties of starbursts, we here extend the calculations of Schaerer (2003) to eight different IMFs. The resulting model grids, available in electronic format, should provide state-of-the-art predictions for the interpretation of high redshift

galaxies, to estimate their contribution to cosmic reionization, and for other topics.

The paper is structured as follows. In Sect. 3.2 we describe the input physics and the model calculations with our evolutionary synthesis code and with the photoionization code CLOUDY. The predictions from the synthesis models concerning the UV continuum, the ionizing flux, Ly α and He II λ 1640 emission are presented in Sect. 3.3. In Sect. 3.4 we discuss the results from the photoionization models using black body spectra, explain the deviations from case B and provide simple formulae to describe these effects on Ly α . In Sect. 3.5 we show how to connect realistic SEDs with results from photoionization models using black body ionizing spectra. Our results and several implications are discussed in Sect. 3.6. The main results are summarised in Sect. 3.7.

3.2 Modelling techniques

3.2.1 Synthesis models

We have used the evolutionary synthesis code of Schaerer & Vacca (1998) with the physical ingredients (stellar tracks, atmospheres, and prescriptions for nebular line and continuum emission) from Schaerer (2003). In particular these models allow us to predict the integrated properties of stellar populations at all metallicities from zero (Population III) to “normal”, solar-like metallicity. The computations have been done for the same metallicities as in Schaerer (2003).

Table 3.1: Summary of IMF model parameters. Model ID is the label used in the Figures, colour code the colour and linestyle. Note: the definition of M_c and σ is as in Tumlinson (2006). In particular sigma is the variance in $\ln(m)$, not $\log(m)$!

Model ID	colour code	M_{low}	M_{up}	α	M_c	σ	reference/comment	ID in files
Salpeter	black	1	100	2.35			A in Schaerer (2003)	S
B	green, dashed	1	500 ^a	2.35			B in Schaerer (2003)	B
C	cyan, dashed	50	500 ^a	2.35			C in Schaerer (2003)	C
Scalo	blue	1	500 ^a	2.7 ^b			Scalo (1986)	Sc
TA	red	1	500 ^a		10.	1.0	A in Tumlinson (2006)	TA
TB	magenta	1	500 ^a		15.	0.3	B in Tumlinson (2006)	TB
TE	yellow	1	500 ^a		60.	1.0	E in Tumlinson (2006)	TR
L05	blue, dashed	1	100		5.		Larson (1998)	l0

^a For metallicities $Z \geq 0.0004 = 1/50Z_{\odot}$, we adopt $M_{\text{up}} = 120M_{\odot}$, the maximum mass for which Geneva stellar evolution tracks are available.

^b Power-law exponent for $M \geq 2M_{\odot}$.

Stellar initial mass function

The main extension presented here with respect to the calculations of Schaerer (2003) concerns different assumptions regarding the stellar IMF. A wide range of IMFs has been considered, including power-law IMFs, such as the Salpeter or Scalo (1986) IMFs, log-normal IMFs, and the Larson (1998) IMF. The corresponding parameters are summarised in Table 3.1. The stellar mass range is defined by the lower and upper mass cut-offs, M_{low} and M_{up} respectively. α being the slope of the power-law. The log-normal IMFs are described by the characteristic mass M_c and its dispersion σ . The cases computed here correspond to the cases A, B, and E in the chemical evolution study of Tumlinson (2006). The Larson (1998) IMF is described by a single parameter, its characteristic mass M_c . We have computed one such case, assuming the same value of M_c as Ciardi et al. (2001) in their reionization calculations. Note, that at $Z \geq 0.0004 = 1/50 Z_{\odot}$ the upper mass cut-off is set to $M_{\text{up}} = 100$ or $120 M_{\odot}$ for all IMFs, since tracks for more massive stars are not available. The quantities discussed here are insensitive to assumptions on the IMF at low masses. Our absolute quantities may therefore simply be rescaled to other IMFs including e.g. an extension below $1 M_{\odot}$.

Current knowledge suggests that the IMF for massive stars is close to Salpeter with an upper limit of $M_{\text{up}} \sim 100\text{--}120 M_{\odot}$ from solar metallicity down at least to $\sim 1/50 Z_{\odot}$, and that a qualitative shift of the IMF towards higher characteristic masses occurs below a critical metallicity of the order of $Z_{\text{crit}} \sim 10^{-5 \pm 1} Z_{\odot}$ (Schneider et al. 2002, 2003).

Star formation histories

For each metallicity Z and IMF we have computed evolutionary synthesis models for the two limiting cases of 1) an instantaneous burst, and 2) constant star formation (CSFR). Results for other star formation histories can be derived from the electronic files for the simple stellar population (burst) models (see Sect. 3.2.1). In both cases the calculations have been carried out with a small timestep (0.1 Myr) to ensure the accuracy of the time integrated quantities for the CSFR case. The calculations have to be carried out up to ages of 1 Gyr. This covers the allowed ages and of galaxies at redshifts $z \gtrsim 5.8$, of interest here, as well as sufficiently long star formation timescales to reach equilibrium in various observable properties (cf. below).

Nebular emission

To include nebular emission (recombination lines and continuum processes) in our synthesis models we initially make the following ‘‘standard’’ simplifying assumptions (see Schaerer 2002, 2003): ionization bounded nebula, constant electron temperature and density (T_e , n_e), and case B. case B in particular assumes that the recombinations to the ground-state immediately yield locally another ionization, and that photoionizations occur only from the ground-state. As we will see below, the latter may not be true in very metal-poor nebulae, leading to significant changes in the predicted spectrum of hydrogen. With these assumptions both the H and He recombination lines as well as nebular continuum emission

(including free-free and free-bound emission from H, neutral He, and singly ionized He, and two-photon emission of H) are fully specified and their luminosity is proportional to the ionizing photon flux Q in the appropriate energy range. To reflect to first order the changes of the conditions in the H II regions with metallicity, the value of the line luminosity coefficient and nebular continuous emission coefficients at metallicities $Z/Z_\odot < 10^{-3}$ are changed as in Schaerer (2003). More precisely we adopt $T_e = 30$ (20) kK for lines (continua) $Z/Z_\odot < 10^{-3}$ and $T_e=10$ kK for higher metallicities, and a low ISM density $n_e = 100 \text{ cm}^{-3}$.

For the Ly α luminosity we have, with the assumptions just spelled out:

$$L_B(\text{Ly}\alpha) = (1 - f_{\text{esc}})Q(\text{H}) \times h\nu_{\text{Ly}\alpha} \times \frac{\alpha_{2^2P}^{\text{eff}}}{\alpha_B} \quad (3.1)$$

where the index ‘B’ stands for case B, $\alpha_B = \alpha_{2^2P}^{\text{eff}} + \alpha_{2^2S}^{\text{eff}}$ is the total case B recombination coefficient, and f_{esc} is the escape fraction of ionizing photons out of the H II region (or galaxy). In all Figs. shown in this paper we assume $f_{\text{esc}} = 0$. In typical conditions $\alpha_{2^2P}^{\text{eff}}/\alpha_B \approx 0.6\text{--}0.7$. In other words approximately 2/3 of the Lyman continuum photons give rise to the emission of a Ly α photon, the assumption commonly made. Similar relations also hold for other recombination lines, such as He II $\lambda 1640$, which is of special interest here. In our “standard” synthesis models we simply assume

$$L_B(\text{Ly}\alpha) = Q(\text{H}) \times c_1, \quad (3.2)$$

$$L_B(\text{He II}\lambda 1640) = Q(\text{He}^+) \times c_2, \quad (3.3)$$

with $c_1 = 1.04 \times 10^{-11}$ erg, and $c_2 = 5.67 \times 10^{-12}$ (6.04×10^{-12}) erg for $Z \leq 1/50 Z_\odot$ ($> 1/50 Z_\odot$), and for $f_{\text{esc}} = 0$. The atomic data is from Hummer & Storey (1995) for low densities (cf. Schaerer 2003), and $Q(\text{H})$ and $Q(\text{He}^+)$ are the ionizing photon flux (in photon s^{-1}) above 13.6 and 54 eV respectively.

Continuous nebular emission including free-free and bound-free emission by H, neutral He, He^+ , and He^{+2} , as well as the two-photon continuum of hydrogen is included as described in Schaerer (2002), assuming $T_e = 20$ kK for $Z/Z_\odot \leq 5. \times 10^{-4}$ and $T_e = 10$ kK otherwise.

As we will show below (Sect. 3.4), a proper treatment of all relevant processes leads to significant deviations from case B at very low metallicities, increasing in particular the Ly α luminosity, $L(\text{Ly}\alpha)$. In this case the $L(\text{Ly}\alpha)$ can be rewritten as

$$L(\text{Ly}\alpha) = L_B(\text{Ly}\alpha) \times P \times \frac{\tilde{f}_{\text{coll}}}{2/3}, \quad (3.4)$$

where P and \tilde{f}_{coll} are terms describing the mean photon energy in the Lyman continuum, and accounting for collisional effects at high density. To compute the Ly α equivalent width $W(\text{Ly}\alpha)$ we proceed as in Schaerer (2002, 2003), where we use the continuum flux at 1215.67 Å obtained from linear interpolation of the total (stellar + nebular) continuum (in log) between 1190 and 1240 Å, chosen to avoid underlying stellar Ly α absorption and other absorption lines if present. The predicted stellar Ly α absorption is small compared to the emission, except for “post-starburst” phases (see e.g. Fig3. in Schaerer & Verhamme 2008).

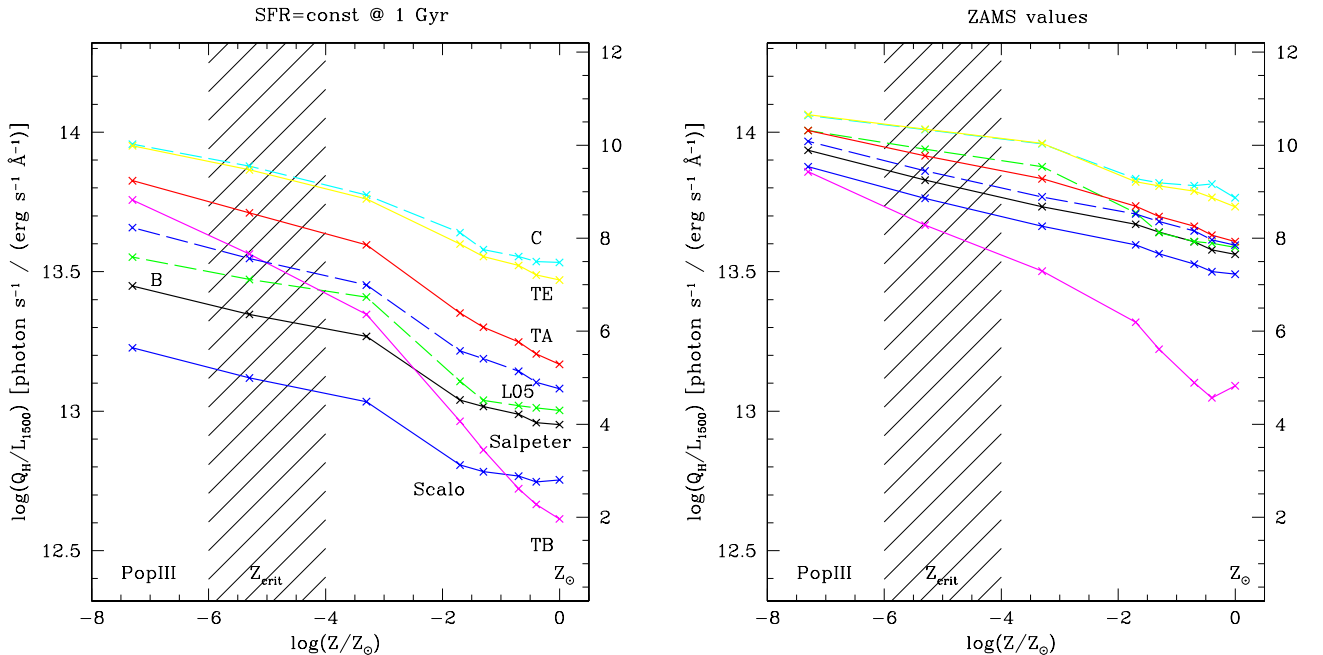


Figure 3.1: Relative output of hydrogen ionizing photons to UV continuum light, measured at 1500 \AA restframe, Q_H/L_{1500} , as a function of metallicity for constant star formation over 1 Gyr (left panel) and very young bursts (right panel). Q_H/L_{1500} is given in L_λ units on the left side of each panel, and in L_ν units on the right. Results for different IMFs are shown using the colour codes and labels summarised in Table 3.1. The shaded area indicates the critical metallicity range where the IMF is expected to change from a “normal” Salpeter-like regime to a more massive IMF (see text).

Model output

Our evolutionary synthesis code predicts a large variety of observable and related quantities derived from the detailed synthetic spectra. Here we focus on mostly on quantities describing the spectrum in the Lyman continuum, the UV (rest-frame) spectrum, as well as the $\text{Ly}\alpha$ and $\text{He II } \lambda 1640$ emission lines. The full set of model results, including also numerous other quantities not discussed in this paper, are available in electronic format upon request to one of the authors (DS), on <http://obswww.unige.ch/sfr>, or via the CDS.

3.2.2 Photoionization models

To predict more accurately the nebular emission from starbursts and to investigate possible departures from the simplified assumptions made in our synthesis models we use the photoionization code CLOUDY version 08 (Ferland et al. 1998). The models we consider are ionization-bounded with a closed, spherical geometry and constant density. These assumptions imply in particular that all ionizing photons are absorbed in the H II region, i.e.

$f_{\text{esc}} = 0$. In certain circumstances, especially in high redshift galaxies, a fraction of the Lyman continuum photons are expected to escape (see e.g. Gnedin et al. 2008; Wise & Cen 2009; Razoumov & Sommer-Larsen 2009). To first order the results obtained in this paper can simply be rescaled to such cases, as discussed below. The main input parameters of our models are: the spectral energy distribution (SED) of the ionizing source, the nebular density (given by n_H , the hydrogen number density), the ionization parameter (U), and the nebular metallicity (Z_{neb}). For the SED we adopt black-body spectra described by T_{bb} and SEDs from our evolutionary synthesis models. The ionization parameter (at the inner edge of the cloud) is defined as:

$$U = \frac{Q(\text{H})}{4\pi r_{\text{in}}^2 \times n_H \times c} \quad (3.5)$$

where r_{in} is the inner radius of the nebula which has been kept constant in our models (10^{17} cm) and c is the speed of light. The small inner radius used in our calculations results in a sphere-like (not shell-like) geometry of the nebulae. The ionization parameter can change throughout the nebula (decrease towards outer parts).

First, we have calculated the grid of photoionization models using the photoionization code CLOUDY covering $\log(U) = -4, -3, -2, -1$; $T_{bb} = 40,000 - 150,000$ K; $\log(n_H) = 1, 2, 3, 4 \text{ cm}^{-3}$ for a primordial nebula and a number of higher metallicities. In total 192 models were computed for each metallicity. In order to keep the same ionization parameter while changing the density of the gas, we adapt the number of ionizing photons (keeping the shape of the SED). The metallicity is defined by scaling the solar abundance pattern.

Note that the electron temperature is neither constant nor fixed in our models. Its spatial distribution results from the computation of each photoionization model and it is a function of depth in the nebula. In practice it depends on all the parameters that are being investigated (T_{bb} , n_H , U , Z_{neb}). For the coolest primordial model (the coolest black body, the lowest density and the lowest ionization parameter) the temperature in the inner part of the cloud is around 12,000 K and for the hottest ones it reaches $\sim 38,000$ K.

Selected models were subsequently computed using the SEDs from the synthesis models described above.

3.3 Predicted UV properties from synthesis models

We now present and discuss one-by-one the main predictions of our synthesis models for different IMFs (see Table 3.1), for metallicities from zero (Pop III) to solar, and for two different limiting star-formation histories (bursts and $\text{SFR}=\text{const}$). Since properties of stars below $Z \lesssim 10^{-9}$ (i.e. $Z/Z_{\odot} \lesssim 10^{-7.3}$) essentially converge to those of metal-free stars we assign this metallicity value to Pop III stars, as in Schaerer (2003).

Note that all UV continuum predictions from the synthesis models described in this Section are based on the simplified assumptions spelled out above to compute nebular emission. This implies in particular that at low metallicities the contribution from the

two-photon continuum process should be higher, increasing thus e.g. the predicted UV luminosity at 1500 Å, for the reasons discussed in Sect. 3.4.

3.3.1 Ionizing photon production

A quantity of interest, e.g. to determine the contribution of galaxies to cosmic reionization, is the the relative output of hydrogen ionizing photons to observable UV light. Here we provide Q_H/L_{1500} , where the Lyman continuum flux Q_H is expressed in units of photon s^{-1} , and the UV restframe luminosity at 1500 Å is L_{1500} in L_λ ($\text{erg s}^{-1} \text{Å}^{-1}$) or L_ν ($\text{erg s}^{-1} \text{Hz}^{-1}$) units ¹. Alternatively, to derive the Lyman continuum output per unit stellar mass (or per baryon), Q_H/L_{1500} discussed here can be combined with the ratio SFR/L_{1500} given below, or can directly be derived from the available data files.

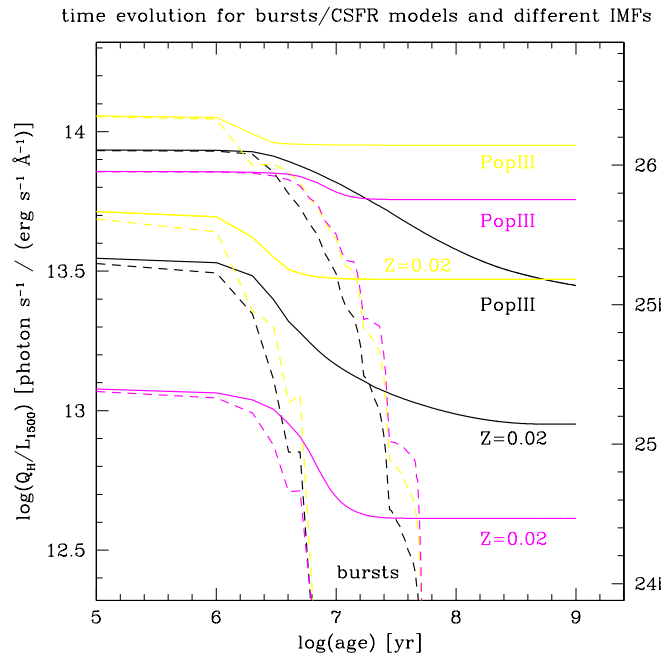


Figure 3.2: Temporal evolution of Q_H/L_{1500} for selected IMFs (Salpeter, TB, TE, colour-coded as in previous Figs.) and metallicities (Pop III, Z_\odot , labeled). The solid curves show the time evolution for constant SFR models towards their equilibrium value, the dashed curves instantaneous burst models. See text for discussion.

In Fig. 3.1 we show Q_H/L_{1500} as a function of metallicity for constant star formation over 1 Gyr (CSFR, left panel), and very young ($\lesssim 0\text{--}4$ Myr) populations (right panel). As expected Q_H/L_{1500} increases with decreasing metallicity, since the ionizing flux depends very strongly on the effective stellar temperature and hence increases more rapidly than the UV luminosity. The IMF dependence also behaves as expected, with the IMFs favouring

¹The transformation is $\log(Q_H/L_\lambda(1500\text{Å})) = \log(Q_H/L_\nu(1500\text{Å})) - 12.12$.

the most massive stars showing also the highest the Q_H/L_{1500} ratios, since Q_H increases more rapidly with stellar mass than the UV luminosity. Notable is actually the increase of Q_H/L_{1500} from Z_\odot to $\sim 10^{-4}Z_\odot$, where no major change of the IMF is expected (and a Salpeter IMF is favoured). For CSFR and for a fixed IMF, the increase of the relative ionizing power from solar metallicity to Pop III is typically ~ 0.4 – 0.5 dex, i.e. a factor 2 to 3. When considering an IMF change from Salpeter to a massive IMF (i.e. all cases except Salpeter and Scalo) the increase of Q_H/L_{1500} is larger, approximately 0.6 to 1 dex between solar and zero metallicity. Only for the “TB” IMF, a narrow, log-normal mass function peaked at $M = 15M_\odot$, we find a more extreme dependence on metallicity. This is precisely due to the fact that this IMF singles out a narrow mass range, instead of averaging the metallicity dependence of stellar properties over a larger interval in mass.

The right panel of Fig. 3.1 shows a narrower range of Q_H/L_{1500} for zero age or very young ($\lesssim 0$ – 4 Myr) populations. This is natural, since in this case no “average” is made over populations of very different stellar ages and hence over strong variations of stellar parameters. More important is the fact that *higher values of Q_H/L_{1500} are obtained for young populations*. This is mostly due to the fact that such populations emit a lower UV luminosity per unit SFR since a longer timescale is needed to reach the “equilibrium value” of the UV output (cf. below). The ZAMS values shown here correspond to the maximum of Q_H/L_{1500} expected for stellar populations of different ages and SF histories.

To illustrate this dependence on the SF timescale, $Q_H/L_{1500}(t)$ is shown in Fig. 3.2 for selected IMFs and metallicities. These curves show the smooth transition from the predicted “ZAMS” to the CSFR values over timescales from $\sim 10^7$ yr for massive IMFs (e.g. TE, TB) to ~ 0.4 – 1 Gyr for the Salpeter IMF. Note also that the timescale for UV properties to reach equilibrium increases with decreasing metallicity, due to the higher effective temperatures on the ZAMS at low Z . In short, we caution that the relative ionizing photon to UV ratio Q_H/L_{1500} may be uncertain by a factor of ~ 4 depending on the SF timescale (for constant SF), or even more for bursts.

Finally, it should be noted that at low metallicity the contribution of the two-photon continuum may be larger, as shown later in Sect. 3.4, leading to somewhat lower values of Q_H/L_{1500} . For constant SF this amounts to a decrease of Q_H/L_{1500} by ~ 0.2 dex for Pop III and the most extreme IMFs (TE, C), and smaller changes otherwise. For zero metallicity populations on the ZAMS Q_H/L_{1500} should be reduced by ~ 0.15 – 0.3 dex for all IMFs, and less at higher metallicity.

3.3.2 Properties of the ionizing spectra

The properties of the ionizing spectra, such as their hardness, detailed shape and others have already been discussed in Schaerer (2003) and shall not be repeated here. For example, the hardness $Q(\text{He}^+)/Q(\text{H})$, measured by the ratio of He^+ (> 54 eV) to hydrogen ionizing (> 13.6 eV) photons, we predict from our new models are already bracketed by the values predicted in Schaerer (2003) (see their Fig. 5) for the Salpeter and the “C” IMF.

An interesting quantity describing the ionizing spectra is the average energy of the photons emitted in the Lyman continuum $\overline{E}(Q(\text{H}))$ (see definition in Eq. 3.6). This quantity

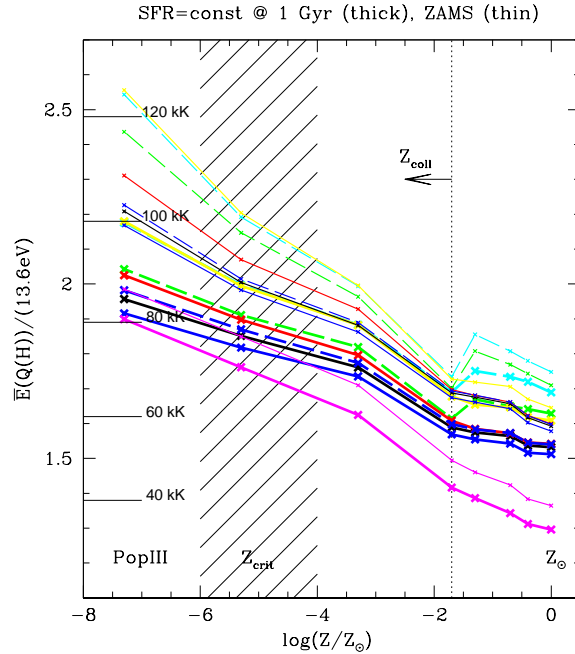


Figure 3.3: Mean ionizing photon energy in units of 13.6 eV as a function of metallicity, shown for SFR=const (thick lines) and for the ZAMS (thin lines). Results for different IMFs are shown using the same colour codes as in Fig. 3.1 (cf. Table 3.1). Lined and labels on the left indicate the corresponding black body temperatures. Z_{coll} shows the approximative metallicity limit below which collisional effects lead to significant departures from case B.

and its dependence on metallicity and IMF is plotted in Fig. 3.3 for constant SF (thick lines) and for the ZAMS (thin lines). The corresponding black body temperatures T_{bb} with the same mean ionizing photon energy are also shown for illustration. Typically $\overline{E}(Q(\text{H}))$ is found to ~ 1.5 – 2.5 times 13.6 eV, the ionizing potential of neutral hydrogen, and its behaviour with IMF, metallicity, and age behaves as expected. These values correspond to a range of black body temperatures from ~ 50 to 120 kK for the hardest spectra.

On this Figure we also indicate the approximate metallicity limit Z_{coll} , below which collisional effects lead to significant departures from case B, as shown below. In this metallicity range $\overline{E}(Q(\text{H}))$ can also be used to compute more accurately the intrinsic Ly α emission line strength (see Eq. 3.8).

3.3.3 SFR calibrations from the UV continuum

Figure 3.4 illustrates the variation of the UV luminosity for CSFR as a function of metallicity and for the different IMFs. Plotted is the conversion factor c , defined by $\text{SFR} = c \times L_{\nu}$, where L_{ν} is the UV luminosity in units of $\text{erg s}^{-1} \text{Hz}^{-1}$, and SFR is the star formation rate in $M_{\odot} \text{yr}^{-1}$. As expected, our model with Salpeter IMF agrees well with the widely used calibration from Kennicutt (1998) at Z_{\odot} after rescaling the latter by a factor 2.55 to

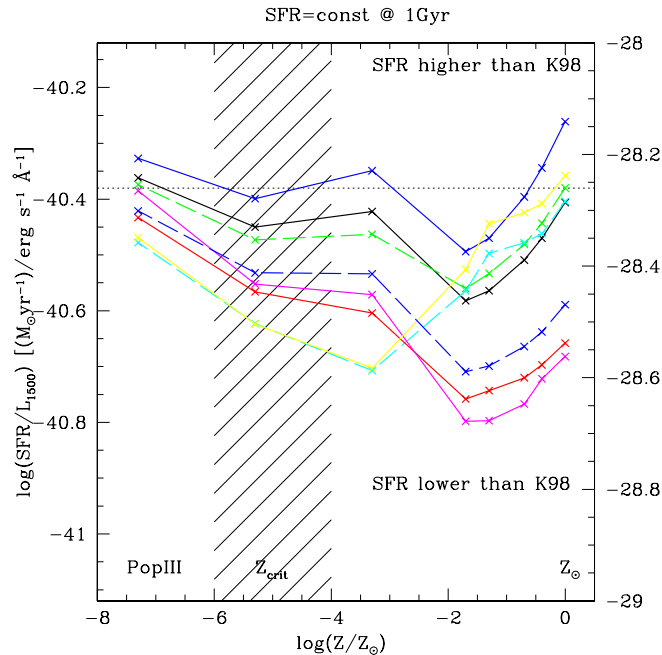


Figure 3.4: Dependence of the SFR(UV) calibration on metallicity and IMF. Shown is the SFR per unit UV luminosity at 1500 Å in units of $M_{\odot} \text{ yr}^{-1}$ per $(\text{erg s}^{-1} \text{ \AA}^{-1})$ on the left y-axis, or in $M_{\odot} \text{ yr}^{-1}$ per $(\text{erg s}^{-1} \text{ Hz}^{-1})$ on the right y-axis. Same symbols and colours as in previous Figures (cf. Table 3.1). These values assume constant SF over 1 Gyr. The dotted horizontal line show the value of the Kennicutt (1998) SFR(UV) calibration rescaled to a Salpeter IMF with $M_{\text{low}} = 1 M_{\odot}$ for comparison. Above/below this line the SFR deduced from the UV luminosity is higher/lower.

account for our adopted value for the lower mass cut-off ($M_{\text{low}} = 1 M_{\odot}$)². This Fig. clearly shows that in most cases the use of the Kennicutt calibration at low metallicity may overestimate the SFR, given the higher intrinsic UV output of such stellar populations. However, this may not be realistic since it relies on the assumption of CSFR over a long timescale (gtrsim $10^{8.3...9}$ yr). In younger populations the UV luminosity per unit SFR is lower, and hence c and the determined SFR higher (e.g. Schaerer 2000).

In fact, the non-monotonous behaviour of SFR/L_{1500} with metallicity observed in Fig. 3.4 is due to the dependence of the stellar contribution to the total UV output at this wavelength. Indeed, the stellar UV output increases with decreasing Z down to $\sim 1/50 Z/Z_{\odot}$, due to the decrease of the average temperature of stars over their lifetime. At even lower metallicities, however, their UV output (per unit SFR) *decreases* since the bulk of their flux is emitted at $\ll 1500 \text{ \AA}$ (cf. Fig. 2 in Schaerer 2003). This implies, for a fixed IMF, a re-increase of SFR/L_{1500} at $Z/Z_{\odot} \lesssim 1/50$, which is only somewhat moderated by the increasing nebular contribution. Indeed, the latter contributes typically $\sim 10\text{--}40\%$ of

²More explicitly the Fig. shows $\log c$, where $\log \text{SFR} = \log c + \log L_{1500} + \log c_M$, and $c_M = 2.55$ for the IMF adopted by Kennicutt ($M_{\text{low}} = 0.1 M_{\odot}$), or $c_M = 1$ for $M_{\text{low}} = 1 M_{\odot}$.

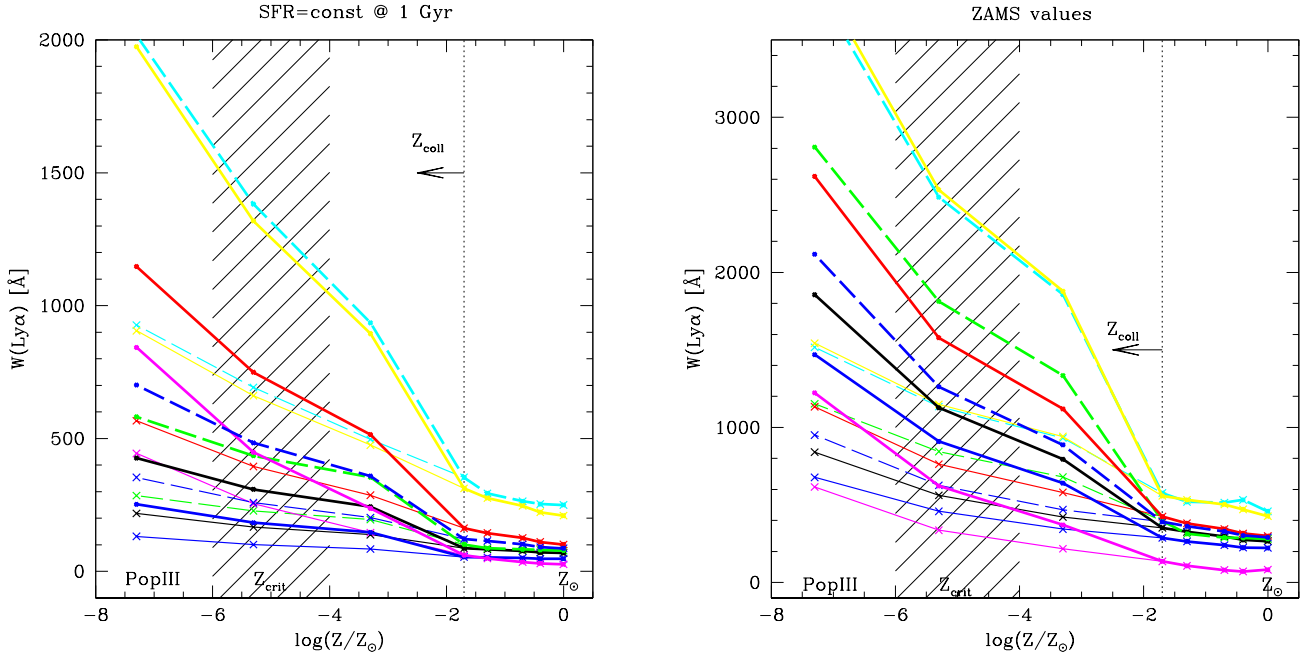


Figure 3.5: Predicted Ly α equivalent width as a function of metallicity for constant star formation (left panel) and very young ($\leq 1\text{--}2$ Myr) bursts (right panel). Note the different vertical scales on the two plots. Thin lines show our “standard” predictions, thick lines the predicted $W(\text{Ly}\alpha)$ accounting to first order for departure from case B following Eq. 3.8 (assuming low density, i.e. $f_{\text{coll}} = 2/3$, and neglecting the increase of the two-photon continuum), leading to an increase by up to a factor $\sim 1.5\text{--}2.5$ at low metallicities ($Z \lesssim Z_{\text{coll}}$). Results for different IMF’s are shown using the same colour codes as in Fig. 3.1 (cf. Table 3.1).

the flux at 1500 \AA at SF equilibrium (see Fig. 3.8). In other words neglecting the nebular continuum would lead to differences of $\sim 0.05\text{--}0.15$ dex in the SFR calibrations. At low metallicity the contribution of the two-photon continuum may be larger, as shown in Sect. 3.4, leading to somewhat lower values of SFR/L_{1500} than shown in Fig. 3.4. For Pop III and the most extreme IMF’s (TE, C) this implies a downward revision of ~ 0.2 dex.

3.3.4 Predicted Ly α emission

The Ly α equivalent widths predicted by our standard models (using Eq. 3.2) for all IMF’s and metallicities are shown with thin lines in Fig. 3.5 for constant star-formation (left panel) and for the ZAMS (right), the latter representing the maximum of $W(\text{Ly}\alpha)$ for each IMF. The dependences of $W(\text{Ly}\alpha)$ are as expected from Q_H/L_{1500} and the values shown here bracket those already presented in Schaerer (2003) (with more limited variations of the IMF). To illustrate the departure from case B found at low metallicity from photoionization models (see Sect. 3.4), we also show $W(\text{Ly}\alpha)$ computed from Eq. 3.4 in the low density

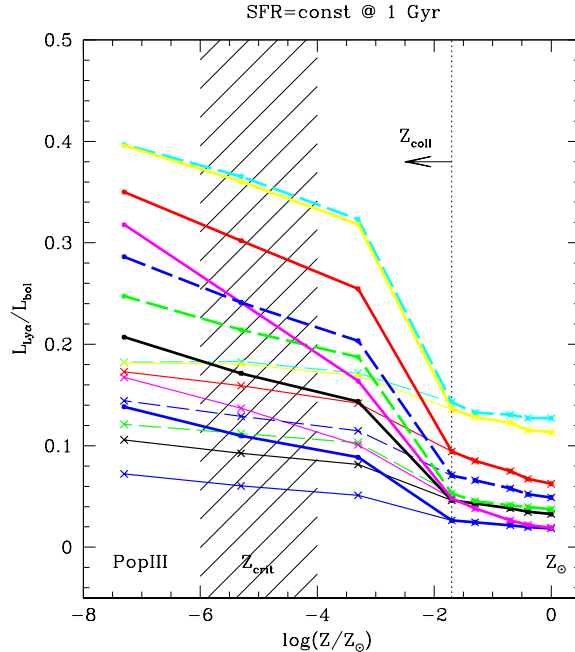


Figure 3.6: Fraction of the Ly α luminosity to the total bolometric luminosity, $L(\text{Ly}\alpha)/L_{\text{bol}}$ for SFR=const as a function of metallicity and IMF. Results for different IMFs are shown using the same colour codes as in Fig. 3.1 (cf. Table 3.1). Thin lines show results using our “standard” Ly α predictions; thick lines the improved results accounting for departures from case B at very low metallicity. Note the resulting strong increase of our revised $L(\text{Ly}\alpha)/L_{\text{bol}}$ values from solar to very low metallicity!

regime (i.e. for $\tilde{f}_{\text{coll}} = 2/3$, thick lines). Here, the equivalent widths are a factor ~ 1.5 – 2.5 higher than our “standard” predictions (cf. Fig. 3.3), since we assume that the continuum close to Ly α is unchanged by this departure from case B.

A few words of caution about $W(\text{Ly}\alpha)$ are appropriate. First, note that for our computations of $W(\text{Ly}\alpha)$ we use the continuum flux at 1215.67 \AA obtained from linear interpolation of the total (stellar + nebular) continuum (in log) between 1190 and 1240 \AA , chosen to avoid underlying stellar Ly α absorption and other absorption lines if present. While $W(\text{Ly}\alpha)$ is well defined theoretically, comparisons with observations require some caution, given the possible complexity of the continuous spectrum shortward (due to the IGM in particular) and longward of Ly α (due to non-monotonic shape of the nebular continuum), and given different choices of broadband filters (see e.g. the simulations of Hayes & Östlin (2006)).

How much of the total radiative energy from the starburst is emitted in the Ly α line? For constant star-formation the fraction of the Ly α to the bolometric luminosity, $L(\text{Ly}\alpha)/L_{\text{bol}}$, is shown in Fig. 3.6 for all metallicities and IMFs. At solar metallicity and for a Salpeter IMF we obtain the well-known estimate of $L(\text{Ly}\alpha)/L_{\text{bol}} \sim 3$ – 6% found in the first papers promoting Ly α searches at high redshift (e.g. Partridge & Peebles 1967). The fraction of

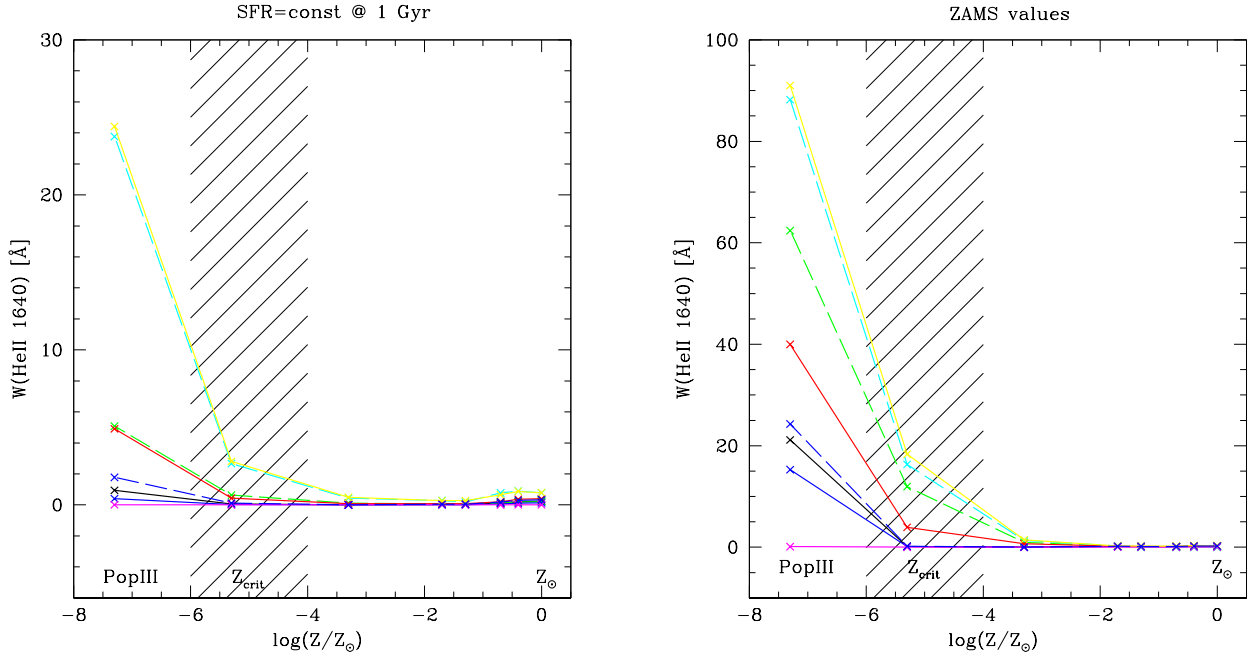


Figure 3.7: Predicted He II $\lambda 1640$ equivalent width as a function of metallicity for constant star formation (left panel) and very young ($\leq 1\text{--}2$ Myr) bursts (right panel). Note the different vertical scales on the two plots. Results for different IMFs are shown using the same colour codes as in Fig. 3.1 (cf. Table 3.1). Note that photoionization models predict generally fainter He II $\lambda 1640$ emission, hence lower equivalent widths, except for high ISM densities (see Sect. 3.4.3).

luminosity emitted in Ly α increases with decreasing metallicity, due to the higher ionizing photon flux output per unit stellar mass. When case B departures at low metallicity are taken into account, we find that $L(\text{Ly}\alpha)/L_{\text{bol}}$ can reach up to $\sim 20\text{--}40\%$ depending on the IMF, i.e. up to 10 times more than expected from earlier calculations! The highest values are comparable to those from the photoionization models of Panagia (2002) using very hot black body spectra. For younger populations $L(\text{Ly}\alpha)/L_{\text{bol}}$ is less dependent on the IMF than for SFR=const shown here; values of $L(\text{Ly}\alpha)/L_{\text{bol}} \sim 0.15\text{--}0.20$ (0.35–0.40) are obtained at low Z with our standard (departure from case B) assumptions.

3.3.5 He II line emission from very metal-poor starbursts

Our standard predictions for He II $\lambda 1640$ (using Eq. 3.3) for constant star-formation and young bursts are shown in Fig. 3.7. They complement our earlier predictions in Schaerer (2003), and show the expected behaviour. Clearly, strong nebular He II $\lambda 1640$ emission from starbursts is only expected at very low metallicity and for IMFs producing enough massive stars. As we will show below, the predicted intensity of He II $\lambda 1640$ (and other He⁺ recombination lines) depends, however, also on the ionization parameter and on the ISM

density to some extent. Complete photoionization models predict generally fainter He II $\lambda 1640$ emission, as discussed in Sect. 3.4.

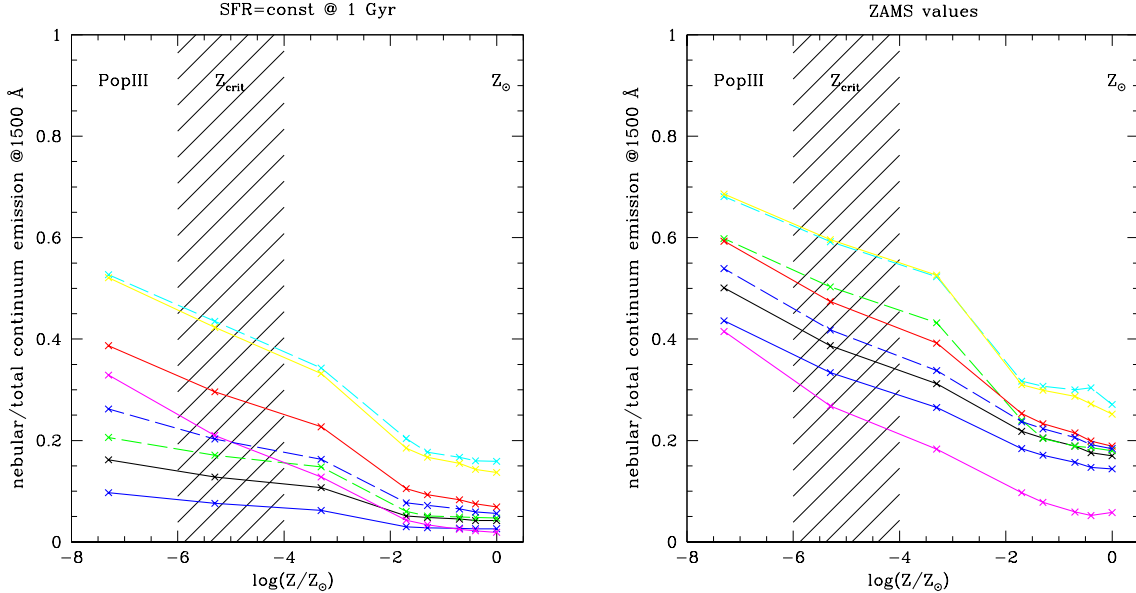


Figure 3.8: Contribution of nebular continuum emission to the total emission in the rest-frame UV at 1500 \AA as derived from our evolutionary synthesis models. Shown are model for constant star formation (left panel) and very young ($\leq 1\text{--}2 \text{ Myr}$) bursts (right panel). Results for different IMFs are shown using the same colour codes as in Fig. 3.1 (cf. Table 3.1).

3.3.6 Importance of the nebular continuum

Figure 3.8 shows the contribution of nebular continuous emission to the total UV light at 1500 \AA for all metallicities, IMFs, and for the usual limiting cases of star-formation histories. Whereas for ‘normal’ metallicities and IMFs the contribution is relatively small ($\lesssim 5\%$ for SFR=const), the importance of the nebular continuum is larger for young bursts and/or low metallicity, as already stressed by Schaerer (2002) and Schaerer (2003).

Since the nebular continuum at 1500 \AA is generally dominated by the two-photon continuous emission process, departures from case B will lead to stronger nebular emission than shown here at very low metallicity (see Sect. 3.4). To first order, the total two-photon emission is then enhanced by a factor P for low ISM densities, increasing thus the contribution of the nebular continuum to the total (stellar + nebular) emission. At high density, the two-photon emission tends to zero. However, since the shape of the nebular continuum depends on the detailed conditions in the nebula (density, temperature, etc.) which are not constant as assumed in the synthesis models, it is not possible to predict more accurately how departures from case B affects the nebular continuum, without resort to photoionization models.

3.3.7 Predicted UV slope

From our synthesis models we also measured the slope of the UV continuum with and without nebular emission (cf. Schaerer & Pelló 2005). In Fig. 3.9 we show a condensed overview of various β -slopes for very young populations (ZAMS), representing the steepest slopes, i.e. the minimum for β , predicted from models. As before, the predictions are shown for all IMFs and metallicities. Thick (thin) lines show β_{1550} (β_{2000}), defined as the slope between 1300–1800 (1800–2200) Å respectively³. The upper set of lines shows the β slopes of the total spectrum, including stellar and nebular continuum, the lower lines using the pure stellar spectrum.

Clearly, the UV slope is strongly affected by nebular emission, leading to a significant flattening of the spectrum (cf. Figs. 2 in Schaerer 2003). While the stellar SED becomes steeper with decreasing metallicity, the total spectrum exhibits the opposite behaviour. If we assume a varying contribution of the nebular continuum we may obtain any intermediate value of β between the “stellar+nebular” and “pure stellar” cases. This fact and the dependence of β on the star-formation history and age (see e.g. Fig. 1 in Schaerer & Pelló 2005), shows that the UV slope cannot be used to determine metallicity. For constant star-formation (not shown here), the bulk of the models show equilibrium values of $\beta \sim -2.6$ to -2 , quite independently of metallicity and IMF.

Fig. 3.9 also shows a difference of the order of 0.2–0.3 between β_{1500} and β_{2000} . Such differences may be relevant for comparisons of the UV slope estimated from broad-band filters. Last, but not least, the precise shape of the nebular continuum is determined by the detailed nebular structure (i.e. its detailed temperature and density structure) and can be affected by departures from case B, as the case of the two-photon continuum discussed in depth below.

3.4 Nebular predictions using photoionization models

For low metallicity nebulae ionized by very hot stars, the conventional case B predictions for line and continuum emission are not good approximations to the appropriate nebular astrophysics. In this Section we present the predictions of detailed photoionization modelling for such nebulae with metallicities ranging from zero (primordial = Pop III) to solar, explain the origin of departures from case B, and present a parameterisation of the results than can be readily employed for the interpretation of low metallicity nebulae. For simplicity, we first use black body spectra as ionizing sources and discuss later how to compare these with stellar SEDs. We have examined the nebular emission as a function of the stellar (black body) temperature T_{bb} , the hydrogen number density n_H , the ionization parameter (U), and the nebular metallicity (Z_{neb}), using the models described above (Sect. 3.2.2).

Our analysis will focus mainly on the Ly α line and the associated two-photon continuum emission, on nebular He II emission, and on the global nebular continuum.

³ We use the standard definition $F_\lambda \propto \lambda^\beta$.

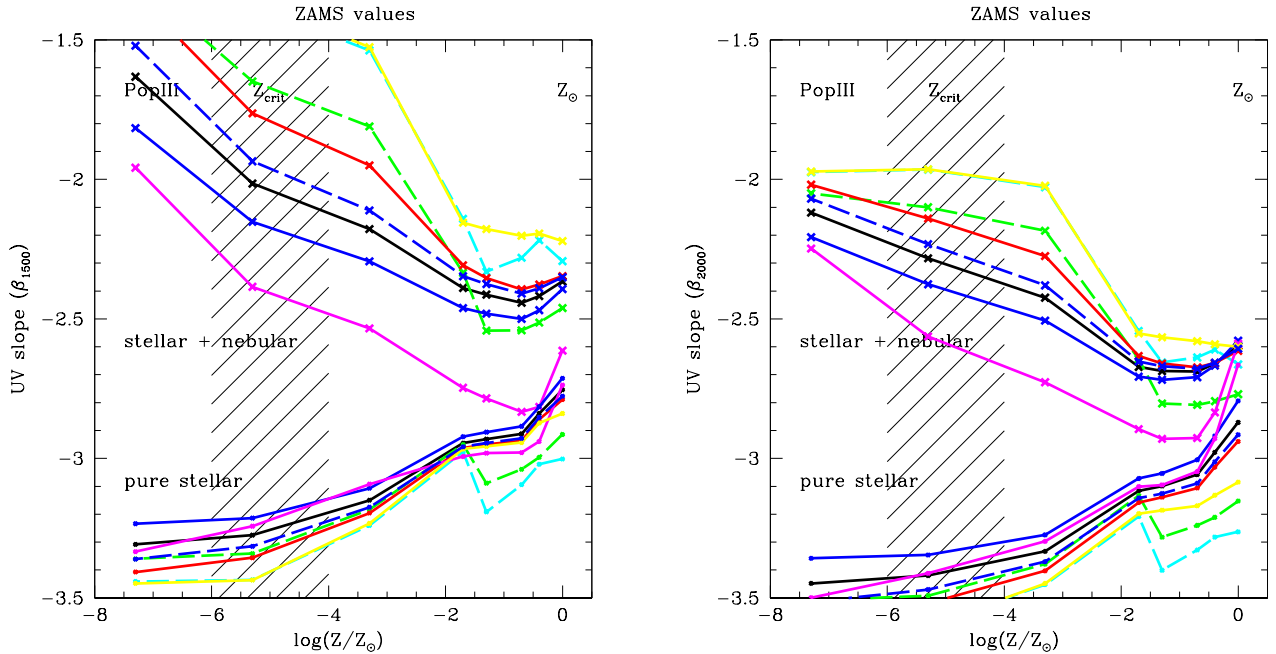


Figure 3.9: Predicted UV slopes β_{1500} and β_{2000} for all IMFs and metallicities. The values are shown for very young (ZAMS) populations, which correspond to the bluest possible slopes (i.e. minimal β values). The upper set of lines shows the UV slopes of the total spectrum (stellar + nebular continuum), the lower lines using the pure stellar spectrum. Results for different IMFs are shown using the same colour codes as in Fig. 3.1 (cf. Table 3.1).

3.4.1 Ly α line and two-photon continuum emission

In Fig. 3.10 we show the deviation of the Ly α (black symbols) and 2γ emission (red) and other quantities as predicted from photoionization models with primordial composition and different densities with respect to their case B values. To calculate case B luminosities we adopt Eq. 3.2 and assume $L(2\gamma) = 0.5 c_1 Q(\text{H})$ for the luminosity in the two-photon continuum. The numerical factor $0.5 \approx \alpha_{22S}^{\text{eff}}/\alpha_{22P}^{\text{eff}}$ is appropriate for low densities. For simplicity we always compare the results to the low density limit case B predictions.

At low density, the luminosity of both Ly α and 2γ emission are increased by a factor of ~ 1.3 to 3 over the black body temperature range considered here. The physical reason for this strong departure from case B is due to collisional effects, which increase the population of the $n = 2$ level of hydrogen from which additional ionizations can take place, leading overall to an increased ionization rate in the nebula. In equilibrium, this implies an increased recombination rate and higher Ly α and 2γ luminosities. Collisional excitation is significant in (very) low metallicity nebulae with hot ionizing sources because radiative cooling is reduced, leading to higher electron temperatures. Photoionization from excited states (here from $n = 2$), in particular, is not taken into account under case B assumptions.

To describe quantitatively the effect of enhanced photoionization rates, including ionization from the excited $n = 2$ state, it is sufficient to consider the mean energy of the ionizing photons in units of the ionization potential of hydrogen, P , given by

$$P = \frac{\overline{E}}{13.6 \text{ eV}} = \left(\frac{\int_{13.6 \text{ eV}}^{\infty} F_{\nu} d\nu}{\int_{13.6 \text{ eV}}^{\infty} \frac{F_{\nu}}{h\nu} d\nu} \right) / (13.6 \text{ eV}), \quad (3.6)$$

where \overline{E} is the average ionizing photon energy in the Lyman continuum in units of eV. Indeed, as Figure 3.10 shows, the enhancement of the Ly α and two-photon continuum emission, which both measure the effective recombination rate, scales very accurately with P at low density. This scaling shows that the available energy of the Lyman continuum photons – which is in excess of the necessary minimum of 13.6 eV – is “optimally” used to maximise the number of photoionizations, leading to an effective increase of the ionization rate from $\propto Q(\text{H})$ to $\propto P \times Q(\text{H})$, and hence to the same increase in the recombination rates, i.e. also in the Ly α and 2γ luminosities.

The effect of “boosted” Ly α and 2γ emission just discussed depends on the nebular metallicity. This is because more metals are present and more efficient cooling results in cooler gas than in the primordial metallicity case, decreasing the collisional effects for H. The range over which these effects take place is discussed below.

Density effects

Figure 3.10 also shows that Ly α is further enhanced at high densities at the expense of two-photon emission, the sum of the two luminosities being essentially constant if all other parameters are kept fixed. Collisional mixing of the relative populations of the $n = 2$ levels between 2^2S and 2^2P of hydrogen alters the relative importance of the rates of Ly α and two-photon transitions resulting in increased line emission relative to the 2γ continuum.

To correct for this effect under case B assumptions, Panagia (1973, see also Stiavelli 2009) writes $L(\text{Ly}\alpha) = Q(\text{H}) \times h\nu_{\text{Ly}\alpha} \times f_{\text{coll}}$ (cf. Eq. 3.1), where

$$f_{\text{coll}} \approx \frac{1 + a \times n_p}{1.5 + b \times n_p}, \quad (3.7)$$

with $a = b = 1.35 \times 10^{-4}$, and where n_p is the proton density. In this way the factor f_{coll} ranges from $2/3 \approx \alpha_{2^2P}^{\text{eff}}/\alpha_B$ for low densities to $f_{\text{coll}} = 1$ for high densities. Under these assumptions, the two-photon continuum luminosity is $L(2\gamma) = Q(\text{H}) \times h\nu_{\text{Ly}\alpha} \times (1 - f_{\text{coll}})$.

To derive the corresponding numerical factor from our detailed photoionization models and to separate the density effect from the enhancement factor P found above, we define \tilde{f}_{coll} through:

$$L(\text{Ly}\alpha) = (1 - f_{\text{esc}})Q(\text{H}) \times h\nu_{\text{Ly}\alpha} \times P \times \tilde{f}_{\text{coll}}. \quad (3.8)$$

The corresponding values of \tilde{f}_{coll} , obtained for our grid of models for primordial nebulae are plotted in Figure 3.11 as a function of the input hydrogen density. Also shown is, for comparison, Panagia’s expression (Eq. 3.7) assuming $n_p = n_H$. Notice that \tilde{f}_{coll} presented

here is not derived from the Ly α and 2 γ luminosities (which ranges from 2/3 to 1 as in Panagia’s formula) but it is the fitting formula which has been calculated by comparing the right hand side of equation 3.8 with our CLOUDY results.

For convenience, we derive the following 3-parameter fit:

$$\tilde{f}_{\text{coll}} \approx \frac{1 + a \times n_H}{b + c \times n_H}. \quad (3.9)$$

with $a = 1.62 \times 10^{-3}$, $b = 1.56$ and $c = 1.78 \times 10^{-3}$. The coefficients obtained here differ from those of Panagia (1973) due to the fact that we have used a suite of photoionization models covering a wide range of T_{bb} and U resulting in different T_e and a different balance between processes in the nebula. However, the change in \tilde{f}_{coll} has little effect on the values of $L(\text{Ly}\alpha)$ for low density. We use \tilde{f}_{coll} defined in this way for convenience since it allows us to reproduce the CLOUDY results. As Fig. 3.11 shows, our fit formula allows us to describe density effects with an accuracy of $\pm 10\%$ at high density and somewhat better at low n_H .

The black dashed lines in Figure 3.10, showing $P \times \tilde{f}_{\text{coll}}/\tilde{f}_{\text{coll}}(\log(n_H = 1))$, show how well our analytical prediction for Ly α , including also density effects, works at primordial metallicity.

Applicable metallicity range

The effect of collisional excitations, allowing for photoionization of H from excited states, depends on the electron temperature of the nebula, and hence on its metallicity. To find the range of nebular metallicity where our analytic expressions for $L(\text{Ly}\alpha)$ holds, we have computed model grids at different metallicities. We can then ascertain how much our fit to the primordial case deviates from CLOUDY models as a function of metallicity.

The critical metallicity where the luminosity obtained by our fit deviates on average (for the entire grid of models) by 10 % from the correct one is $Z_{\text{coll}} \approx 0.03 Z_{\odot}$. At higher metallicities, cooler nebulae are produced and hence collisional effects play a smaller role in boosting hydrogen emission. However, the effect only decreases gradually for higher metallicities and depends on the detailed condition of the gas. For instance, in our simulations for $Z_{\text{neb}} = 0.05 Z_{\odot}$, the average deviation of the results obtained with our formula (primordial case) with respect to the CLOUDY results is 13%, while for $Z_{\text{neb}} = 0.1 Z_{\odot}$ it is 20%. The value of the “transition” metallicity $Z_{\text{coll}} \approx 0.03 Z_{\odot}$ below which Ly α (and the 2 γ continuum) are significantly boosted (modified) by departures from case B should therefore only be taken as an indicative value. Tailored photoionization models are necessary for more accurate predictions.

3.4.2 Other H lines

The luminosities of other hydrogen lines are close to their case B predictions as is shown in Figure 3.10 for H α (green symbols) and H β (blue symbols). They are basically independent of U .

These lines are used to calculate the Balmer decrement which is conventionally used to measure the extinction. The Balmer decrement ($H\alpha/H\beta$) obtained from our grid of models for $\log(U) = -1$ is shown in Figure 3.12. It increases towards higher T_{bb} and exceeds the values commonly used, for example 2.86 for $n_e = 10^2 \text{ cm}^{-3}$ and $T_e = 10 \text{ kK}$ (Dopita & Sutherland 1996). The reason for the enhanced $H\alpha/H\beta$ ratio is the collisional excitation of hydrogen, one of the contributors to enhanced $\text{Ly}\alpha$ and 2γ emission. This effect (see Osterbrock 2006) occurs when photoelectrons carrying enough energy when colliding with H atoms, excite higher levels followed by radiative cascade. Enhanced $H\alpha$ emission increases the Balmer decrement which must be accounted for when calculating the extinction. An enhanced Balmer decrement was already found, e.g. in tailored photoionization models for the metal-poor galaxy I Zw 18 (Davidson & Kinman 1985; Stasińska & Schaerer 1999) and other giant H II regions (cf. Luridiana et al. 2003), and has also been addressed by Luridiana (2009).

3.4.3 He II lines

The He II 1640 Å line is of a particular interest since it has been considered as one of the signatures of Pop III or very metal-poor stars, which are expected to have a very hard ionizing spectrum emitting copious He^+ ionizing photons. Figure 3.10 (orange symbols) shows He II 1640 Å emission line luminosities relative to their case B values, calculated for the same T_e and n_e as the hydrogen lines. For lower ionization parameters, the line becomes weaker. This is due to an effect already discussed by Stasińska & Tylenda (1986) in the context of planetary nebulae. Photons with sufficient energy to ionize He^+ are also able to ionize hydrogen. When calculating the luminosity of He II in synthesis models, it is assumed that every photon with an energy $>54 \text{ eV}$ ionizes one He^+ ion. The absorption of some high energy photons by H atoms results in a decrease in the number of photons available for producing He II emission. The effect becomes significant at low ionization parameters since then the He^+/H^0 fraction decreases and the probability of the high energy photon being absorbed by a H atom rather than by He^+ is higher. This means that the synthesis models give an upper limit for the He II luminosity. We have not found a simple analytical prescription to account for the effect of this process on the He II luminosity.

The behaviour of the equivalent width of He II is discussed in Sect. 3.5.

3.4.4 Nebular continuum emission

Nebular emission arising in H II regions can contribute significantly to the measured spectrum. The total nebular continuum is the sum of the free-free, free-bound and 2γ continua of hydrogen and helium. Several nebular parameters affect its shape. It depends on the electron temperature, ionization parameter, nebular metallicity and particle density in the gas, as e.g. illustrated by Bottorff et al. (2006).

In Figure 3.14 we show the density dependence of the nebular continuum, which mainly affects the 2γ emission and hence also the shape of the continuum between $\text{Ly}\alpha$ and the Balmer jump. Figure 3.13 shows the dependence on the nebular metallicity. For higher

metallicities, the increased cooling lowers the total emission in the nebular continuum, and its shape is altered as expected from atomic physics (see Bottorff et al. 2006) due to the decrease of the average electron temperature at higher metallicity. Evolutionary synthesis models such as ours, cannot properly describe the variety of shapes and strengths of the nebular continuum shown here, since they rely on simple assumptions such as constant nebular density and temperature. Again, tailored photoionization models are necessary for more accurate predictions.

3.5 Photoionization models for realistic SEDs

In this Section we show how to relate realistic SEDs obtained e.g. from evolutionary synthesis models with the results from the photoionization models discussed above, which used black body spectra. Finally, we show the updated predictions for the equivalent widths of Ly α and He II λ 1640 lines obtained from our CLOUDY models.

3.5.1 How to connect realistic SEDs with black body calculations

Since the number of H ionizing photons and their mean energy are the main parameters determining the luminosity of the H recombination lines and of the 2γ continuum, $Q(H)$ and P suffice to compute these quantities from arbitrary SEDs. To account also for density effects, Eqs. 3.8 and 3.9 can be used to yield the correct Ly α luminosity. Numerical tests using SEDs described in Sect. 3.3 show the validity of this result, typically within 2-3 %. For black bodies the relation between P and T_{bb} is given by

$$T_{\text{bb}}[\text{kK}] = -53.42 + 69.85 P \quad (3.10)$$

to a good approximation. The black body temperature $T_{\text{bb}}(P)$ corresponding to the more realistic SED is thus easily determined.

For other quantities, such as the He II line luminosity, the correspondence between black bodies and other SEDs is different. For example, since the relative line ratios of He II/H lines depend to first order on the relative number of He $^+$ /H ionizing photons, the black body with the same hardness $Q(\text{He}^+)/Q(\text{H})$ is the most appropriate. For black body spectra one has, to a good approximation:

$$T_{\text{bb}}[\text{kK}] = 314.6 + 382.4 x + 268.7 x^2 + 103.3 x^3 + 20.12 x^4 + 1.545 x^5. \quad (3.11)$$

where $x = \log(Q(\text{He}^+)/Q(\text{H}))$. Again, we have tested a number of models and confirmed that one can get the same luminosity (within a few %) using SEDs and corresponding black body models, for otherwise identical nebular parameters. Differences of $\sim 10\%$ can appear in case of significantly (several eV) different values of P . In principle not only the stellar $Q(\text{He}^+)/Q(\text{H})$ ratio determines the He II emission, but also the conditions in the

gas. Since P establishes the electron temperature, significant differences in P result in different luminosity coefficients (recombination rates and emissivities).

In Fig. 3.15 we show such a comparison between a realistic SED from our synthesis models (Pop III, Salpeter IMF 1–100 M_{\odot} at zero age, instantaneous burst) and the appropriate black body, chosen such as to reproduce the correct H line luminosities and nebular continuum. Here the average photon energy in the Lyman continuum is $\bar{E} = 30.033$ eV, hence $T_{\text{bb}} = 102$ kK. The input spectra, shown on the left panel, are scaled to the same total Lyman continuum flux $Q(H)$. The nebular parameters are $\log(n_H) = 1 \text{ cm}^{-3}$, $\log(U) = -1$, and primordial composition.

Several interesting points are illustrated with this figure. First, as the left panel shows, it must be remembered that realistic SEDs show a Lyman break due to the hydrogen opacity in the atmosphere of the hot stars responsible for the flux. For young ages this break corresponds typically to a flux increase by ~ 0.2 - 0.3 dex at 912 \AA , as discussed e.g. by Schaerer (2003)⁴. In consequence, calculations relying on black body spectra underestimate the observable UV continuum, as shown in the right panel of Fig. 3.15, leading to non-negligible differences e.g. for equivalent widths predictions of emission lines (cf. below). In Fig. 3.15 (right panel) we also show the stellar + nebular SED predicted by our synthesis models assuming constant nebular density and temperature and case B (green line). The differences between this and the full CLOUDY model are mainly due to the boosting of the 2γ continuum discussed earlier, and to varying n_e and T_e .

3.5.2 Ly α equivalent width predictions

The measurement of the equivalent width of Ly α is both observationally and interpretationally difficult, since the continuum around it is affected on one side at high redshifts by Ly α forest absorption and on the other by an unknown combination of 2γ continuum and starlight. Furthermore, when not measured from spectroscopy, it is common practice to measure $W(\text{Ly}\alpha)$ via a line to continuum ratio with the continuum estimated at another (usually longer) wavelength λ_{cont} , e.g. $W_{\lambda} = L_{\text{line}}/F_{\lambda_{\text{cont}}}$. Different methods to measure $W(\text{Ly}\alpha)$ have been reviewed by Hayes & Östlin (2006). To illustrate the possible impact or uncertainty related to the way the continuum is estimated we subsequently plot Ly α equivalent widths predicted from the CLOUDY models using the continuum at both 1240 and 1500 \AA as a reference.

Figure 3.16 shows the predictions for $W(\text{Ly}\alpha)$ from all CLOUDY models for primordial composition, as a function of T_{bb} , ionization parameter and hydrogen density. Black symbols show the predictions using black body spectra and accounting for the nebular continuum; red symbols the same but neglecting the nebular continuum. Blue symbols show the results from CLOUDY models using SEDs from our Pop III synthesis models for zero age populations, plotted at the corresponding $T_{\text{bb}}(P)$ value (see above). Pink symbols

⁴The amplitudes of the Lyman break, $912^+/912^-$, given in Schaerer (2003) for very low metallicities are correct, but misleading. Indeed, with the definition adopted there, the 912^+ flux average (over 1080 – 1200 \AA) includes strong absorption from the He II $\lambda 1084$ line. This leads to values of $912^+/912^- < 1$ despite the fact that all models show a Lyman break in absorption.

show $W(\text{Ly}\alpha)$ predicted from our standard synthesis models neglecting the boost of $\text{Ly}\alpha$ (case B departure).

Overall $W(\text{Ly}\alpha)$ increases with the T_{bb} or equivalent since the $\text{Ly}\alpha$ luminosity ($\propto Q(H) \times P$) increases more rapidly than the continuum flux close to $\text{Ly}\alpha$. For very hot models and if 1500 \AA is taken as a reference for the continuum, $W(\text{Ly}\alpha)$ tends to a maximum value (here $\sim 2000 \text{ \AA}$, as shown in col. 2) since line emission and the dominating nebular continuum scale in the same manner. For the reasons discussed above (absence of the Lyman break), predictions based on black body spectra (black and red symbols) overestimate $W(\text{Ly}\alpha)$ compared to models including more realistic stellar SEDs (in blue). Differences between black body models including or neglecting the nebular continuum (black and red) decrease with increasing ISM density, because of the decrease of the 2γ continuum. This also explains the decreasing difference between $W(\text{Ly}\alpha)$ using 1240 and 1500 \AA as a reference, when n_H increases. Last, but not least, $W(\text{Ly}\alpha)$ predicted by our standard synthesis models for the ZAMS (pink symbols) fall below the more accurate CLOUDY predictions (blue), since the latter account for case B departures. Once applying the simple correction given by Eq. 3.4 one obtains the result which takes into account the increase in $\text{Ly}\alpha$ line flux. However, that is only the first order correction which does not include the difference coming from the continuum, mainly a similar increase in the 2γ continuum. In cases when the continuum is measured around $\text{Ly}\alpha$ (1240 \AA) stellar flux is dominant so the correction described above gives a good estimate of the correct $W(\text{Ly}\alpha)$ value (see Fig. 3.17).

3.5.3 He II $\lambda 1640$ equivalent width

The right column in Fig. 3.16 shows the predicted He II $\lambda 1640$ equivalent widths for the same CLOUDY models except that $T_{\text{bb}}(x)$ from Eq. 3.11 is used here. The nebular continuum predicted at 1640 \AA is included in all calculations of $W(1640)$. In contrast to $\text{Ly}\alpha$, the He II equivalent width depends on the ionization parameter, since the line luminosity changes due to the ‘‘Stasinska-Tylenda effect’’. For high ISM densities $W(1640)$ increases due to the decrease of the nebular continuum. Differences between models assuming black body spectra (black symbols) and realistic SEDs (blue) are minor for $W(1640)$ as long the nebular continuum dominates at these wavelengths. This is true for sufficiently hot spectra ($\gtrsim 80 \text{ kK}$). Compared to predictions from our standard evolutionary synthesis models (pink symbols) the He II $\lambda 1640$ equivalent widths predicted by CLOUDY are significantly lower for $T_{\text{bb}} \gtrsim 100 \text{ kK}$. This is due to two effects, the Stasinska-Tylenda effect reducing the line flux, and the increase of the 2γ nebular continuum. At lower T_{bb} , case B predictions give an upper limit (corresponding to our highest ionization parameter case) for He II $\lambda 1640$. Only for a high ionization parameter and/or high density do photoionization models predict $W(1640)$ values as high as those given by Schaerer (2003).

3.5.4 Summary: correction of evolutionary synthesis model results for departures from case B

In this Section we give a recommended step-by-step procedure which allows the correction of the synthesis models for the departures from case B in ionization bounded regions (i.e. with no leakage of Lyman continuum photons), relevant especially for the case of very hot stars and very low metallicities.

For L(Ly α):

- Take the SED (function of age, IMF, ...).
- Get (or compute) the mean energy of Lyman continuum photons, P , in units of 13.6 eV.
- Compute the “collisional” factor \tilde{f}_{coll} from our fit formula (Eq. 3.9).
- Multiply the synthesis model result $L(\text{Ly}\alpha)$ by $P * \tilde{f}_{\text{coll}}/(2/3)$ (Eq. 3.4).

For W(Ly α): divide the equivalent width obtained by the synthesis model of interest by 2/3 and multiply it by $P * \tilde{f}_{\text{coll}}$. This provides the first order correction for $W(\text{Ly}\alpha)$, neglecting the increase of the nearby nebular continuum. An example following this procedure is shown by the green symbols in Fig. 3.17.

For He II recombination lines: no simple correction is possible. Synthesis models give an upper limit for the luminosity, an upper limit for equivalent width up to $\log(Q(\text{He}^+)/Q(\text{H})) \sim -1.2$ for the primordial metallicity case and overestimate it for the highest $Q(\text{He}^+)/Q(\text{H})$ cases (low density) due to the lack of accounting for enhanced 2γ emission.

3.6 Discussion and implications

3.6.1 Dependence on model assumptions

All our CLOUDY models have been computed for ionization bounded nebulae corresponding to no escape of Lyman continuum photons, i.e. $f_{\text{esc}} = 0$. For density (or matter) bounded cases with $f_{\text{esc}} > 0$, quantities such as hydrogen recombination line luminosities and the luminosity of the nebular continuum longward of Ly α can be rescaled to first order by scaling with $(1 - f_{\text{esc}})$, as already introduced in Eq. 3.8. Such a scaling is appropriate since the corresponding emissivities are approximately constant across the nebula. However, since He $^+$ recombination lines (if present) are emitted only in the innermost parts of the nebula, He II line luminosities will not be reduced in density bounded regions, as long the radius of the He $^+$ sphere remains smaller than that of density bounded H II region. These behaviours are also expected in non-spherical regions, as demonstrated e.g. by Johnson et al. (2009). In consequence, both $L(\text{Ly}\alpha)$ and $W(\text{Ly}\alpha)$ will decrease with increasing Lyman continuum escape (although the latter not proportionally with f_{esc}), whereas the opposite will be true for $W(\text{He II } \lambda 1640)$ and for other He II lines, where the underlying continuum is mostly

of nebular origin. In other words, the decrease of $W(\text{He II } \lambda 1640)$ found in this paper due to competition with H ionizing photons, may be mitigated in objects with significant leakage of Lyman continuum radiation, leading again to higher He II equivalent widths (cf. Schaerer 2002, 2003). For other effects of “leaking”, i.e. star-forming galaxies with density bounded H II regions, see the photoionization models of Inoue (2010).

We shall now discuss some implications of our modelling for the interpretation of the hydrogen and helium emission lines and the nebular continuum observed in high redshift emission line galaxies.

3.6.2 Lyman continuum output

As metallicity decreases, the Lyman continuum output of the stellar population, both relative to the observed stellar UV continuum longward of $\text{Ly}\alpha$ and per unit stellar mass, increases. The amount of this increase depends obviously also on the detailed shape of the IMF. For example, for a Salpeter IMF with a uniform upper mass cut-off of $100 M_{\odot}$, the ionizing photon rate per unit UV luminosity, Q_H/L_{1500} , increases by a factor 3 approximately between solar and zero metallicity. For the most extreme IMF considered here this increase is up to a factor 10 (see Fig. 3.1). The effect of this is to increase the line and nebular continuum emission relative to any observable stellar continuum. In extreme cases (e.g., Raiter et al. 2010) the nebular emission may completely dominate the UV/visible/NIR spectrum. Also, if low metallicity objects and/or different IMFs are relevant for the sources of cosmic reionization, their intrinsic Lyman continuum flux, generally estimated from UV restframe observations, may need to be revised accordingly.

3.6.3 SFR(UV)

The estimation of SFR from the level of the UV continuum (cf. Kennicutt 1998) is based on evolutionary synthesis models assuming “standard” stellar populations and IMFs. At metallicities below solar, the output of observable UV continuum radiation (i.e. typically at 1500 \AA restframe) per unit stellar mass increases somewhat, due to the increasing average temperature of the stars (cf. Fig. 3.4). A maximum in L_{1500} is typically reached at $Z/Z_{\odot} \sim 1/100$. Below this, the average spectrum shifts more strongly into the Lyman continuum, leading to a decrease of stellar radiation in the observable UV, which is, however, compensated by increasing nebular emission. The net result, illustrated in Fig. 3.4 for constant SFR, is that star-formation rates derived from the UV may need to be revised downward at low metallicities with respect to the “standard” calibration of Kennicutt (1998), but typically by less than a factor 2.

3.6.4 $\text{Ly}\alpha$

One of the main findings of our study is the enhancement of $\text{Ly}\alpha$ emission at low metallicities with respect to the commonly used case B value. This departure from case B occurs even at moderately low metallicity, say $Z/Z_{\odot} \lesssim 1/10$, and becomes more important for

lower Z . In consequence, higher intrinsic Ly α line luminosities relative to the UV continuum (to L_{bol} , SFR, or to another measure of the rate of massive star-formation) are expected and higher Ly α equivalent widths. Even higher values of $W(\text{Ly}\alpha)$ can be obtained in regions with a high ISM density, where Ly α emission can further be “boosted” at the expense of the 2-photon nebular continuum (see Fig. 3.10).

With respect to our earlier predictions (cf. Schaerer 2003), $W(\text{Ly}\alpha)$ is increased by a factor 2–2.5 for Pop III objects, and by more than 70% at moderately low metallicity ($Z/Z_{\odot} \lesssim 1/20$, cf. Fig. 3.5), for a given IMF. This increase of Ly α may help to understand objects with large Ly α equivalent widths found in some surveys, without the need for recourse to unusual IMFs or to a clumpy ISM (cf. Malhotra & Rhoads 2002; Dawson et al. 2004; Finkelstein et al. 2008).

Finally, the enhanced Ly α emission found here should represent good news for searches for very distant/early galaxies, since the intrinsic Ly α emission of metal-poor objects is shown to be considerably higher than previously thought, reaching up to 20–40% of L_{bol} in Pop III dominated objects. Of course, the intrinsic Ly α emission (and hence also $W(\text{Ly}\alpha)$) will be lower in objects, having a non-zero escape of flux from the Lyman continuum. Furthermore, several processes exist (e.g. dust absorption, scattering out of the line-of-sight in the ISM and/or IGM), which will reduce the Ly α emission on the way from the source to the observer.

3.6.5 He II emission

The reduced He II emission found in this paper, compared to our earlier predictions assuming simple case B recombination, may indicate that ongoing searches for signatures of Pop III stars using this feature (see e.g. review by Schaerer 2008) could be more difficult than anticipated so far. The corresponding upper limits of Pop III star-formation rate density derived e.g. from the survey of Nagao et al. (2008) need then to be revised upwards.

The detection of the He II $\lambda 1640$ line indicates a significant number of high energy photons in the ionizing spectrum. This line has therefore been sought, but not detected so far at high- z (Nagao et al. 2008). Prescott et al. (2009) have detected this line from a $z=1.67$ spatially extended nebula (or Ly α blob) but have not been able to determine the nature of the ionizing source. We find that the line (and therefore the equivalent width) could be fainter than expected previously, due to its dependence on the ionization parameter. This suggests that deeper observations will be needed to detect it. Additionally, another difficulty comes from the fact that for the hottest (the highest $Q(\text{He}^+)/Q(\text{H})$ ratio) stars the strongest enhancement in 2γ continuum is predicted which further decreases the measured $W(1640)$. However, if Pop III stars are present in objects with significant escape fractions in the Lyman continuum, the He II $\lambda 1640$ equivalent width may again be stronger, due to the reduced nebular continuum (cf. Sect. 3.6.1).

3.6.6 Nebular continuous emission

The overall nebular continuum emission is dependent on several nebular parameters and can result in a variety of spectral shapes (Fig. 3.13 and 3.14). Note that our simulations have been carried out in the absence of dust which would add another parameter affecting the shape of the continuum.

Proper photoionization modelling shows the importance of the 2γ continuum produced in a nebula ionized by very hot stars. At low ISM density and primordial/low metallicity, it is boosted in the same way as $\text{Ly}\alpha$ and can completely dominate the nebular emission at 1216 – 1600 Å. This can affect the broadband flux measurements and reduce the equivalent widths of UV emission lines, particularly He II. The strength of the nebular continuum and the expected variations of its spectral shape also indicate that measurements of the $\text{Ly}\alpha$ equivalent width from photometry may be more uncertain than naively expected (cf. Hayes & Östlin 2006).

As can be seen from Fig. 3.15, the slope of the UV continuum between $\sim 1300 - 2000$ Å obtained from our CLOUDY model is very similar to that predicted by the evolutionary synthesis models assuming the same case B assumption, constant electron density and temperature. When the 2γ continuum is included, one cannot obtain significantly steeper slopes than found for this Pop III simulation, since the electron temperature which affects the shape of 2γ emissivity (cf. Bottorff et al. 2006) becomes lower as metallicity increases.

3.7 Conclusions

Building on the earlier calculations of Schaerer (2002, 2003), we have computed evolutionary synthesis models for a wide range of metallicities from Pop III (zero metallicity) to solar metallicity covering a wider range of IMFs – including power laws and log-normal IMFs with different characteristic masses – than before. Using these synthesis models, we present the expected UV properties of star-forming galaxies, including their Lyman continuum fluxes, UV luminosity, and properties of the continuum (e.g. β -slopes), as well as properties of important emission lines such as $\text{Ly}\alpha$ and He II $\lambda 1640$ (see Sect. 3.3).

To investigate possible departures from the simple case B recombination theory assumed in many synthesis models, including ours, we have then computed large grids of CLOUDY photoionization models for zero and low metallicity nebulae, using both black-body spectra and the SEDs predicted by our synthesis models (Sects. 3.4 and 3.5).

Our main conclusions from the photoionization models are the following:

- Due to departures from case B (collisional excitation and ionization from excited levels) both $\text{Ly}\alpha$ and 2γ continuum emission can be significantly enhanced at low nebular densities. Their strengths is found to scale with the mean photon energy of the ionization source in the Lyman continuum.
- The equivalent width of $\text{Ly}\alpha$ can be larger than expected from case B calculations due to the line flux enhancement. The measurement can also be affected by 2γ emission if the continuum is measured at longer wavelength.

- Further enhancement of Ly α at the expense of 2 γ emission can occur due to collisional mixing between the hydrogen 2²S–2²P levels at higher densities.
- He II emission line fluxes (and consequently their equivalent widths) can be significantly decreased due to their dependence on the ionization parameter. This could make searches for the He II λ 1640 line at high- z more difficult.
- The enhancement of the 2 γ continuum and its dependence on nebular parameters can result in reduced equivalent widths of the UV emission lines and also change the UV restframe colours of high- z galaxies.

Our results are of relevance to searches for, and interpretation of observations of metal-poor and/or high- z galaxies which may host the first stars that appeared in the Universe.

Acknowledgements

We thank Suzy Collin, Mike Fall, Grazyna Stasińska for helpful discussions.

Some of explorations of photoionization models were already undertaken earlier with Francois Ricquebourg and Michael Zamo. DS wishes to thank them here for their contributions. The work of DS is supported by the Swiss National Science Foundation. DS is thankful for support from the ESO visitor program, during which part of this work was done.

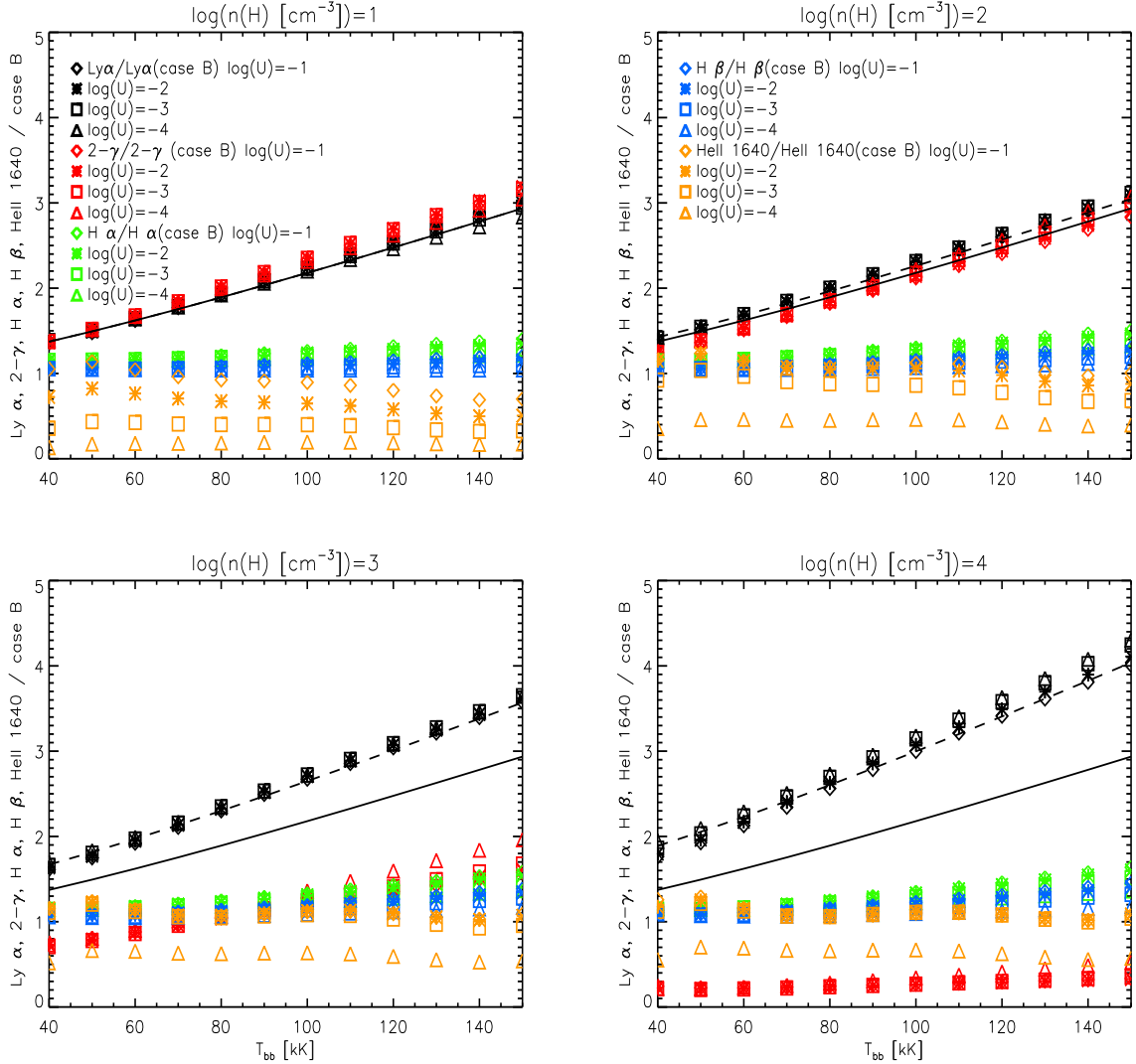


Figure 3.10: $\text{Ly}\alpha$ (black), 2γ (red), $\text{H}\alpha$ (green), $\text{H}\beta$ (blue), $\text{He II } 1640 \text{ \AA}$ (orange) luminosities over their predicted case B luminosities for the primordial nebula. The black solid line shows P (Eq. 3.6), the dashed lines show $P \times \tilde{f}_{\text{coll}}/\tilde{f}_{\text{coll}}(\log(n_H = 1))$ (cf. Eq. 3.7). Different symbols represent different ionization parameters, namely open diamonds correspond to $\log(U) = -1$, stars to $\log(U) = -2$, open squares to $\log(U) = -2$, and open triangles to $\log(U) = -4$. It can be seen that $\text{Ly}\alpha$ and 2γ luminosities scale with P at low densities and $\text{Ly}\alpha$ is further enhanced at higher density. Case B values have been calculated using luminosity coefficients for $T_e=30,000 \text{ K}$ and $n_H=10^2 \text{ cm}^{-3}$ from Schaerer (2003). For simplicity we always compare the results to the low density case B limit.

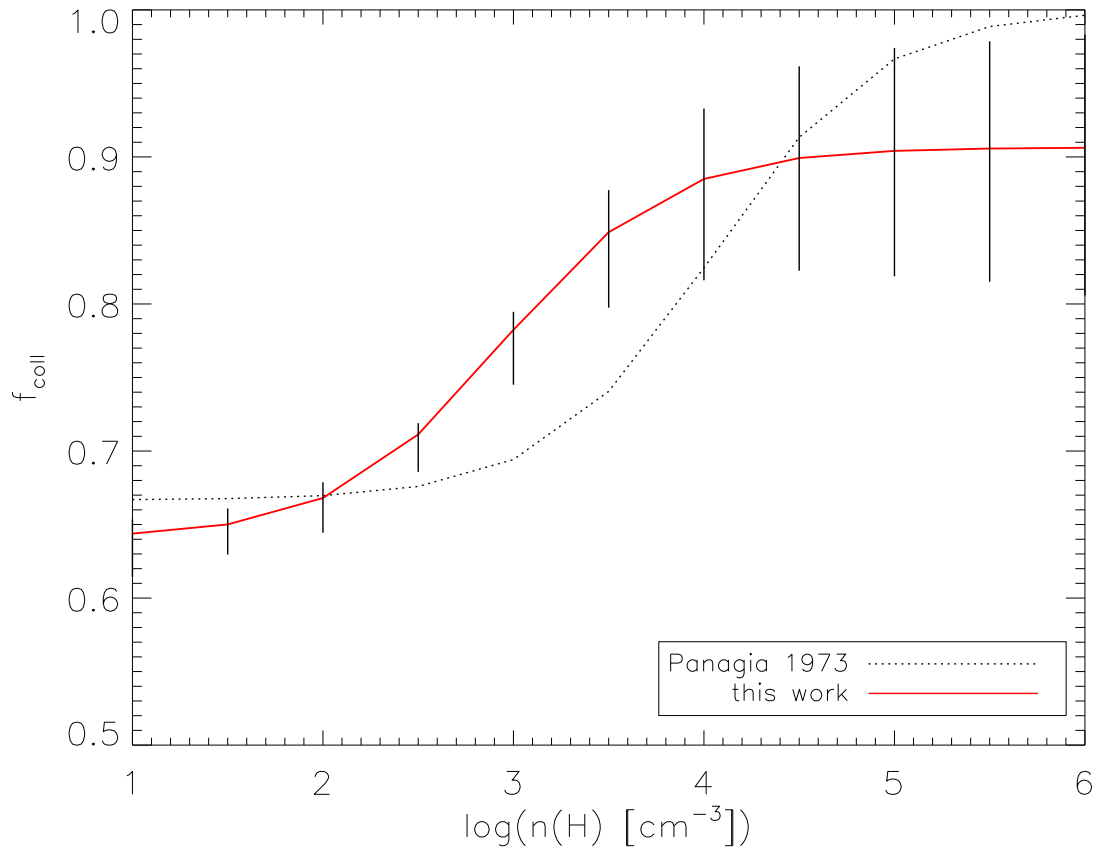


Figure 3.11: f_{coll} factor accounting for the density effects. The red line represents the 3-parameter fit obtained on the basis of the photoionization modelling (\tilde{f}_{coll}) to be used in formula 3.8 to calculate $L(\text{Ly}\alpha)$. At each density, vertical lines show the spread in \tilde{f}_{coll} values arising from the different T_{bb} and U models used: models with higher T_{bb} and lower U have higher \tilde{f}_{coll} values. The fit has been made for primordial nebular abundances and the black dotted line is f_{coll} from Panagia (1973).

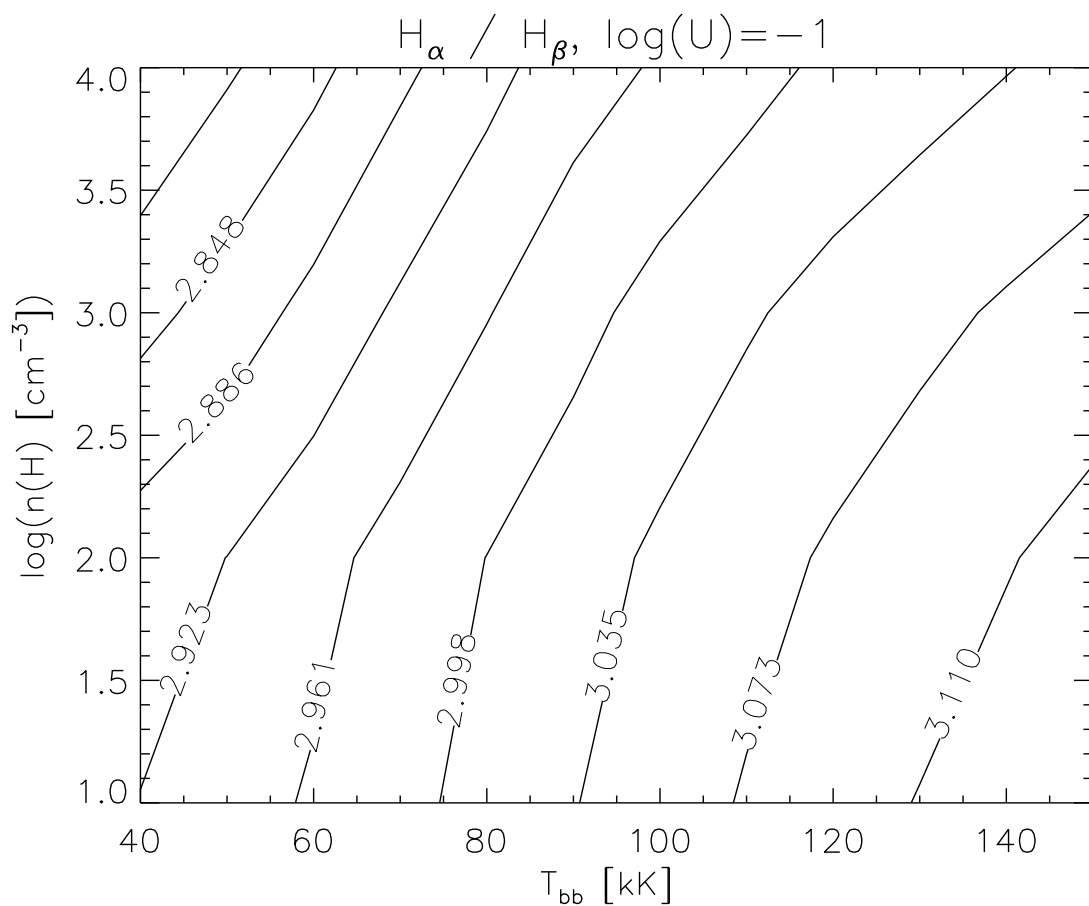


Figure 3.12: The Balmer decrement as a function of T_{bb} and n_H for primordial metallicity case. Note that $H\alpha$ is boosted for high T_{bb} due to collisional excitation of hydrogen.

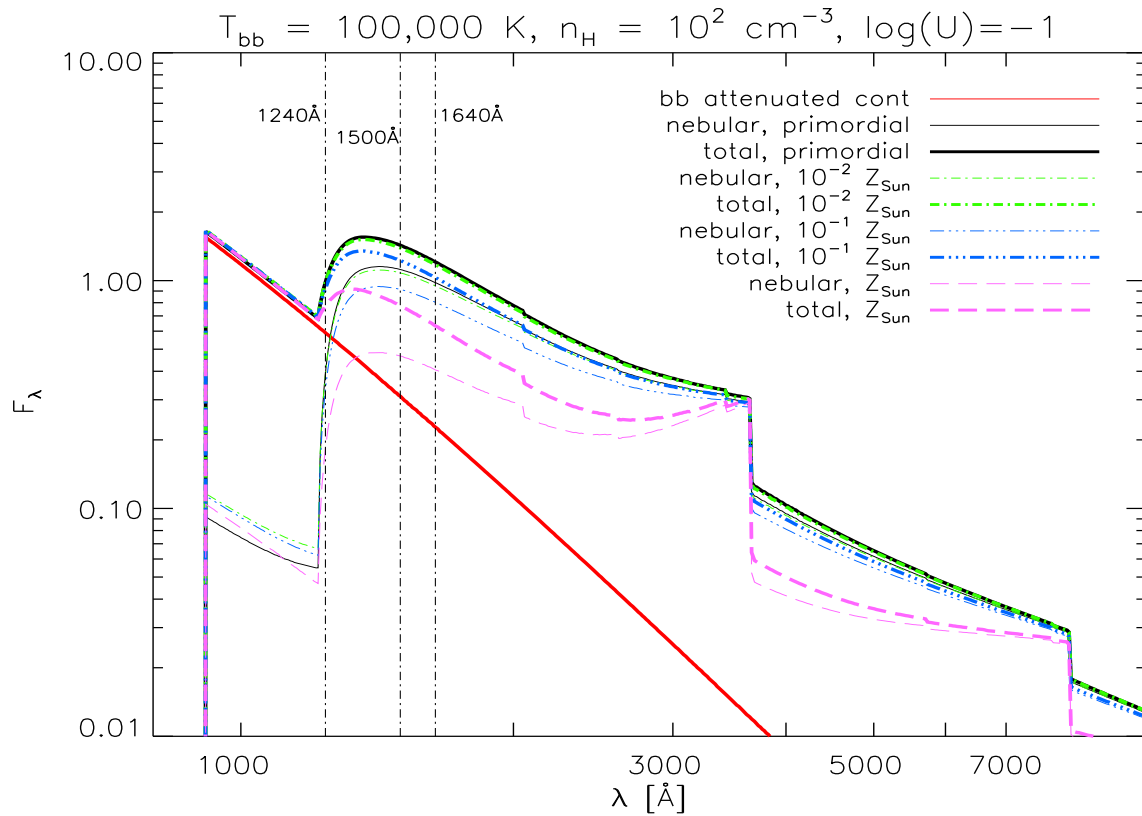


Figure 3.13: Continuum of $T_{bb}=100,000 \text{ K}$ models as a function of the nebular metallicity for a constant density and ionization parameter. The red solid line represents the transmitted stellar (black body) continuum. The thin lines are nebular only contributions to the continuum. The thick lines are the total continuum emission (stellar + nebular). The first model is normalized at 1240 \AA and the rest rescaled accordingly.

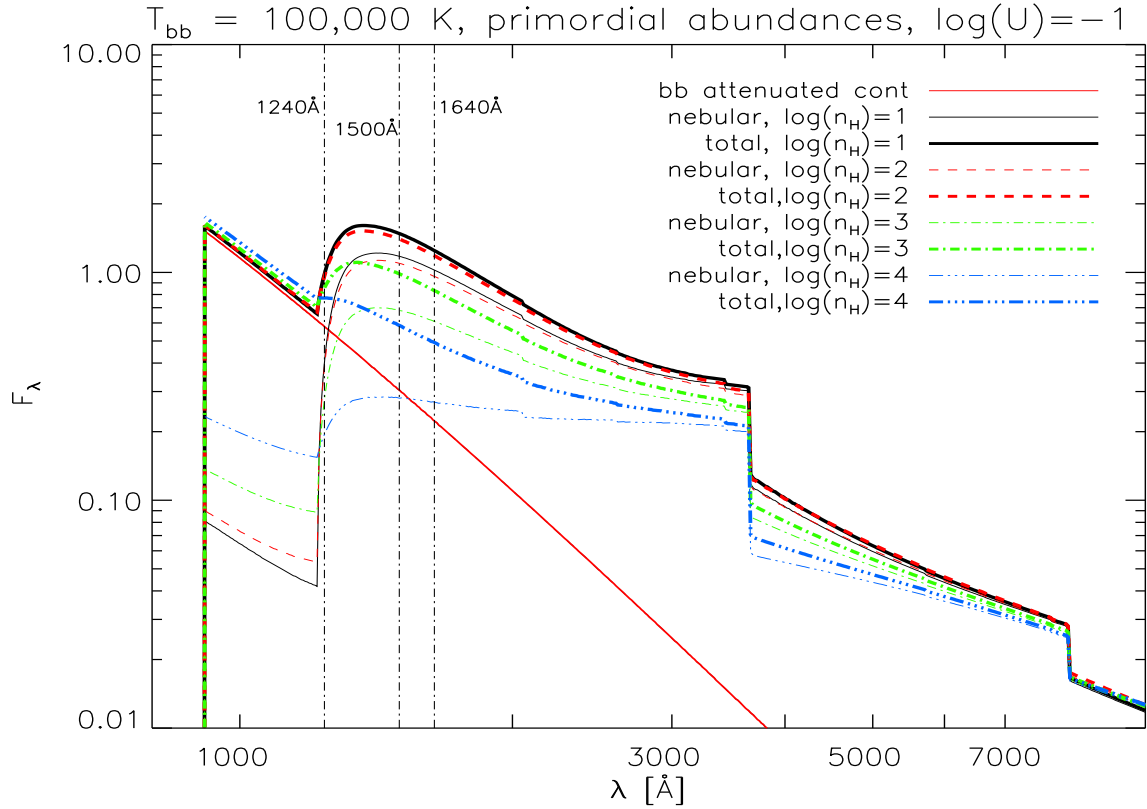


Figure 3.14: Continuum of $T_{bb}=100,000 \text{ K}$ models as a function of the hydrogen number density at the primordial metallicity and constant ionization parameter. The red solid line represents the transmitted stellar (black body) continuum. The thin lines are only nebular contributions to the continuum. The thick lines are the total continuum emission (stellar + nebular). At higher densities 2γ continuum gets destroyed due to collisions. First model normalized at 1240 \AA and the rest rescaled accordingly.

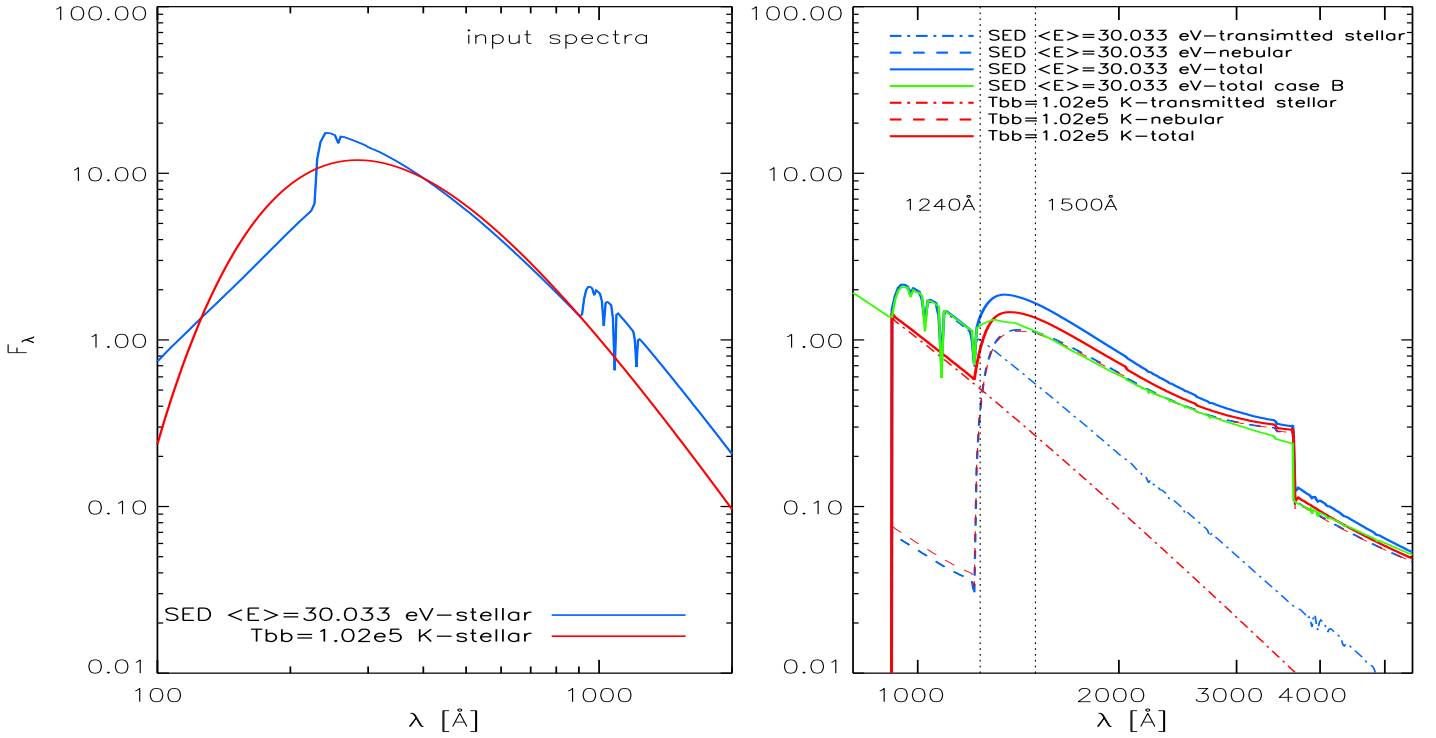


Figure 3.15: **Left:** Comparison of input stellar spectra for photoionization models showing a realistic SED (blue line; Pop III, Salpeter IMF 1-100 M_\odot at zero age) and the corresponding black body spectrum (red line) with the same average photon energy ($\bar{E} = 30.033$ eV) in the Lyman continuum. The SED model is normalized at 1240 Å and the rest rescaled to match the same ionizing flux $Q(H)$. **Right:** Input stellar spectra (dash-dotted, same colours as left panel) and predicted nebular and total continua from our CLOUDY models for $\log(n(H)) = 1 \text{ cm}^{-3}$ and $\log(U) = -1$ (solid lines, using same colours as in left panel; cf. also inset for symbols). The green solid line shows the total (stellar + nebular) SED from our evolutionary synthesis model assuming constant nebular density and temperature and case B. Notice the difference between case B and the CLOUDY result due to enhanced 2γ emission.

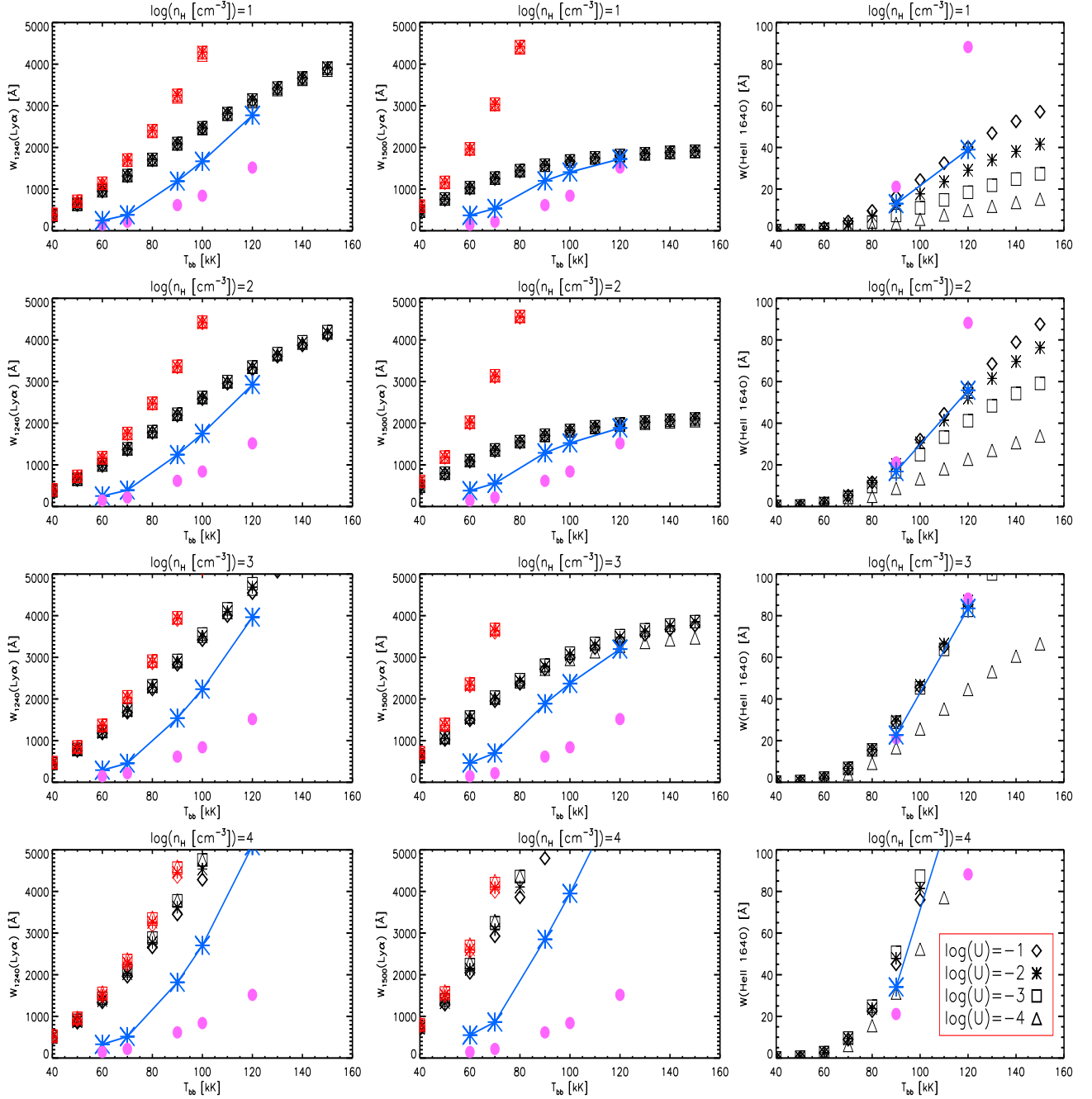


Figure 3.16: Equivalent widths (W_λ) of Ly α at 1240 (column 1) and 1500 Å (column 2) and He II λ 1640 (column 3) for a primordial metallicity nebula at different densities and ionization parameters (marked with different symbols as defined in the inset). The red symbols show an upper limit for W_λ (Ly α) since they are calculated using only stellar (black body) continuum. Blue symbols – the most realistic predictions – show the results obtained for the corresponding stellar population SEDs (models with the same P in the case of Ly α and with the same $\log(Q(\text{He}^+)/Q(\text{H}))$ for the He II analysis, for simplicity only models with $\log(U) = -1$ are shown) and the pink ones their case B predictions. Notice the dependence of the He II λ 1640 equivalent width on the ionization parameter and the discrepancy between its case B and photoionization model predictions for real SEDs.

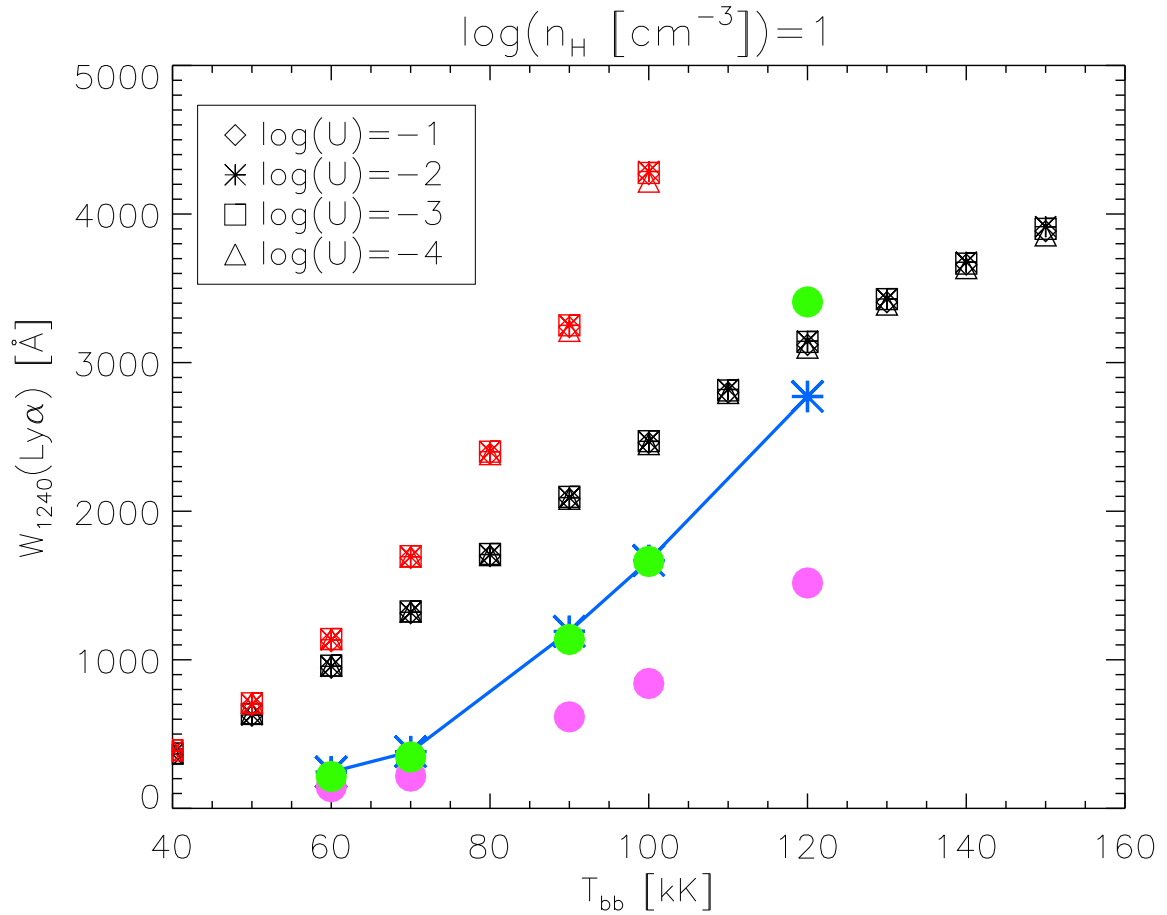


Figure 3.17: Equivalent widths (W_{λ}) of $\text{Ly}\alpha$ at 1240 \AA (first column, second row of Fig. 3.16). All the symbols as in Fig. 3.16. Additionally, the green symbols show the case B SED results (pink symbols) corrected using our formula (first order correction; only the enhancement in the line flux is taken into account, there is no correction for the continuum). The difference coming from not correcting for the nebular continuum enhancement is visible for the hottest model.

Chapter 4

Ly α emitters in the GOODS-S field: The powerful pure nebular SED with N IV] emission at $z=5.563$

Raiter A., Fosbury R., Teimoorinia H.

A & A 2010, 510, 109

4.1 Introduction

The Ly α emission line is a beacon that can be recognised from the ground in objects with redshifts larger than about 1.8. When seen on its own, its interpretation is complicated by radiative transfer effects both within the emission region itself and in the intervening Lyman forest. With the detection of other emission lines and/or a recognisable continuum, a spectrum can however provide a rich source of information about physical conditions and chemical composition. Of particular interest for the identification of primordial starforming objects are the so-called “dual-emitters”: sources that emit both Ly α and the He II line at 1640 Å (Dawson et al. 2004; Nagao et al. 2005; Ouchi et al. 2008) which are interpreted as very metal-poor nebulae ionized by massive, hot and presumably metal-free stars. So far, intermediate band imaging surveys have not been very successful in discovering genuine, stellar-ionized H/He II dual emitters (Nagao et al. 2008).

The Great Observatories Origins Deep Survey (GOODS) spectroscopic observations in the Chandra Deep Field South (Vanzella et al. 2005, 2006, 2008, 2009; Popesso et al. 2009) have accumulated, using the FORS2 and VIMOS instruments on ESO’s Very Large Telescope, spectroscopy of essentially all accessible sources. The source GDS J033218.92–275302.7

(hereafter GDS18.92–02.7) was selected for the spectroscopic programme as a V_{606} -band dropout and has a blue $i_{775-z_{850}}$ colour due to a strong Ly α emission line falling in the i_{775} -band. It was subsequently studied in the context of SED fitting by Stark et al. (2007) and by Wiklind et al. (2008) who both conclude, on the basis of its apparently large Balmer break, that it is a high mass, old stellar population. Since the rest-frame UV images obtained with the ACS on HST show a very small angular size, the implication is that this is an example of an ultradense spheroid at a very early epoch. A significant fraction of other Ly α emitters from GOODS, showing apparent Balmer breaks, have also been interpreted as evolved, massive stellar populations (Pentericci et al. 2009).

The presence of strong emission lines in the UV spectrum carries implications about the effect of nebular emission processes on the rest of the observable SED. There are circumstances in which the combination of nebular continuum from bound-free and two-photon emission together with emission lines can influence the appearance of, or even completely dominate, an underlying stellar population throughout the UV, optical and NIR spectrum. In this paper, we exploit the presence of a second emission line, identified as the [N IV], N IV] intercombination doublet at 1483, 1486 Å, to estimate the implied SED and compare with the extensive GOODS photometry of this object.

The presence of significant N IV] emission is rather rare in known astronomical objects. At low redshifts it is seen in some compact planetary nebulae and in peculiar very hot stars such as η Carinae (Davidson et al. 1986). It is also sometimes detected in AGN and quasar spectra but with an intensity that is low with respect to lines such as C IV and N V, although there are rare examples of “Nitrogen Loud” quasars that exhibit unusually strong nitrogen lines, e.g. Baldwin et al. (2003). At a redshift of 3.4, the Lynx arc (Fosbury et al. 2003, hereafter F03), is known to show N IV] with a strength comparable to other UV intercombination lines such as O III] and C III] and the resonance doublet C IV. This object is interpreted as an H II region ionized by very hot stars ($T_{\text{eff}} \sim 80$ kK) with a nebular metallicity a few per cent of solar. In this case, the entire observed SED is nebular in origin and the stellar emission is not detected longward of Ly α . Glikman et al. (2007) report two N IV] emitting low luminosity ‘quasars’ one of which, DLS 1053–0528 at $z = 4.02$, has an intensity ratio of N IV]/ C IV = 1.9, a weak continuum and an SED which is considerably bluer than a typical quasar. This object has relatively narrow lines and may be more closely related to the Lynx arc than to an AGN.

In this paper we examine a sample of Ly α emitters from the GOODS spectroscopic data with redshifts spanning the range $3.5 \leq z \leq 5.9$ and present new photometric measurements from the most recent releases of the HST, VLT and Spitzer imaging data. For our selected N IV] emitter, we use a photoionization modelling code to investigate the range of model nebulae that will produce the observed N IV] emission flux. Given the GOODS broadband photometric measurements that extend from the U-band to the Spitzer MIPS 24 μm channel, we calculate the contribution of the nebular line and continuum emission to these bands in order to constrain the nature of any non-nebular light that may contribute. In addition to modelling the SED of this one object, we address the possibility that nebular emission may contribute significantly to other sample members, a possibility that has already been suggested by Zackrisson et al. (2008). Our conclusions are of relevance to

the interpretation of the SEDs of other high redshift Ly α emitters, where the emission line strength suggests that the nebula may be a significant contributor to the spectrum longward of the Ly α line. We adopt a cosmology with $\Omega_{\Lambda} = 0.7$, $\Omega_{\text{M}} = 0.3$ and $H_0 = 70 \text{ km s}^{-1} \text{ Mpc}^{-1}$. The *AB* magnitude system is used throughout.

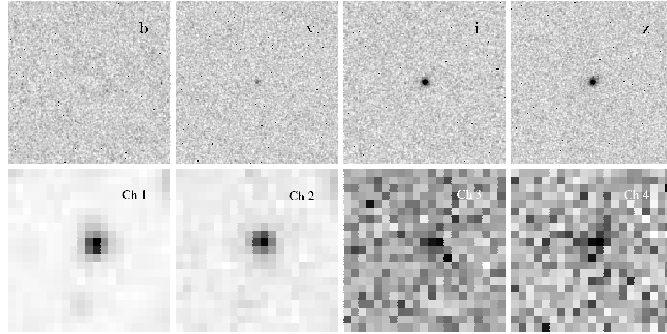


Figure 4.1: Image cutouts of GDS18.92–02.7 from HST/ACS (top-row) and Spitzer/IRAC (bottom-row). The ACS stamps are 5 arcsec on a side and the IRAC stamps are 25.6 arcsec.

4.2 Data

4.2.1 Sample

We have spectroscopically selected a sample of Ly α emitters from the publicly available data for the southern field of the Great Observatories Origin Deep Survey (see Dickinson & GOODS Legacy Team 2001; Giavalisco et al. 2004, for a review of the GOODS project). The multi-wavelength observations provide us with information on the *U* (VLT), *B*₄₃₅, *V*₆₀₆, *i*₇₇₅ and *z*₈₅₀ (HST), *J*, *H*, *K*_s (VLT), 3.6, 4.5, 5.8, 8.0 and 24 μm (Spitzer) bands. Many other observations have been carried out, including deep integrations in the X-ray and radio domains from Chandra and the Very Large Array, respectively.

The spectroscopic observations carried out with the ESO VLT FORS2 instrument yield a wavelength coverage from approximately 0.55–1 μm with a resolving power of $R \approx 660$. This programme has produced about one thousand redshift determinations between redshift 0.5 and 6.2, with more than one hundred Lyman break galaxies confirmed at redshifts beyond 3.5 (Vanzella et al. 2005, 2006, 2008).

From the GOODS data product archive <http://www.eso.org/science/goods>, we used the FORS2 online engine to select all the qf (quality flag) = A ‘emission’ objects at $z \geq 3.5$. A few objects were excluded because of spectral contamination, one because it showed no Ly α emission and one because of positional uncertainty. This process yielded 23 objects from which an additional five were excluded due to large photometric errors in some passbands.

4.2.2 Photometry

Due to the different telescopes in use, the GOODS images are characterised by a large range in point spread function (PSF) dimension. An unbiased estimate of the colours is essential for analysis of the SED. We have used a PSF-matched photometric technique to obtain the AB magnitudes of each object in each band in a given aperture size. In the presence of potential contamination by neighbouring objects, we have used an optimum circular aperture which maximises the S/N of each object in all passbands simultaneously. For example, in the case of the match between ACS and groundbased Ks or IRAC images, components may be clearly resolved by ACS but be merged in IRAC, or very red objects may be detected at the longer wavelengths but show no counterpart in the optical images. A curve-of-growth analysis yielded the optimum uncontaminated aperture.

Each source was examined in a 12×12 arcsec² cutout and a Monte-Carlo method used to estimate the background. The photometric measurements were made with SExtractor (Bertin & Arnouts 1996), where the background used was consistent with Monte-Carlo simulations. Finally, by selecting some bright but unsaturated stars near each galaxy, we computed the convolution kernel required to match the PSF of all the images to that with the largest. We generated about 200 PSF kernels of stars in different filters in order to find the best kernel using a χ^2 minimisation method. All magnitudes were corrected to a 6 arcsec circular aperture. The results for all bands appear in Table 4.4. We also use SExtractor to measure the “half-light” (or “effective”) radius of each galaxy in the z_{850} -band (also listed in Table 4.4).

4.2.3 The N IV] emitter

Of the 18 Ly α emitters in our sample, only one shows a clearly detected second emission line. Galaxy GDS18.92–02.7 with $z_{850}=24.5$, was selected as a V_{606} -band dropout and has been confirmed to be at redshift 5.563 (redshift of the Ly α line uncorrected for absorption). The spectrum, included in Figure 4.3 and shown in detail in Figure 4.4, was extracted from several individual FORS2 multi-object masks and corresponds to a total exposure time of 14.4 ksec (Vanzella et al. 2006). Detailed measurements of the spectrum of this object are presented in Vanzella et al. (2010) and the parameters relevant to our modelling are summarised in Table 4.1.

The main spectral features are the Ly α emission line (rest-frame equivalent width (EW) ~ 60 Å), the break of the continuum just blueward of the line, and the intercombination emission doublet [N IV], N IV] 1483.3, 1486.5 Å, whose intensity ratio can be used to estimate electron density (see Figure 4.4). We note that there is no clear detection of Si IV 1394, 1403 Å in absorption or emission nor of N V 1239, 1243 Å in emission by Vanzella et al. (2010) who also note that the object is extremely compact but marginally resolved in the ACS images.

Table 4.1: Summary of the physical quantities derived from the optical spectral features of GDS18.92–02.7 taken from Vanzella et al. (2010).

Quantity	Value	Comment
z (Ly α peak)	5.563	no abs. correction
L (Ly α)	$3.8 \pm 0.3 \times 10^{43}$ erg sec $^{-1}$	
EW $_0$ (Ly α)	59^{+195}_{-29} Å (rest-frame)	89 Å with Ctm $_{\text{phot}}$
z (N IV]	5.553 (1486.5 Å)	high-density limit
L (N IV]	$1.3^{+0.3}_{-0.4} \times 10^{43}$ erg sec $^{-1}$	
EW $_0$ (N IV]	22^{+64}_{-10} Å (rest-frame)	33 Å with Ctm $_{\text{phot}}$
L (Si IV)	$\leq 0.11 \pm 0.07 \times 10^{43}$ erg sec $^{-1}$	(1393.8, 1402.8 Å)
L (N v)	$\leq 0.11 \pm 0.06 \times 10^{43}$ erg sec $^{-1}$	(1238.8, 1242.8 Å)

Equivalent width values are also given using the continuum level derived from the photometry (Ctm $_{\text{phot}}$).

4.3 SED modelling

In this chapter, we first discuss the modelling of GDS18.92–02.7. We then use a grid of similar photoionization models in order to assess the potential importance of nebular emission for interpreting the SED of the other sources in our sample.

4.3.1 GDS J033218.92-275302.7

Two previous studies have attempted to fit the SED of GDS18.92–02.7 using the apparently large Balmer break to resolve the age-extinction degeneracy. Stark et al. (2007), using ID=32.8020, and Wiklind et al. (2008), as BBG 5197, both obtain an age of 0.9 Gyr, a stellar mass of close to $10^{11} M_{\odot}$ and zero extinction. The latter authors, who use the two longer wavelength IRAC channels, 5.7 and 8.0 μm , note that their fit is worsened by a deviant 5.7 μm point.

Our nebular modelling is motivated by the realisation that a source with such strong emission lines in the FUV will necessarily have nebular contributions at longer wavelengths. Also, by analogy with the Lynx arc at the lower redshift of 3.4, it is possible that the significant jump in brightness between the K-band and the IRAC 3.6 μm filter could be caused by strong [O III] 4959, 5007 Å emission lines producing an apparent, but false Balmer break signal. The nature of the photoionizing source can be inferred from the strength of N IV] and the non-detection of N v which also lies in a favourable region of the FORS2 spectrum. Again, by analogy with the arguments already used for the Lynx arc (F03; Binette et al. 2003; Villar-Martín et al. 2004), the limit on this line ratio can be used to argue for a hot black body-like source rather than the hard power law spectrum associated with an AGN. The absence of detectable radio (Kellermann et al. 2008) or X-ray (Giacconi et al. 2002) emission from the source at very low flux levels is also evidence

against an AGN interpretation.

Since our modelling is designed to provide a “proof of concept” rather than a detailed SED fit, we use a set of blackbodies ranging from 60 to 120 kK as ionization sources. The use of hot stellar models having low or zero metallicity would have little effect on the gross properties of the predicted spectrum although they would be required to fit individual emission line fluxes if more observations were available. The *effective* temperature (the temperature of the black body which produces the same bolometric luminosity) of such stellar models would be somewhat lower (by $\approx 10 - 15$ kK) than the black body temperatures we use here.

The principal requirement of a model is to produce the observed luminosity of the N IV] doublet. The combination of density and ionization parameter, U (defined at the inner edge of the nebula) is constrained by the measured upper limit on the source size:

$$U = \frac{Q(\text{H})}{4\pi r_{\text{in}}^2 n_{\text{H}} c}$$

where $Q(\text{H})$ is the rate of hydrogen ionizing photons radiated by the source, r_{in} is the inner radius of the cloud, n_{H} is the hydrogen number density of the cloud and c is the speed of light. Since, for all of our models, the depth of the ionized gas is small compared with the observed size of the source, we associate r_{in} approximately with the PSF-corrected measurement from the z_{850} ACS image of r_e (Table 4.4) which corresponds to 580 pc. The observed wavelength of N IV], compared with that of the blue-absorbed Ly α line, suggests that the doublet is emitted from a region that is in the high density regime (show an enlarged plot of the spectrum of this region Vanzella et al. 2010) with $n_e \gtrsim 10^{4.5} \text{ cm}^{-3}$, see: Osterbrock & Ferland (2006). We note, however, that in the Lynx arc, the density derived from N IV] doublet is significantly higher than the value of $\lesssim 3000 \text{ cm}^{-3}$ derived from those of C III] and Si III] (Villar-Martín et al. 2004)¹.

We use the photoionization code CLOUDY version 08.00 (Ferland et al. 1998) to calculate the models of H II regions exposed to the black body radiation. We assume an ionization bounded spherical geometry (i.e., the outer radius of the cloud is not defined) which means that the ionizing photon escape fraction is zero. The nebular gas is assumed to have constant density. From the output of the CLOUDY models, which includes both nebular continuum and line emission, we compute the theoretical magnitudes for all the photometric filters to compare with the GOODS observations.

We have calculated a grid of models exploring the parameter space of T_{bb} of the black body, the ionization parameter (U) and the nebular metallicity (Z_{neb}), investigating how the changes in these parameters affect the N IV] luminosity and the observed SED. We have assumed the solar relative abundances (as defined in CLOUDY) with the realisation that this is unlikely to be entirely appropriate at this epoch. In practice, this means that our calculated magnitudes will be affected by the abundance-dependent strength of lines

¹But note that, for the observed line ratio, the N IV] density in this paper should be 10^5 cm^{-3} , according to the method presented in Keenan et al. (1995), rather than the quoted $2 \times 10^4 \text{ cm}^{-3}$.

Table 4.2: Parameters of the fiducial photoionization model.

Parameter	Value	Unit
T_{bb}	100	kK
$\log(U)$	-1	
Z_{neb}	0.05 Z_{\odot}	
$Q(\text{H})$	3×10^{55}	s^{-1}
n_{H}	$10^{2.9}$	cm^{-3}
r_{in}	10^{21}	cm

from individual ions. The most important of these is the [O III] 4959, 5007 Å doublet that is included in the IRAC1 band. Note that, with the range of abundance considered here, oxygen is not the dominant coolant and so this emission line strength is proportional to abundance. Consequently, our principal assumption regarding abundances is that of a solar N/O ratio. Guided by the example of the Lynx arc, we have performed our modelling assuming that dust is not present. However, given the conclusions of the Ly α profile modelling discussed by Vanzella et al. (2010), we do later examine the possibility of some dust extinction being present.

In addition to their fluxes, the emission line equivalent widths (EW) are an important constraint because of their dependence on the strength of the continuum. In our models, the continuum under the N IV] line is dominated by hydrogen two-photon emission which becomes collisionally de-excited above an electron density of $\sim 10^4 \text{ cm}^{-3}$. The observed EW (Table 4.1) provides an additional constraint on T_{bb} , U , n_e and Z_{neb} .

Guided by the results of χ^2 testing of our model grid against the observed photometry and N IV] emission line flux, we choose a “fiducial” model that represents our best estimate for the model parameters (see Figure 4.6). Because of our spectroscopic observation, high weight is accorded to the luminosity and the equivalent width of the N IV] doublet. This gives the parameters shown in Table 4.2.

It is significant to note that this is very close to the set of parameters as derived for the Lynx arc (F03) based on the fitting of many individual emission lines. There are differences in the assumed geometry and the particle density but these have only minor effects on the emitted spectrum. We have used a higher density in order to keep the nebula small enough to be consistent with the imaging data. The SED derived from this fiducial model is shown in Figure 4.5 and the luminosities of some principal emission lines in Table 4.3. This model produces an H II region with an ionization structure and electron temperature distribution that results in a radially-averaged electron temperature of 23 kK.

In this model, the K_s band samples mostly nebular continuum while IRAC1 is dominated by very strong [O III] line emission resulting in a jump of 1.3 magnitudes between rest-frame wavelengths of 0.33 and 0.54 μm . The IRAC2 band is significantly influenced by H α and IRAC4 by He I 10830 Å, this latter line becoming stronger at higher density (see the third panel of Figure 4.6). Examination of Figure 4.6 (which has 3- σ error-bars) shows that our fiducial model falls below the low signal/noise data from the IRAC3 and IRAC4 filters

Table 4.3: Fiducial model emission line spectrum.

λ_{rest}	$\log(L [\text{erg s}^{-1}])$	$I/I_{H\beta}$
O VI 1035	40.984	0.007
Si III 1207	41.589	0.026
Ly α 1215	44.724	36.011
N V 1240	42.229	0.115
Si IV 1397	42.564	0.249
O IV 1402	42.416	0.177
N IV] 1486	42.938	0.590
C IV 1549	44.054	7.698
He II 1640	43.026	0.7217
C III] 1909	42.985	0.657
[O II] 3727	41.411	0.018
He II 4686	42.127	0.0911
[O III] 5007	43.936	5.865
H α 6563	43.625	2.867

Note that no resonance line absorption is accounted for in these values. For the doublets, including [O III] 4959, 5007 Å, the number represents the sum of the two lines.

(see Figure 4.1). The IRAC3 band in our model is dominated by bound-free continuum and is little affected by changing model parameters within the range we have considered. Although the IRAC4 band model also falls below the data, the amount can be lessened significantly by changing the density or adding a higher density component. Given the marginal formal significance of these two discrepancies we do not consider it justified to attempt to add an additional source that would contribute flux at these wavelengths without destroying the fit at shorter wavelengths. In order to provide enough light from stars, the population would need to be old, massive and significantly reddened. Vanzella et al. (2010) have examined SED fits using both single and fixed stellar population models. These both require an old, > 700 Myr for a single and ~ 400 Myr for a mixed, massive, $\sim 10^{11} M_{\odot}$, population in order to provide the light seen in the IRAC bands. Such an addition would completely change the nature of the young, low-mass model we are proposing.

In addition to the requirement to explain the strength of the N IV] line, an important constraint is to not over-predict other emission lines within the FORS2 spectrum. The absence of N V 1243 Å has already been used to argue against an AGN-like ionizing continuum but it also limits the temperature of the black body to $\lesssim 100\text{kK}$. The O IV/Si IV complex from 1394–1413 Å increases in strength at the higher temperatures and is still predicted to be significant in our fiducial model (see Table 4.3). It is not seen in our data but, since we have no a priori information about the abundance of silicon, we do not consider this to be sufficient grounds for rejecting the model. The C IV resonance doublet is very close

to the long wavelength limit of the observed spectrum and its detection is dependent on the effective redshift which can be influenced, like $\text{Ly}\alpha$, by absorption. If it has the same redshift as $\text{N IV}]$, the observational limit is below the prediction of our fiducial model by a factor of nearly 20 while if it is at the redshift of $\text{Ly}\alpha$ it would be undetected (as discussed by Vanzella et al. 2010).

4.3.2 Sample modelling

The source GDS18.92–02.7 is the only member of our sample that contains a clearly detected second emission line in the FORS2 spectroscopy. There is, however, one source with groundbased IR spectroscopy that allows the measurement of $[\text{O II}]$, $[\text{O III}]$ and $\text{H}\beta$ line strengths. This is object CDFS 6664 (GDS J033233.33–275007.4) at a redshift of 3.791 from the AMAZE programme (Maiolino et al. 2008).

The presence of significant $[\text{O II}]$ emission (i.e., comparable to $\text{H}\beta$) rules out the high temperature and high ionization parameter models that we need to explain strong $\text{N IV}]$ emission. Since all of the spectra reported by Maiolino et al. (2008) do show $[\text{O II}]$, their use of the locally calibrated R_{23} parameter and other line ratios to estimate metallicity is justified although it would not be for a $\text{N IV}]$ -emitter, since it was not designed for the high ionization parameter cases. While we might expect the higher redshift sources to show evidence of hotter ionizing stars, the Lynx arc is at a similar redshift to the AMAZE sources but shows no $[\text{O II}]$ and strong $[\text{O III}]$ and $\text{N IV}]$ lines. From Figures 4.2 and 4.3, we see that most of our sample exhibit the rather flat spectra in f_ν that is a characteristic of the nebular models. However, without the evidence provided by emission line measurements in addition to $\text{Ly}\alpha$, it is not possible for us to disentangle the stellar and nebular contributions. The relative importance of starlight and nebular emission in high redshift starforming galaxies has been discussed by Zackrisson et al. (2008) who model the effect of individual strong emission lines on multi-band SED observations. As we have confirmed, both with the Lynx arc and with GDS18.92–02.7 the $[\text{O III}]$ lines can carry enough flux to affect significantly the magnitudes in even rather broad photometric bands and it is in the regime where its strength is proportional to oxygen abundance. The presence of a significant excess flux in the band that includes these lines can be a hint that we are dealing with an SED with a significant nebular component.

4.4 Discussion

The model we employ for GDS18.92–02.7 is clearly rather rudimentary and is not expected to produce a detailed match to even the somewhat modest data set that we have. Simply summing models with a range of model parameters, notably density, would be more realistic and would tend to produce a better match to the observed SED at the longer wavelengths. However, the general properties of this kind of model are clear: the nebular continuum is approximately flat in f_ν and is modulated by the presence of strong lines in particular photometric bands.

Although there appear to be no low redshift analogues of GDS18.92–02.7, the recent discovery of “Green Peas” by the Galaxy Zoo project (Cardamone et al. 2009) does, however, show that there exists a population of compact, strong [O III] emitting sources with high specific star formation rates, low metallicities and low reddening in the local Universe. These sources demonstrate that vigorously star forming galaxies can exhibit SEDs with very significant nebular contributions to broad-band photometric measurements.

Arguments for thermal rather than non-thermal (AGN) photoionization were given in Section 4.3.1. It should also be noted that the upper limit on the MIPS 24 μm flux (Table 4.4 and Figure 4.5) excludes the steeply-rising SED from warm dust typical of AGN of types 1 and 2 (Miley & De Breuck 2008). Upper limits (3σ) are available also on the MIPS 70 and 160 μm fluxes of 2,500 and 33,000 μJy respectively (Dickinson, M., priv. comm.; Coppin et al. (2009)) but these values are, unfortunately, not strong discriminants. The source DLS 1053–0528 at $z = 4.02$ discussed by Glikman et al. (2007) appears in a list of low luminosity type 1 AGN because its emission lines have a broad component with a FWHM $> 1000 \text{ km s}^{-1}$. However, aside from this characteristic, this object shares emission line and SED characteristics more closely with GDS18.92–02.7 and the Lynx arc than with typical AGN, notably the great relative strength of the nitrogen line with $\text{N IV}] / \text{C IV} > 1$.

The lower limit on the baryonic mass for our fiducial model is the sum of the masses of the ionizing stars plus the mass of the ionized nebula. To estimate the first of these components we use the zero metallicity models of Schaerer (2002) which give a value of $Q(\text{H})$ per star. We choose his $T_{\text{eff}} = 85 \text{ kK}$ model since it produces a similar ionization structure to our fiducial model. Such stars have a mass of $50 M_{\odot}$ and $Q(\text{H}) \approx 3 \times 10^{49}$ photons s^{-1} . Given the $Q(\text{H})$ required for our model of 3×10^{55} photons s^{-1} , we need a million stars with a total mass of $5 \times 10^7 M_{\odot}$. The mass of ionized gas from the fiducial CLOUDY model is $2.7 \times 10^8 M_{\odot}$, giving a total minimum mass of $3.2 \times 10^8 M_{\odot}$, more than two orders of magnitude smaller than the stellar masses estimated by Stark et al. (2007) and Wiklind et al. (2008).

The need to properly include the nebular emission in high redshift starforming galaxies is not a new idea, e.g., Schaerer (2002); Zackrisson et al. (2008); Schaerer & de Barros (2009), but we believe that the Lynx arc at redshift 3.4 (F03) and GDS18.92–02.7 at $z = 5.6$ are the only such objects known where the entire observed SED longward of Ly α may be contributed by nebular emission. The implication of this is that most of the stellar flux is emitted in the Lyman continuum. As shown by F03, a stellar population with a normal IMF that produces sufficient ionizing photons to produce the observed emission line fluxes would be easily detected in the rest-frame UV. Unless we have a mechanism, such as a dust screen, that selectively absorbs this starlight in our line of sight, we are forced to the conclusion that we have a large population of stars with an effective temperature close to 100 kK. The absence of light from cooler stars implies that the cluster is either very young or has an intrinsically top-heavy IMF. The latter is an expectation for Population III stars. While we have no direct method to measure the *stellar* metallicity in these two objects, we do have estimates of the *nebular* metallicity of $\approx 5\%$ solar. This may seem high compared with normal estimates for a Pop III environment (Bromm et al. 2001) but we need to better

understand the rate of self-pollution within a cluster of a million stars in a deep potential well with temperatures around 80–100 kK and lifetimes of just a few million years.

Our modelling has been carried out without the inclusion of dust reddening. It is possible, however, to maintain a reasonable fit with the same model parameters other than an increased intrinsic luminosity (and total mass) by including $E(B - V) \lesssim 0.1$ of Galactic dust for a screen model or $E(B - V) \lesssim 0.2$ for a mixed model. The presence of some dust may be necessary to explain the Ly α profile (Vanzella et al. 2010).

Once the need for a hot, thermal photoionization source is identified, it is natural to associate this solely with the presence of massive stars. Other sources of thermal radiation could be present, e.g., from shocks associated with a high supernova rate but, even if the entire kinetic luminosity of a core-collapse supernova $\sim 10^{51}$ erg (Woosley & Weaver 1986) could be converted to Lyman continuum photons, this falls far short of the $\sim 10^{54}$ erg of ionizing radiation emitted by a massive star during its lifetime (Schaerer 2002).

4.5 Conclusions

The possibility of starforming galaxies at high redshift, where very hot ionizing stars are expected, having rest-frame UV through MIR SEDs containing significant nebular contributions has been discussed for the last decade. The detection of emission lines in addition to Ly α provides, by using photoionization models, a way of quantifying this contribution. Compact objects containing very hot ionizing stars capable of producing lines such as N IV] and He II will also emit strong nebular continuum which we show can dominate the Rayleigh-Jeans tail from the ionizing stars. The presence of other strong lines falling within a photometric band can result in SED features than can be confused with jumps such as the Balmer break in conventional stellar population models. It is important to realise that the detection of a luminous emission line such as N IV] *necessarily implies* a substantial nebular contribution to the overall SED and therefore effectively excludes models which use purely stellar continuum contributions. The large equivalent widths of the emission lines can be used to limit the contribution of stars significantly cooler than 100 kK to the SED and so constrain the age of the cluster or its stellar IMF.

These highly ionized nebulae appear very different from the majority of H II regions in the local Universe due to the higher temperature stars and higher ionization parameters. The rest-frame UV spectrum is rich with emission lines such as the intercombination doublets of C, N, O and Si which can be used for reliable abundance determinations.

Determined efforts with large groundbased telescopes equipped with efficient red and NIR spectrographs may allow us to observe some of the first stellar nucleosynthesis products from the young Universe.

Acknowledgments

We thank Mario Nonino for so quickly finding this source in the GOODS spectroscopy after he had been tipped off about the importance of the N IV] line. Daniel Schaerer and

Daniel Pequinot gave us much useful modelling advice. We thank Francesca Matteucci for helpful discussions about the chemical evolution of galaxies. AR would like to thank Massimo Stiavelli for hosting her visit to STScI to learn and discuss matters pertaining to early star formation. In particular, we thank Eros Vanzella for his sterling work on the reduction and analysis of the GOODS/FORS2 spectroscopy and both he and Piero Rosati for many inputs to and discussions about this work.

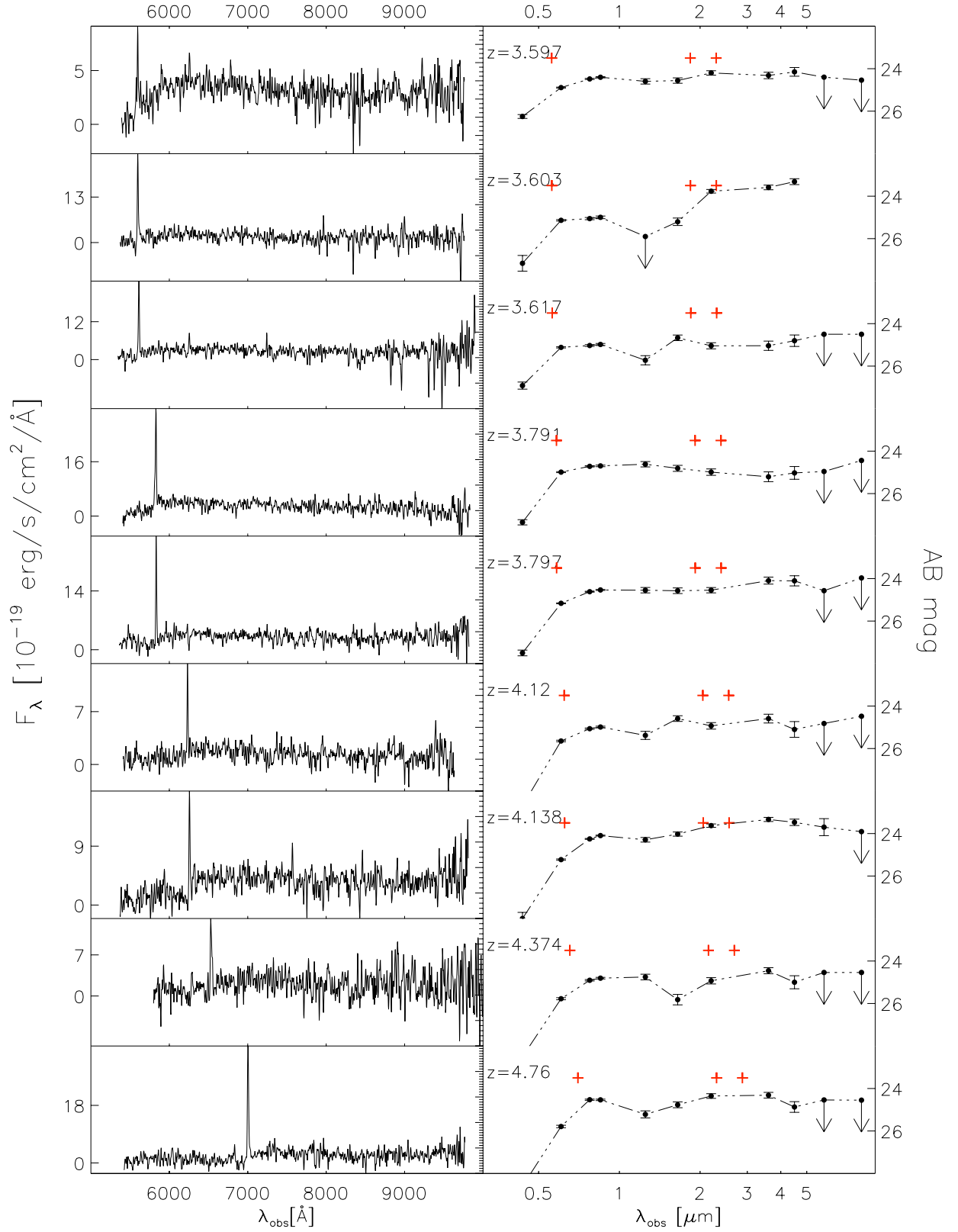


Figure 4.2: FORS2 spectra and photometric SED – part 1 (redshifts 3.6–4.8). The photometric points are: B_{435} V_{606} i_{775} and z_{850} (HST), J_s , H , K_s (VLT), 3.6, 4.5, 5.8, 8.0 (Spitzer). The sources are presented in order of increasing redshift and so can be cross-referenced to Table 4.4. The (red) + ‘plusses’ for each SED represent the wavelengths of $\text{Ly}\alpha$, the 4000 Å Balmer break and the [O III] 5007 Å line. The photometric error bars are 1σ .

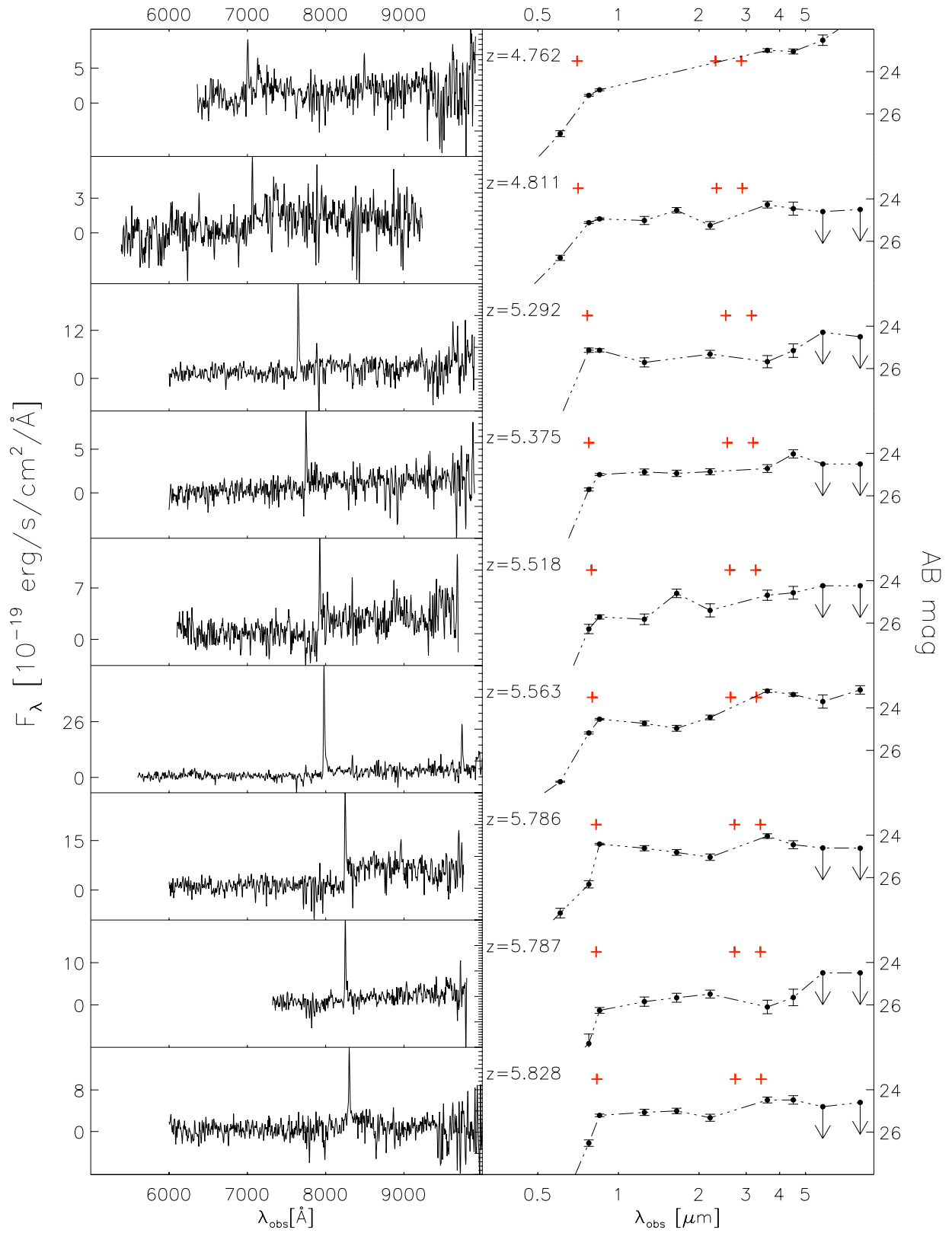


Figure 4.3: FORS2 spectra and photometric SED – part 2 (redshifts 4.8–5.9).

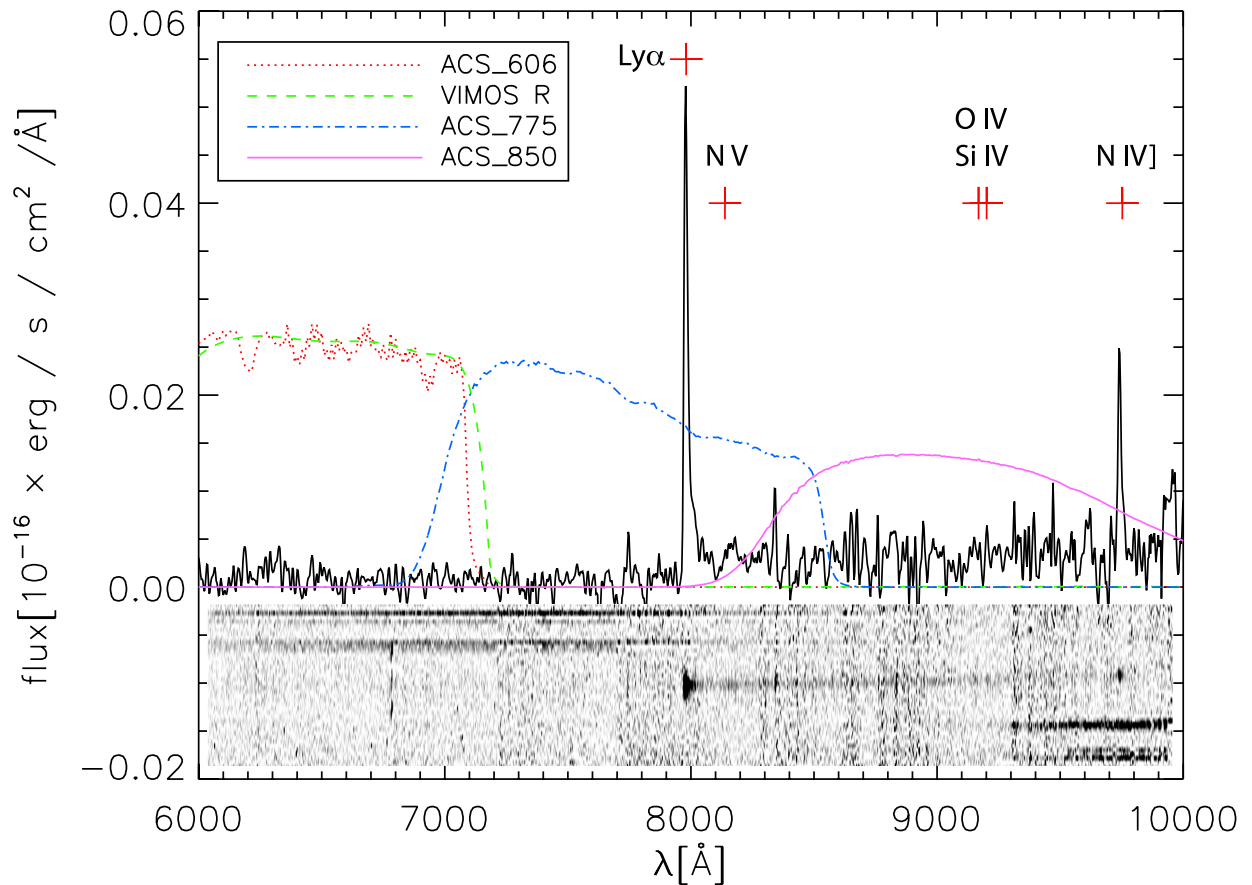


Figure 4.4: FORS2 spectrum of source GDS18.92–02.7 showing the Ly α and N IV] emission lines and the ACS and VIMOS filter passbands. The expected positions of the N V, O IV and Si IV lines are also marked.

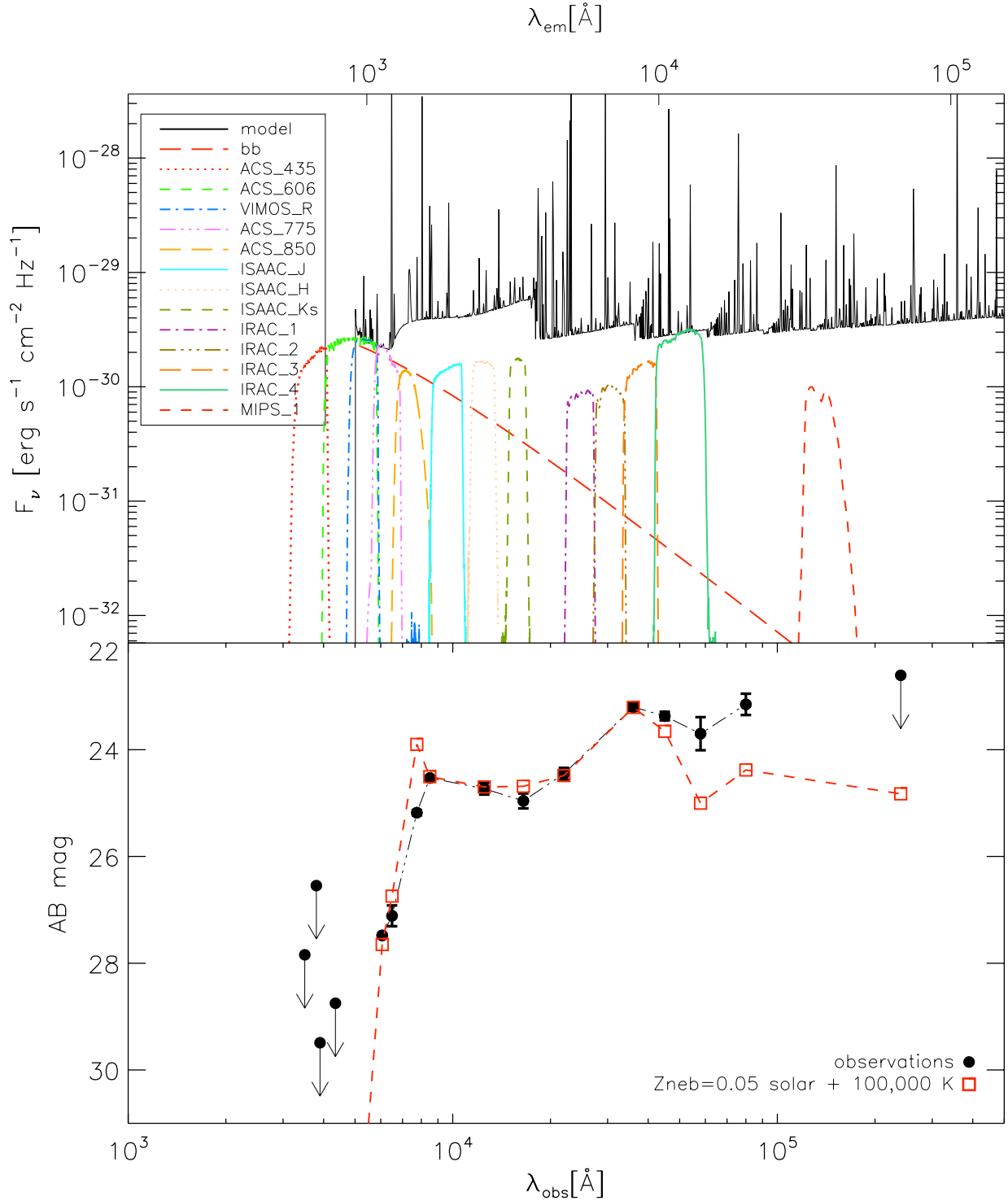


Figure 4.5: Observed and modelled SED of GDS18.92–02.7. *Top panel:* the computed nebular spectrum from the fiducial model, the Rayleigh-Jeans tail of the ionizing black body spectrum and the GOODS filter passbands. *Bottom panel:* the observed and computed photometric SED. Additionally VIMOS R (VLT) and MIPS $24\ \mu\text{m}$ (Spitzer) magnitudes are included in the SED (Santini et al. 2009). The observed points have 1σ error bars or are 1σ upper limits. The points below Ly α have been corrected for IGM absorption. Our model does not model the Ly α radiative transfer and so the i_{775} point is really an upper limit. Note that the Ks band samples almost pure nebular continuum.

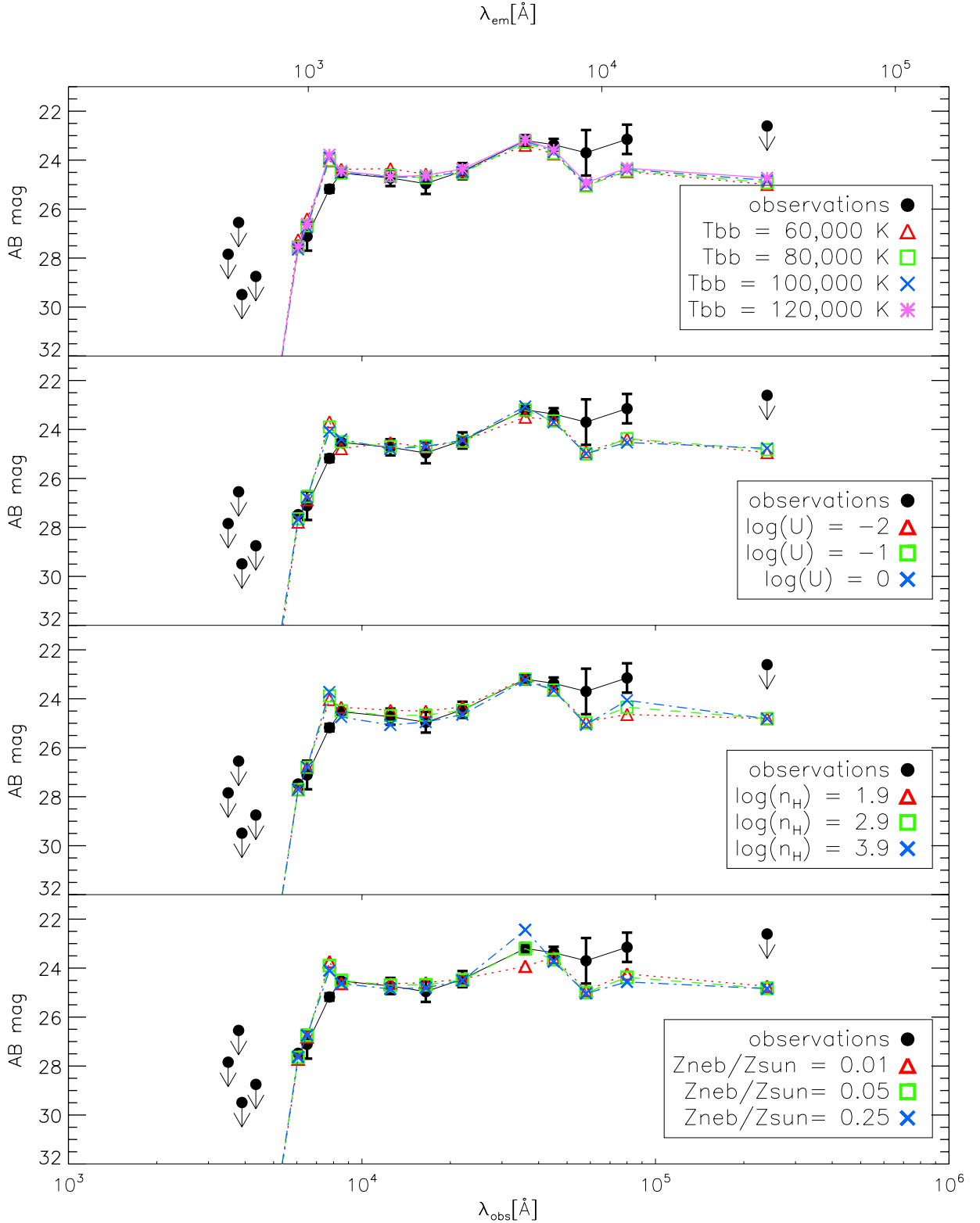


Figure 4.6: As Figure 4.5 but showing the effects of varying the four model parameters: *upper panel:* T_{bb} , *second panel:* $\log(U)$, *third panel:* $\log(n_{\text{H}})$ and *lower panel:* Z_{neb} . Note the effect of metallicity on the IRAC1 band (due to [O III]) and the effect of the density on IRAC4 due to changes in the He I 10830 \AA line. To improve visibility in this plot, note that the error bars (but not the upper limits) are 3σ .

Table 4.4: Photometry (AB magnitudes) of sample sources in the GOODS passbands with their 1σ errors.

GDS-id	r_e (")	z	IRAC4	IRAC3	IRAC2	IRAC1	K_s	H	J	z	i	V	B
J033229.14-274852.6	0.138	3.597	-24.54	-24.40	24.15±0.21	24.32±0.15	24.20±0.10	24.56±0.13	24.60±0.13	24.40±0.03	24.48±0.03	24.89±0.02	26.25±0.09
J033201.84-274206.6	0.169	3.603	23.32±0.14	23.59±0.11	23.77±0.08	25.21±0.18	-25.90	25.00±0.06	25.06±0.05	25.14±0.03	27.16±0.37
J033217.13-274217.8	0.127	3.617	-24.50	-24.50	24.80±0.27	25.04±0.22	25.04±0.15	24.67±0.13	25.72±0.22	24.98±0.05	25.03±0.04	25.12±0.03	26.92±0.17
J033233.33-275007.4	0.138	3.791	-24.44	-24.96	25.03±0.30	25.21±0.23	24.99±0.15	24.81±0.14	24.62±0.13	24.70±0.04	24.72±0.03	24.99±0.02	27.35±0.12
J033236.83-274558.0	0.153	3.797	-23.97	-24.57	24.11±0.24	24.10±0.16	24.55±0.13	24.57±0.13	24.55±0.13	24.54±0.02	24.62±0.02	25.16±0.02	27.50±0.14
J033240.38-274431.0	0.111	4.12	-24.48	-24.82	25.10±0.37	24.59±0.21	24.93±0.15	24.59±0.13	25.38±0.19	24.99±0.04	25.07±0.03	25.64±0.04	-28.70
J033234.36-274855.8	0.251	4.138	-23.91	23.70±0.40	23.47±0.15	23.34±0.10	23.63±0.08	24.03±0.10	24.29±0.11	24.10±0.02	24.25±0.02	25.23±0.03	28.00±0.29
J033248.24-275136.9	0.146	4.374	-24.54	-24.54	25.00±0.31	24.46±0.14	24.93±0.15	25.82±0.25	24.75±0.13	24.81±0.04	24.91±0.03	25.78±0.05	-28.51
J033257.17-275145.0	0.173	4.76	-24.55	-24.54	24.87±0.25	24.32±0.13	24.36±0.11	24.77±0.14	25.22±0.17	24.54±0.03	24.53±0.03	25.79±0.06	-28.60
J033229.29-275619.5	0.156	4.762	21.31±0.24	22.52±0.25	23.05±0.12	23.00±0.08	24.86±0.05	25.12±0.04	26.93±0.14	-28.86
J033210.03-274132.7	0.112	4.811	-24.5	-24.60	24.46±0.31	24.27±0.16	25.25±0.18	24.54±0.13	25.02±0.19	24.94±0.05	25.12±0.05	26.78±0.12	-28.61
J033221.30-274051.2	0.155	5.292	-24.5	-24.29	25.15±0.32	25.68±0.29	25.32±0.18	...	25.71±0.22	25.14±0.08	25.13±0.10	28.33±0.25	-29.50
J033245.43-275438.5	0.190	5.375	-24.5	-24.50	24.02±0.19	24.71±0.18	24.86±0.14	24.94±0.15	24.88±0.14	25.00±0.05	25.70±0.07	-28.97	-28.76
J033237.63-275022.4	0.263	5.518	-24.24	-24.24	24.57±0.30	24.69±0.24	25.40±0.31	24.60±0.20	25.82±0.25	25.71±0.10	26.28±0.22	-29.50	-29.50
J033218.92-275302.7	0.109	5.563	23.15±0.20	23.70±0.31	23.37±0.08	23.20±0.07	24.45±0.11	24.96±0.14	24.73±0.11	24.53±0.04	25.18±0.05	27.48±0.03	-28.75
J033225.61-275548.7	0.110	5.786	-24.61	-24.60	24.45±0.19	24.04±0.11	25.04±0.15	24.81±0.14	24.61±0.12	24.42±0.04	26.32±0.17	27.67±0.23	-29.51
J033246.04-274929.7	0.120	5.787	-24.49	-24.49	25.65±0.39	26.10±0.32	25.49±0.19	25.66±0.21	25.85±0.22	26.26±0.14	27.83±0.45	-29.08	-29.21
J033240.01-274815.0	0.120	5.828	-24.6	-24.80	24.48±0.20	24.49±0.14	25.32±0.17	25.00±0.13	25.07±0.15	25.21±0.06	26.52±0.15	-29.65	-29.46

Negative numbers indicate upper limits. Also given are the half-light radii and the redshift measured from Ly α .

Chapter 5

Analysis of other examples of N IV] emitters

5.1 J033217.22-274754.4

This source is another N IV] emitter found in the GOODS-S field in the FORS2 spectroscopic sample. The spectrum is shown in Fig. 5.1. The spectroscopic redshift of the source is 3.652 and it shows N IV] line emission with $L(\text{N IV])} = (1.89 \pm 0.14) \times 10^{42}$ erg/s and $\text{EW} = 11.32 \pm 1.48$ Å. This source was at first classified as ‘qf = B’ and that is why it was not included in Raiter et al. (2010) sample. However, in Vanzella et al. (2009) the quality flag has been changed to ‘A’. Therefore, it is another source of this type and we have carried out a similar analysis of the N IV] line and the modelling of the resulting observed SED. In this case the GOODS magnitudes have been taken from MUSIC v2 catalogue (Santini et al. 2009). This is a new updated version of the MUSIC catalogue. The difference between this catalogue and its first version (Grazian et al. 2006) is mainly in the IRAC bands and additionally the MIPS 24 μm magnitudes are included.

The SED is modelled in the same way as for the GDS18.92–02.7 source. Figure 5.2 shows the SED and overplotted a number of photoionization models for different T_{bb} , U , n_H and Z_{neb} . The models are again calculated using black bodies as the ionizing sources and all the same assumptions on the nebular gas. For this galaxy the number of ionizing photons has been calculated from H band flux, which is dominated by the nebular continuum emission, however with around 0.3 magnitude contribution from emission lines.

Using the spectroscopic redshift from the catalog we get Lyman break at 4242 Å (B band), Ly α at 5652 Å (V band), 2 γ continuum (1200 - 1600 Å) at $\sim 5580 - 7445$ Å (V and I bands), [O III] $\lambda\lambda 4959, 5007$ lines at 23069 and 23296 (K band), He I 1.0830 μm at 50381 Å (IRAC 3). In this case [O III] $\lambda\lambda 4959, 5007$ lines fall in the Ks ISAAC filter, however on its edge so they don’t have such a big impact on the calculated model magnitude.

There is an almost constant offset of around 1 magnitude in all IRAC bands. After examining HST ACS images we have noticed a nearby galaxy (with photometric redshift 3.76, MUSIC v2) only around 1 arcsec away from our source, therefore not resolved on

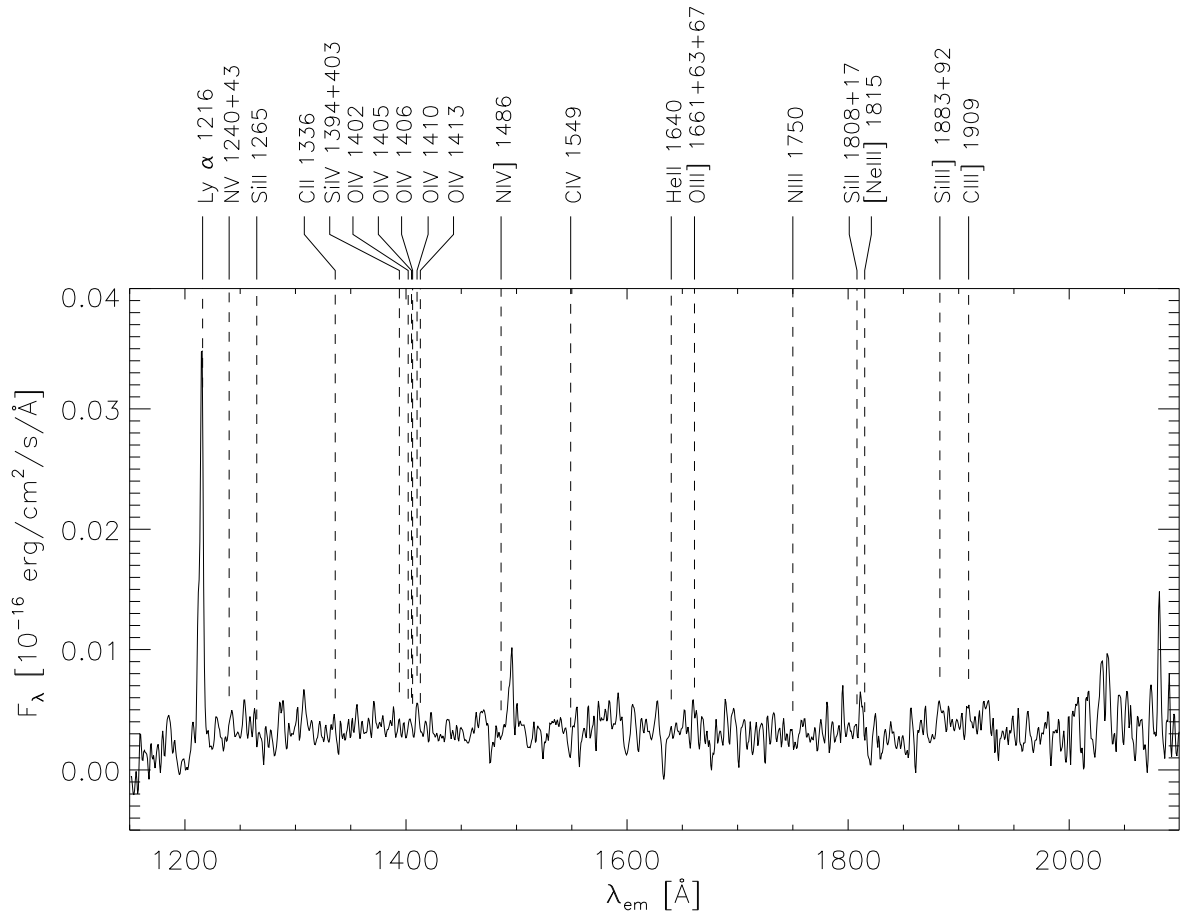


Figure 5.1: FORS2 spectrum of J033217.22-274754.4 source showing N IV] detection. Wavelength shifted to the rest-frame.

IRAC images. It could be a possible source of contamination. Both SEDs are plotted in Figure 5.3.

We analyse the models in terms of magnitudes as well as of the luminosity and the EW of the N IV] line. After checking the grid of photoionization models (where the hydrogen number of ionizing photons is fixed in the way that the observed H band flux is produced by each model) we conclude that the observed measured luminosity of N IV] (considered as total luminosity of both lines in the doublet) and the SED can be reproduced the best by the model with $\log U = -1$, $n_H = 10^2 \text{ cm}^{-3}$, $Z_{\text{neb}} = 0.05 Z_{\odot}$ and $T_{\text{bb}} = 80,000 \text{ K}$. That model gives $L(\text{N IV])} = 1.78 \times 10^{42} \text{ erg/s}$ which is within the errorbar measured from the spectrum. That value of nebular metallicity also produces the right K band flux (which includes [O III] lines).

Interestingly, for this source due to its lower redshift (compared to GDS18.92–02.7) a wider wavelength range is observed in the rest-frame UV, from ~ 1200 till $\sim 2080 \text{ \AA}$.

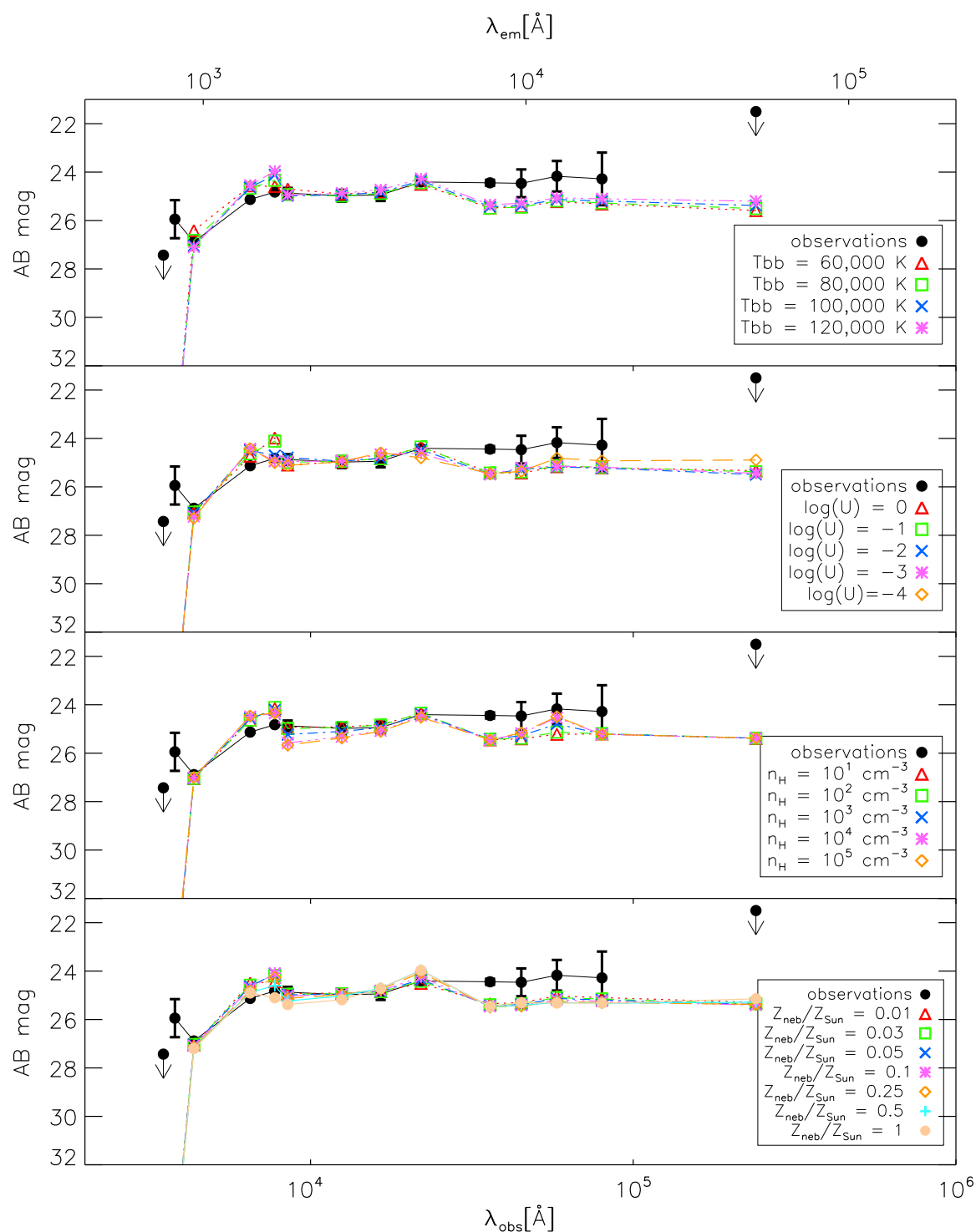


Figure 5.2: Observed SED of J033217.22-274754.4 source at $z=3.652$ (black symbols) along with the photoionization models for different T_{bb} , U , n_H and Z_{neb} overplotted.

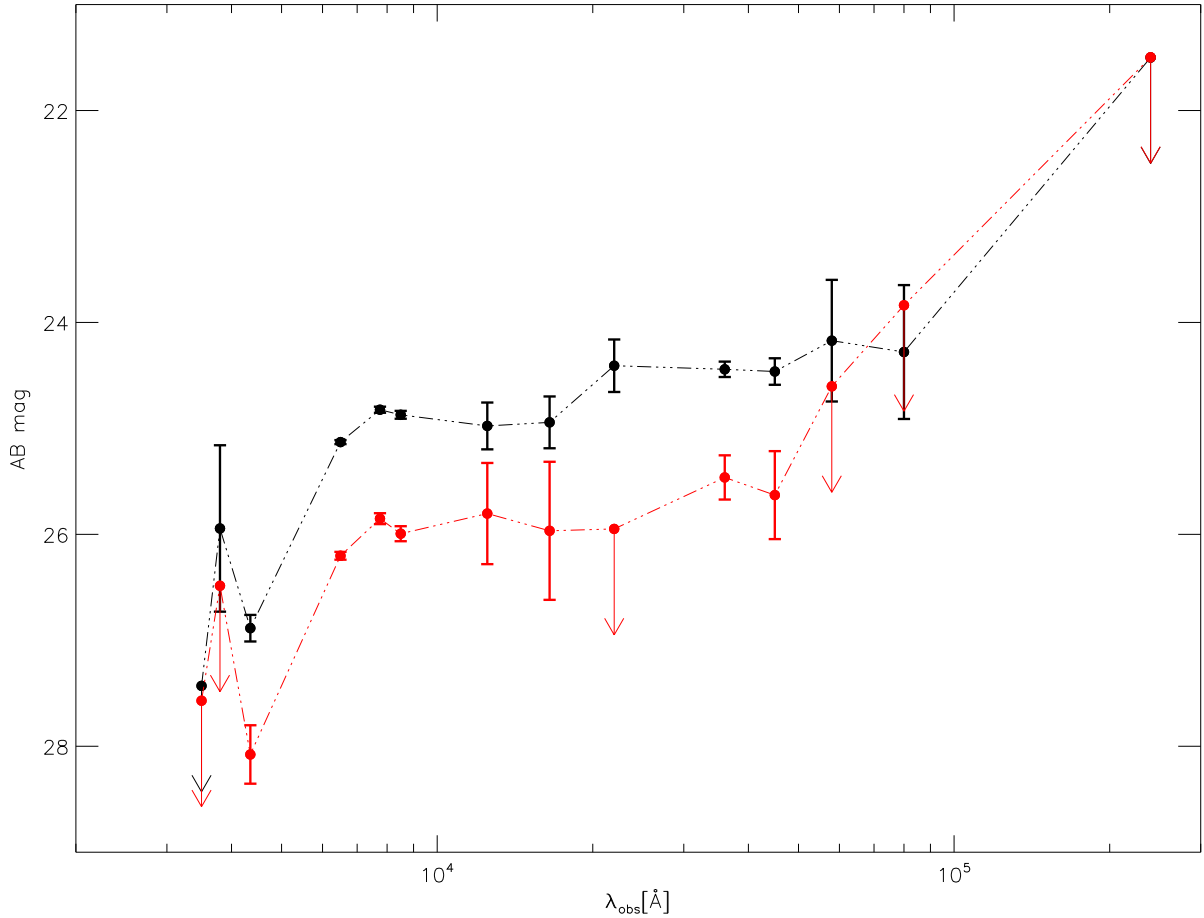


Figure 5.3: Observed SED of J033217.22-274754.4 source (black symbols) and the nearby source at $z=3.76$ (red symbols) which might be contaminating the measured magnitudes.

However, besides N IV] no other emission lines are detected. This allows putting upper limits on line fluxes/luminosities.

The following lines have been considered: N V $\lambda\lambda 1239, 1243$; Si IV $\lambda\lambda 1394, 1403$; C IV $\lambda\lambda 1549, 1551$; He II $\lambda 1640$; O III] $\lambda\lambda 1661, 1666$; N III] $\lambda 1750$; Si III] $\lambda\lambda 1883, 1892$; C III] $\lambda\lambda 1907, 1909$. Although the N IV] line shows only its longer wavelength component of the doublet, which implies higher density (see Fig. 1.5), low density has been kept in order to reproduce the [O III] lines, which would get destroyed by collisional deexcitations if higher density was used. For this reason in the models considered here the luminosity of the doublet is compared to the measured luminosity of the longer wavelength component of N IV]. To determine the upper limits for all the other lines I have checked the exact wavelength in the atomic data and have considered $\pm 10 \text{ \AA}$ region around each line/component of the multiplet, excluding N III] line since it has several components. For simplicity all the components of this line are considered together. The luminosities have been inferred from upper limits for fluxes and assumption of Gaussian line profiles. The corresponding line

widths σ 's that would allow line detections are assumed, they are usually very low i.e. < 100 km/s. This number seems reasonable since measured σ 's of metal emission lines in the UV for the Lynx arc are 80, 35, 30 km/s for C IV $\lambda\lambda 1549, 1551$, O III] $\lambda 1666$ and C III] $\lambda 1907$, respectively. Also for GDS18.92–02.7 the σ of N IV] $\lambda 1486$ is ~ 150 km/s. By analogy, the lines are expected to be narrow. The inferred σ 's are used to integrate over the line profile to calculate the total line luminosities.

The grid of models has been constructed where the model parameters are fixed to be the ones that produce the right N IV] flux (including the low density), i.e. $T_{\text{bb}} = 80,000$ K, $\log U = -1$ and $n_{\text{H}} = 10^2 \text{ cm}^{-3}$ and fixed number of ionizing photons, except the nebular metallicity which is a parameter being varied within the range from 10^{-3} till 1 solar. In the grid all the elemental abundances are being varied together. The luminosities obtained consist of all the components of the doublets/multiplets, therefore I sum up the measured upper limit luminosities in order to compare them with those models. That would be precise if the lines were not resolved. In the FORS2 spectrum they would be resolved, however due to density dependence of some and the fact that the density is kept constant due to the reason mentioned above, this comparison seems reasonable. N V $\lambda\lambda 1239+1243$, Si IV $\lambda\lambda 1394+1403$, O III] $\lambda\lambda 1661+1666$ and N III] $\lambda 1750$ lines are always below their upper limits. C IV $\lambda\lambda 1549+1551$ line is overproduced (even by more than order of magnitude) by almost all the models, except the lowest and the highest metallicity ones. He II $\lambda 1640$ line is overproduced by all the models by ~ 1.5 factor. C III] $\lambda\lambda 1907+1909$ line is overproduced by models with Z_{neb} from ~ 0.02 till $\sim 0.8 Z_{\odot}$. This supports the conclusion that C abundance needs to be reduced as expected from the analysis of C IV lines, i.e. if the lack of C IV lines would be only due to the fact that they are formed in less ionized regions, we could expect to observe C III] lines, which is not the case.

The above analysis is simplified, i.e. all the abundances are being varied together. Especially the oxygen lines which are the main coolants affect the strengths of other emission lines, i.e. if the oxygen abundance would be varied separately and other abundances would be kept constant some lines would become stronger for lower oxygen abundance.

However, I have attempted to find the model which would show by how much the abundances, especially the carbon one, must be changed in order to not exceed the upper limits for luminosities found for the UV emission lines. After analysing a number of models where carbon and silicon abundances are changed and nitrogen and oxygen abundances are kept constant (0.05 solar), I have found that once 0.05 solar oxygen and silicon abundances are acceptable (also in terms of producing enough [O III] $\lambda\lambda 4959, 5007$ line fluxes to account for the K band magnitude), the carbon abundance must be reduced by a factor of around 20 (with respect to the initially assumed 0.05 solar), i.e. should be ~ 0.25 % of the solar value. This implies an upper limit for the abundance ratio $C/N = 5$ % $(C/N)_{\odot}$.

It is difficult to talk about exact abundance analysis in this case, when only upper limits for line luminosities are available. Additionally, they are calculated by assuming certain shapes of the lines. However, it is striking that the C/N ratio must be reduced significantly compared to the solar value.

Different densities implied by [O III] and N IV] lines suggest that there are regions with different physical conditions within the nebula and the lines have been produced in the

gas of different densities. High spatial resolution would be required in order to study the structure and dynamics of the gas. This level of detail is not available at the moment for high- z galaxy observations with current observing facilities.

It is striking that He II $\lambda 1640$ line is always too strong in the grid of analysed models. The explanation of this problem might be the fact that I have used always black body shape of the ionizing continuum. This implies larger $Q(\text{He}^+)/Q(\text{H})$ ratio compared to population synthesis models for the same fixed number of H ionizing photons.

On the other hand, we have looked also at the EW of the N IV] line and compared it with the models (see Appendix). The photoionization models where the population synthesis spectra are used as the ionizing source do not produce as large EW(N IV]) as measured for this source, no matter the age, metallicity, density of the gas or ionization parameter. That large EWs can be produced by photoionization models with black body ionizing sources under certain conditions (high temperature $\gtrsim 80,000$ K, high ionization parameter and few % solar nebular metallicity) due to less stellar continuum in the rest-frame UV.

5.1.1 IRAC bands fluxes

While modelling J033217.22-274754.4 source with the nebular models the same problem as in the case of GDS18.92–02.7 source occurs with IRAC band fluxes. They are always quite significantly underestimated, by around 1 magnitude each one. One explanation of this problem might be the low resolution of the images, i.e. the objects are not resolved, therefore there might be some contaminating flux from a neighboring galaxy causing erroneous magnitude measurements.

Although the errors on the magnitudes are large, it is worth considering other possible sources of radiation in those bands.

In the IRAC3 band (for GDS18.92–02.7 source in IRAC4) there is the He I $1.083 \mu\text{m}$ line, whose influence on the model SED can be noticed in Fig. 5.2 in the panel showing different n_H photoionization models. Since it becomes stronger for higher density, it is another hint (along with the N IV] lines) suggesting higher density regions existing in the galaxy.

It has also been suggested and discussed in Chapter 4 (and in detail for GDS18.92–02.7 source in Vanzella et al. 2010), that the light in the IRAC bands comes from the old stellar population, which is supported by standard SED fitting method. However, to produce the observed N IV] lines in case of both sources the young (hot) stars are required. The co-existence of very young and very old stellar population in one compact galaxy would perhaps be an explanation, but then the rest-frame UV continuum flux is too strong, due to stronger underlying stellar continuum, and large observed emission line EWs cannot be achieved.

The explanation of this problem remains unclear.

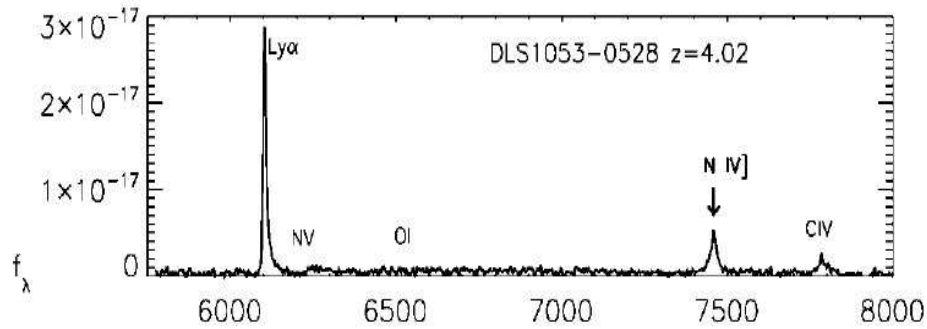


Figure 5.4: The observed spectrum of DLS 1053–0528 at $z = 4.02$ clearly showing N IV] and C IV emission lines and no detection of N V, Glikman et al. (2007).

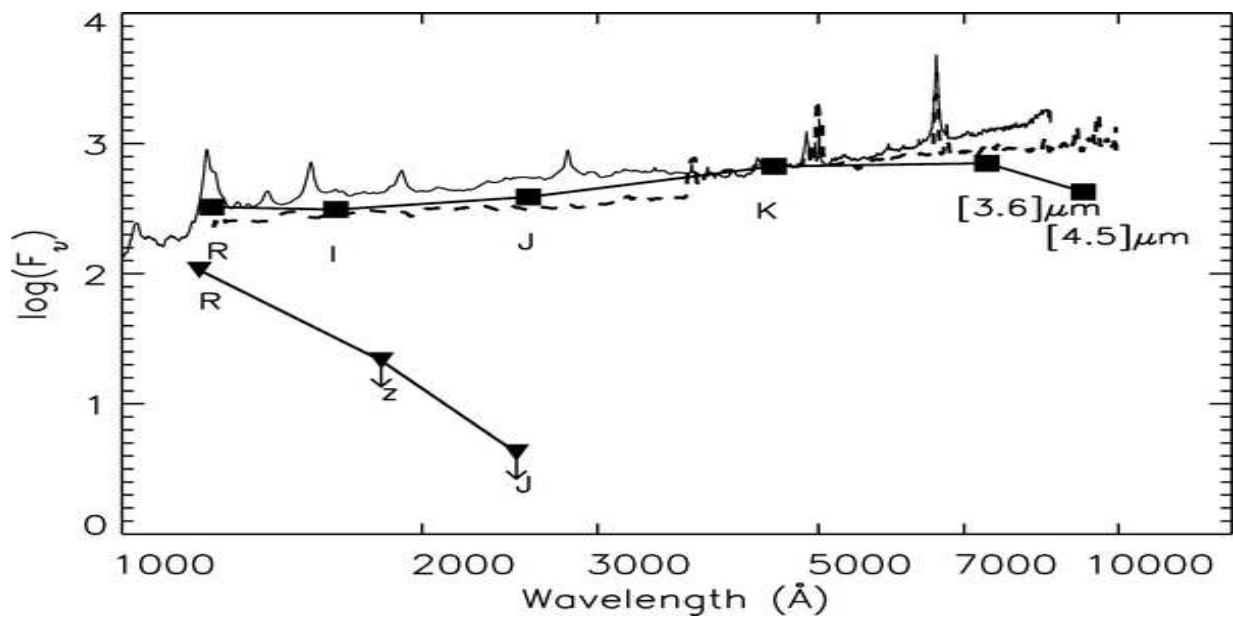


Figure 5.5: Rest-frame SED of DLS 1053–0528 (filled triangles) compared to the SDSS quasar composite spectrum (solid line) and unobscured starburst template with low extinction (dashed line), Glikman et al. (2007).

5.2 DLS 1053–0528

As already mentioned in Chapter 4, DLS 1053–0528 is the source at $z = 4.02$ described in Glikman et al. (2007). Although classified as QSO, it clearly does not have the QSO-like SED (see Fig. 5.5). It shows N IV] $\lambda 1486$ and C IV $\lambda 1549$ emission lines with fluxes $(1.048 \pm 0.08) \times 10^{-16}$ and $(0.55 \pm 0.02) \times 10^{-16}$ erg/cm²/s, corresponding to luminosities $(1.63 \pm 0.01) \times 10^{43}$ erg/s and $(8.56 \pm 0.31) \times 10^{42}$ erg/s, respectively. This gives the line ratio N IV]/C IV = 0.52. The rest-frame EWs of the lines are 280 and 91 Å and the σ 's 344 and 469 km/s, respectively. The spectrum and the SED are presented in Figs. 5.4 and 5.5 and the zoom of N IV] line in Fig. 5.6.

Having only measured the nitrogen and carbon line fluxes available, in order to find a model producing observed C/N ratio and get some hint on the abundances, I assume the ionization parameter and T_{bb} the same as for J033217.22-274754.4, which is reasonable since only the N IV] line is observed and the N V is not detected. I also assume low density and check the sum of the lines in the doublet from the models. I use the nebular metallicity of $0.05 Z_{\odot}$ particularly nitrogen and oxygen abundances are equal to 0.05 of the solar values. Those abundances are somewhat arbitrarily chosen and cannot be treated as accurate values, however it seems reasonable to assume N abundance of few % solar, since it is around this value where N IV] becomes strong. The carbon abundance is a free parameter and I have run the optimization method built-in in CLOUDY code which based on the χ^2 test searches for the best fitting model. The luminosities of the lines and the line ratio are reproduced with good accuracy when the carbon abundance is ~ 0.18 % solar, which implies the abundance ratio of $C/N \simeq 0.035 (C/N)_{\odot} \simeq 3.5$ % $(C/N)_{\odot}$. Although it is far from being accurate, the same conclusion as for J033217.22-274754.4 source is derived - C abundance is significantly lower than the N abundance with respect to their solar values.

Interestingly, the EWs are again very large, especially the one of N IV]. That large EW of N IV] line is impossible to obtain with any photoionization model that uses realistic population synthesis spectra as ionizing source. For C IV the observed value of EW can be produced by models with few % metallicity (stellar and nebular), which is much above the carbon abundance that has been derived from the line ratio. Large values are possible if the black body ionizing source is used in the models. Does this suggest a different (top-heavy) IMF? Or large extinction in the continuum? However, the Ly α arc, based on the emission lines, is concluded to be extinction-free.

5.3 GOODS-N source

Another source has been found in the GOODS-North spectroscopic data (courtesy: D. Stern) at $z \sim 3.55$. The spectrum is very noisy, however the N IV] and C IV lines are detected above 3σ level (C IV shows both components of the doublet). There is no detection of N V lines (Fig. 5.7). The nitrogen and carbon lines are shown in Figs. 5.8 and 5.9 respectively. Their measured line ratio is $N IV]/C IV = 0.637 \pm 0.087$ (the lines have been fitted with Gaussian profiles).

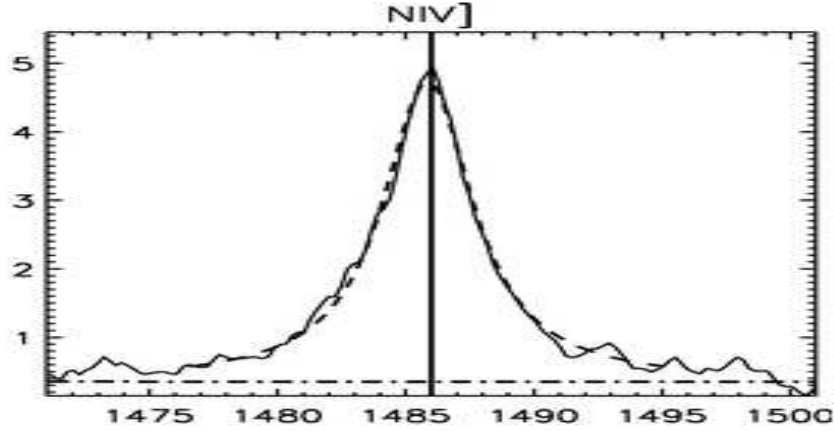


Figure 5.6: N IV] emission line (only high density component is detected) in the spectrum of DLS 1053–0528, λ in rest-frame, Glikman et al. (2007).

Since no public photometric catalog is available, we are only able to use the measured line ratio in order to build some model. Again, the model is searched by analogy to other sources, since the N IV] emission is clearly detected and there is no N V emission. $\log U = -1$, $n_H = 10^2 \text{ cm}^{-3}$ and $T_{\text{bb}} = 80,000 \text{ K}$, $Z_{\text{neb}} = 0.05 Z_{\odot}$ have been assumed in the modelling. The nitrogen abundance is fixed to be 0.05 solar and the carbon abundance is treated as free parameter. Since all the conditions as well as the line ratio are similar to the ones for $z = 4.02$ source, a very similar model is obtained from optimization driver run, where carbon abundance is ~ 0.22 solar, implying $C/N \simeq 0.044 (C/N)_{\odot} = 4.4 \% (C/N)_{\odot}$. Again, the model might be different for different oxygen abundance.

I have not attempted to analyse the line EWs due to low S/N.

5.4 Conclusions

Several additional sources similar to GDS18.92–02.7 have been discussed. All of them show N IV] emission. Although a proper abundance analysis is impossible, we have attempted to determine C/N ratios under reasonable assumptions. In all the cases carbon is significantly depleted compared with nitrogen with respect to their solar values. The exact amount is difficult to obtain having only two lines observed. Particularly, no hint about the electron temperature is available, which would allow the use of the direct method in order to determine the abundances.

It is worth comparing those results with the Lynx arc abundance analysis, where many more lines are available. Interestingly, for this source the carbon lines are stronger than

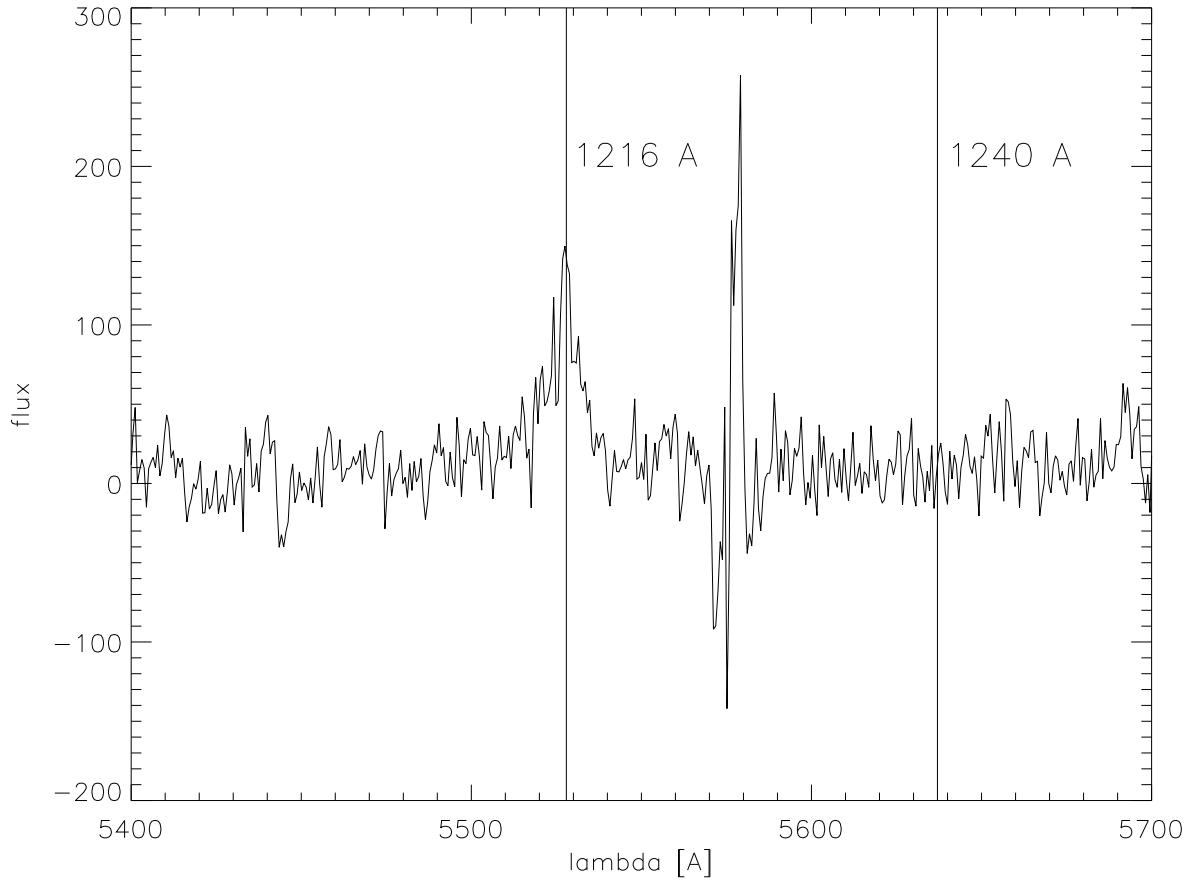


Figure 5.7: Ly α line and no detection of N v in the spectrum of the GOODS-N source (flux in arbitrary units, λ in observed frame).

nitrogen lines. Since clear absorption features are observed in C IV line profiles, the flux has been absorption corrected, resulting in ~ 6 times stronger intrinsic flux obtained. Even then the photoionization model with $Z_{\text{neb}} = 0.05 Z_{\odot}$, where solar abundance pattern is used to determine the nebular metallicity, overestimates the C IV/H β ratio by factor of ~ 2 .

Villar-Martín et al. (2004) have attempted to study individual element abundances in the Lynx arc with the direct method assuming the electron temperature $T_e = 16,000$ K (17,000 K). They obtain $C/N \simeq 0.6 (C/N)_{\odot} = 60 \% (C/N)_{\odot}$ ($C/N \simeq 0.59 (C/N)_{\odot} = 59 \% (C/N)_{\odot}$). It is significantly more than what is calculated for the sources discussed above. While the $z = 4.02$ source does not show any absorption features in the carbon C IV line profile, for $z = 3.652$ we have only an upper limit for the line flux and in the case of the GOODS-N source the spectrum is noisy, so it is difficult to study the line profile. In case there was any absorption in the line, that has attenuated the observed flux, for those two sources the carbon line fluxes (and therefore the abundance ratios) should be treated

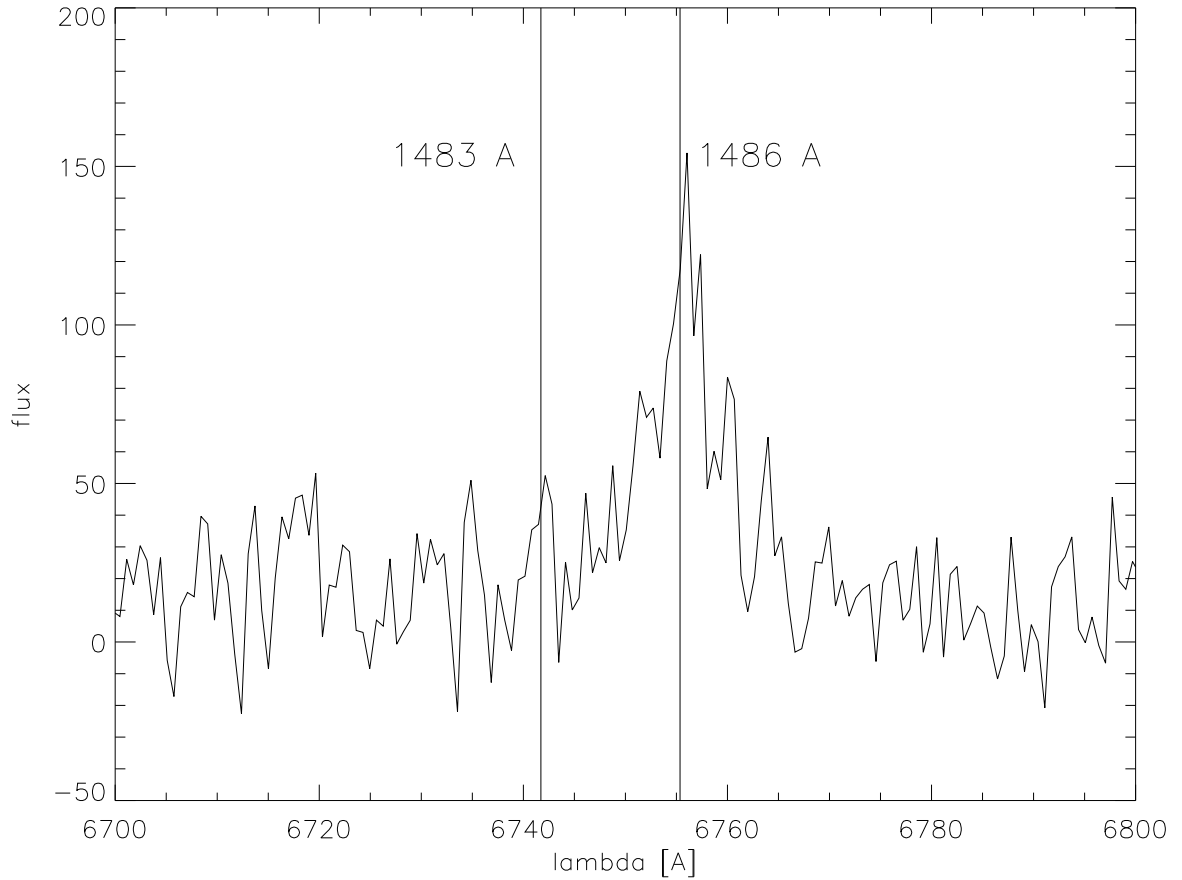


Figure 5.8: N IV] line in the spectrum of the GOODS-N source (flux in arbitrary units, λ in observed frame).

only as lower limits.

The possible scenario explaining objects with significantly depleted carbon is rather unclear. Meynet et al. (2006) present the wind and SN yields of very metal-poor stars (with metallicities 10^{-8} and 10^{-5}) for models with and without rotation. Although the CNO cycle products are always enhanced for rotating models, interestingly, only the most metal-poor model with rotation including only wind yields produces nitrogen much enhanced with respect to carbon. However, an additional issue is the mixing of the elements with the gas in the galaxy/H II region, which might also affect the observed spectrum.

More lines should be observed in order to build more accurate photoionization models and study the gas phase abundances. A number of lines are important since they are the main cooling agents, particularly [O III] $\lambda\lambda 4959, 5007$ not observed for the sources analysed above. Their strengths might affect the strengths of other lines.

It is worth noticing that for the N IV]-emitting sources discussed here, the N IV] line shows only the high density component. Expected strong [O III] lines require lower density

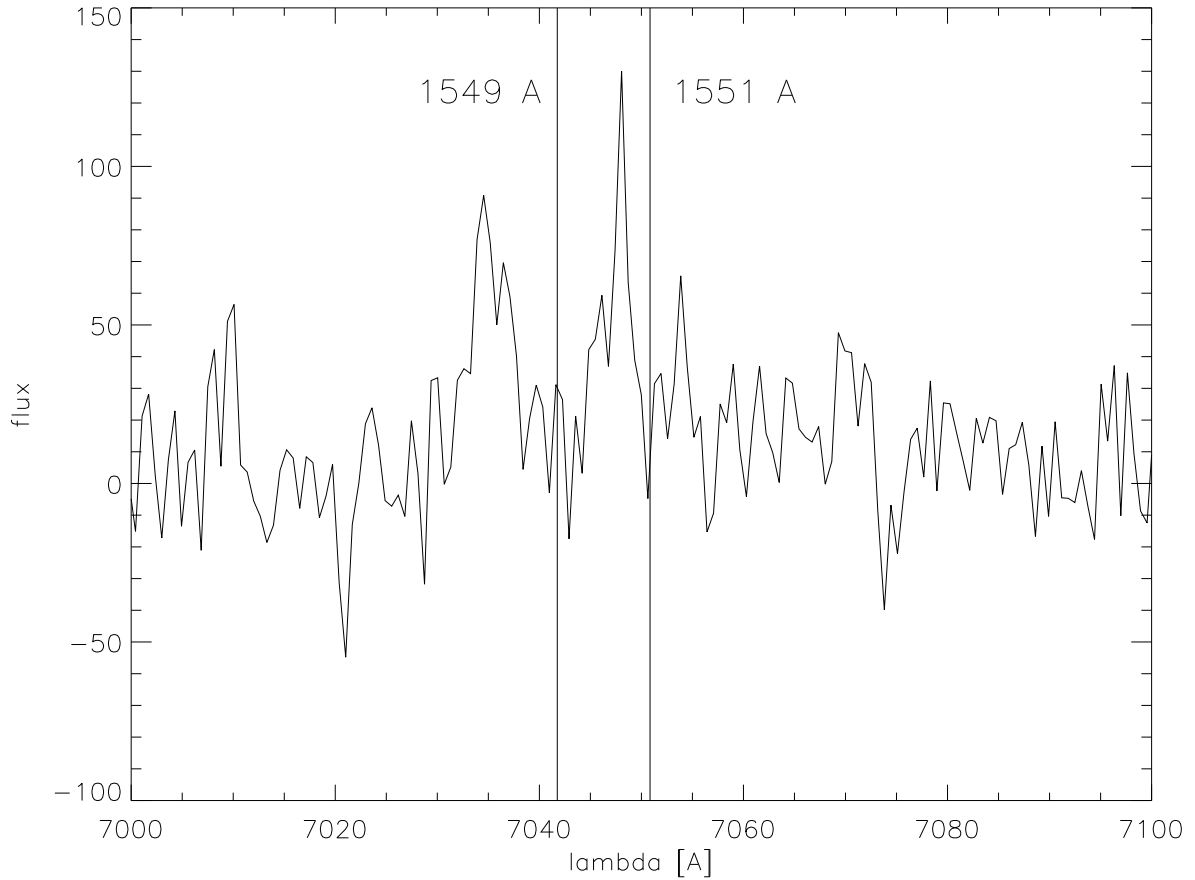


Figure 5.9: C IV lines in the spectrum of the GOODS-N source (flux in arbitrary units, λ in observed frame).

gas. Therefore, probably in those nebulae different density regions coexist. One scenario that could produce high density filaments is the interaction of stellar winds.

It is important also to notice that the abundance ratios discussed above are relevant only for the regions where the detected lines have been formed. Regions of different physical conditions might contain elements not observed in the analysed spectra. Lines of those elements might be then observed at different wavelengths, e.g. carbon cooling line at $157 \mu\text{m}$ (rest-frame). This possibility will be discussed in more details in Section 6.2.

Strikingly similar properties of the objects discussed above suggest that a new class of objects can be defined. It will need detailed studies with future facilities.

Chapter 6

Observational attempts to study objects with strong nebular emission

Hot stars, producing ionized nebulae, can be observed through the nebular emission. A number of observational characteristics have been discussed including: enhanced 2γ continuum, enhanced Ly α emission, flat continuum (in F_ν), rich rest-frame UV emission line spectrum, strong [O III] $\lambda\lambda 4959, 5007$ emission lines with large EWs in case of the nebula contaminated with some metals (few % solar metallicity) possibly influencing the SED shape. This Chapter presents several observational ideas (ESO proposals) to study objects dominated by the nebular continuum/line emission.

6.1 GDS J033218.92-275302.7 – X-shooter follow-up

Subsequently, as a follow-up observation, we have submitted a proposal to observe the NIV] emitter described in Chapter 4.

6.1.1 X-shooter

X-shooter (Vernet & Mason 2010) is a single object spectrograph mounted on the VLT UT2 telescope at the Cassegrain focus. It produces simultaneously the spectrum in the ultraviolet (UVB), visual (VIS) and near-infrared (NIR). This splitting maximizes the sensitivity in the spectral range. X-shooter provides intermediate resolution spectra ($R = 4000 - 14000$ depending on the slit width and wavelength) and operates in the slit as well as in the IFU mode. It was commissioned in November 2008 and January, March and May 2009 and started the operations in ESO Observing Period 84.

6.1.2 The proposal

based on the ESO X-shooter proposal

“A Ly α - NIV] emitter at $z=5.56$ – prospects for measuring the first stellar nucleosynthesis episodes”

PI: A. Raiter, CoIs: R. Fosbury, E. Vanzella
ESO Observing Period 84

Since the photoionization model for this object described in Chapter 4 predicts other emission lines of highly ionized species in the rest frame UV of the spectrum, namely C IV 1549 Å, He II 1640 Å, O III] 1665 Å, N III] 1750 Å, C III] 1909 Å, we have decided to utilize the possibilities of the new ESO instrument, X-shooter, and try to detect them. That would allow the determination of abundances of several elements and the verification of our photoionization model which due to lack of any hints simply assumes the solar abundance pattern. Additionally, the possible detection of the He II line would help to get some information on the nature of the ionizing source.

We submitted a short proposal (total requested time \lesssim 10 hours) in the ESO Observing Period 84. We used the X-shooter Exposure Time Calculator (ETC) version 3.2.8 to calculate the exposure time. We based our calculation on the N IV] line which is resolved in FORS2 spectrum, we measured its full width at half maximum (FWHM=1.7 nm) and the integrated line flux (0.4×10^{-16} erg s $^{-1}$ cm $^{-2}$) and calculated the S/N per spectral bin assuming seeing=0.8” and airmass = 1.2 and 1 \times 2 binning (binned in spectral direction). The other intercombination lines from our photoionization modelling are expected to have similar fluxes. For the N IV] line we predicted S/N = 3.27 (0 days after the new Moon), so we expected after further binning S/N \sim 8 per spectral bin (assuming 5 pixels/FWHM). We got that using 53 exposures \times 600 s, adding overheads (pointing + acquisition + slit setup = 570 s + readout time (slow) = 53 \times 48 s = 2544 s + telescope offsets = 53 \times 15 = 795 s) gives in total 10 hours.

6.1.3 Observations

The observations were executed in visitor mode (observer: A. Raiter) on 17/18 and 18/19 December 2009. The slit width in the VIS and NIR was 0.9”. We prepared the second phase of the proposal using ESO tool p2pp, we decided to use slit mode with 5” nodding and a random jitter within 1” box. This allows better sky subtraction.

We took a special care about the accurate offset from the reference star since our source is very compact and invisible on the pre-images. We obtained in total 42 frames in each UVB, VIS and NIR arms. The seeing was always good (only in 2 cases around 1.5”, otherwise less). The Ly α line was visible on the single raw spectrum (10 minutes), which allowed the verification of the positioning during the observations.

6.1.4 Data reduction

The data have been reduced using X-shooter pipeline version 1.0.0 (Modigliani 2010) following all the necessary steps of echelle data reduction. The UVB part of the data is not used.

In the VIS part each frame has been reduced in the stare mode. The position of the object on the slit has been first determined by looking at Ly α emission for each frame. Master flat field and master bias frames have been prepared by combining a number of frames from both observing nights. Bad pixels are negligible in the VIS arm, cosmic ray hits have been removed in 10 iterations. All the reduced frames have later been stacked.

In the NIR part the data has been reduced in the nodding mode using the master flat field frame and the prepared bad pixel map. Since the observations consist of 10 ABBA sequences (where A and B are positions on the slit) + 1 AB sequence (giving in total 42 frames), the pipeline has been run for each sequence separately. Since in the NIR the sky emission lines contamination is much worse than in the VIS part, this procedure of using nodding mode of the pipeline should improve the sky subtraction.

6.1.5 Results

The results are shown in Figures 6.1 and 6.2 for the VIS part and in Figures 6.3, 6.4, 6.5, 6.6, 6.7 for the NIR part.

6.1.6 Conclusions

Our observations proved the presence of N IV] emission in the spectrum of this source. Due to the much larger spectral resolution the Ly α profile is more detailed than the one presented before and obtained with FORS2 instrument. The comparison of the Ly α line profile with the simulated lower resolution (close to the FORS2 one) profile is shown in Fig. 6.1. Interestingly, the redshift measured from the Ly α peak is slightly different (lower) than the one measured previously from the FORS2 spectrum. It is equal to 5.557, while the FORS2 one was 5.563 (partially explained by the more accurate identification of the Ly α peak due to the higher resolution).

Possibly we detect the longer wavelength component of the C IV line, as shown in Fig. 6.3. However, it is below 3σ significance level. There is also a “blob” at $\lambda \sim 10800.5 \text{ \AA}$ which might be an emission line as shown in Fig. 6.4, but assuming that it is indeed He II line and using its rest-frame wavelength to calculate the redshift of the source, we obtain quite a different redshift $z=5.5857$.

Unfortunately, no clear detection of any emission line in the observed NIR part is found. More sensitive instruments/deeper observations are necessary to obtain this kind of data.

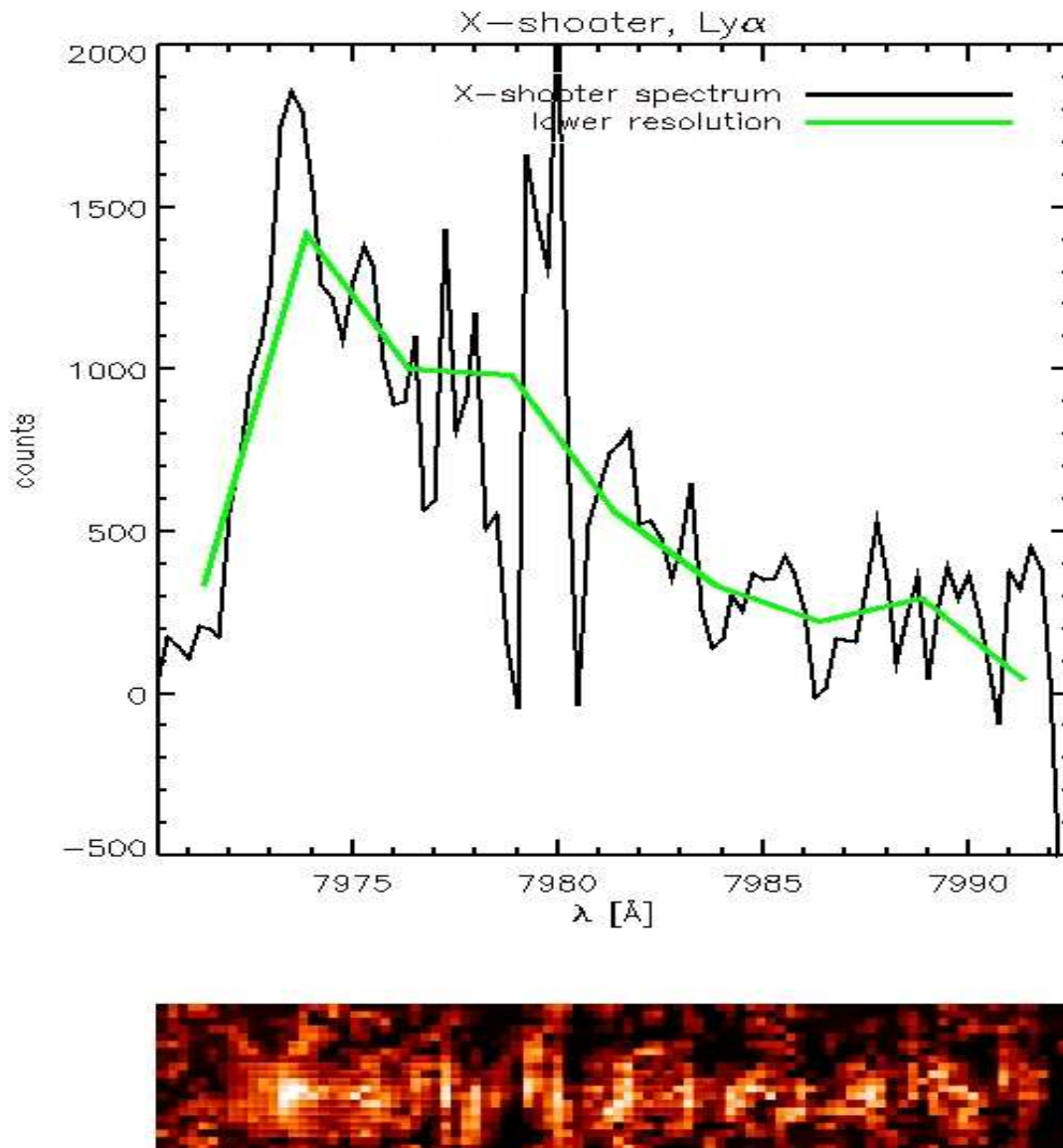


Figure 6.1: VIS X-shooter results: Ly α (rest-frame wavelength 1216 Å). Notice how the higher (than in FORS2 spectrum) spectral resolution makes the line profile more detailed.

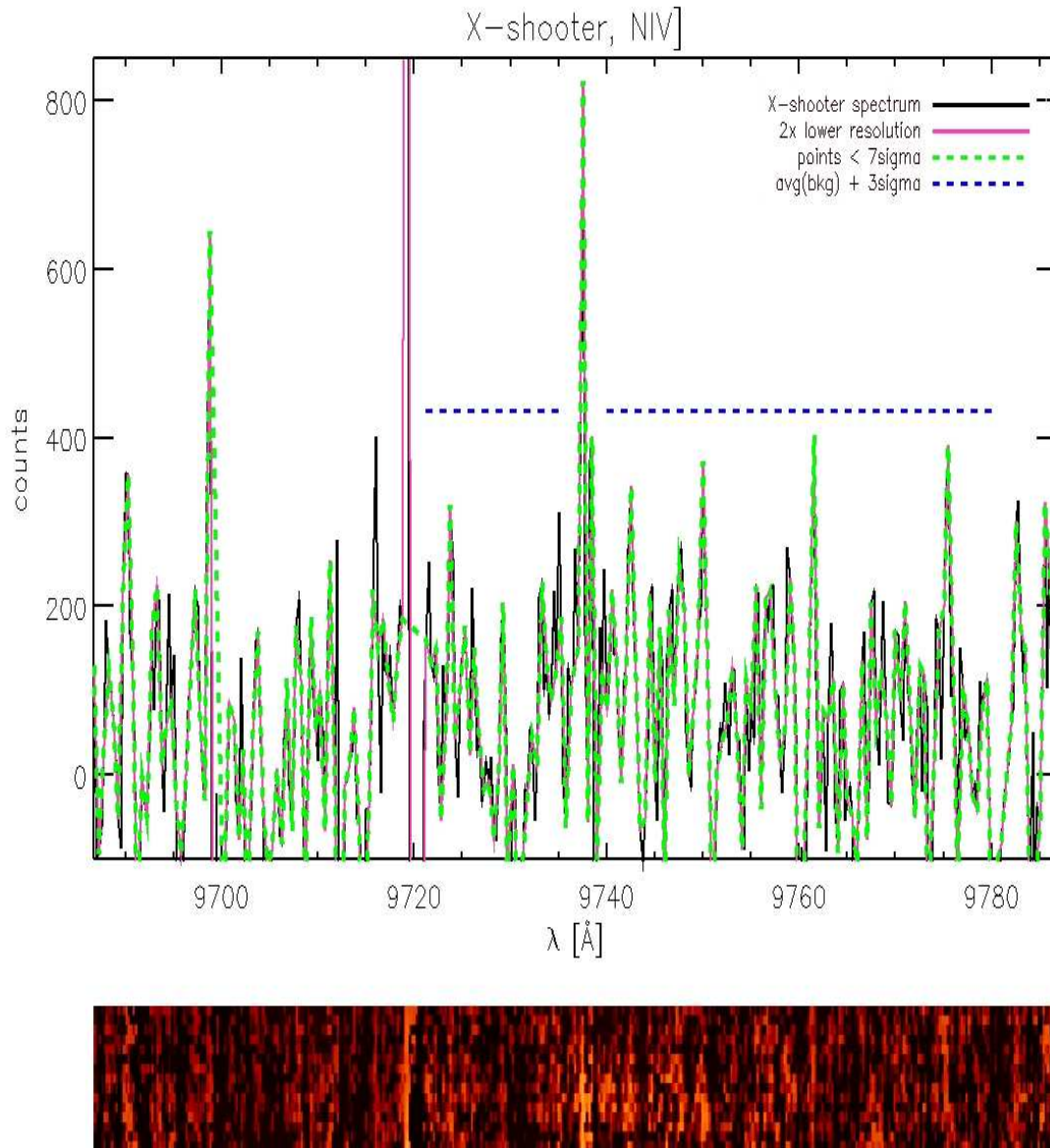


Figure 6.2: VIS X-shooter results: N IV] (rest-frame wavelength 1486 Å).

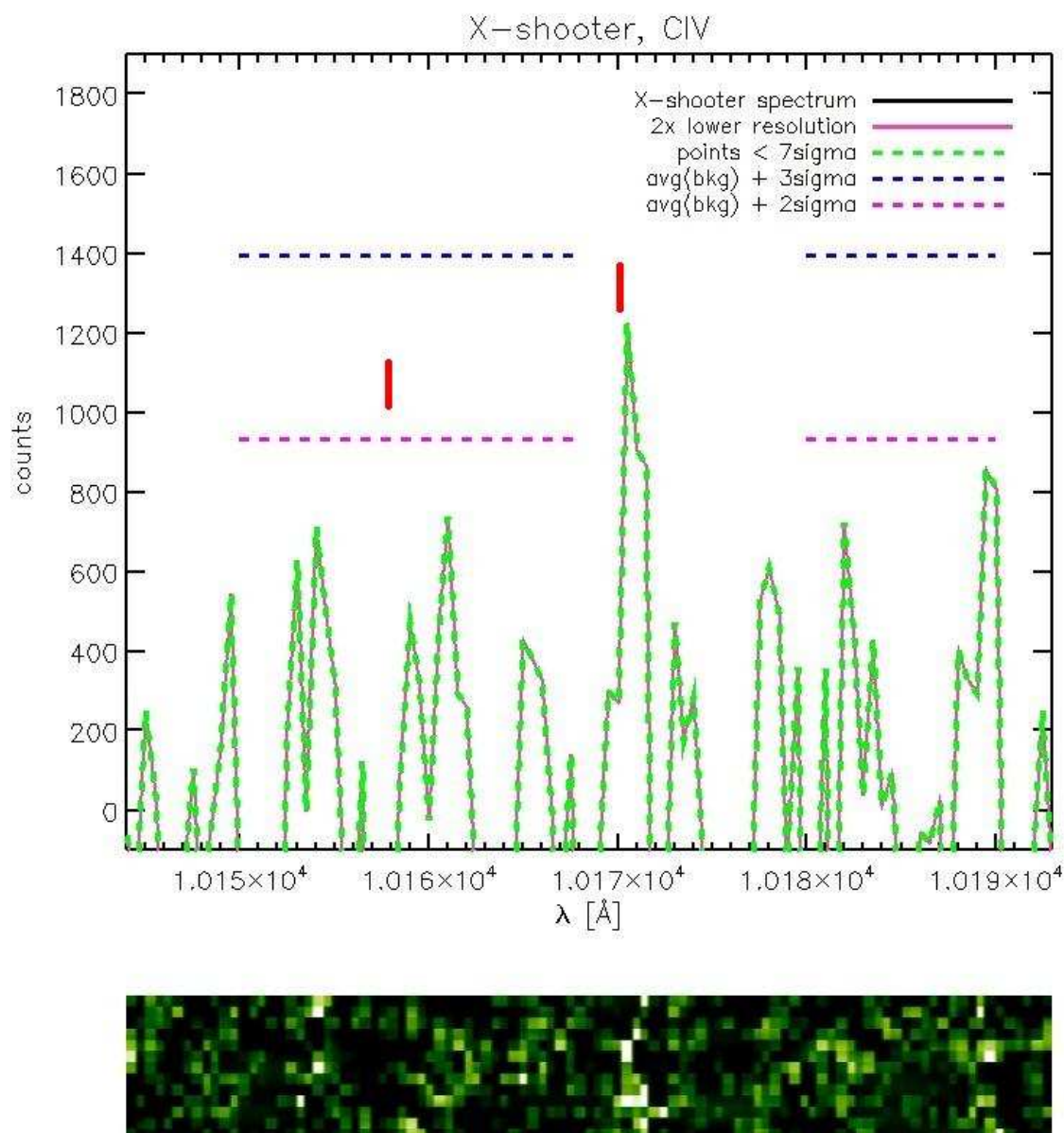


Figure 6.3: NIR X-shooter results: CIV (rest-frame wavelength 1549, 1551 \AA). The red lines mark the expected positions of the lines assuming the redshift obtained from Ly α peak ($z=5.557$).

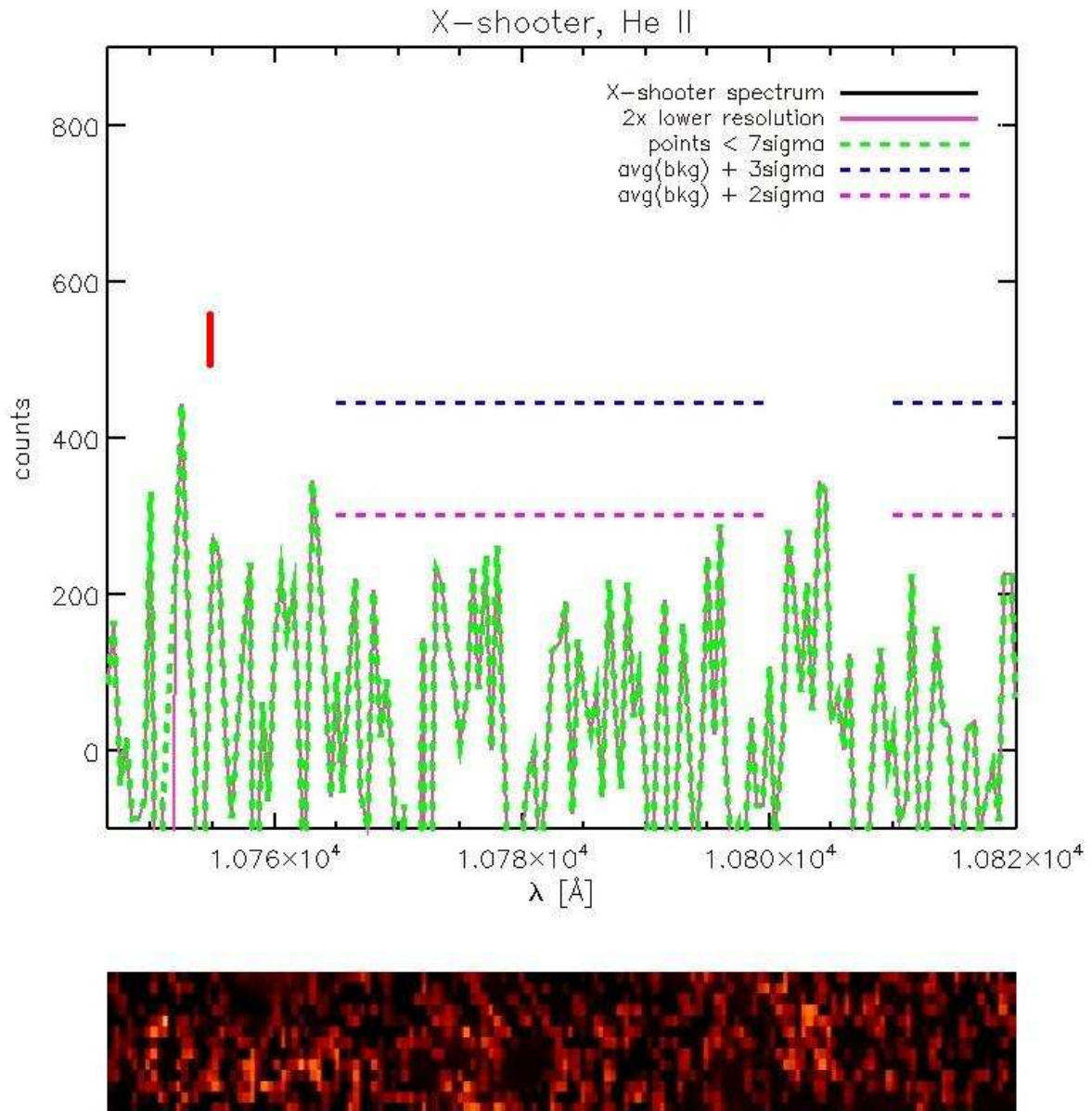


Figure 6.4: NIR X-shooter results: He II (rest-frame wavelength 1640 Å). The red line marks the expected position of the line assuming the redshift obtained from Ly α peak ($z=5.557$).

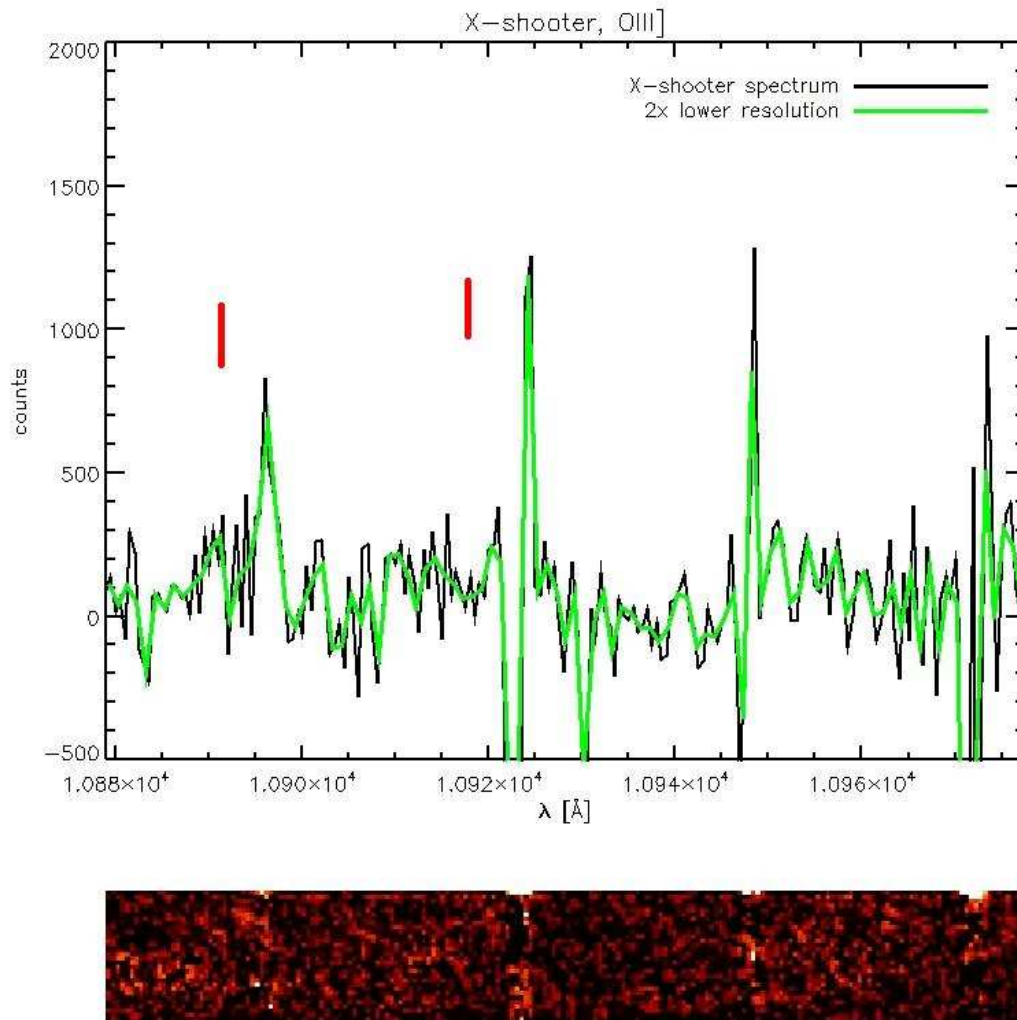


Figure 6.5: NIR X-shooter results: O III] (rest-frame wavelength 1661, 1666 Å). The red lines mark the expected positions of the lines assuming the redshift obtained from Ly α peak ($z=5.557$).

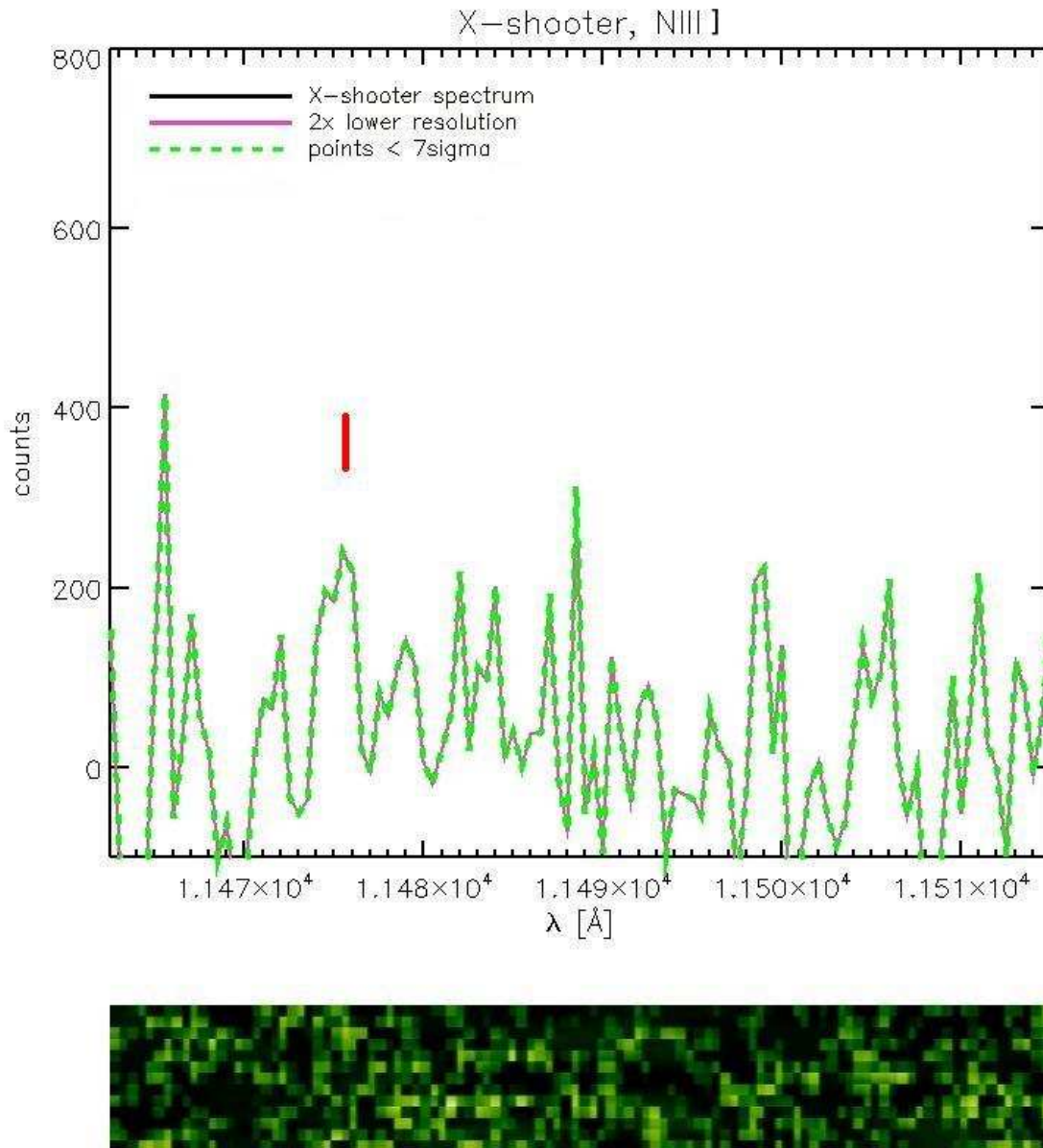


Figure 6.6: NIR X-shooter results: N III] (rest-frame wavelength 1750 Å). The red line marks the expected position of the line assuming the redshift obtained from Ly α peak ($z=5.557$).

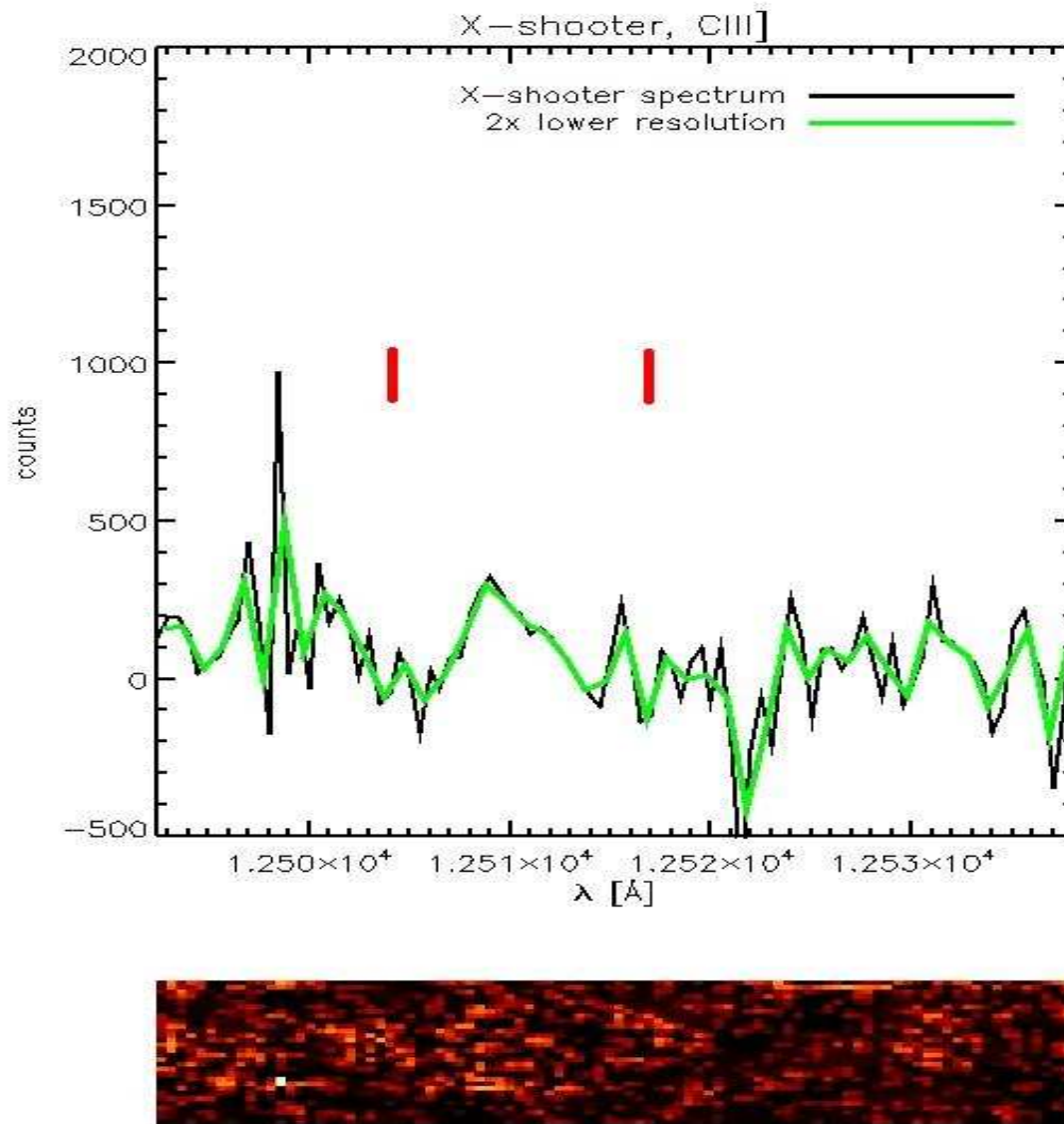


Figure 6.7: NIR X-shooter results: C III] (rest-frame wavelength 1907,1909 Å). The red lines mark the expected positions of the lines assuming the redshift obtained from Ly α peak ($z=5.557$).

6.2 GDS J033218.92-275302.7 – APEX follow-up – FIR [C II] cooling line

based on the ESO APEX¹ proposal

“The [C II] 157 micron cooling line from massive star formation at $z = 5.553$ ”

PI: R. Fosbury, CoIs: A. Raiter, C. De Breuck, D. Schaerer, P. Caselli, R. Maiolino, L. Testi

ESO Observing Period 85

After being allocated (384.A-0886(A)) X-shooter time for further studies of J033218.92-275302.7 source from the GOODS field, we submitted the proposal whose objective was the detection of far infrared fine structure cooling line of [C II] 157 microns of this source shifted to ~ 1 mm.

There is evidence that dust reddening in such sources must be low. In the two objects we have studied so far, the Lynx arc and J033218.92-275302.7 there is no detection of a FIR continuum. At such an early phase, it would not be surprising if little dust had formed and that the carbon remained in atomic form. It is possible, therefore, that the starbursting region is surrounded by an extensive *photodissociation region* (PDR²) that would be cooling via the [C II] 157 micron fine structure line. The detection of this line in our source would open a new exciting possibility of observing a range of other fine structure cooling lines with ALMA³ in sources where the first products of stellar nucleosynthesis are present. Measurements of the relative abundances of C, N and O would give an insight into the nature of early nucleosynthesis processes. Detection of the fine structure lines also gives direct measures of the amount of neutral gas that is available for further star formation.

Figure 6.8 presents the measurements of $L_{[\text{C II}]} / L_{\text{FIR}}$ (Maiolino et al. 2005), where L_{FIR} is the luminosity emitted in the far infrared. It can be noticed from the studies of the local Universe (black points) that there is a class of galaxies where the ratio is lower (HyLIRGs - hyperluminous infrared galaxies are galaxies with $L_{\text{FIR}} \gtrsim 10^{13} L_{\odot}$) which is due to the fact that [C II] line is a less efficient coolant in the most powerful FIR sources than in other galaxies. Observations show also that those objects at high- z (dashed red line in Fig. 6.8) have $L_{[\text{C II}]} / L_{\text{FIR}}$ ratios enhanced by about an order of magnitude compared with the local ones (black solid line). Maiolino et al. (2009) have detected a very strong [C II] line in gravitationally lensed quasar at $z=4.43$ that has a FIR luminosity lower by an order of magnitude compared to previous high-redshift detections which seems to confirm the

¹APEX - Atacama Pathfinder Experiment - is a 12-metre diameter millimetre and submillimetre telescope, located on the Chajnantor plateau on the Atacama desert in Chile.
<http://www.eso.org/public/teles-instr/apex/index.html>

²PDR - region surrounding H II region (Stromgren sphere) produced by lower energy photons which ionize and excite atoms and molecules.

³ALMA - Atacama Large Millimeter/submillimeter Array - is millimetre-/submillimetre-wavelength interferometer array telescope being built by ESO and other institutes on the Chajnantor plateau in the Chilean Andes, it will consist of 50×12 -metre antennas plus 12×7 -metre and 4×12 -metre antennas in the Atacama Compact Array.

<http://www.eso.org/public/teles-instr/alma.html>

offset found for local galaxies. Therefore, observations of high- z sources less luminous in FIR may have a double boosting factor in [C II]: high- z enhancement and because of the more efficient cooling in [C II] comparing with LIRGs.

In GDS J033218.92-275302.7 [C II] 157 microns line is redshifted to 1.034 mm (290.03 GHz). Although the expected emission is highly uncertain, we have based our calculation of the exposure time on the photoionization model published in Raiter et al. (2010). The lower limit on the bolometric luminosity of the source is that of the population of massive, hot

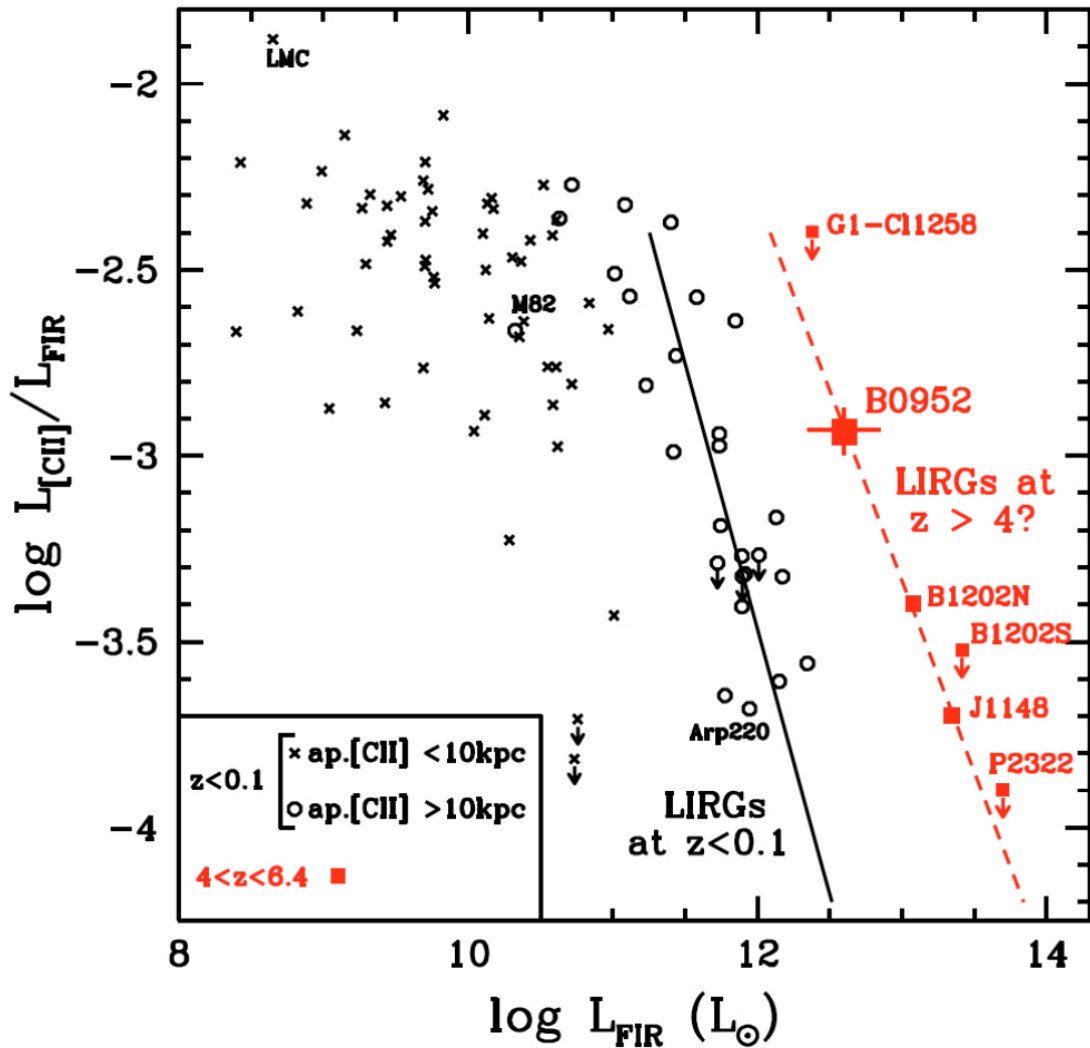


Figure 6.8: $L_{[\text{C II}]} / L_{\text{FIR}}$ as a function of L_{FIR} (from Maiolino et al. 2009). Black points correspond to the local galaxies and red points to the high- z ones. Black solid line is a fit to the local LIRGs (luminous infrared galaxies), i.e. with $L_{\text{FIR}} \geq 10^{11} L_{\odot}$, red dashed line is the fit to the detections at high- z .

stars needed to produce 3×10^{55} ionizing photons per second predicted by the model which corresponds to $\log[L_{\text{bol}}/L_{\odot}] = 11.7$. We take it as an estimate of L_{FIR} assuming that there is sufficient amount of dust to intercept significant fraction of the stellar radiation. This value for L_{FIR} is at least an order of magnitude smaller than the current observed upper limit (a flux of 3 mJy) at 850 microns for this source (De Breuck, private communication). The conversion into $L_{[\text{C II}]}$ is done on the basis of Fig. 6.8, from which we actually take $L_{[\text{C II}]} / L_{\text{FIR}}$ ratio for the LMC ($L_{[\text{C II}]} / L_{\text{FIR}}(\text{LMC}) = 0.013$) which we consider to be a local analogue of GDS J033218.92-275302.7 source. Low metallicity and reduced dust abundance implies low attenuation of the UV photons and therefore results in the C^+ -emitting regions being larger because the photo-dissociating photons can traverse a larger volume of the molecular cloud as in the case of LMC (Rubin et al. 2009). This results in a [C II] line peak of 23 mJy assuming a line-width of $350 \pm 60 \text{ km s}^{-1}$ derived from the FORS2 spectrum of the N IV] line. We use exposure time calculator version 3.2. By setting the channel width to 100 km s^{-1} and aiming for a 4σ detection in each of three channels covering the line, we use our flux estimate of 23 mJy ($=0.14 \text{ mK}$) to derive a total integration time of 34 hours including all overheads. The proposal was accepted and executed in August 2010. Preliminary analysis shows a possible detection. More detailed data reduction and analysis in the near future will be done to confirm the detection and perform the modelling.

If successful the detection of [C II] in GDS J033218.92-275302.7 would demonstrate the presence of an extensive PDR and open the possibility of observing it in other fine structure lines.

6.3 The effect of [O III] lines for $z \sim 3.5$ galaxies

based on the ESO DDT (Director's Discretionary Time) SINFONI proposal

*"Searching for primordial star clusters at redshift ~ 3.5 "*⁴

(PI: A. Raiter, CoIs: R. Fosbury, P. Rosati)

As shown in Chapter 4 [O III] $\lambda\lambda 4959, 5007$ can significantly influence the colours of $z \sim 6$ galaxies. That effect is worth investigating at other redshifts. Particularly interesting seems the case of $z \sim 3.5$ sources where those lines redshifted to the K band region might be observed by current instruments. There is only limited number of observations where [O III] lines have been observed at such a high redshift (Maiolino et al. 2008).

Our aim is to test a spectroscopic/photometric search technique for very high temperature stellar clusters that could be candidates for first generation star formation. For high colour temperature stellar clusters the stellar continuum is too weak to be detected in the observable Rayleigh-Jeans UV tail. Once the surrounding material becomes polluted by supernova ejecta, emission lines from C, N and O will begin to make an appearance and become quite strong (and due to little underlying continuum have large equivalent widths) even at metallicities of one hundredth of solar. The search of that kind of objects at lower redshifts is justified by the theoretical and observational findings. This is distinct from

⁴This proposal although accepted, could not be executed.

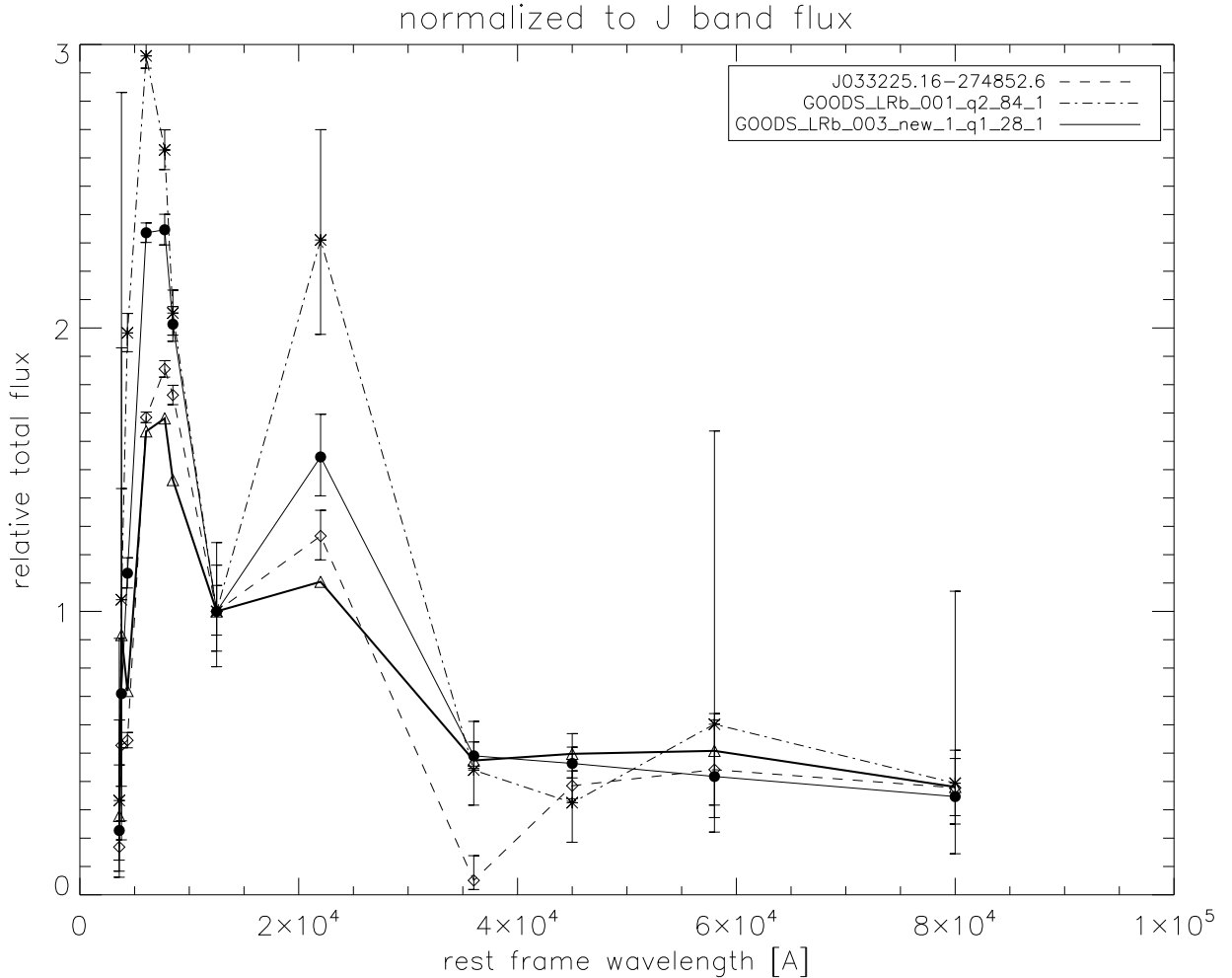


Figure 6.9: Normalized (to J band) total flux in U, B, V, i, z, J, K and 3.6, 4.5, 5.8, 8 μm (shown for rest frame wavelength) bands shown for the whole sample of Ly α emitters (indicated by thick solid line) and 3 chosen candidates with the strongest K band flux excess.

some current searches for the joint emission of Ly α and HeII expected from primordial stars and nebulae since it relies on the HII region already being polluted by supernovae in the cluster.

We seek to develop the technique of finding sources similar to the Lynx arc and GDS J033218.92-275302.7 (i.e. very hot, massive stars, $T_{\text{eff}} \sim 80,000$ K, in conjunction with a significantly polluted HII region) at redshift ~ 3.5 in deep, multi-band GOODS photometric and spectroscopic catalogues. The idea is to anticipate that the nebula surrounding a primordial cluster will very rapidly become polluted with metals which will produce characteristically strong intercombination and forbidden emission lines in the rest-frame UV and optical spectrum. The lines would affect the measured photometric fluxes. An archetype Lynx arc has indeed the K band flux dominated by the [O III] nebular lines.

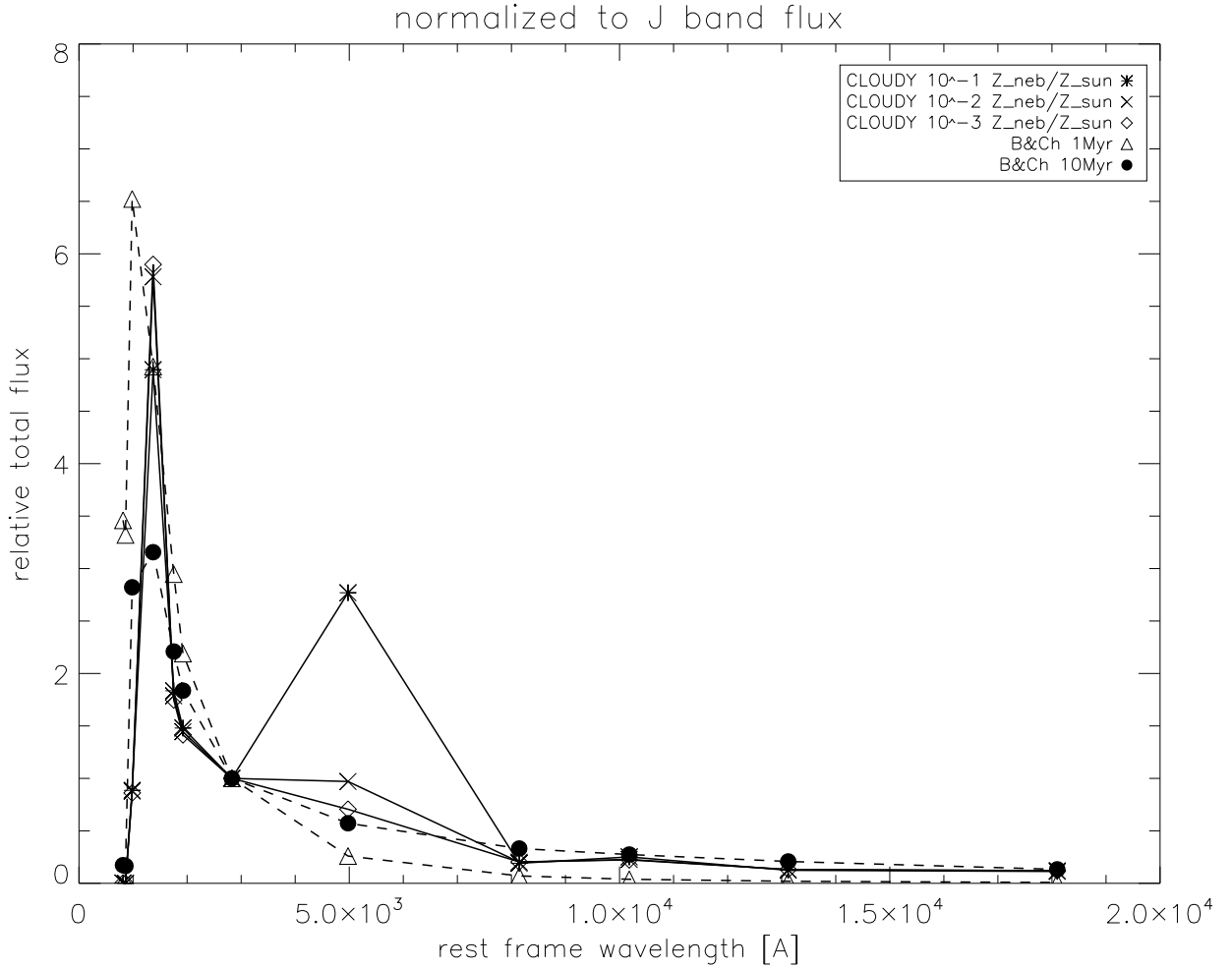


Figure 6.10: Figure similar to Figure 6.9 but showing the results for the models. Lines intensities assumed to be intrinsic. No extinction assumed, no IGM absorption assumed due to Ly α forest effect.

For this purpose we have built a sample of strong Ly α emitters (with good quality flags for spectroscopic redshift determination) from the FORS2 and VIMOS GOODS spectroscopic programmes, choosing a redshift range that would place the [O III] line in the K band, i.e. $z \sim 3.5$, with no AGN characteristics. We have found 15 candidates with single photometric matches (i.e. no confusion): 7 from FORS2 and 8 from VIMOS. For these 15 sources the calculated average SED obtained from the multi-band GOODS photometric catalogue is shown in Fig. 6.9 along with the SEDs of 3 chosen candidates whose photometry suggests strong [O III] $\lambda\lambda 4959, 5007$ emission lines in the K band (with the strongest K band flux excess).

We can now compare those observations with the models. Fig. 6.10 shows the same as Fig. 6.9 relative fluxes but for 5 theoretical cases: 3 photoionization models with hot black body ionizing source and contaminated by metals nebular gas with $Z_{\text{neb}} = 0.001$,

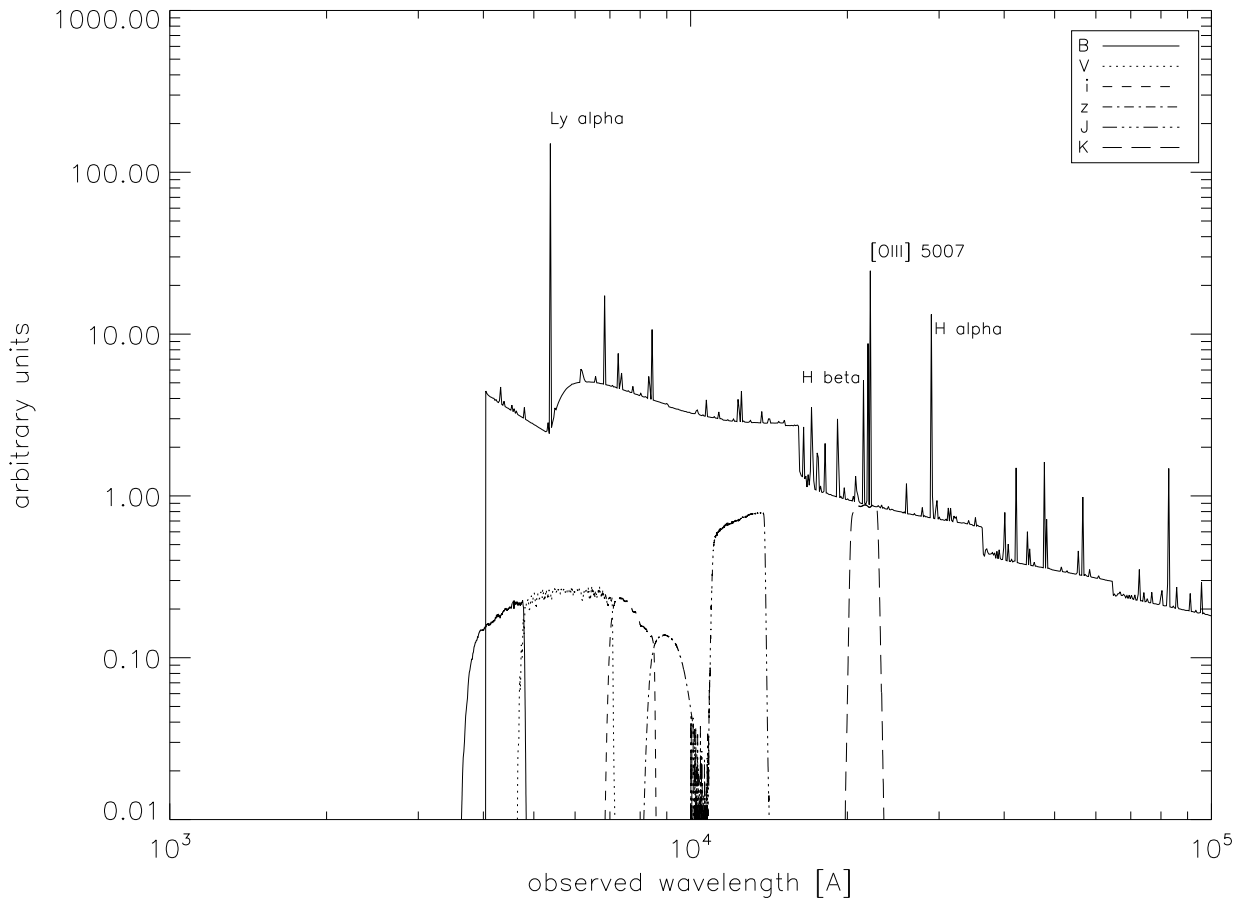


Figure 6.11: CLOUDY model (νF_ν versus λ) calculated for 10^{-1} solar nebular metallicity for redshift $z=3.42$ (average redshift of the sample) with B, V, i, z, J, K filter response curves overplotted. No extinction, no absorption in IGM assumed.

0.01, 0.1 Z_\odot (“polluted Pop III” models) and 2 stellar population synthesis models from Bruzual & Charlot (2003) with no nebular emission for 1 and 10 Myrs. Only models with the nebular metallicity of few % solar produce strong K band excess due to strong [O III] lines. The CLOUDY spectrum for the last case is shown in Fig. 6.11 for the average redshift of the entire sample $z=3.42$ with the GOODS optical and NIR filter passbands superimposed. The behaviour with redshift of the J-Ks colour of the models is shown in Fig. 6.12.

Remarks

It is clear that the significant K band flux excess for sources at $z \sim 3.5$ can be produced by strong [O III] emission in the case when the hot ionizing source is surrounded by slightly contaminated (until few % solar metallicity) diffuse gas. From Fig. 6.12 it can be noticed that J-K colour becomes very red in that case, and there is not many objects occupying that region of the plot ($z = 3.5$) taking into account the entire galaxy population from the

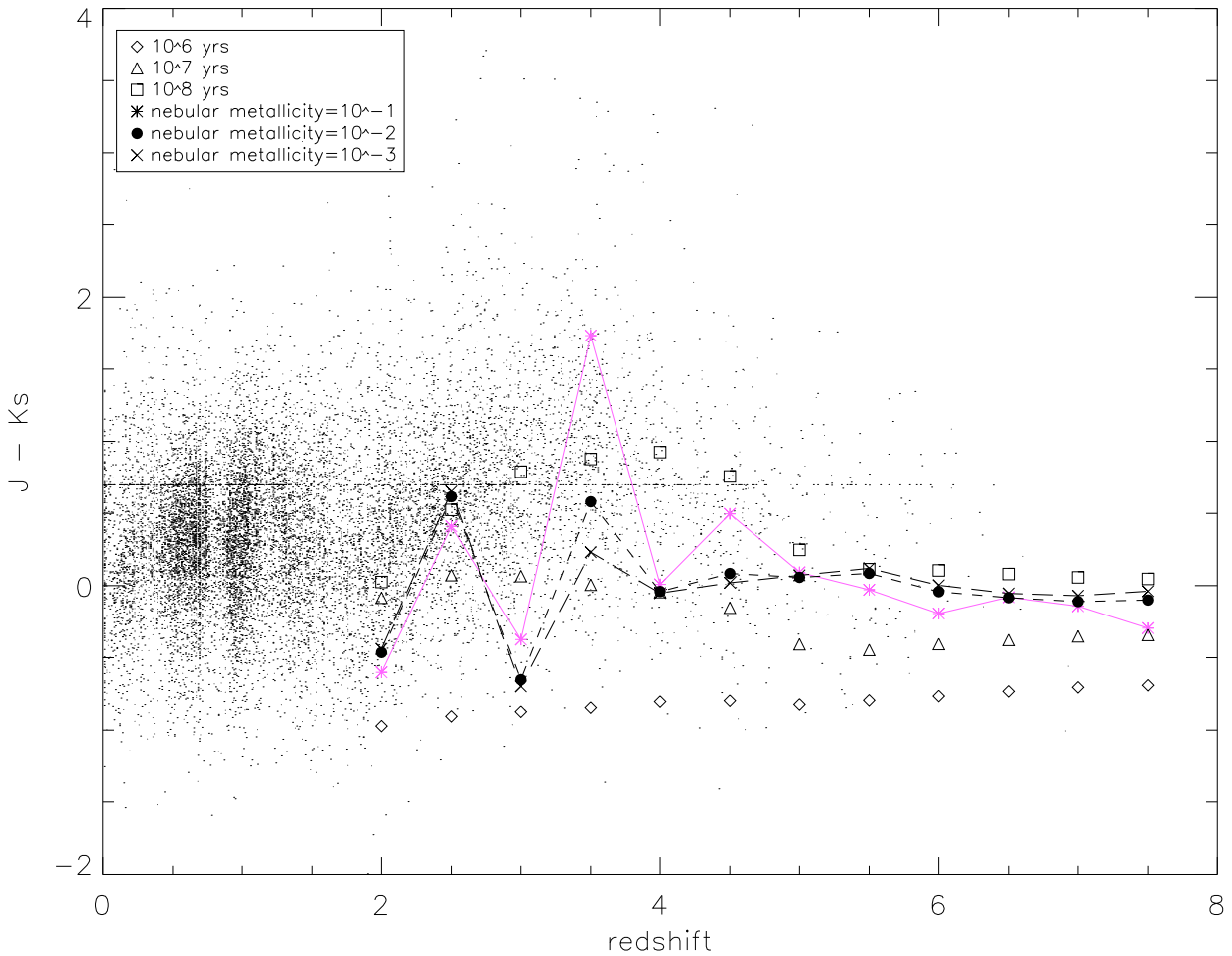


Figure 6.12: Evolution of J - Ks colour with redshift for 3 stellar population synthesis models with different ages and 3 CLOUDY models with different nebular metallicities. Lines intensities assumed to be intrinsic. No extinction assumed. Small black dots are data from MUSIC catalog.

MUSIC catalogue. Fig. 6.12 shows for comparison also one ‘older’ model, with age of 100 Myrs. In that case the colour is also red which might be the reason of confusion, similarly to $z \sim 6$ galaxies (Schaerer & de Barros 2009). Our 3 candidates were selected by requiring the excess in K band only, i.e. K band flux was in excess comparing with shorter as well as longer wavelength band fluxes. Perhaps, if one wants to perform an automatic selection of possible candidates, also K-3.5 μm (or other longer wavelength band) colour should be added as a second criterion.

An advantage of obtaining the spectra for those sources would be that for this redshift range we have the possibility of detecting also the H and He II $\lambda 4686$ emission which would provide some initial spectroscopic diagnostics. While the measurement of Ly α and [O III] alone does not conclusively demonstrate the high stellar temperatures expected for such clusters, the presence of a high [O III]/H ratio and a weak continuum will mark an excellent

candidate for further spectroscopic study.

In this Section I have presented the possible selection method for finding candidates of first generation star formation at lower redshifts. It still remains to be tested.

6.4 Low redshift analogs ? - “Green Pea” galaxies

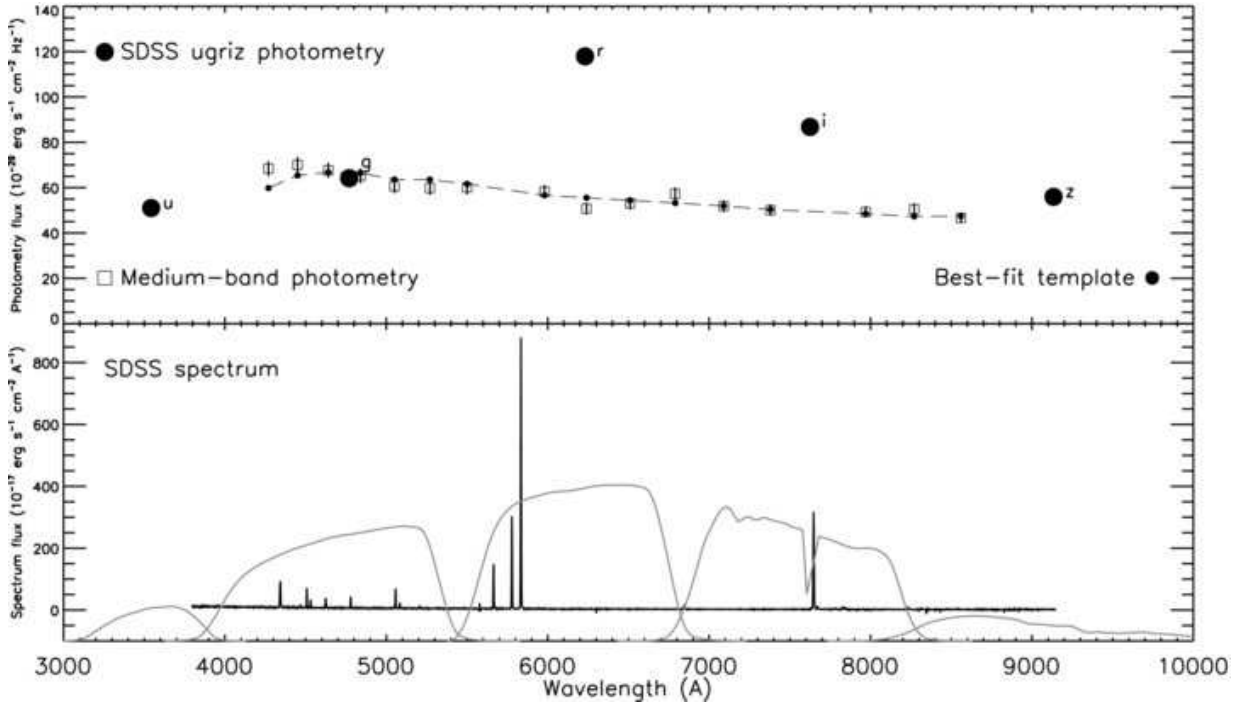


Figure 6.13: SED of an example “Green Pea” galaxy, Cardamone et al. (2009).

This Section describes a class of compact starforming galaxies at redshifts $\sim 0.1-0.4$ recently discovered (Cardamone et al. 2009) in the “Galaxy Zoo” project which might be the low- z analogues of high- z emission nebulae being discussed in this thesis.

Due to small sizes and unusually large equivalent widths of $[\text{O III}] \lambda\lambda 4959, 5007$ they appear as green peas in SDSS colour images. They show a weak continuum and strong nebular emission lines (see a typical spectrum in Fig. 6.13, lower panel). In addition to hydrogen Balmer series lines and very strong $[\text{O III}] \lambda\lambda 4959, 5007$ lines a number of other emission lines are detected in the SDSS DR7 spectra, including $[\text{Ne III}]$, $[\text{O II}]$, $[\text{O III}] \lambda 4363$, $[\text{O I}]$, $[\text{N II}]$ and $[\text{S II}]$. These objects have SFRs reaching $\sim 30 M_{\odot}/\text{yr}$ and low masses (median mass of the sample is $10^{9.5} M_{\odot}$). That implies very high specific star formation rates (SSFRs), i.e. star formation rates per unit mass, amongst the highest in the local Universe. They have low reddening $E(B - V) < 0.25$ and relatively low metallicities. Their mean metallicity is close to solar: $\log(\text{O}/\text{H})+12 \sim 8.7$, calculated using $[\text{N II}] \lambda 6584 / [\text{O II}] \lambda\lambda 3726, 3729$ vs $\log(\text{O}/\text{H})+12$ calibration from Kewley & Dopita (2002). However, the direct method which takes into account the calculation of the electron temperature gives low

metallicities, $\sim 20\%$ solar, i.e. $\log(\text{O}/\text{H})+12 \sim 8$ (Amorín et al. 2010). They reside in low density environments. The distribution of the EWs of “Green Pea” galaxies is shown in Fig. 6.14 along with the EWs for other galaxy samples for comparison. It is possible to reproduce those high EWs with photoionization models (where all contributions to the underlying continuum are properly accounted for) when one considers very young starbursts (see Figures in Appendix for line EWs, Fig. 7.11), however from the observational point of

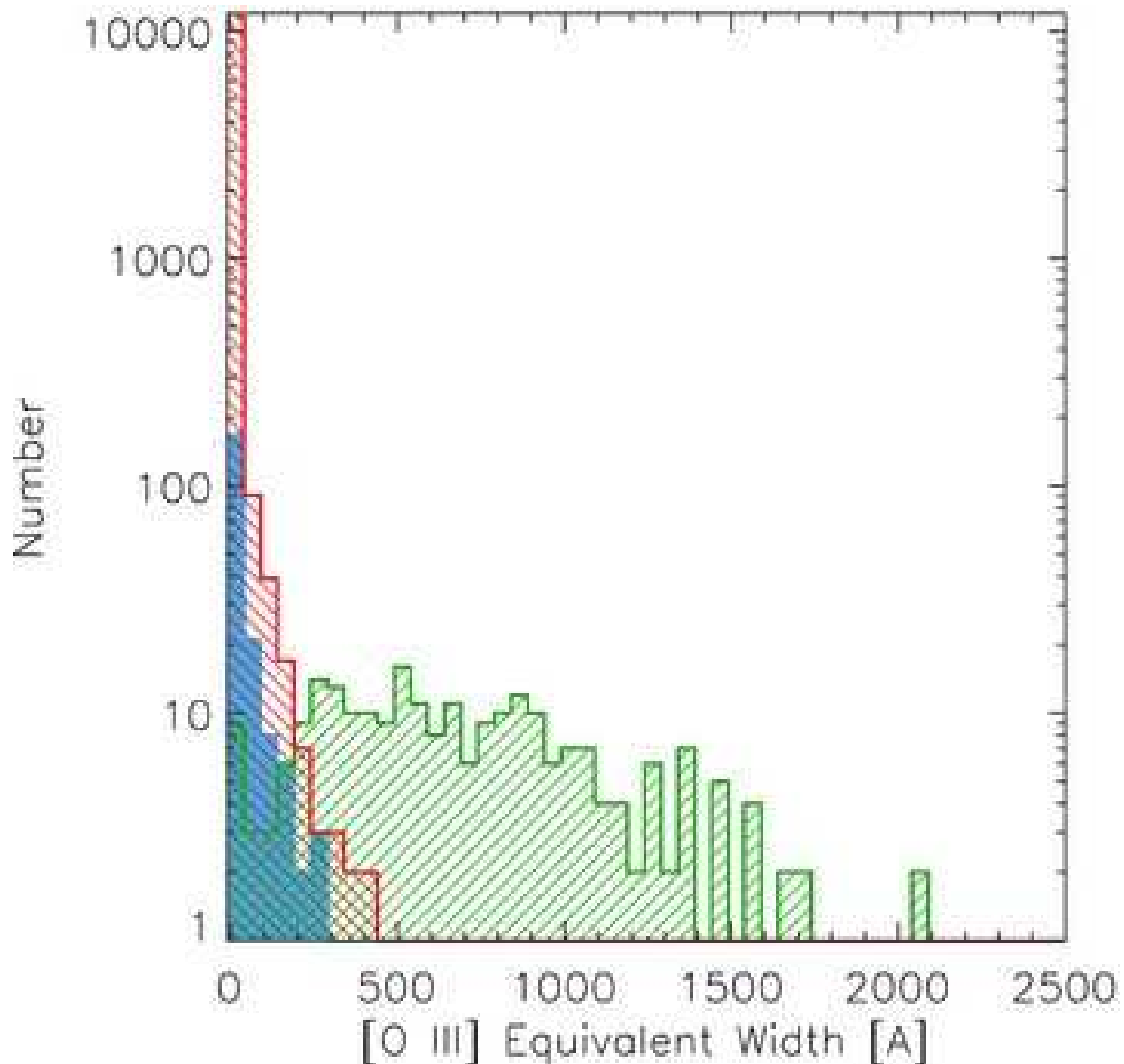


Figure 6.14: $[\text{O III}] \lambda 5007$ equivalent widths distribution: “Green Peas” (green-lined histogram), $\sim 10\,000$ comparison SDSS galaxies at the same redshift range (red-lined histogram) and local UV-luminous galaxies (UVLG) sample (SDSS DR3, blue solid histogram), Cardamone et al. (2009).

view they are very unusual in the local Universe.

Having a relatively low mass, low metallicity, very high [O III] EWs, a high SSFR and residing in low density environments, these objects appear to be the closest analogues in the local Universe to vigorously starforming objects at early epochs and makes them similar to the Ly α -N IV] emitting galaxies at high- z which contain very hot stars: Lynx arc (Fosbury et al. 2003), GDSJ033218.92-275302.7 (Raiter et al. 2010). Consequently, they are the only currently available laboratories to study extreme star forming environments.

Remarks

It would be worth performing a detailed spectroscopic study of a sample of “Green Peas” in order to obtain a clearer understanding of the physical properties and evolutionary status of this class of objects⁵. Such an understanding would create a firmer foundation for the impending campaigns, with JWST, ALMA, E-ELT and other facilities, to trace the earliest star formation episodes to occur in the Universe and to elucidate the nature of the first post Big Bang nucleosynthesis processes. Wide wavelength coverage spectra in conjunction with photoionization modelling capabilities could be used to model the nebular spectrum, both lines and continuum, to establish the properties of the photoionizing stars and measure the abundance distribution; measure emission line widths and, where possible, gradients to estimate dynamical masses; using a suitable binning, determine the shape of the continuum and, in conjunction with the modelling, distinguish the stellar from the nebular continuum; utilise the wide wavelength coverage to quantify the dust reddening separately for the lines and continuum.

⁵We have submitted an ESO X-shooter proposal “*The connection between “Green Peas” and high- z Ly α -emitters*” (PI: A. Raiter, CoIs: R. Fosbury, R. Kennicutt, H. Taimoorinia, C. Cardamone, B. Venemans) for ESO observing Period 86 aimed to observe 4 selected “Green Peas” at redshifts $z = 0.304, 0.165, 0.1621, 0.261$, however it was not accepted.

Chapter 7

Conclusion and future prospects

In this thesis I have attempted to study the rest-frame UV spectrum of high- z sources in order to search for very hot stars and provide the background for future observations. It is relevant in the context of searches for the first objects that appeared in the Universe, Pop III stars/primordial star formation sites, sources that reionized the Universe, as well as of the interpretation of already existing observations of high- z galaxies.

Theoretical properties of very metal-poor starburst galaxies in the early Universe have been discussed. Particularly, if the ionizing source is hot and the nebular metallicity is low, an enhancement of the 2γ continuum emission is expected with respect to the standard population synthesis + case B predictions. This is a feature that can be searched for in existing observations. This enhancement can affect (decrease) the EWs of UV emission lines, especially it can decrease the He II $\lambda 1640$ EW which is expected to be visible in these cases. The decreased EW of He II can be also a result of its ionization parameter dependence. Therefore, this line can be more difficult to detect at high- z than previously expected. Similar enhancement is found for Ly α line emission, the only line observed in high- z galaxy spectra. Ly α line and 2γ continuum luminosity enhancement is caused by the departures from case B recombination, which occur when the very low metallicity gas is ionized by very young and very low metallicity sources, i.e. the energies of ionizing photons significantly exceed the minimum hydrogen ionization energy (13.6 eV). Our analysis adds one more scenario that might help to explain large EW of Ly α line found in galaxy surveys and usually interpreted as a sign of top-heavy IMF or clumpy ISM. Further enhancement of Ly α at the expense of 2γ luminosity appears at higher nebular densities, as already predicted by case B recombination theory.

The observations of high- z metal UV emission lines analysed here are rather limited. However, several objects that have been found reveal similar properties, particularly the emission of N IV] line at 1486 Å (rest-frame), which indicates high stellar effective temperature. Therefore, a hot thermal ionizing source is favoured. As discussed, an AGN photoionization seems to be excluded due to the different UV spectrum expected from the models and lack of X-ray and radio emission from those sources. One could also consider shock produced by exploding SNe providing the ionizing energy. However, the kinetic energy output from one exploding supernova type II (10^{51} ergs) available for shock ionization

is around 2 orders of magnitude less than the energy available for ionization from a single star (for a star with $Q(\text{H}) = \sim 3 \times 10^{49}$, $M_{\star} = 50 M_{\odot}$ and $T_{\text{eff}} = 85$ kK as deduced in Section 4.4) over its lifetime (assumed to be 3 Myrs). The nature of the ionizing source still remains an open question.

A number of other parameters characterising those galaxies have been analysed. The density of the gas might be quite high as indicated by the detection of longer wavelength N IV] component. Possibly different density regions coexist.

The required effective stellar temperature based on the presence of N IV] emission implies very low metallicity population. Interestingly, this scenario suggests that the nebular gas metallicity is different (higher) than the stellar one. The analysis of element abundances is very difficult at the moment with so few lines available. From the analysis presented it turns out that in the region where the observed lines have been formed, carbon is significantly depleted compared to nitrogen with respect to their solar abundance ratio. High density regions (as suggested by the nitrogen line doublet ratio) might be the regions of stellar wind interactions. Perhaps, carbon might be located in the regions with different physical conditions (PDR) and possibly could be observed in a different part of the spectrum. This issue needs to be further investigated when more lines are available for observations. Detailed abundance studies will allow the tracing of nucleosynthesis products and their mixing with the ISM, which in the case of very high- z galaxies will give us an insight into the first stellar nucleosynthetic episodes in the Universe.

Apart from large emission line EWs being a result of a very weak nebular radiation-dominated continuum, the properties of the overall shape of the SED have been analysed. The shape of the flat (in F_{ν}) continuum is modulated in the presence of strong nebular emission lines. In this context, a particularly interesting feature is the presence of strong [O III] $\lambda\lambda 4959, 5007$ lines, which in the broad-band photometry dominating the flux in one of the bands, can mimic the Balmer break of an old stellar population. This causes the confusion in the determination of the age of the population, and therefore an old galaxy with a strong Balmer break can be inferred instead of a very young starburst.

Not including the nebular radiation (continuum and lines) in the standard SED fitting procedure, commonly used to infer the properties of galaxies, can cause confusion. At high- z the longer wavelength spectrum is not available, therefore it is difficult to infer the nature of the source having only the UV part of the spectrum. Consequently, it is valuable to study similar sources at low- z . The so-called ‘‘Green Pea’’ galaxies reveal very similar properties, however it remains a subject for future investigations, whether they are low- z analogs of high- z rapidly star forming Ly α emitters.

The scenario of evolution of N IV]-emitting galaxies is not clear. Are they just a very short-lived phase in early galaxy evolution? That would explain the very small number of sources found. Assuming the mass found for the $z=5.56$ source, the number of galaxies implied by the galaxy mass function obtained from the GOODS-S data implies the probability of finding N IV]-emitting source between redshift 3 and 4 (where one source has been found) of $\approx 2 \times 10^{-4}$ (assuming that all the galaxies have gone through N IV]-emitting phase in this redshift interval). This corresponds to a very short duration of this phase of galaxy evolution. Pockets of pristine material are expected to exist until quite low- z (~ 2.5) as

shown by numerical simulations. Are N IV] emitting galaxies remaining lower- z primordial star formation sites with unusual (top-heavy) IMF ? It remains an open question for future studies.

The observations of more emission lines, IR spectra of high- z sources at higher spatial resolution and higher sensitivity will allow more detailed studies, as well as the discovery of more sources of this kind. Future facilities will also push the observations to higher redshifts reaching the epoch when truly primordial galaxies can be observed. In a few years JWST, E-ELT and ALMA will greatly improve the ability to study objects at very high- z and start delivering exciting discoveries. I'm looking forward to learning more about the early Universe using those telescopes and hope to continue my work on this exciting topic!!!

Appendix

Equivalent widths of 11 emission lines are shown as calculated based on CLOUDY photoionization models. Schaerer’s evolutionary stellar population synthesis models with Salpeter IMF 1-100 M_{\odot} and SFH = “instentaneous burst” (for simplicity one IMF and one SFH) are used to define the ionizing source. The nebular metallicity is assumed to be equal to the stellar one and defined by scaled solar abundances. “Total” indicates that the sum of line fluxes in case of doublets/multiplets has been taken into account.

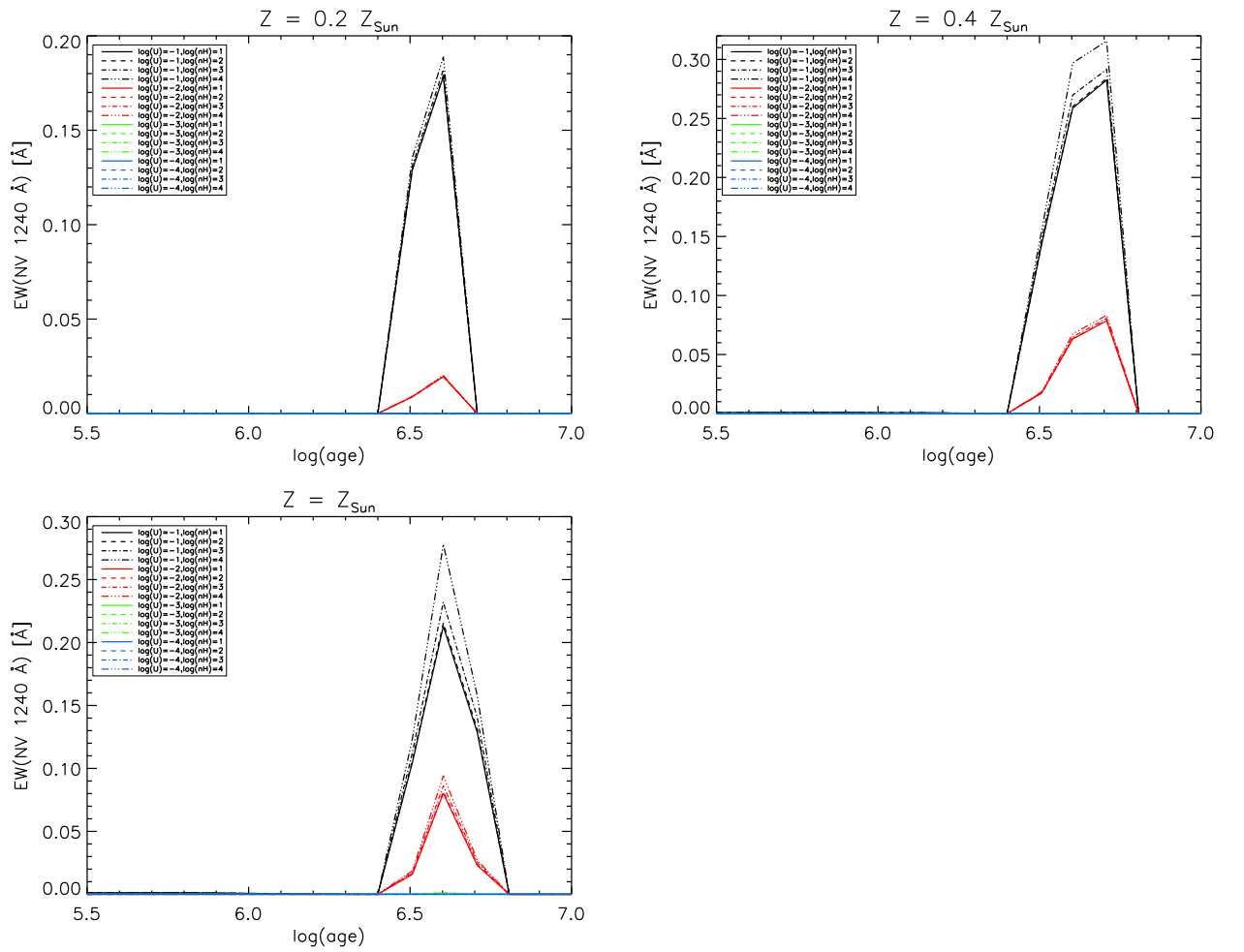


Figure 7.1: N v 1240 Å (total) line EW for 3 different metallicities: 0.004, 0.008, 0.02 (0.2, 0.4, 1 Z_{\odot}).

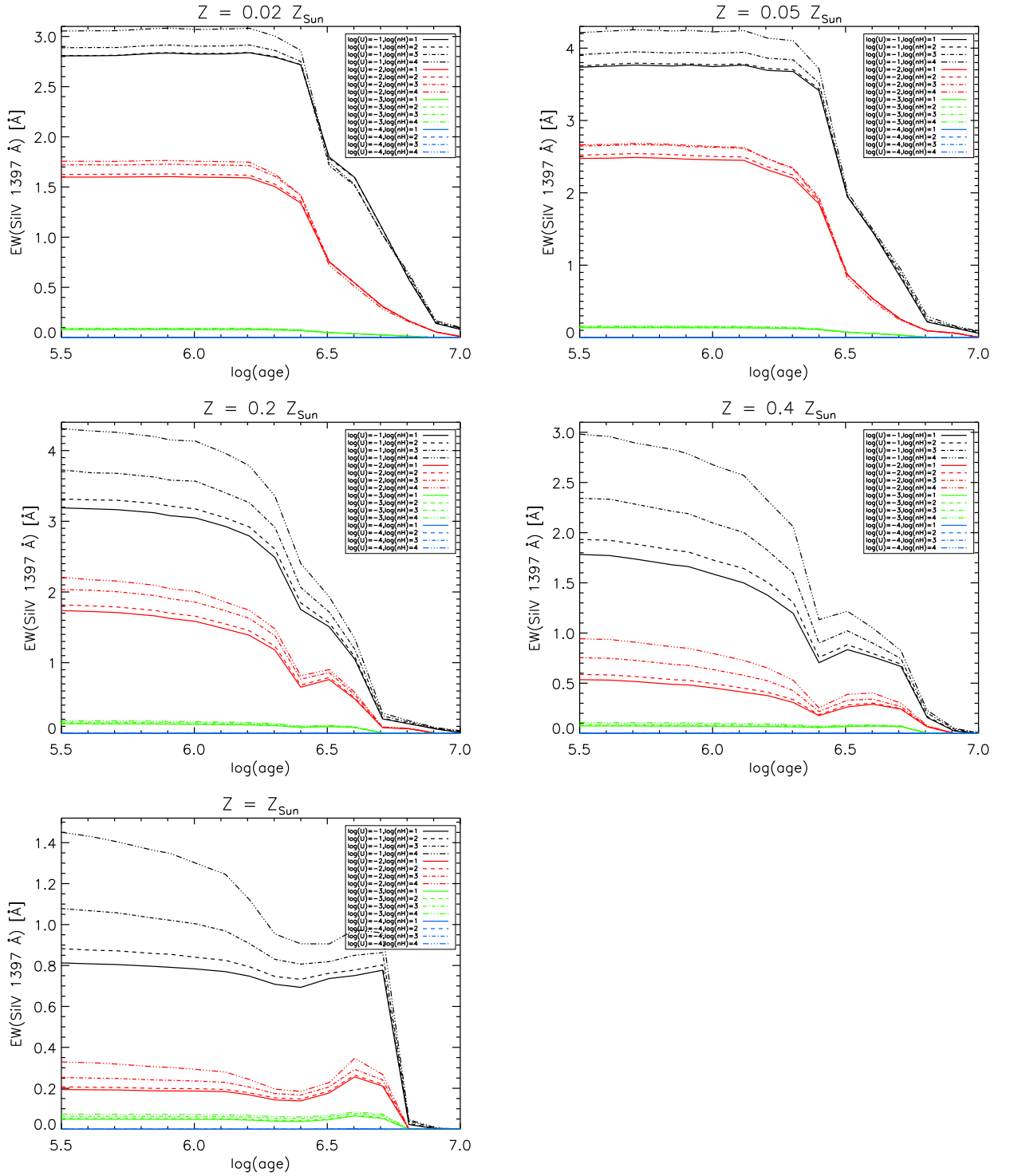


Figure 7.2: SiIV 1397 \AA (total) line EW for 5 different metallicities: 0.0004, 0.001, 0.004, 0.008, 0.02 (0.02, 0.05, 0.2, 0.4, 1 Z_{\odot}).

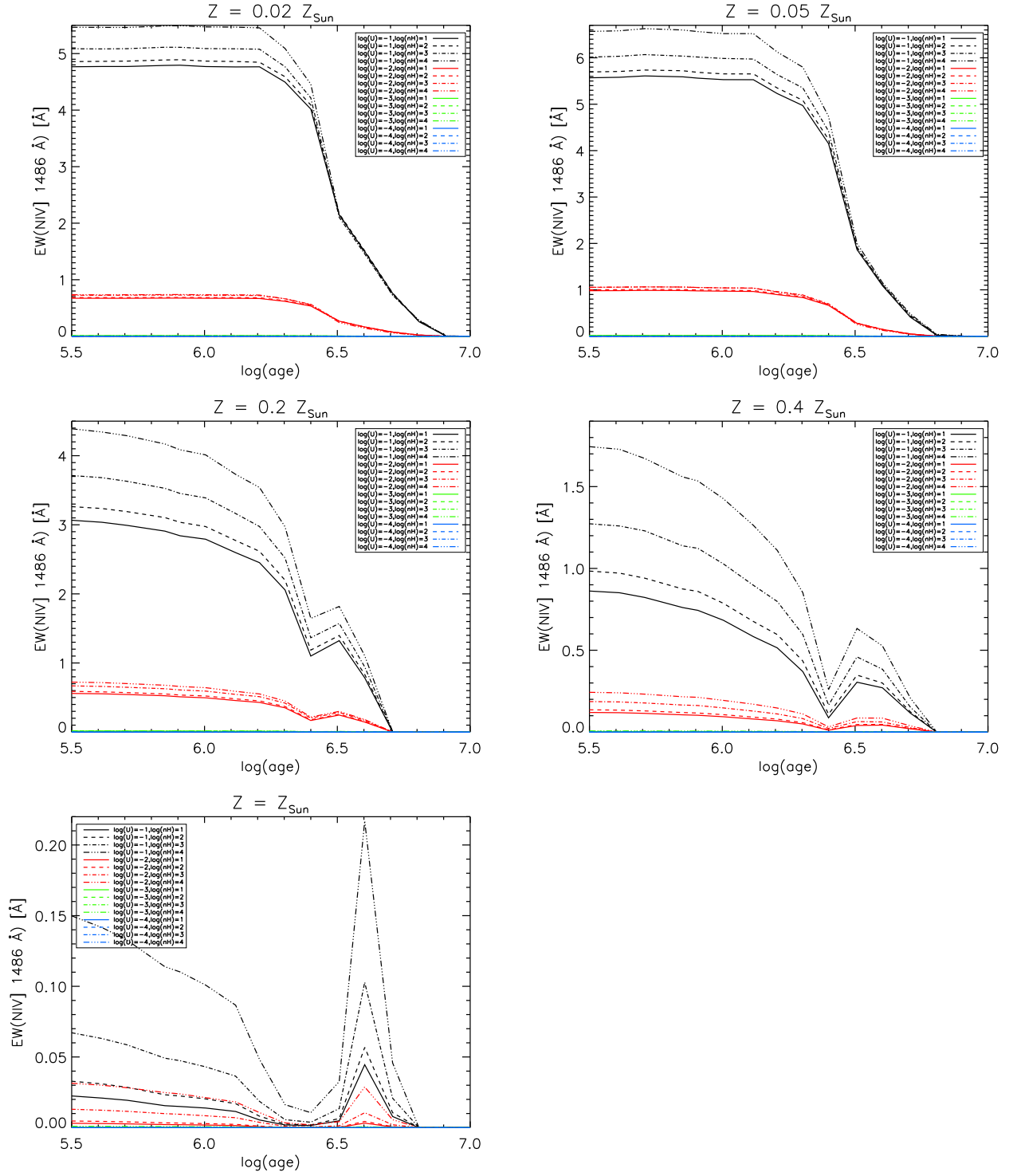


Figure 7.3: N iv] 1486 Å (total) line EW for 5 different metallicities: 0.0004, 0.001, 0.004, 0.008, 0.02.

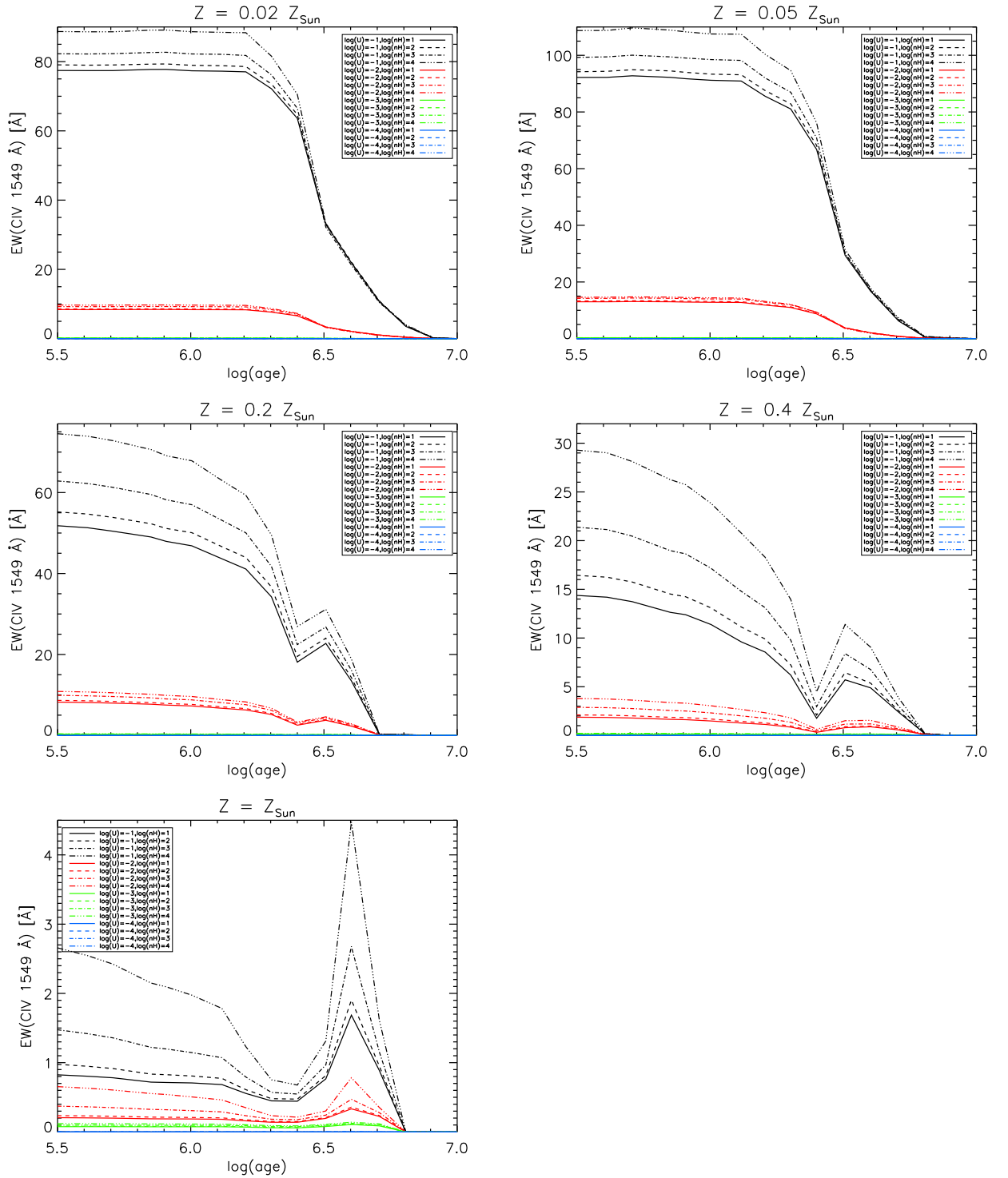


Figure 7.4: C IV 1549 Å (total) line EW for 5 different metallicities: 0.0004, 0.001, 0.004, 0.008, 0.02.

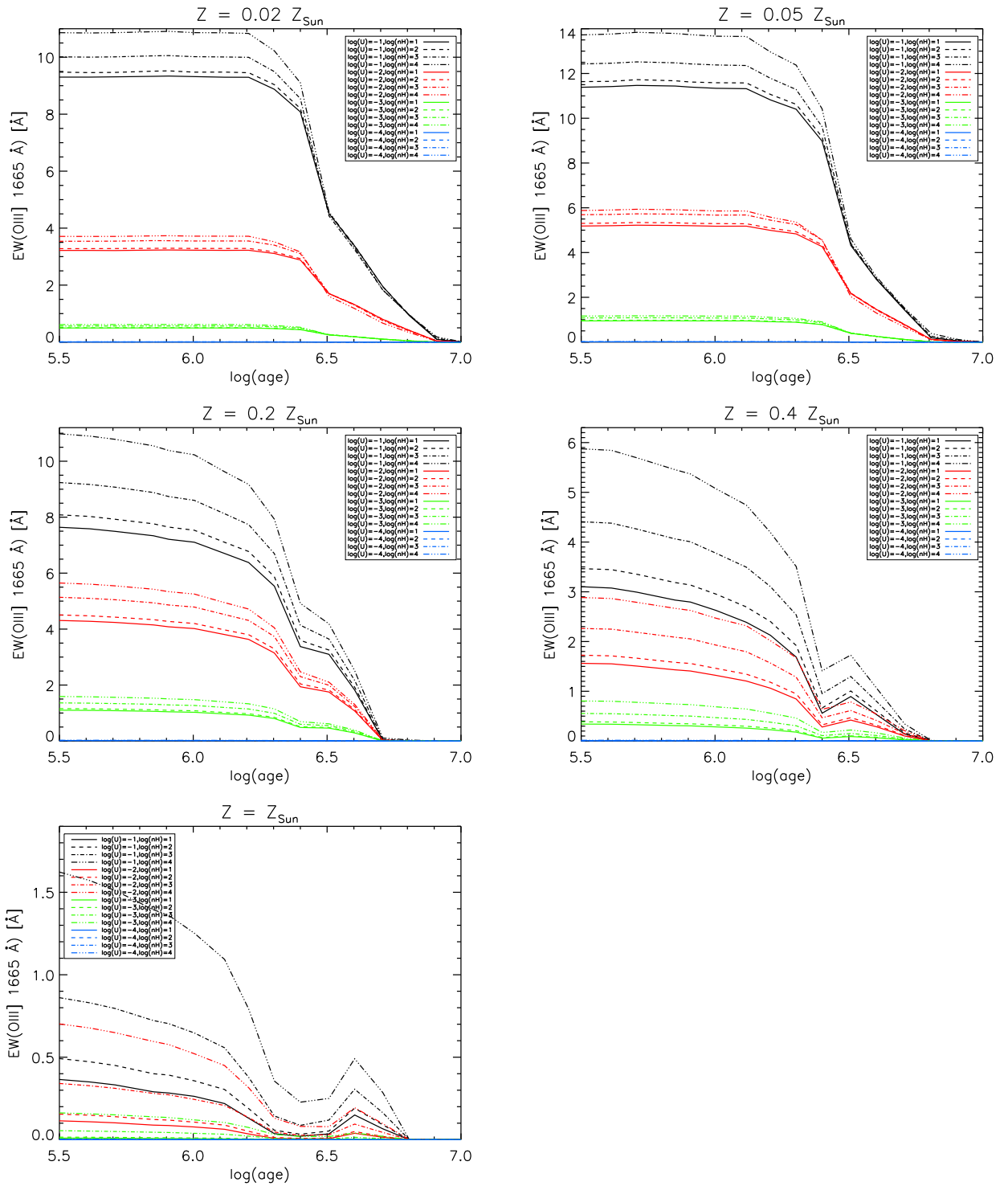


Figure 7.5: O III] 1665 Å (total) line EW for 5 different metallicities: 0.0004, 0.001, 0.004, 0.008, 0.02.

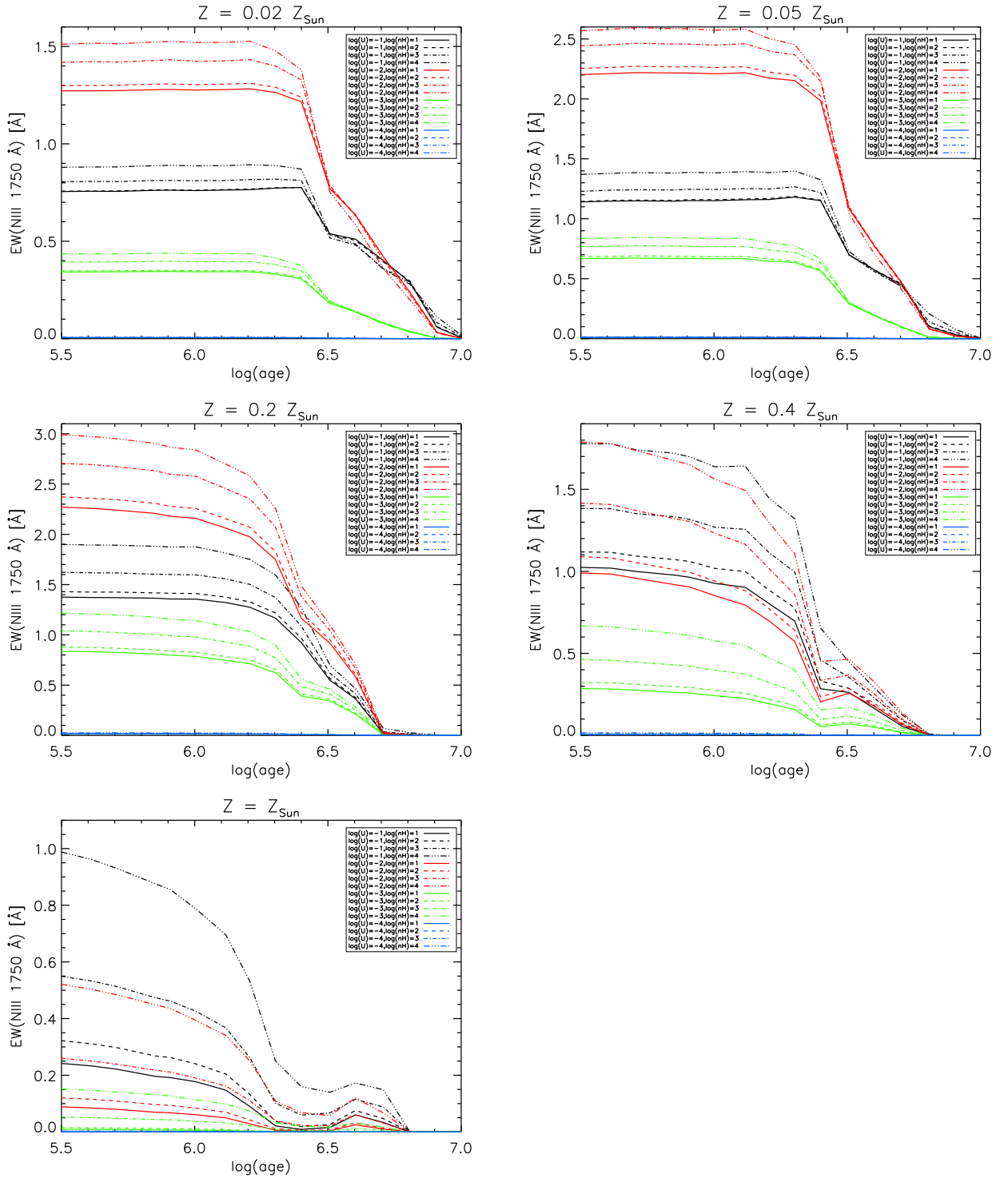


Figure 7.6: N III] 1750 \AA (total) line EW for 5 different metallicities: 0.0004, 0.001, 0.004, 0.008, 0.02.

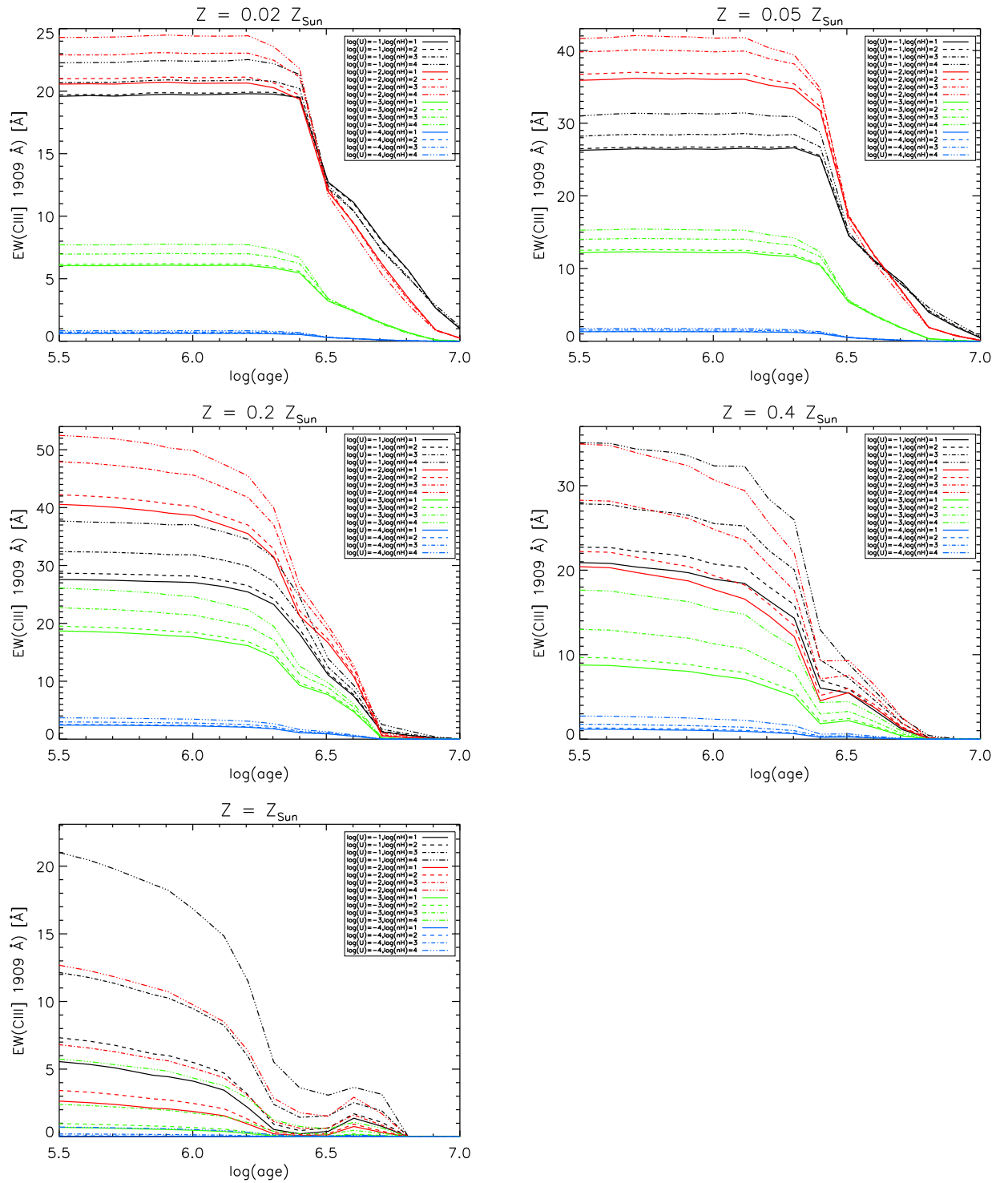


Figure 7.7: C III] 1909 \AA (total) line EW for 5 different metallicities: 0.0004, 0.001, 0.004, 0.008, 0.02.

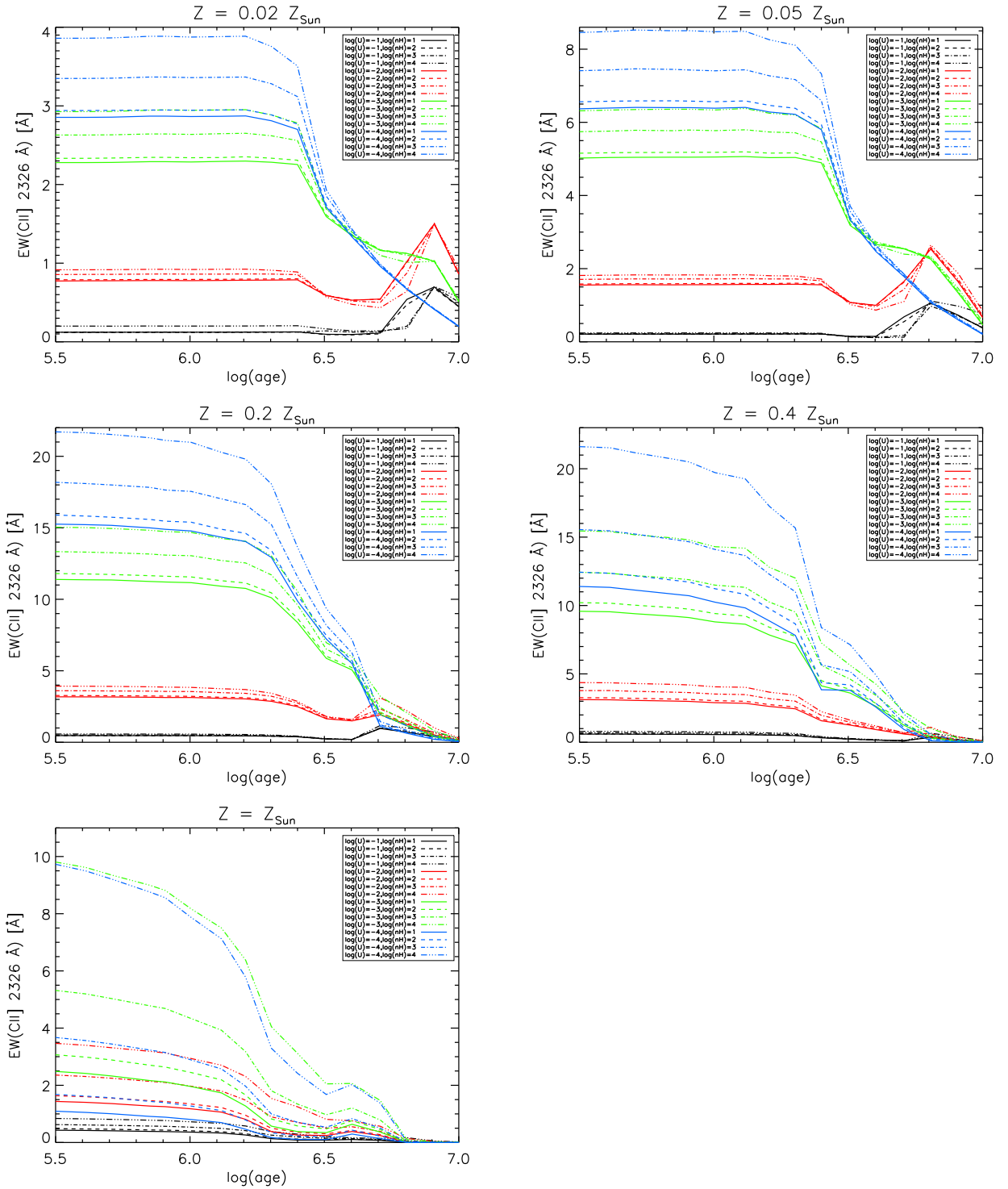


Figure 7.8: C II] 2326 Å (total) line EW for 5 different metallicities: 0.0004, 0.001, 0.004, 0.008, 0.02.

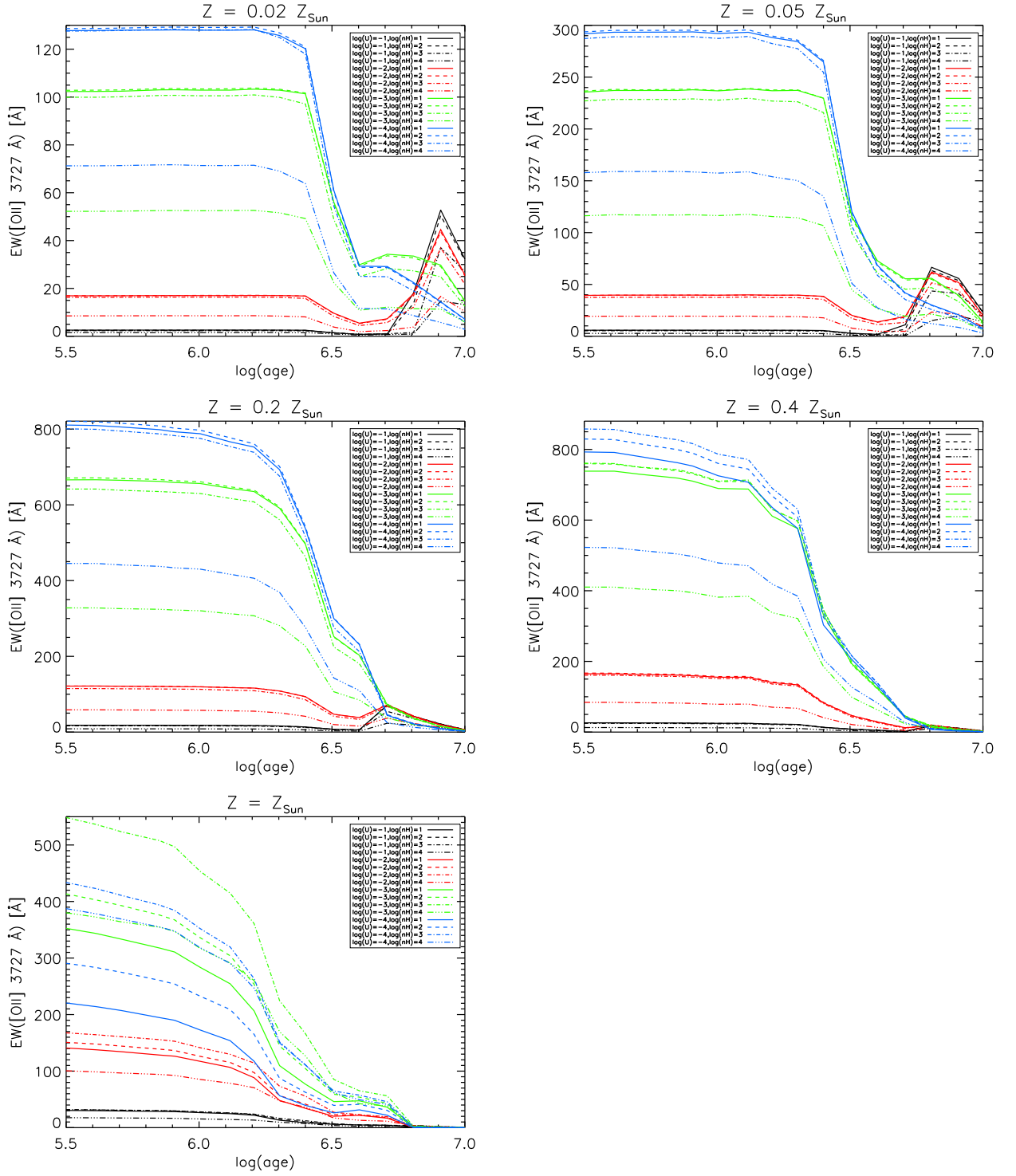


Figure 7.9: [O II] 3727 (total) Å line EW for 5 different metallicities: 0.0004, 0.001, 0.004, 0.008, 0.02.

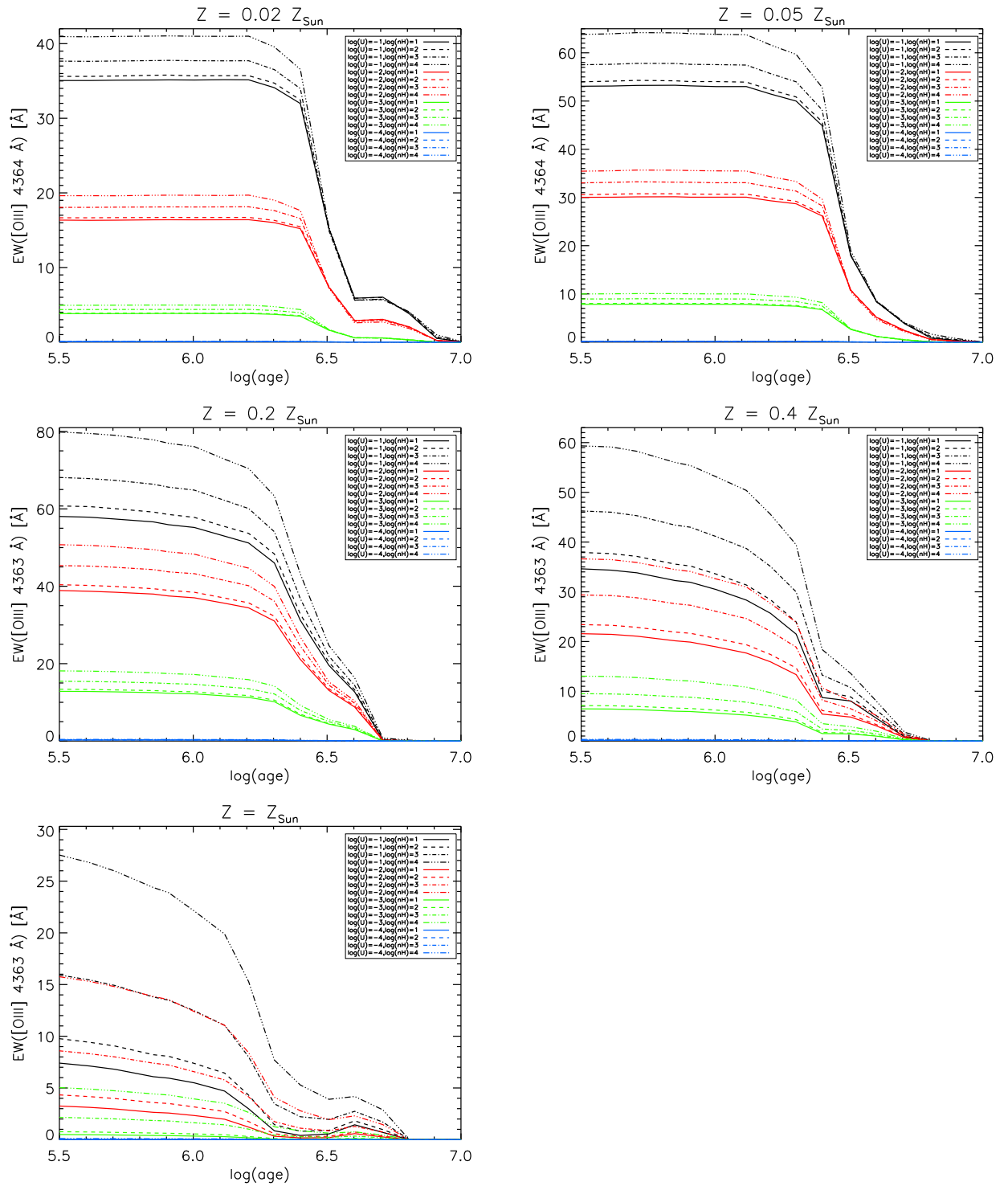


Figure 7.10: [O III] 4363 Å (total) line EW for 5 different metallicities: 0.0004, 0.001, 0.004, 0.008, 0.02.

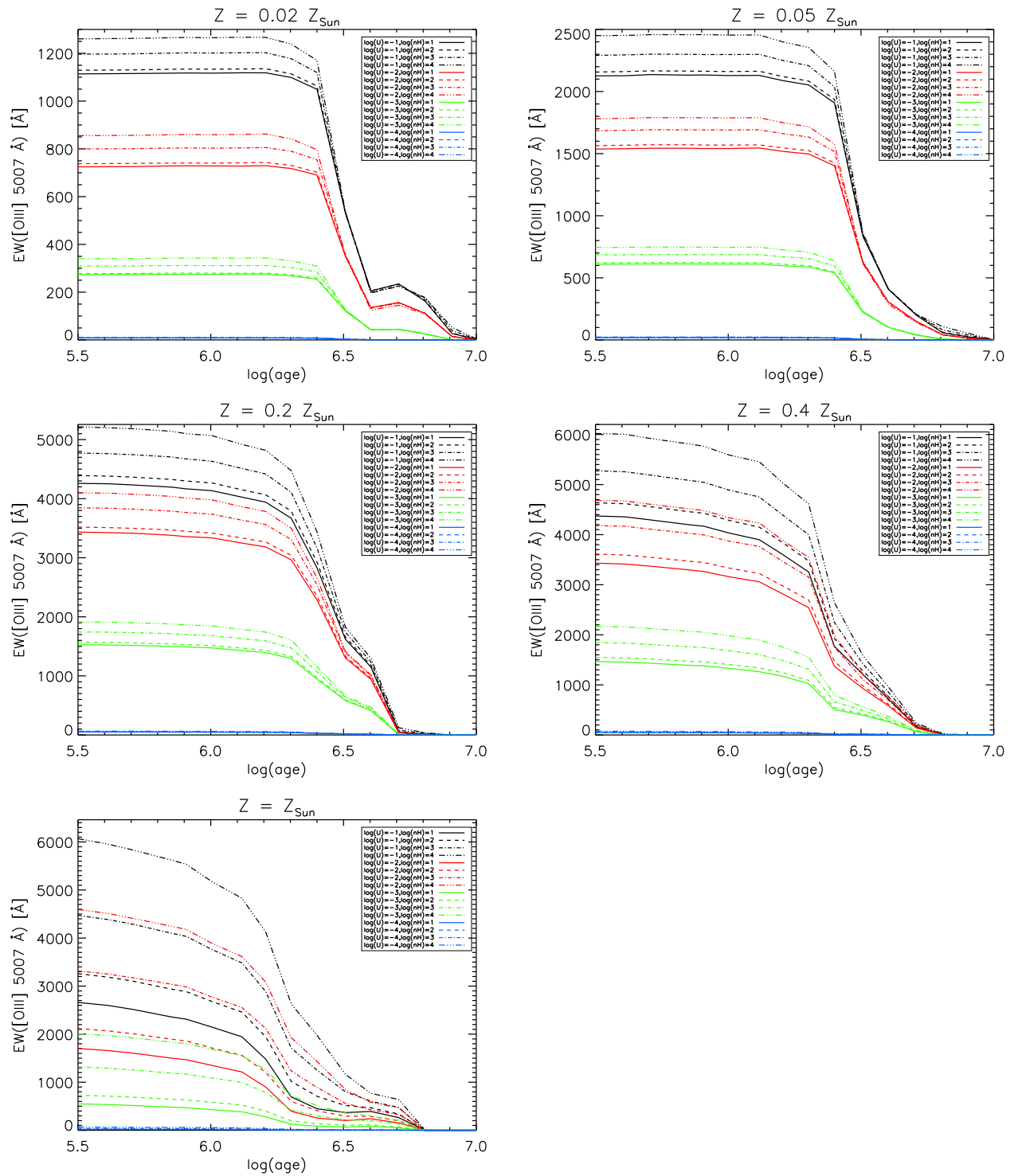


Figure 7.11: [O III] 5007 Å line EW for 5 different metallicities: 0.0004, 0.001, 0.004, 0.008, 0.02.

Bibliography

- Abel, T., Bryan, G. L., & Norman, M. L. 2000, *ApJ*, 540, 39
- Abel, T., Bryan, G. L., & Norman, M. L. 2002, *Science*, 295, 93
- Amorín, R. O., Pérez-Montero, E., & Vílchez, J. M. 2010, *ApJ*, 715, L128
- Baldwin, J. A., Hamann, F., Korista, K. T., et al. 2003, *ApJ*, 583, 649
- Baldwin, J. A., Phillips, M. M., & Terlevich, R. 1981, *PASP*, 93, 5
- Balestra, I., Mainieri, V., Popesso, P., et al. 2010, *A&A*, 512, A12+
- Bertin, E. & Arnouts, S. 1996, *A&AS*, 117, 393
- Binette, L., Groves, B., Villar-Martín, M., Fosbury, R. A. E., & Axon, D. J. 2003, *A&A*, 405, 975
- Bond, J. R., Arnett, W. D., & Carr, B. J. 1984, *ApJ*, 280, 825
- Bottorff, M. C., Ferland, G. J., & Straley, J. P. 2006, *PASP*, 118, 1176
- Bouwens, R. J., Illingworth, G. D., Oesch, P. A., et al. 2010, *ApJ*, 709, L133
- Bromm, V., Coppi, P. S., & Larson, R. B. 1999, *ApJ*, 527, L5
- Bromm, V., Kudritzki, R. P., & Loeb, A. 2001, *ApJ*, 552, 464
- Bruzual, G. & Charlot, S. 2003, *MNRAS*, 344, 1000
- Cardamone, C., Schawinski, K., Sarzi, M., et al. 2009, *MNRAS*, 399, 1191
- Christlieb, N., Bessell, M. S., Beers, T. C., et al. 2002, *Nature*, 419, 904
- Ciardi, B., Ferrara, A., Marri, S., & Raimondo, G. 2001, *MNRAS*, 324, 381
- Coppin, K. E. K., Smail, I., Alexander, D. M., et al. 2009, *MNRAS*, 395, 1905
- Cowie, L. L., Songaila, A., Hu, E. M., & Cohen, J. G. 1996, *AJ*, 112, 839
- Davidson, K., Dufour, R. J., Walborn, N. R., & Gull, T. R. 1986, *ApJ*, 305, 867

- Davidson, K. & Kinman, T. D. 1985, *ApJS*, 58, 321
- Dawson, S., Rhoads, J. E., Malhotra, S., et al. 2004, *ApJ*, 617, 707
- Dickinson, M. & GOODS Legacy Team. 2001, in *Bulletin of the American Astronomical Society*, Vol. 33, *Bulletin of the American Astronomical Society*, 820–+
- Ellis, R. S. 2008, *Observations of the High Redshift Universe*, ed. Loeb, A., Ferrara, A., & Ellis, R. S., 259–364
- Ellison, S. L., Songaila, A., Schaye, J., & Pettini, M. 2000, *AJ*, 120, 1175
- Ferland, G. 2008, *Hazy*, A brief introduction to Cloudy, version 08
- Ferland, G. J., Korista, K. T., Verner, D. A., et al. 1998, *PASP*, 110, 761
- Finkelstein, S. L., Papovich, C., Giavalisco, M., et al. 2010, *ApJ*, 719, 1250
- Finkelstein, S. L., Rhoads, J. E., Malhotra, S., Grogin, N., & Wang, J. 2008, *ApJ*, 678, 655
- Fosbury, R. A. E., Villar-Martín, M., Humphrey, A., et al. 2003, *ApJ*, 596, 797
- Frebel, A., Aoki, W., Christlieb, N., et al. 2005, *Nature*, 434, 871
- Giacconi, R., Zirm, A., Wang, J., et al. 2002, *ApJS*, 139, 369
- Giavalisco, M., Ferguson, H. C., Koekemoer, A. M., et al. 2004, *ApJ*, 600, L93
- Glikman, E., Djorgovski, S. G., Stern, D., Bogosavljević, M., & Mahabal, A. 2007, *ApJ*, 663, L73
- Gnedin, N. Y., Kravtsov, A. V., & Chen, H. 2008, *ApJ*, 672, 765
- Grazian, A., Fontana, A., de Santis, C., et al. 2006, *A&A*, 449, 951
- Hayes, M. & Östlin, G. 2006, *A&A*, 460, 681
- Heger, A., Fryer, C. L., Woosley, S. E., Langer, N., & Hartmann, D. H. 2003a, *ApJ*, 591, 288
- Heger, A. & Woosley, S. E. 2002, *ApJ*, 567, 532
- Heger, A., Woosley, S. E., Fryer, C. L., & Langer, N. 2003b, in *From Twilight to Highlight: The Physics of Supernovae*, ed. W. Hillebrandt & B. Leibundgut, 3–540
- Hopkins, A. M. 2004, *ApJ*, 615, 209
- Inoue, A. K. 2010, *MNRAS*, 401, 1325
- Jimenez, R. & Haiman, Z. 2006, *Nature*, 440, 501

- Johnson, J. L., Greif, T. H., Bromm, V., Klessen, R. S., & Ippolito, J. 2009, MNRAS, 399, 37
- Karlsson, T., Johnson, J. L., & Bromm, V. 2008, ApJ, 679, 6
- Kauffmann, G., Heckman, T. M., Tremonti, C., et al. 2003, MNRAS, 346, 1055
- Keenan, F. P., Ramsbottom, C. A., Bell, K. L., et al. 1995, ApJ, 438, 500
- Kellermann, K. I., Fomalont, E. B., Mainieri, V., et al. 2008, ApJS, 179, 71
- Kennicutt, Jr., R. C. 1998, ARA&A, 36, 189
- Kewley, L. J. & Dopita, M. A. 2002, ApJS, 142, 35
- Krtićka, J. & Kubát, J. 2006, in Astronomical Society of the Pacific Conference Series, Vol. 353, Stellar Evolution at Low Metallicity: Mass Loss, Explosions, Cosmology, ed. H. J. G. L. M. Lamers, N. Langer, T. Nugis, & K. Annuk, 133–+
- Larson, R. B. 1998, MNRAS, 301, 569
- Luridiana, V. 2009, Ap&SS, 324, 361
- Luridiana, V., Peimbert, A., Peimbert, M., & Cerviño, M. 2003, ApJ, 592, 846
- Maiolino, R., Caselli, P., Nagao, T., et al. 2009, A&A, 500, L1
- Maiolino, R., Cox, P., Caselli, P., et al. 2005, A&A, 440, L51
- Maiolino, R., Nagao, T., Grazian, A., et al. 2008, A&A, 488, 463
- Malhotra, S. & Rhoads, J. E. 2002, ApJ, 565, L71
- Meynet, G., Ekström, S., & Maeder, A. 2006, A&A, 447, 623
- Miley, G. & De Breuck, C. 2008, A&A Rev., 15, 67
- Modigliani, A. 2010, Very Large Telescope - X-shooter Pipeline User Manual
- Mori, M. & Umemura, M. 2006, Nature, 440, 644
- Nagao, T., Motohara, K., Maiolino, R., et al. 2005, ApJ, 631, L5
- Nagao, T., Sasaki, S. S., Maiolino, R., et al. 2008, ApJ, 680, 100
- Nonino, M., Dickinson, M., Rosati, P., et al. 2009, ApJS, 183, 244
- Ono, Y., Ouchi, M., Shimasaku, K., et al. 2010, ArXiv e-prints

- Osterbrock, D. E. & Ferland, G. J. 2006, *Astrophysics of gaseous nebulae and active galactic nuclei*
- Ouchi, M., Ono, Y., Egami, E., et al. 2009, *ApJ*, 696, 1164
- Ouchi, M., Shimasaku, K., Akiyama, M., et al. 2008, *ApJS*, 176, 301
- Pagel, B. E. J., Edmunds, M. G., Blackwell, D. E., Chun, M. S., & Smith, G. 1979, *MNRAS*, 189, 95
- Panagia, N. 1973, *AJ*, 78, 929
- Panagia, N. 2002, *ArXiv Astrophysics e-prints*
- Panagia, N. 2005, in *Astrophysics and Space Science Library*, Vol. 327, *The Initial Mass Function 50 Years Later*, ed. E. Corbelli, F. Palla, & H. Zinnecker, 479–+
- Partridge, R. B. & Peebles, P. J. E. 1967, *ApJ*, 147, 868
- Pentericci, L., Grazian, A., Fontana, A., et al. 2009, *A&A*, 494, 553
- Popesso, P., Dickinson, M., Nonino, M., et al. 2009, *A&A*, 494, 443
- Prescott, M. K. M., Dey, A., & Jannuzi, B. T. 2009, *ApJ*, 702, 554
- Pritchett, C. J. 1994, *PASP*, 106, 1052
- Raiter, A., Fosbury, R. A. E., & Teimoorinia, H. 2010, *A&A*, 510, A109+
- Razoumov, A. O. & Sommer-Larsen, J. 2009, *ArXiv e-prints*
- Retzlaff, J., Rosati, P., Dickinson, M., et al. 2010, *A&A*, 511, A50+
- Rubin, D., Hony, S., Madden, S. C., et al. 2009, *A&A*, 494, 647
- Salpeter, E. E. 1955, *ApJ*, 121, 161
- Santini, P., Fontana, A., Grazian, A., et al. 2009, *A&A*, 504, 751
- Scalo, J. M. 1986, *Fundamentals of Cosmic Physics*, 11, 1
- Scannapieco, E., Schneider, R., & Ferrara, A. 2003, *ApJ*, 589, 35
- Schaerer, D. 2002, *A&A*, 382, 28
- Schaerer, D. 2003, *A&A*, 397, 527
- Schaerer, D. 2008, in *IAU Symposium*, Vol. 255, *IAU Symposium*, ed. L. K. Hunt, S. Maden, & R. Schneider, 66–74

- Schaerer, D. & de Barros, S. 2009, *A&A*, 502, 423
- Schaerer, D. & de Barros, S. 2010, *A&A*, 515, A73+
- Schaerer, D. & Pelló, R. 2005, *MNRAS*, 362, 1054
- Schaerer, D. & Vacca, W. D. 1998, *ApJ*, 497, 618
- Schaerer, D. & Verhamme, A. 2008, *A&A*, 480, 369
- Schneider, R., Ferrara, A., Natarajan, P., & Omukai, K. 2002, *ApJ*, 571, 30
- Schneider, R., Ferrara, A., Salvaterra, R., Omukai, K., & Bromm, V. 2003, *Nature*, 422, 869
- Songaila, A. 2001, *ApJ*, 561, L153
- Stark, D. P., Bunker, A. J., Ellis, R. S., Eyles, L. P., & Lacy, M. 2007, *ApJ*, 659, 84
- Stasińska, G. 2007, ArXiv e-prints
- Stasińska, G. & Schaerer, D. 1999, *A&A*, 351, 72
- Stasińska, G. & Tytenda, R. 1986, *A&A*, 155, 137
- Stiavelli, M. 2009, *From First Light to Reionization: The End of the Dark Ages*, ed. Stiavelli, M.
- Tinsley, B. M. 1980, *Fundamentals of Cosmic Physics*, 5, 287
- Tornatore, L., Ferrara, A., & Schneider, R. 2007, *MNRAS*, 382, 945
- Tumlinson, J. 2006, *ApJ*, 641, 1
- Tumlinson, J., Giroux, M. L., & Shull, J. M. 2001, *ApJ*, 550, L1
- Tumlinson, J. & Shull, J. M. 2000, *ApJ*, 528, L65
- Tumlinson, J., Shull, J. M., & Venkatesan, A. 2003, *ApJ*, 584, 608
- Vanzella, E., Cristiani, S., Dickinson, M., et al. 2008, *A&A*, 478, 83
- Vanzella, E., Cristiani, S., Dickinson, M., et al. 2005, *A&A*, 434, 53
- Vanzella, E., Cristiani, S., Dickinson, M., et al. 2006, *A&A*, 454, 423
- Vanzella, E., Giavalisco, M., Dickinson, M., et al. 2009, *ApJ*, 695, 1163
- Vanzella, E., Grazian, A., Hayes, M., et al. 2010, *A&A*, 513, A20+
- Vernet, J. & Mason, E. 2010, *ESO*, 397

Villar-Martín, M., Cerviño, M., & González Delgado, R. M. 2004, MNRAS, 355, 1132

Wiklind, T., Dickinson, M., Ferguson, H. C., et al. 2008, ApJ, 676, 781

Wise, J. H. & Cen, R. 2009, ApJ, 693, 984

Woosley, S. E. & Weaver, T. A. 1986, ARA&A, 24, 205

Yamada, S. F., Sasaki, S. S., Sumiya, R., et al. 2005, PASJ, 57, 881

Zackrisson, E., Bergvall, N., & Leitert, E. 2008, ApJ, 676, L9

Acknowledgements

This work would not have been possible without the support of many people.

First of all I would like to express my thanks to my supervisor, Robert Fosbury. Bob, you were the best PhD supervisor !!! I was very very lucky to have a chance to work with you. I would like to thank for all the help and support, time given to me, great atmosphere at work, sharing your passion for science with me and for teaching me to not be afraid of new ideas !

I would like to thank Daniel Schaerer, who I had a chance to work with during my PhD and who greatly contributed to this work. It was a very good collaboration which I hope to continue. I'm grateful also for hosting me in Geneva Observatory in June 2009.

I thank Hossein Taimoorinia, who contributed to Chapter 4 of this thesis working on the photometry; Massimo Stiavelli and Nino Panagia for hosting me at STSCi in Baltimore in February/March 2008; everybody who collaborated with me on the proposals; everybody who helped me to deal with the X-shooter data: Joel Vernet, Andrea Modigliani, Lise Christensen, Bram Venemans; Piero Rosati for being my second supervisor; Alex Böhnert for translating the abstract to German; and everybody at ESO who helped me in any way, I was very lucky to work in this friendly and lively scientific atmosphere.

I would like to thank my Master project supervisor, Bronisław Rudak, who convinced me to apply to the IMPRS school and kept supporting me during my PhD.

Szczególne podziękowania składam mojej rodzinie, w szczególności rodzicom, za ich ciągłe wsparcie i wiarę we mnie.

I would like to thank my friends for their support, especially the ones in Garching who made the time I spent here very enjoyable, in particular:

Monique: Por todas as grandes festas (eu nunca dançei tanto quanto durante meu doutorado!!), por admirar as pessoas lá ;), pelos cafés, as caminhadas ao redor do lago, jogar conversa fora, as risadas, os jantares, por dividir vídeos “interessantes”, e todo o tempo que passamos juntas, obrigada!!!

Robo: Ďakujem za všetky spoločne strávené chvíle a za všetku zábavu, predovšetkým tancovanie. Bez teba by to nebolo ono Šuhada !

Pooja: Dhanyavad Pooja mere saath samay bitaney ke liyee aur mera khyal rakhney

ke liye. Tumahrey saath kaafi, nasta, chai aur wartalap main bitayey pal mere liye anmol hai aur main usey hamesa yaad rakhungi.

I thank Dudu for reading this thesis and his (very) critical comments ;) Beijos !

Curriculum Vitae

Anna Raiter

European Southern Observatory
Karl-Schwarzschild-Str. 2
85748 Garching, Germany

Personal data

- Date of birth: 7th June 1983
- Birthplace: Szczecin, Poland
- Nationality: Polish
- Home address: Rynek 15b / 5, 66-440 Skwierzyna, Poland

Education

- MSc in Astronomy, Nicolaus Copernicus University, Torun, Poland, 2002 – 2007
- PhD in Astrophysics (International Max Planck Research School), European Southern Observatory / Ludwig – Maximilians – Universität, Munich, Germany, 2007 – 2010

Publications

- “*Lyman alpha emitters in the GOODS-S field – the powerful pure nebular SED with NIV] emission at $z = 5.563$* ”, Raiter A., Fosbury R., Taimoorinia H., A & A 2010, 510, 109
- “*Predicted UV properties of the very metal-poor starburst galaxies*”, Raiter A., Schaerer D., Fosbury R., arXiv:1008.2114, A & A 2010 in press

Conferences, schools

- XX International Conference for Physics Students, 12 – 18 August 2005, Coimbra, Portugal, poster contribution
- II Polish Astronomy Students Seminar, 27 – 30 September 2005, Warsaw, Poland
- IV Polish Physics Student Clubs Session, 18 – 20 November 2005, Cracow, Poland
- Summer School “Evolution of Galaxies and their large-scale environment”, 2 – 7 July 2006, Bad Honnef, Germany
- XXI International Conference for Physics Students, 14 - 21 August 2006, Bucharest, Romania, poster contribution
- III Polish Astronomy Students Seminar, 19 - 22 September 2006, Torun, Poland
- Astro-PF Workshop on Gamma-Ray Bursts, 4 - 6 October 2006, Warsaw, Poland
- XVIII Canary Islands Winter School of Astrophysics “The emission line Universe”, 20 November – 1 December 2006, Puerto de la Cruz, Tenerife, Spain, poster contribution
- IAU Symposium “Low metallicity star formation: from the first stars to dwarf galaxies”, 16 – 20 June 2008, Rapallo , Italy
- XXIVth IAP Colloquium “Far away: light in the young Universe at redshift beyond 3”, 7 – 11 July 2008, Paris, France, poster contribution
- “When the Universe formed stars”, 17 – 21 November 2008, Martinique Island, France, poster contribution
- XXVth IAP Colloquium “The Lyman alpha Universe”, 6 – 10 July 2009, Paris, France, oral contribution
- “Cosmological reionization”, 16 – 20 February 2010, Allahabad, India, oral contribution
- IMPRS Summer School “First stars & cosmic reionization”, 6 – 10 September 2010, Heidelberg, Germany

Practice/visits

- Summer Project at Nicolaus Copernicus Astronomical Center, Polish Academy of Sciences, supervisor: Prof. B. Rudak, July / August 2006 (5 weeks)
- 18 February – 7 March 2008 (3 weeks) – visitor at Space Telescope Science Institute, Baltimore, USA, advisors: Dr. Massimo Stiavelli, Prof. Nino Panagia

- 22 – 26 June 2009 (one week) – visit at the Geneva Observatory, Switzerland, hosted by Prof. Daniel Schaerer

Teaching experience

- September – October 2005 (5 weeks) – teaching practice (physics and astronomy) at W. Jagiello Junior High School (age: 13-16), Skwierzyna, Poland
- September – October 2006 (5 weeks) – teaching practice (physics and astronomy) at S. Lem Technical High School (age: 16-19) Skwierzyna, Poland